NOVEL ARCHITECTURES FOR BROADBAND FREE-SPACE OPTICAL COMMUNICATIONS: DEEP-SPACE AND TERRESTRIAL OPTICAL LINKS

A Thesis
Presented to
The Academic Faculty

by

Ali Javed Hashmi

In Partial Fulfillment
of the Requirements for the Degree
Doctor of Philosophy in Electrical and Computer Engineering

Georgia Institute of Technology
August 2010

COPYRIGHT 2010 BY ALI JAVED HASHMI

NOVEL ARCHITECTURES FOR BROADBAND FREE-SPACE OPTICAL COMMUNICATIONS: DEEP-SPACE AND TERRESTRIAL OPTICAL LINKS

Approved by:

Dr. Ali Adibi, Advisor
School of Electrical and Computer Engineering
Georgia Institute of Technology

Dr. Gee-Kung Chang
School of Electrical and Computer Engineering
Georgia Institute of Technology

Dr. W. Russell Callen, Jr.
School of Electrical and Computer Engineering
Georgia Institute of Technology

Dr. Hao-Min Zhou
School of Mathematics
Georgia Institute of Technology

Dr. John R. Barry
School of Electrical and Computer Engineering
Georgia Institute of Technology

Date Approved: April 14, 2010

In the name of God, the Most Gracious, the Most Merciful

To my parents (Tariq and Noveen), in-laws (Shujaat and Tahira), wife (Sameen), and kids (Ibrahim, Halima, and Zainab)

and

in the loving memory of my grandmother (Khanum)

ACKNOWLEDGEMENTS

First and Foremost, I thank God, the Almighty, who gave me life, health, strength, wisdom, and helped me in achieving this magnanimous milestone in my life. I am also thankful to him for blessing me with great teachers, family, and friends, whom I am going to mention and thank next.

I wish to thank my advisor at Georgia Tech, Prof. Ali Adibi for welcoming me in his group and for his guidance, support, and encouragement. He granted me great flexibility and freedom in my research. I am also thankful to him for carefully going over my publication drafts, presentations, and teaching me the academic and research skills. I found him an extremely intelligent and a humane person. He was appreciative of the fact that I had an uphill task of raising and supporting a family with two kids along with withstanding the rigors of pursuing a Ph.D. degree. For this, I owe him an eternal gratitude. I am happy to have known him and worked with him; it was one of the excellent opportunities of my life.

I am very grateful to my proposal and thesis defense committee members for their advice and helpful suggestions: Dr. W. Russell Callen, Jr., Dr. Gee-Kung Chang, Dr. Thomas K. Gaylord, Dr. John R. Barry, Dr. Hao-Min Zhou, and Dr. Farid Amoozegar. I also acknowledge the financial and technical support of Jet Propulsion Laboratory (NASA), California Institute of Technology, which guided my research work in the exciting field of deep-space optical communications.

My special thanks to Mr. Ali Asghar Eftekhar (a fellow group member) for the helpful technical discussions, which helped a lot in shaping up the research. I am also

extremely thankful to Dr. Siva (post-doctoral fellow at my group) for teaching me some practical skills needed for optical experiments. Technical discussions with Dr. Babak Momeni, Farasat Munir, Pouyan, and Saeed also helped in understanding some intricate technical concepts. I am also grateful for the privilege to work with a wonderful group of colleagues, including Dr. Omid Momtahan, Dr. Aliakbar Jafarpour, Dr. Mohammad Soltani, Dr. Majid Badiei, Dr. Babak Momeni, Dr. Charles Reinke, Dr. Chaoray Hsieh, Dr. Arash Karbaschi, Murtaza, Ehsan, Amir, Fengtao, Charlie, Qing, Payam, Ali Behrooz, Farshid, James, Reza, and Zhixuan. My special thanks to Farasat, Maysam, and Saeed for the helpful discussions and advises regarding some general aspects of technical research and life. I would also like to earnestly thank a local family at Atlanta (Mr. Tahseen Raja and Mr. Naeem Raja) for their moral help throughout my stay in Atlanta.

I would also like to sincerely thank the faculty of Georgia Tech, especially, Dr. Gordon L. Stuber, Dr. Gee-Kung Chang, Dr. Stephen E. Ralph, Dr. Marry A. Ingram, Dr. Erik I. Verriest, Dr. David S. Citrin, and Dr. Magnus Egerstedt, for their exemplary attitude both inside and outside the class. I enjoyed and learnt a lot of Engineering from the courses I took with these instructors. I would also like to acknowledge the help and concern of the administrative staff at the School of ECE. I am especially thankful to Ms. Marilouise Mycko and Ms. Sharon Lawrence for their help.

My last thoughts go to my parents in Pakistan. I thank them for inculcating in me the pursuit of excellence, learning, and scholarship. Most of all, I am eternally grateful to them for their loving affection, sacrifices, and prayers. For most of my good personality traits, I am thankful to my late grandmother (Mrs. Khanum) who brought me up in the early childhood. Her meticulous and hardworking nature has been a guiding light for me

throughout my life. My sincere thanks go to my parents-in-laws who always encouraged me in my efforts to achieve my goals. I am thankful to God for blessing me with such loving elders. My love and thanks also goes to my brothers (Omer and Ahmed), sister (Hina), and sisters-in-law, who have always prayed and supported my ambitions. In my absence, they took good care of rest of the family at home. With them around, I was relieved of some of my family duties and my long absence from home was not felt.

Last and not the least, my most affectionate thoughts go to my lovely and beautiful wife, Sameen, and adorable kids Ibrahim and Halima. I got married to Sameen when I was 22 and our married life journey is almost 12 years old now. She is the best thing that ever happened to me. She gracefully accepted all the hardships and turmoil of the life, especially, wife of a student husband. She bore the burden of my workload, busy weekends, never-ending publication deadlines, long assignments, and an empty bank account. I thank her for appreciating the value of my work and her sacrifices in sharing the burden of raising two kids. I am lucky to have kids like Ibrahim and Halima. It is an unmatched experience to be a student along with ones kids also being students. Our house always resonated with the worries of home-works, assignments, grades, and exams. My kids shared the burden of my efforts and joys of my accomplishments. I saw them getting excited on the news of acceptance of my technical papers, good grades, and accomplishment of every milestone in pursuing my Ph.D. Words cannot express my appreciation and gratitude for my family for providing the comfort of a good home, great companionship, and moral and psychological support. Surely, I would not have been what I am now without my parents, teachers, wife, and kids.

TABLE OF CONTENTS

LIST OF TABLES

LIST OF FIGURES

LIST OF SYMBOLS AND ABBREVIATIONS

C_n^2	Index-of-refraction structure constant
D	Telescope diameter
D_s	Normalized photodetector size
f	Focal length
F	Telescope F-number
G_T	Transmitter antenna gain
G_R	Receiver antenna gain
M	PPM order
T_s	PPM slot-width
K_s	Signal photon
K_b	Background noise photon
L	Background noise spectral radiance in units of μW/(cm^2-sr-nm)
L_o	Turbulence outer scale
l_o	Turbulence inner scale
η_{det}	Photodetector quantum efficiency
r_o	Atmospheric Fried parameter
λ	Free-space wavelength
σ_φ^2	Wavefront error variance
ς	Zenith angle
1D	One Dimensional
2D	Two Dimensional
3D	Three Dimensional

AO	Adaptive Optics
AOA	Angle of Arrival
DSN	Deep-Space Network
DCR	Dark Current Rate
ESA	European Space Agency
FA	Focal Anisoplanatism
FOV	Field of View
FPA	Focal Plane Array
FSO	Free-Space Optics
FWHM	Full Width at Half Maximum
HPF	High Pass Filter
DAQ	Data Acquisition
IR	Infrared
JAXA	Japanese Aerospace Exploration Agency
LOS	Line of Sight
LGS	Laser Guide Star
NASA	National Aeronautics and Space Administration
ODSC	Optical Deep-Space Communications
OTF	Optical Transfer Function
OOK	On-Off Keying
PPM	Pulse-Position Modulation
PBE	Probability of Bit Error
PDF	Probability Distribution Function
PRF	Pulse Repetition Frequency
PSE	Probability of Symbol Error

RF	Radio Frequency
SEP	Sun-Earth-Probe
SNR	Signal-to-Noise Ratio
SPD	Single Photon Detector
SPE	Sun-Probe-Earth
SR	Strehl Ratio
SHEDS	Super High Efficiency Diode Sources
RMS	Root Mean Square

SUMMARY

Optical communications technology shows promising prospects to fulfill the large bandwidth communications requirements of future deep-space exploration missions, which are launched by NASA and various other international space agencies. At Earth, a telescope with a large aperture diameter ($\cong 10$ m) is required to capture very weak optical signals that are transmitted from deep-space distances. An array of relatively smaller sized telescopes connected to form an aggregate aperture area equivalent to a single large telescope is a viable alternative to a monolithic gigantic aperture for such applications.

In this research, the design concept and analysis of different architectures of telescope array-based receivers for an inter-planetary optical communications link between Earth and Mars are presented. Pulse-position modulation (PPM) is used at the transmitter end and photon-counting detectors, along with the direct-detection technique, are employed at each telescope element in the array. First, models for the received signal photons and background noise photons are developed to simulate an optical communications channel between Earth and Mars. A method for optimization of various important system parameters such as detector sizes (i.e., receiver field-of-view), PPM slot-width T_s, and PPM order M, is presented to maximize the communications system performance. Then, the performance of different array architectures is evaluated through analytical techniques and Monte-Carlo simulations for a broad range of deep-space operational scenarios, such as Earth-Mars conjunction, Earth-Mars opposition, and different background and turbulence conditions. It is shown that the performance of array-based receivers consisting of up to 100, 1 m telescopes is almost equivalent to a

single large telescope with 10 m aperture diameter. It is also revealed that compared to current radio frequency (RF) technology, telescope array-based optical receivers can provide several orders of magnitude greater data rates from Mars.

However, array architectures for deep-space optical communications have several unique challenges. Due to very narrow optical beams, the requirement of spatial tracking of the transmitter line-of-sight at the receiver telescopes (to minimize power losses caused by the tracking errors) is very stern. In addition, detected signals at individual telescope elements in an array need to be synchronized with the receiver clock and with each other before data decoding. Compared to a monolithic large telescope, individual telescope elements in an array receive and detect much less optical power. This phenomenon renders the tracking and synchronization tasks at individual telescopes quite difficult. In the next step, the design of tracking and synchronization subsystems for the array receiver is discussed. The performance of different array architectures, after incorporation of these subsystems, is evaluated for a deep-space optical communications link between Earth and Mars operating in the presence of random tracking and synchronization errors. It is shown that even in the worst-case channel conditions, the designed subsystems successfully perform the tracking and synchronization functions; the impact of synchronization and tracking errors is almost negligible for an array consisting of 100, 1 m telescopes. The tracking and synchronization analysis further solidifies the theoretical foundations and feasibility investigation of telescope arrays for deep-space optical communications.

Atmospheric turbulence and diffused background light from the sky during daytime are the major limiting factors in a deep-space optical communications link. This

part of the research is focused on developing techniques to mitigate these deleterious effects. Adaptive optics (AO) technology is commonly employed in astronomy to mitigate the turbulence effects. First, laser guide star (LGS)-based AO systems are designed and incorporated in array receivers, and their performance is analyzed for a communications link between Earth and Mars in extreme turbulence and background conditions. It is shown that the incorporation of LGS-based AO systems results in a substantial improvement in the performance of array receivers. Next, a novel space-time adaptive processor (STAP) is developed for post-detection processing and mitigation of background noise effects. The STAP processor can be thought of an electronic counterpart of an active AO system and is very easy and cost-effective to implement. The performance analysis shows that the incorporation of the STAP processor results in several orders of magnitude performance improvement in strong background conditions. The experimental investigation of the use of adaptive optics (AO) subsystems for turbulence and background noise compensation is also carried out.

In the last part of the thesis, short-range, terrestrial, free-space optical (FSO) communications links are analyzed. It is believed that FSO systems can solve the last mile connectivity problem faced by the current commercial telecom market. An efficient general-purpose simulation tool is developed that can model and predict the parameters of interest of a laser beam propagating through a turbulent channel in FSO systems. This simulation tool can also be employed to analyze the performance of a short-range FSO system operating in any link condition. The developed code also has the option of incorporating a closed-loop adaptive optics subsystem for mitigation of atmospheric turbulence effects and estimating the resultant performance improvement.

CHAPTER 1

INTRODUCTION

Optical communications technology has revolutionized the modern-era telecommunications enabled by the deployment of fiber optics technology and networks around the globe. In fiber optics, an optical signal travels in a guided channel: the fiber. The line-of-sight (LOS) free-space optical (FSO) communications also shows promising prospects to fulfill the data communication needs of many government, military, and commercial organizations. Recently, FSO systems are being considered for certain customized applications such as deep-space communications, and certain commercial short-range communications links as a solution to the "last mile connectivity" problem. Most of this thesis is focused on the deep-space optical communications. However, a small part of the research is also dedicated to terrestrial, short-range, FSO communications links.

1.1. Introduction to Deep-Space Communications

The international scientific community and various space agencies such as National Aeronautics and Space Administration (NASA), European Space Agency (ESA), and Japanese Aerospace Exploration Agency (JAXA) continue to send discovery missions into deep-space to unravel the mysteries of planets in the solar system, galaxies, and the universe [1-5]. These great voyages of exploration have evolved from early reconnaissance flybys and orbiters to a new data-intensive paradigm of constellations of planetary landers and spacecraft probes. In planetary landers missions, mobile robotic vehicles such as "Mars Exploration Rover" land on the surface of a planet and collect

data through state-of-the-art on-board instruments and sensors. This data is relayed to a spacecraft in the planet's orbit, such as "Mars Odyssey." A large bandwidth, integrated, and reliable communications link is required between a deep-space transmitter and a receiver at Earth to transport huge volumes of scientific data, including but not limited to hyper-spectral images and real-time high-definition video [6]. The strength of the transmitted signal decreases with the square of the distance R between the transmitter and the receiver. Hence, communication over deep-space distances is an extremely challenging task due to a very weak received signal (because of $(1/R^2)$ loss in the communications link budget) [7]. For example, the distance between Earth and a geostationary (GEO) satellite is approximately 40,000 km, which is considered to be in near-space. Whereas, deep-space distances are millions and billions of kilometers far away from Earth. For instance, the distance from Mars to Earth can be about 3×10^8 km, and distance from Neptune or Pluto to Earth can be approximately 4×10^9 km. Data communication over such huge distances is a challenging and formidable task.

NASA deep-space ventures so far have relied upon a global RF-based deep-space network (DSN) to capture the communications signal returns from distant planets. The conventional DSN uses X-band, and more recently, Ka-band capabilities have been successfully tested [8-11]. Current RF technology has reached an extremely high limit of performance, since spacecraft antenna sizes and transmitter powers are already at the maximum feasible limit. On Earth, DSN antennas are enormous (34 m and 70 m aperture diameter), and the receiving systems are operating at just a few degrees above absolute zero [7]. Even with this sophisticated technology, the maximum achievable data rates from Mars using experimental Ka frequency band are limited to 6 Mbits/s during Earth-

Mars opposition phase and about 500 Kbits/s during Earth-Mars conjunction phase [9,12]. This data return capability is insufficient and orders of magnitude lower than that required for current and future planetary exploration missions [7]. Due to this constraint, the spatial and spectral sensitivities of scientific instruments and robotic probes sent to deep-space exploration missions have been very limited and significantly below what scientists are doing for Earth observations today. There is always a need for advanced architectures and technologies that can enhance the data return capabilities from deep-space. The future efforts in this regard include the improvement in NASA existing RF-based DSN [6], and development of new communications technologies, such as optical communications. Design and analysis of novel optical communications receiver architectures and subsystems that can support much larger bandwidth from deep-space is the main topic of this thesis.

1.2. RF versus Optical Communications

Both radio frequency (RF) radiation and optical radiation are a subset of the much broader electromagnetic radiation (EMR) spectrum. The EMR spectrum is shown in Figure 1.1 [13]. The range of frequencies between 3 KHz to 300 GHz band (with corresponding wavelengths between 100 km to 1 mm) constitutes the RF and microwave spectrum. The optical band consists of infrared (IR), visible, and ultraviolet (UV) regions, which have much higher frequencies. For instance, an optical signal in the IR region can have a central frequency of 300 THz with a free-space wavelength of $1\,\mu$m. Optical communications refers to the use of carrier frequencies in the optical band to transfer the information. The communications process in those frequency bands differs significantly

from that of RF systems and has its own unique advantages and challenges. The most vital advantage is due to the much higher central frequency of the optical signal.

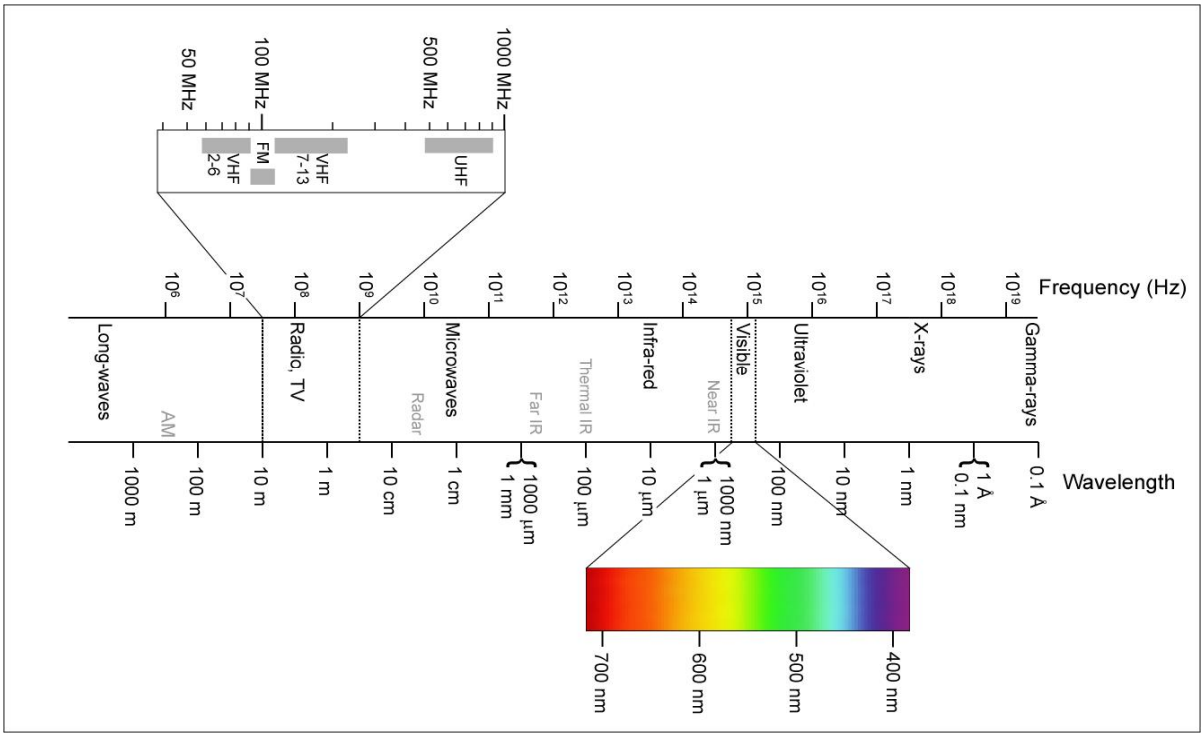

Figure 1.1. The Electromagnetic radiation spectrum [13].

Over the history of deep-space communications employing NASA DSN, conventional RF-based communications performance has improved by about 12 orders-of-magnitude [7]. These improvements have been made possible by many technological advancements. However, more significant improvements were achieved when the operating carrier frequency of the communications signal was increased (i.e., wavelength decreased). Specifically, the deep-space communications operations at DSN started in the S-band (2-4 GHz) [14,15]. Currently, the primary frequency band used for deep-space communications at DSN is the X-band (approx. 8 GHz) [7,15,16], and the operations in

Ka-band (32 GHz) have been experimentally tested [8-11]. The change from X-band to Ka-band has a theoretical improvement of 11.6 dB, although practical factors (e.g., atmospheric losses) have restricted the improvement to about 6 dB [7]. The carrier frequencies in the optical band are much higher than RF frequencies. For example, the center frequency of a laser generating a carrier in the near-IR region is about 3×10^5 GHz (i.e., 300 THz) that is about 10^4 times the carrier frequency in Ka-band. Hence, the promise of switching to optical frequencies (e.g., for achieving higher data rates and higher operation bandwidths) is substantial.

The relationship between the use of higher frequencies (i.e., smaller wavelengths) and improvements in the communications system performance can be understood by employing the basic antenna theory. The gain of an antenna is inversely proportional to the square of the operating wavelength λ. For a circular antenna with an aperture diameter *D*, the gain (to the first order approximation) is given by [17]

$$Gain \cong \left(\frac{4D}{\lambda} \right)^2. \tag{1.1}$$

Similarly, the transmitted beam width is directly proportional to the wavelength λ, and (to the first order approximation) the planar beam width is given by [17]

$$Beam\,width \cong \left(\frac{\lambda}{D} \right). \tag{1.2}$$

It is clear from Equations (1.1) and (1.2) that switching to higher frequencies (smaller wavelengths) results in larger antenna gains and smaller beam widths. Figure 1.2 shows an example of the calculations of antenna gains and beam widths for RF and optical frequencies. It is shown that for an antenna operating at 1 GHz RF frequency, a gain of 60 dBi (dB relative to an isotropic radiator) and a beam width of about

3×10^3 μ radians are achieved with a 100 m aperture diameter. However, for an antenna operating at an optical frequency of 300 THz (1 μ m wavelength), a gain of 112 dBi and a beam width of 6 μ radians are achieved by a lens with just 10 cm aperture diameter. The transmitter and receiver antenna gains play an important role in the communications link budget and the received power density depends upon the transmitted beam width (beam spread). Hence, the benefits of switching to higher (optical) frequencies are obvious due to larger gains and superior received power densities due to smaller beam spreads. Moreover, at optical frequencies, these performance gains are obtained with much smaller component sizes, which is a very important consideration in space technologies.

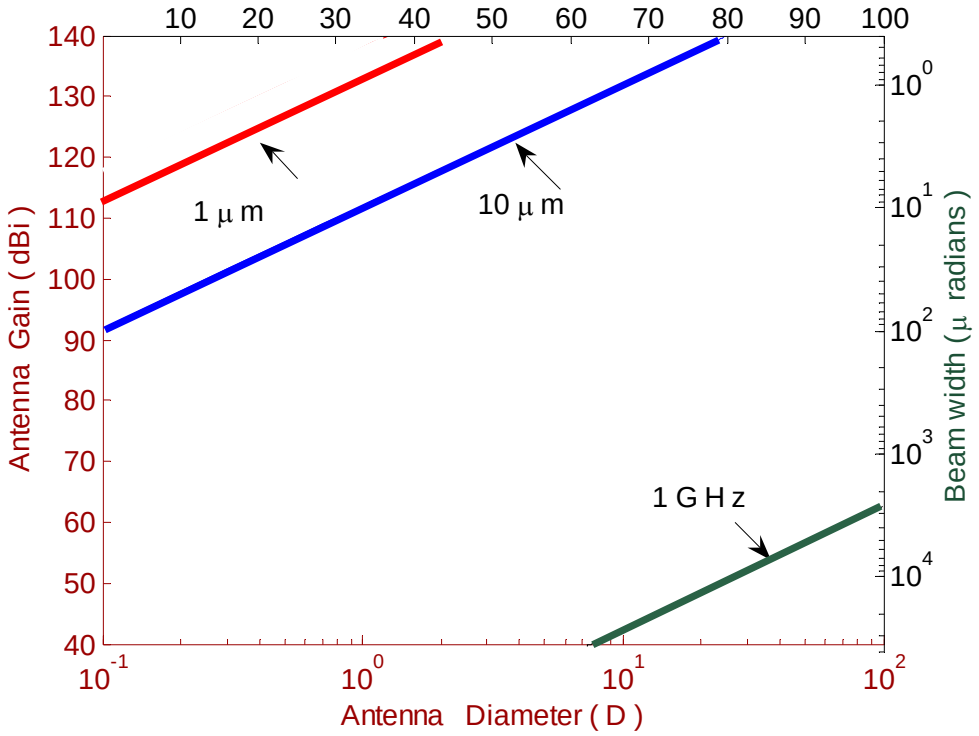

Figure 1.2. Antenna gain and transmitted beamwidth versus the antenna diameter for differrent operating frequencies. Aperturte diameter *D* is in meter.

A practical example of smaller beam spread offered by the optical transmission is given in Figure 1.3 [7], which compares the RF and optical beam spreads when transmitted from Saturn to Earth. The left side of the figure shows the transmitted beam from the Voyager spacecraft in the Saturn's orbit operating at X-band. The transmitting antenna is 3.7 m in diameter. By the time the RF beam reaches Earth from Saturn, the signal is spread out over an area with the width equivalent to 1000 Earth-diameters due to the diffraction (a fundamental property of EM beams). The right side of the figure shows a transmitter operating at an optical frequency of 300 THz (wavelength of 1 μm). The transmitting antenna in this case is a much smaller 10 cm diameter telescope and the resulting spot size at Earth is just one Earth-diameter wide. The optical case represents a factor of 1000 times less spread (or diffraction) and more concentration of the received energy in both the horizontal and vertical directions (a factor of 10^6 in power density). The benefits of switching to optical frequencies are evident.

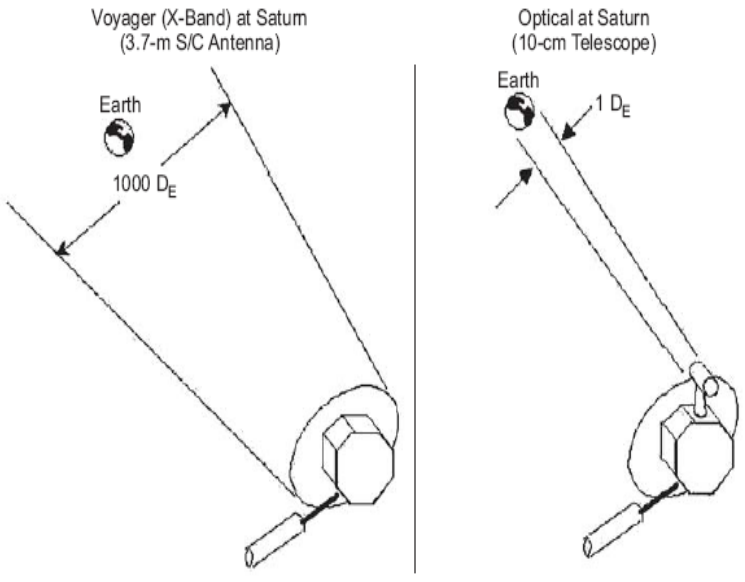

Figure 1.3. Comparison of RF and optical beam spreads from Saturn to Earth [7].

In addition, switching to higher (optical) carrier frequencies theoretically increases the available transmission bandwidth and information capacity of the system. Moreover, in the present era, the optical band is almost free from the spectrum allocation limitations. Due to the above-mentioned advantages, optical communications technology has a tremendous potential and is being strongly considered for future deep-space communications to fulfill the needs that cannot be fulfilled by the conventional RF-based DSN.

To reiterate this point, Figure 1.4 shows the needs of future deep-space probes and instruments versus the current capabilities of the Mars Global Surveyor (MGS) mission [7]. The horizontal axis is the data rate, and the vertical solid (red) line on the left side represents the current MGS capability scaled to the Saturn distance. The ovals represent horizontal data regions where corresponding science instruments are expected to operate. The ovals above the central data-rate-axis represent the scientific investigation needs, whereas, the ovals below the central data-rate-axis represent the commercial telecommunications needs for enhanced public engagement. Regions of anticipated capability improvements for several candidate communications technologies are shown by the rectangles. The specific improvements in individual technologies will be determined by the course of time and current and planned technical research. Nevertheless, optical communications technology shows remarkable potential in communications throughput improvement [7].

Williams *et al.* [18] recently examined high-rate data transfers in deep-space by optical and RF means, and predicted mass and power burdens on host spacecraft for each. This paper claimed that in addition to enhancing the data rate, optical technology also

offered significant mass and power savings for high-rate telecommunications systems [18].

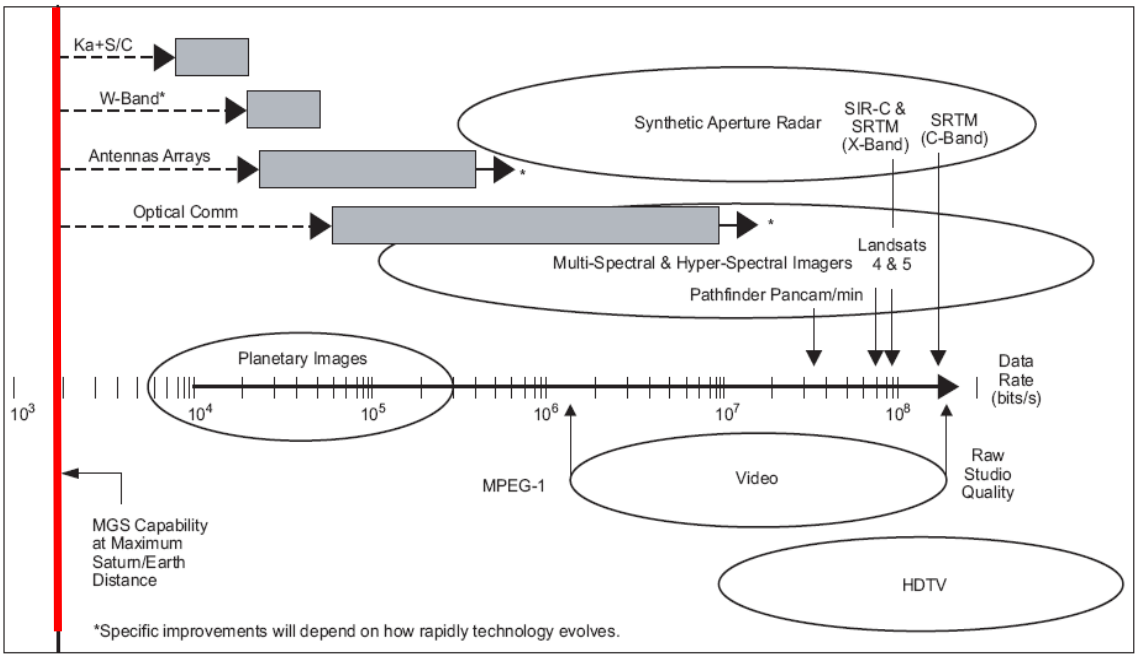

Figure 1.4. Future deep-space data return needs relative to current capabilties based on the Mars Global Surveyor (MGS) at maximum Saturn range [7].

In summary, compared to RF technology, optical communications technology has the added advantages of higher gain, smaller diameter antennas (i.e., telescopes), a much narrower beam width, a greater power density, a higher center frequency for extremely fast modulations, and a wider available bandwidth. Hence, optical communications systems show promising prospects for the broadband deep-space communications. Due to these reasons, the need for deep-space optical communications was articulated in the NASA 2003 strategic plan [19] as a "New Effort Building Block" under the "Communications Technological Barrier" for "providing efficient data transfer across the

solar system." The goal of deep-space optical communications received serious attention and impetus.

The need of development and demonstration of new optical communications technologies in space communications is also reiterated and strongly emphasized in NASA 2010 budget plan [20]. Optical communications has its own unique challenges (availability issues, quantum effects, atmospheric turbulence etc.). Some arduous efforts are being made for the realization of the goal of long-distance optical communications and for mitigation of the limiting factors in optical communications systems [7]. These efforts are diversified in the areas of design of transmitter/receiver subsystems and efficient device technologies that would support future deep-space optical communications. A telescope-based optical communications receiver is an important component in the overall plan of development of deep-space optical communications systems. Design, evaluation, and analyses of novel architectures and subsystems for ground-based receivers operating in deep-space optical communications links are the foci of the research in this thesis.

1.3. Telescope Receivers

The name "telescope" covers a wide range of instruments, which are designed to collect electromagnetic radiations so that they can be observed and analyzed to convey some form of information. However, the design requirements of telescopes for different applications such as astronomy and telecommunications are quite different.

1.3.1. Telescopes in Astronomy

Most common applications of telescopes are in astronomy. Optical astronomical telescopes collect the light (optical part of the electromagnetic spectrum) emanating from

distant stars, planets, and other celestial objects. Their purpose is to increase the apparent angular size and the resolution of the distant objects. Radio telescopes are used for radio astronomy. There are a large number of observatories around the globe, which employ telescopes with very sophisticated technical designs for astronomical observations [21-24].

1.3.2. Telescopes in Communication Systems

The use of telescopes in free-space optical (FSO) communications is a relatively new field. Telescopes act as transmitting and receiving antennas in FSO communications systems. In a transmitter, a telescope concentrates and radiates optical signals toward the receiver. In a receiver, a telescope collects optical signals and concentrates them onto photodetectors in the focal plane for optical to electrical signal conversion.

There are many differences in the design requirements and operations of telescopes in the astronomical and optical communications fields. In astronomical applications, the telescope-based imaging and observation systems operate during nighttime. Many strong background noise sources such as the Sun, diffused light from the sky, and other deleterious factors, such as strong atmospheric turbulence, are absent during nighttime. Whereas, a typical optical communications system operates both during the day and night. During daytime, background noise and atmospheric turbulence are at their respective peaks, which pose formidable challenges for the design of telescope-based optical communications systems. Secondly, in astronomy the objective is to increase the resolution and sharpness of the image of an object, so that very fine details can be observed. If in this process the received energy is less due to some losses, the observation time can be made longer over multiple frames (limited by the available signal

to noise ratio). However, in communications applications, the objective is to detect and decode the received energy over a very limited time-period (normally a transmitted bit period). The challenges and limiting factors for these two separate fields are quite different. Hence, the design, analysis, and operational needs of telescope-based receivers and subsystems are very different for communications and astronomical applications.

1.3.3. Telescope Array Receiver

Because of the power and telescope size limitations at the transmitter spacecraft in deep-space, one of the solutions to increase the link data rate is to increase the telescope (antenna) size and gain at the receiver. Hence, a large aperture diameter telescope is required at an Earth-based receiver to obtain acceptable data rates (i.e., in the Mbits/s range) from deep-space distances [7,25]. A single large telescope has the limitations of high cost, single point failure in case of malfunction, difficulty in maintenance, enormous weight, substantial gravitational effects, and difficulty in manufacturing the high quality optics. In addition, the communications operations with a large telescope for small Sun-Earth-Probe (SEP) angles are very difficult, as a single big lens acts as a formidable solar energy concentrator.

An array of relatively smaller sized telescopes is a viable alternative to a large monolithic telescope receiver. Telescope arrays have advantages of lower cost, improved diffraction-limited performance, less gravitational effects, scalability, ease of maintenance, and redundancy in operations [25]. Due to their unique capabilities, telescope arrays have been of interest recently for deep-space optical communications. Previously, arrays of smaller telescopes have been used in the astronomical field as optical and astronomical interferometers [26]. However, as explained in the previous

paragraphs, the design objectives of systems in the domain of astronomy area are to enhance the imaging and resolution capability of the astronomical observations from celestial objects. It was also explained that the operational scenarios, channel conditions, and limiting factors for these systems are quite different. Moreover, these systems can be regarded as "optical interferometers" or "astronomical interferometers" as the optical signals from different telescopes are optically aligned and combined first, and then detected afterward for imaging applications. One of such systems is designed and built by the Centre for High Angular Resolution Astronomy of the Georgia State University, known as the CHARA array [26]. Examples of some other optical, astronomical, and radio interferometers are given in [27-32]. However, according to the definition given in Refs. [7,33], for a system to qualify as a telescope array receiver in direct-detection optical communications applications, the optical signals need to be first detected at each telescope (antenna) element, converted to electrical signals, and then combined afterward in the electrical domain for further data extraction and coding purposes [7,33,34]. For these reasons, the problem of design, analysis, and evaluation of telescope array receivers and the subsystems for deep-space communications applications is a new challenge, very different from the existing multiple telescope-based optical interferometers for astronomical applications.

1.4. Statement of the Problem

An optical communications system for deep-space communications is a new concept and its practical implementation has not been demonstrated. New architectures for deep-space optical communications need to be analyzed and developed. A telescope array-based receiver seems to be a viable architecture for deep-space optical

communications. However, the performance of telescope arrays needs to be evaluated for a real world operational scenario. In addition, the performance comparison of a single telescope with different array configurations needs to be carried out for an actual deep-space optical link to evaluate the bounds on the number of telescopes in an array receiver and to estimate achievable data rates in the presence of optical channel limiting factors. This analysis will require the modeling of the optical channel, modeling of signal and background noise photons, incorporating the effect of atmospheric turbulence, and modeling various other limiting factors such as synchronization and tracking errors.

The performance of an optical receiver depends upon the number of signal and background photons, which depend upon various system parameters. In this scenario, the optimization of important system parameters needs to be carried out to maximize the communications system performance. Moreover, tracking errors arise because of phenomena like beam wander due to atmospheric turbulence and receiver telescope platform jitter [35,36]. Requirement of spatial tracking the transmitter line-of-sight (LOS) for a deep space optical communications receiver is very rigid due to very narrow receiver field-of-view (FOV) and extremely low received power. When operating at such narrow FOVs, even a small (sub μ *radians*) error in the receiver-tracking angle can result in considerable power losses and deleterious effects on the receiver performance. In a telescope array, each telescope receives much less power but shall retain the same tracking accuracy as that of a single monolithic telescope, which is a challenging task. The tracking subsystems need to be designed for the compensation of these errors and the impact of random tracking errors on the performance of telescope array receivers needs to be evaluated.

Pulse-position modulation (PPM) is a suitable modulation scheme for deep-space optical communications [37,38]. Accurate decoding operations at the receiver require the precise synchronization of the incoming signal-slot boundaries with the receiver clock and an accurate alignment of slot-counts from individual telescopes during the signal combination process. The timing offset errors arise due to a number of reasons such as variations in laser pulsing timings, slowly varying delays due to atmospheric turbulence, and clock jitter. In array-based receivers, each telescope receives only a small fraction of the total transmitted power. Therefore, less power is available for synchronization and clock tracking compared to a single large telescope, which can lead to the performance degradation. Hence, efficient and robust synchronization subsystems need to be developed, and the impact of random synchronization errors on the performance of telescope array-based receivers needs to be evaluated. The design of a synchronization system should be such that to adapt to the channel dynamics.

Background noise is ever-present in a deep-space optical communications link [7, 39]. During daytime, the diffuse light from the sky is a major limiting factor [40,41]. During nighttime, background noise emanates from stars, planets, moon etc. [42-44]. Atmospheric turbulence is another deleterious phenomenon; it severely distorts the phase of the propagating beam thus limiting the focusing capabilities of the telescopes; it induces random beam wander inflicting tracking errors and powers losses; and it causes intensity fluctuations [45-50]. Novel techniques for the mitigation of the coupled effects of atmospheric turbulence and background noise need to be developed and tested on telescope array receivers operating in a deep-space optical communications link.

In summary, the feasibility analysis and performance evaluation of the telescope array-based receiver architectures need to be carried out for a real-world deep-space optical communications link. Optimization of important system parameters needs to be carried out to maximize the communications system performance. Novel techniques and subsystems need to be designed for the mitigation of the major limiting factors, such as background noise, atmospheric turbulence, synchronization, and tracking errors. Practical constraints on the number and size of individual telescopes, in the presence of the above-mentioned subsystems, in an array-based receiver need to be determined. The performance bounds in terms of the achievable data rates for an actual deep-space optical link, i.e., between Earth and Mars, need to be evaluated. The above-mentioned tasks will significantly aid in solidifying the theoretical foundations of the telescope array-based receivers and establishing the viability of employing such architectures for future deep-space optical communications.

1.5. Previous Work

The idea of employing an array of smaller optical apertures for optical communications has been presented in several previous works [25,34,51-54]. A coherent telescope array receiver with self-homodyne interferometric detection and different modulation schemes was presented in Ref. [51]. This work carried out the analysis for general assumed conditions but ignored the important phenomenon of atmospheric turbulence. The performance comparison of single aperture and arrays for terrestrial, short-range, FSO communications links employing the direct-detection technique has been presented in Ref. [52]. However, deep-space links are different from the short-range

terrestrial links in terms of background noise, atmospheric turbulence, subsystems, and components technologies.

Boroson *et al*. at MIT Lincoln Laboratory presented a basic concept of an array of telescopes and discussed its advantages in Ref. [25] for power-limited laser communications systems. Vilnrotter *et al.* at Jet Propulsion Laboratory (JPL) presented a unique aperture-sampling model in Refs. [33,34] to analyze the performance of telescope array receivers. This analysis assumed general link conditions and some arbitrary values of signal and background noise for the channel. A two-element telescope-based field experiment for optical communications has been demonstrated in Ref. [53] for a short-range (140 ft. long) communications link. However, all the above-mentioned works lack the analysis and evaluation of different array architectures operating in a real world, deep-space optical communications link scenario with realistic constraints and values for the signal photons, background noise, and atmospheric turbulence conditions.

Eftekhar *et al.* in my advisor's research group presented a comparison of performance of direct-detection and coherent telescope array receivers for a deep-space optical communications link in Ref. [54]. It was shown that compared to coherent arrays, the direct-detection arrays offer a comparable, simple, and cost-effective solution for deep-space optical communications. However, as mentioned in Section 1.4 entitled "Statement of the Problem," more work was needed to formalize and solidify the concept of telescope array-based architectures operating in deep-space optical communications links. Specifically, the problems of optimization, synchronization, tracking, background noise, and atmospheric turbulence need to be addressed. On replacing a single large telescope with an array of smaller telescopes, the task of tracking and synchronization at

individual telescopes become more difficult due to the lower power levels received at each telescope in an array. The subsystems for the mitigation of these factors need to be developed. The performance of telescope array-based receivers and the designed subsystems need to be evaluated for a realistic operational scenario in the presence of the above-mentioned limiting factors.

1.6. Contributions of the Thesis

In this research, I focused on the design, analysis, and evaluation of different architectures for direct-detection telescope array-based receivers for a real-world operational scenario of a deep-space optical communications link. Mars is the nearest planet to Earth in deep-space and has been the focus of active research by the international scientific community. Hence, in this thesis, all the designed architectures and subsystems are analyzed and evaluated for an optical communications link between Earth and Mars. Nevertheless, the results of this thesis can be extended to other communications links without major modifications.

In the first phase of my research, I design and evaluate different configurations of telescope array-based receivers for a communications link with Mars for a wide range of operational scenarios, such as Earth-Mars opposition, Earth-Mars conjunction, different atmospheric turbulence and background noise conditions ranging from the best to the worst [55-57]. Direct-detection technique along with pulse-position modulation (PPM) scheme is employed. I also present the optimization of important system parameters such as detector size, receiver field-of-view (FOV), PPM order M, and PPM slot-width T_s to minimize the turbulence and background noise effects and to maximize the communications system performance [58]. In this phase, it is shown that the performance

of array-based receivers consisting of up to 100, 1 m telescopes, is almost equivalent to a monolithic telescope with 10 m aperture diameter. It is also shown that the performance of the array receiver degrades eventually as the individual telescope diameter approach that of the atmospheric Fried parameter r_o [55,45]. The performance of array receivers is evaluated in terms of the achievable data rates. Upper and lower bounds on achievable data rates are evaluated corresponding to the best and worst channel conditions. The results show that compared to the current RF-based DSN receivers, an optical array-based receiver consisting of 100, 1 m telescopes can provide orders of magnitude greater data rates from Mars to Earth [55].

In the next phase, the analysis of telescope array-based receivers is carried out in the presence of tracking and synchronization errors. A system level description of acquisition and tracking for a single (Hale) telescope was presented in Ref. [59]. However, the tracking analysis for telescope array receivers had been missing. In the first step, I develop a statistical mathematical model to quantify the impact of tracking errors on general direct-detection optical receivers [60]. Tracking subsystems are designed and incorporated in the array receiver for the compensation of random tracking errors. Next, the performance of different array architectures and tracking subsystems is evaluated for the worst-case Earth-Mars optical channel conditions [61]. The performance bounds and efficacy of the designed tracking subsystem in the presence of random tracking errors is evaluated for the telescope array receiver [61,62].

In the next step, a Kalman filter-based synchronization subsystem is developed for synchronization of the received signals with the receiver clock at individual telescopes and also with each other before signal combining and decoding operations.

The synchronization subsystems are incorporated in the array architecture and their performance is evaluated for a link between Earth and Mars [63]. It is shown that the Kalman filter-based synchronization system in individual telescopes efficiently tracks the time-varying delay fluctuations during worst channel conditions, i.e., when Mars is farthest from Earth, atmospheric turbulence is at its peak, and background noise is very intense[63-64]. The analysis presented in this phase of my research establishes that both the tracking and synchronization errors have negligible impact on the array architecture and do not pose major limitations in going from a single telescope to a multi-telescope array architecture [60-64].

It is important to highlight that following our initial work on telescope arrays and synchronization [60-64]; other groups at JPL and MIT Lincoln lab presented several synchronization schemes for telescope array receivers [65-68]. A synchronization scheme based on the insertion of the periodic pilot symbols and incorporation of a fixed-coefficient first-order loop filter was analyzed for an array consisting of four telescopes in Refs. [65,66]. Comparison of a pilot symbol insertion and inter-symbol guard time insertion techniques was carried out in Ref. [68]. It was shown in Ref. [68] that the pilot symbol insertion technique is more computationally intensive and both techniques perform well for timing errors less that 1 ppm (part per million). However, these techniques are based upon the insertion of several overhead (pilot and training) symbols in the transmitted data stream, which results in the reduction of the overall data throughput. Our designed synchronization scheme still stands out; it does not need overhead symbols and does not reduce the data throughput; it analyzes and compensates much larger errors i.e., 4 ppm [63,64]. In addition, for the highly random and non-

stationary channels, the adaptive filters designed by us perform much better than the fixed coefficients, first and second-order filters [63,64]. Moreover, it is also important to highlight that telescope analysis and subsystems presented by us in Refs. [55-58, 60-64] tackle much broader range of channel conditions, much worst limiting factors, and a wide range of different telescope architectures, compared to other studies [65-68] that followed our work.

Next, the techniques for the mitigation of the coupled effects of atmospheric turbulence and background noise are developed. Adaptive optics technology has been actively used in the astronomical telescopes to mitigate atmospheric turbulence effects [69-73]. First, I design and incorporate an artificial laser guide star (LGS)-based adaptive optics (AO) subsystem in the telescope array receiver. The performance analysis shows that AO subsystems result in a substantial improvement in the performance of the communications system in strong turbulence and background conditions [74-76]. The experimental investigation of the use of AO systems for the compensation of turbulence-induced wavefront aberrations is also carried out.

AO technology is an active optics technique, which can be costly for larger telescopes. The use of adaptive focal plane arrays has been proposed in the Ref. [77] to mitigate the atmospheric turbulence effects in optical communications links. However, the technique developed in Ref. [77] needs an estimation of the signal and background photons. In this phase of my research, I develop a novel, 2-D adaptive Wiener filter based space-time adaptive processor (STAP) for mitigation of turbulence and background noise effects [78, 79]. The developed technique does not need an estimation of the signal and background photons. The analysis of the optical receiver shows that the incorporation of

the STAP processor results in several dBs of performance improvement [78] compared to the previous reported results in Ref. [77]. This technique can be regarded as an electronic counterpart of the active AO technology.

In the last part of the thesis, short-range, terrestrial, free-space optical (FSO) communications links are analyzed. It is believed that FSO systems can solve the last mile connectivity problem faced by the current commercial telecom market. An efficient general-purpose simulation tool is developed that can model and predict the parameters of interest of a laser beam propagating through a turbulent channel in FSO systems. This simulation tool can also be employed to analyze the performance of a short-range FSO system operating in any link condition. The developed code also has the option of incorporating a closed-loop adaptive optics subsystem for mitigation of atmospheric turbulence effects and estimating the resultant performance improvement.

In summary, the main contributions of this thesis are:

- Design, analysis, and performance comparison of different telescope array-based receiver architectures for a deep-space optical communications link between Earth and Mars. The performance analysis is done for a wide range of atmospheric turbulence, background noise, and channel conditions to estimate the upper and lower performance bounds [55-57].
- Optimization of important system parameters such as detector size, receiver FOV, PPM order M, and PPM slot-width T_s to maximize the optical communications system performance between Earth and Mars [55,58].
- Statistical modeling of the impact of random tracking errors on direct-detection optical communications systems; design of a tracking subsystem and analysis of

telescope array-based receivers for deep-space communications in the presence of tracking errors [60-62].

- Design and analysis of a Kalman filter-based synchronization scheme for telescope array receivers operating in a deep-space optical communications link [63,64].
- Design and analysis of a laser guide star (LGS)-based adaptive optics (AO) system in telescope array receivers for mitigation of atmospheric turbulence and background noise effects in deep-space optical communications links [75,76]. Experimental evaluation and demonstration of the use of AO systems to mitigate turbulence-induced phase errors is also performed.
- Design and analysis of a novel 2-D Wiener filter-based space-time adaptive processor (STAP) for mitigation of atmospheric turbulence and background noise effects in a deep-space optical communications link [78,79] .
- Development of a general-purpose software code to simulate and predict the parameters of a laser beam travelling through atmospheric turbulence. The code also has the options to calculate the performance of FSO communications systems in turbulence, and to simulate the effects of AO systems on FSO receivers [74].

1.7. Outline of the Thesis

The thesis is organized as follows: Introduction and background of the research is given in Chapter 1. This chapter explains the challenges of deep-space communications, comparison and benefits of optical communications versus RF communication, a need for telescope array-based receivers, previous work done in this area, and the outline of the thesis. In Chapter 2, the communications system model is developed. The details of the

direct-detection optical communications system, the pulse-position modulation (PPM) scheme, modeling of received signal and background photons, and atmospheric turbulence model are given in this chapter. The details of the transmitter specifications representative of the state-of-the-art space qualified technology are also delineated. The specifications of system detectors are also delineated. These transmitter/detector specifications are used throughout this thesis. The chapter also describes an analytical model for evaluating the performance of a direct-detection optical communications receiver in terms of probability of error and achievable data rates.

Chapter 3 focuses on the development of optimization techniques to maximize the deep-space optical communications performance by choosing the optimal system parameters to minimize the atmospheric turbulence and background noise effects. The examples of optimization are given for different turbulence and background conditions. In Chapter 4, the performance analysis of telescope array-based receivers is given for a deep-space optical communications link between Earth and Mars. The performance of a single telescope-based receiver is compared with those of different array architectures using both analytical calculations and Monte-Carlo simulations. The analysis is carried out for a broad range of operating conditions such as Earth-Mars conjunction, Earth-Mars opposition, different background noise and atmospheric turbulence conditions.

Chapter 5 explains the design and development of an adaptive Kalman filter-based scheme for the synchronization of received signals with the receiver clock at individual telescopes. The mathematical model of clock dynamics, details of the Kalman filter, and steady-state performance is explained. The performance analysis of telescope array-based receivers in the presence of random synchronization errors is also given. In

Chapter 6, a statistical model for the evaluation of the impact of random tracking errors on a direct-detection optical communications receiver is presented. A tracking subsystem is developed for individual telescopes in the array to mitigate random tracking errors. The performance analysis of telescope array-based receivers in the presence of tracking errors is also given for the worst-case channel conditions.

Chapter 7 is focused on the development of techniques for the mitigation of coupled effects of atmospheric turbulence and background noise. LGS-based AO subsystems are designed and incorporated in telescope array-based receivers, and performance improvement of receivers operating in turbulent deep-space optical links is investigated. In Chapter 8, the experimental evaluation and demonstration of the use of AO systems to mitigate turbulence-induced phase errors is presented. In Chapter 9, a 2D Wiener filter-based STAP processor is developed, and its efficacy is tested for the mitigation of atmospheric turbulence and background noise effects.

Chapter 10 is dedicated to short-range, terrestrial, FSO links. The importance of FSO links as a solution to the "last mile connectivity" problem is explained. Next, the details of a general-purpose code are given, which is developed to simulate and calculate various parameters of interest for laser beam propagation through atmospheric turbulence in FSO systems. The use of AO systems is also evaluated for the mitigation of atmospheric turbulence effects in short-range, FSO systems. Finally, summary of key results, concluding remarks, and future directions are delineated in Chapter 11.

1.8. List of Publications

The list of publications that have resulted as a result of this research is as follows:

1.8.1. Journal Papers

[1] **A. Hashmi**, A. A. Eftekhar, A. Adibi, and F. Amoozegar, "Analysis of telescope array receivers for deep-space inter-planetary optical communication link between Earth and Mars," *Optics Communications*, vol. 283, no. 10, May, pp. 2032-2042, 2010.

[2] **A. Hashmi**, A. A. Eftekhar, A. Adibi, and F. Amoozegar, "A Kalman filter-based synchronization scheme for telescope array receivers in deep-space optical communication links," ***submitted.***

[3] **A. Hashmi**, A. A. Eftekhar, A. Adibi, and F. Amoozegar, "Analysis of adaptive optics based telescope array receivers for compensation of atmospheric turbulence effects in a deep-space inter-planetary optical communications between Earth and Mars," ***submitted.***

[4] **A. Hashmi**, A. A. Eftekhar, A. Adibi, and F. Amoozegar, "Telescope array receivers for deep-space laser communications: evaluation and statistical analysis of the performance under random tracking errors***," in preparation.***

[5] **A. Hashmi**, A. A. Eftekhar, A. Adibi, and F. Amoozegar, "A novel space-time adaptive processor (STAP) for mitigation of atmospheric turbulence effects in deep-space optical communication links," ***in preparation.***

1.8.2. Conference Papers

[1] A. A. Eftekhar, **A. Hashmi**, A. Adibi, and F. Amoozegar, "The effect of synchronization errors on the performance of telescope arrays for optical deep space communication," in *Proc. IEEE Aerospace Conference*, 2006, pp. 1-7.

[2] **A. Hashmi**, A. A. Eftekhar, A. Adibi, and F. Amoozegar, "Statistical evaluation of an optical array receiver for deep-space laser communications under random pointing and tracking errors," presented at Optics in the Southeast Conf. Charlotte, NC, 2006.

[3] **A. Hashmi**, A. A. Eftekhar, A. Adibi, and F. Amoozegar, "Effect of tracking errors on performance of telescope array receiver for deep-space optical communication," in *Proc. IEEE Aerospace Conference*, 2007, pp. 1362-1369.

[4] **A. Hashmi**, A. A. Eftekhar, S. Yegnanarayanan, and A. Adibi, "Analysis of optimal adaptive optics systems for hybrid RF-wireless optical communication for maximum efficiency and reliability," in *Proc. IEEE ICET'08*, 2008, pp. 62-67.

[5] **A. Hashmi**, A. A. Eftekhar, A. Adibi, and F. Amoozegar, "A novel 2-D adaptive Wiener-filter-based algorithm for mitigation of atmospheric turbulence effects in deep-space optical communications," in *Proc. of SPIE*, vol. 7442, 2009, pp. 1-10.

[6] **A. Hashmi**, A. A. Eftekhar, A. Adibi, and F. Amoozegar, "Analysis of telescope array-based receiver for deep-space optical communications with Mars," in *Proc. IEEE LEOS Annual Meeting*, 2009, pp. 831-832.

[7] **A. Hashmi**, A. A. Eftekhar, A. Adibi, and F. Amoozegar, "Deep-space optical communication with Mars: achievable data rates," presented at IEEE Southeast Conf. Atlanta, GA, 2009.

[8] **A. Hashmi**, A. A. Eftekhar, A. Adibi, and F. Amoozegar, "Optimization of focal plane detectors for mitigation of atmospheric turbulence effects in deep space optical communication," in *Proc. Conf. on Lasers and Electro-Optics (CLEO)*, 2009.

[9] **A. Hashmi**, A. A. Eftekhar, A. Adibi, and F. Amoozegar, "Adaptive optics based telescope arrays receiver for compensation of optical turbulence effects in a deep-space optical communication link with Mars," in *Proc. IEEE Globecom*, 2009, pp. 1-8.

CHAPTER 2

COMMUNICATIONS SYSTEM MODEL

In this chapter, I will describe the basics of direct-detection optical communications systems and will give details about modeling a deep-space optical communications channel. The chapter starts with a review of optical communications systems, direct-detection optical systems, and pulse-position modulation (PPM). It is followed by the delineation of the transmitter and detector specifications, which are fixed throughout this thesis. Then, models for atmospheric turbulence, signal photons, and background photons are described. Finally, analytical methods to evaluate the performance of direct-detection optical communications systems in terms of probability of error, channel capacity, and achievable data rates are explained.

2.1. Optical Communications Systems

The block diagram of a generic optical communications system is shown in Figure 2.1. It consists of subsystems that are common to any communication system. The data to be transmitted is modulated onto an optical carrier in the transmitter. The modulated carrier is then transmitted through the optical channel (e.g., fiber optic waveguide, free-space, turbulent atmosphere). At the receiver, the transmitted carrier is optically collected, focused on to photodetectors, and further processed for demodulation and information recovery purposes. Due to the use of optical carriers, these systems are quite different from other communications systems in terms of operations, limiting factors, subsystems, and associated characteristics.

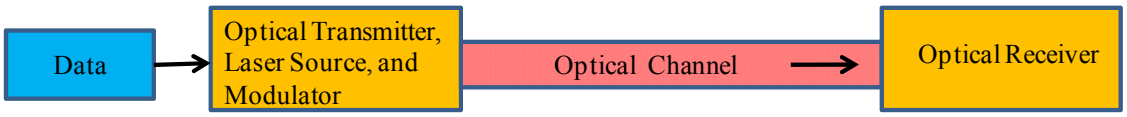

Figure 2.1. Block diagram of an optical communications system.

2.2. Direct-Detection Optical Communications Receivers

Optical receivers can be divided into two types: direct-detection (power detecting) receivers and heterodyning (coherent) receiver. Direct-detection receivers are employed whenever the transmitted information occurs in the power variation of the optical field. These receivers are simpler to implement and are suitable for deep-space turbulent optical links. A block diagram of a typical direct-detection receiver is given in Figure 2.2. The receiver consists of three major blocks: optical front-end, a photodetector, and a post-detection processor. The optical front-end consists of a lens or some form of focusing hardware and optical filters. In case of larger systems, telescopes are used and primary mirror or lens of a telescope acts as the front-end. The optical front-end collects the optical fields and focuses these onto the photodetectors in the focal plane. The photodetector performs an optical to electrical conversion. This is followed by the photon-counters and the post-detection processors, which perform the decoding and information recovery functions.

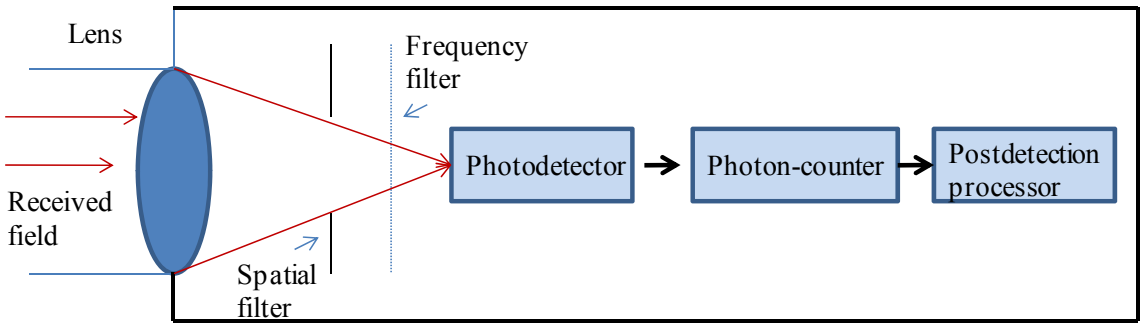

Figure 2.2. Schematic diagram of a direct-detection optical receiver.

2.3. Pulse-Position Modulation (PPM)

Pulse-position modulation (PPM) is a power-efficient modulation scheme suitable for a power-starved and average-power limited channel, such as a deep-space optical communications link. In the $M-ary$ optical PPM [37,38], digital data is encoded by the position of an optical pulse slot within a frame of M possible slots. The PPM order M represents the number of slots in each symbol (frame) and $\log_2 M$ data bits are encoded in one transmitted symbol. The duration of each slot in a PPM symbol is T_s seconds and duration of each symbol is MT_s seconds. The peak power in each transmitted symbol is M times the transmitter laser average power. Hence, PPM order M can be varied to vary the peak power for different situations. The optimization of PPM order M and PPM slot-width T_s is explained in details in Section 3.2. Figure 2.3 shows an example of a PPM symbol with M = 8.

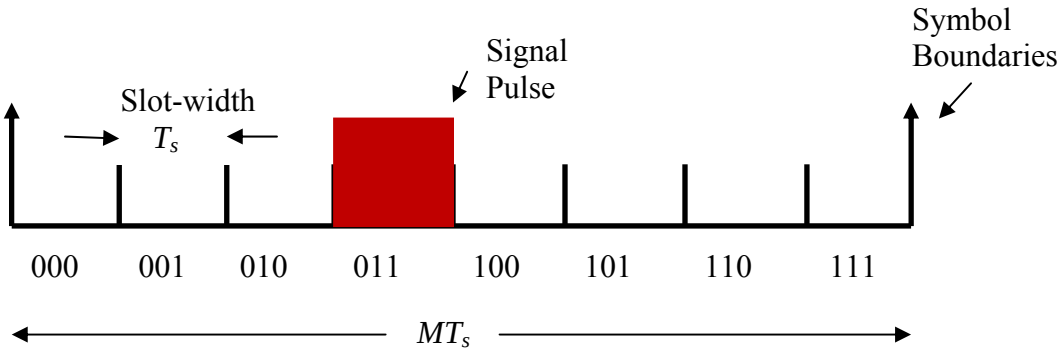

Figure 2.3. A PPM frame with order M = 8 and slot-width T_s seconds.

2.4. Transmitter Specifications

A transmitter (laser and transmitting telescope) deployed on a spacecraft in deep-space has several unique challenges and limitations. Several candidate technologies for a deep-space transmitter fulfilling these requirements are discussed in detail in [7,80].

Based on the current state-of-the-art space qualified technology, following specifications are employed in this thesis for a transmitter at a spacecraft in Mars orbit: a telescope with 30 cm aperture diameter, a laser with an average power of 5 W, and a peak-power of 1.3 kW operating at a wavelength of 1.06 μm [7,81]. A suitable choice for the transmitter laser that satisfy these specifications is a master oscillator power amplifier MOPA-based laser employing an Yb-doped fiber amplifier [7,80].

It is important to mention that the above-mentioned specifications are selected according to the current state-of-the-art technology. However, recent developments, e.g., the Defense Advanced Research Projects Agency's (DARPA) Super High Efficiency Diode Sources (SHEDS) program, have aimed at improving the efficiency of diode lasers that can be used for pumping the active medium (e.g. fiber amplifiers) [82]. Large increases in laser diode efficiency (nearly 60%) have been achieved so far, whereas the program's goal is 80% [80,82]. With the availability of such potent devices in the next decade, space-qualified laser transmitters with much higher peak and average powers are possible.

2.5. Deep-Space Optical Communications Link

A typical deep-space optical communications link is shown in Figure 2.4, which depicts all the major subsystems and limiting factors. A stream of digital data is encoded by modulating a laser carrier employing PPM. A transmitting telescope radiates the PPM frames containing optical pulses towards a ground-based receiver. Optical coupling and pointing losses are inflicted during this process. The optical signals travel hundreds of millions of kilometers distance from deep-space and suffer a huge free-space loss. The optical signals in the form of plane waves impinge upon the Earth atmosphere. As

optical signals traverse through atmosphere, these signals suffer attenuation and severe distortions are induced by the atmospheric turbulence. The turbulence-distorted optical signals are received at the receiving telescopes. Along with the desired signals, background noise emanating from celestial objects during nighttime and diffused sunlight from the sky during daytime also impinges upon the receiver aperture. Front-end optical processing is carried out to filter out the undesired background noise fields and focus the optical fields onto photodetectors. However, some fraction of background light enters the receiver FOV along with the desired optical signals. Optical and tracking errors are inflicted on optical signals at this stage. Photodetectors with the capability of responding to single photon arrivals are employed for photodetection and photon-counting. Photon counts are generated for each PPM slot. Synchronization errors are inflicted at this stage. Photon count (both signal and background count) are sent to the receiver for back-end processing and data decoding. For a photon-counting channel observing Poisson statistics, the performance of an optical communications system depends upon the number of signal and background photons. The main challenge in the design of the receiver is to minimize the losses and impact of limiting factors; increase the number of received photons and reduce the number of background noise photons; and compensate for atmospheric turbulence effects.

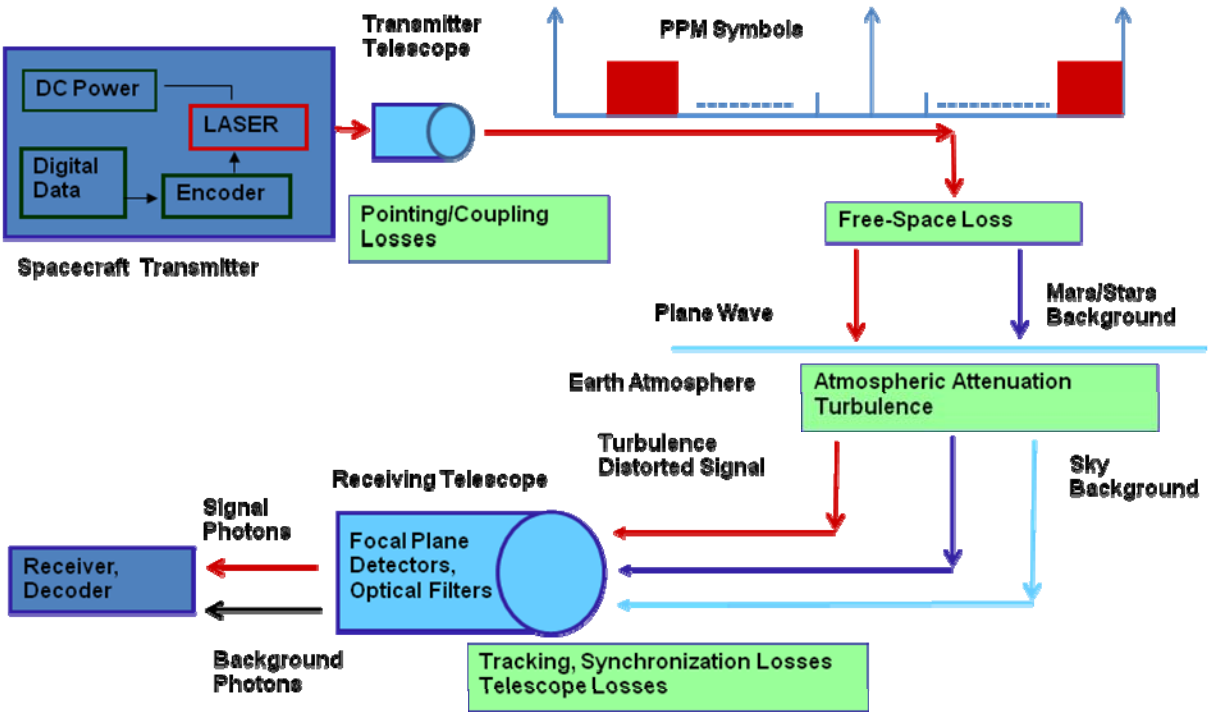

Figure 2.4. A deep-space optical communications link.

2.6. Photodetectors

For a photon-starved link such as a deep-space optical communications link analyzed in this thesis, efficient and sensitive detectors with the capability of responding to and detecting the single photon arrival events (i.e., single photon detectors, SPDs) are needed. Development of advanced, high-speed, low-noise, high-efficiency, and small-jitter SPDs have been pursued and reported at many government and defense organizations, such as JPL and MIT Lincoln Labs [80,81, 83-86]. Many advanced SPDs such as Geiger mode APDs and NbN super-conducting detectors, suitable for deep-space optical communications, have been reported in literature [80]. Recently, Farr *et al.* at JPL have reported the development and implementation of customized systems that can process the output of SPDs in GHz bandwidth range [84].

Several authors at MIT Lincoln Lab have reported the implementation of low dark current rate (DCR), high-efficiency, Geiger Mode APDs (GMAPDs) [81,83,85] with the output pulse rise time of few *ps*. In this thesis, a GMAPD with a quantum efficiency of 0.45 and a DCR of 4×10^4 count/s is employed as the system detector [80,81,83,85]. These detectors are capable of responding to single photon arrival events and their output can be modeled by the Poisson distribution. Since the outputs of GMAPDs are essentially digital, a digital network is used to collect the various measurements [81]. MIT Lincoln Lab has developed custom readout integrated circuits to optimize the GMAPD performance. A GMAPD coupled to a custom integrated circuit that provides for lossless readout via an asynchronous, nongated architecture is reported in Ref. [83].

It is important to mention that the development in SPDs continues to grow without bounds. Projections for the next decade based on what has already been accomplished show great promise for achieving at least 75% detection efficiency, very low intrinsic jitter (less than 30 *ps*), low DCR of around 10K count/s, and 10s of GHz of bandwidth for SPDs at near-infrared wavelengths of (1 - 1.5) μm [80,87].

2.7. Atmospheric Turbulence Model

Atmospheric turbulence along with background noise is a major limiting factor in a deep-space optical communications channel. Turbulence is an ever-present phenomenon in the atmosphere, although its strength varies from time to time within a day and night. Atmospheric turbulence gives rise to *optical turbulence* that is defined as the random fluctuations in the atmospheric refractive index [45]. Optical turbulence inflicts several deleterious effects on the propagating optical signals. These effects include phase distortions, optical scintillations, beam wander, and beam spreading

beyond that due to the pure diffraction [36]. Most of the telescope sizes analyzed in this thesis are greater than or equal to 1 m; for these sizes scintillation effects are negligible due to the aperture-averaging phenomenon [36]. The inclusion of an active tracking system mitigates the beam wander effects. Hence, scintillation effects are ignored (scintillation effects are only considered in Chapter 10 for short-range systems) and the impact of tracking errors is studied in Chapter 5. The turbulence-induced phase distortions break up an incoming plane wave from space into several incoherent random modes, limit the focusing capability of the receiving telescopes, and are the major effect considered here.

2.7.1. Atmospheric Coherence Length

The strength of optical turbulence at a particular location is widely represented by a descriptor called "the Fried parameter" or "Fried's coherence length." The Fried parameter r_o represents the spatial extent over which the phase of an optical beam is preserved or is almost coherent. The small values of r_o represent strong turbulence conditions and vice versa. During daytime, values of r_o range between 20 cm (weak turbulence conditions) and 4 cm (strong turbulence conditions) [34,36,88]. The utility of using Fried parameter as a descriptor of turbulence lies in the fact that it combines several related parameters into one number, which describes the strength of turbulence at a particular site. Fried parameter is usually defined by the expression [36,45]

$$r_o = \left[0.423 k^2 \sec(\varsigma) \int_{path} C_n^2(z)\, dz \right]^{-3/5}, \tag{2.1}$$

where $k = 2\pi / \lambda$, ς is the zenith angle, C_n^2 is the index-of-refraction structure constant, and the integral is over the communications path from the transmitting source to the

ground-based receiver telescope. Under turbulence consitions, the resolution (focusing capability of a telescope) is limited by the Fried parameter rather than the diameter of the telescope. Since r_o ranges from 4 cm to 20 cm in a daytime [34,36], and telescope diameters that are analyzed in this thesis are much larger than these numbers, the communications operation is always limited by the Fried parameter.

2.7.2. Atmospheric Effect on Detected Energy

The receiver FOV (the solid angle subtended on the detector) in a direct-detection optical communications system depends on the detector size in the focal plane. The detector size is chosen just large enough to encircle the focused PSF. In the absence of optical turbulence (i.e., the diffraction-limited case), the PSF in the detector plane is approximately equal to the extent of the Airy pattern and is given by $2.44\,\lambda f / D$ [17], where D is the aperture diameter of the receiving telescope and f is its focal length. A detector with the diffraction-limited spot size is sufficient to collect most of the signal energy in this case. However, in the presence of atmospheric turbulence, the focal spot size is limited by the atmospheric Fried parameter r_o given by $2.44\,\lambda f / r_o$ [17,77,88]. When the collecting aperture diameter D is larger than r_o (which is always true for telescopes and deep-space turbulent links considered in this thesis), optical turbulence results in an increase in the size of the PSF and a random distribution of signal energy into $(D / r_o)^2$ spatial modes in the detector plane [17]. A larger size detector is needed to capture the widespread signal energy, which means that the FOV of the receiver also increases. An increase in the receiver FOV results in an increase in the received background noise as the background noise is directly proportional to the detector

dimensions and receiver FOV [17,34]. The choice of a detector size determines the amount of received signal energy and background noise; hence, the detector size needs to be optimized for specific link conditions. In the turbulence-limited case, the mean fraction of the total signal energy incident on an aperture with diameter D and detected by a detector with normalized radius $D_s = r_d / \lambda F$ (r_d is the detector radius and $F = f / D$ is the telescope F-number) is given by [55,89]

$$\eta_{FOV}(D_s) = 2\pi D_s \int_0^1 OTF_{optics}(\rho)\ OTF_{turbulence}(\rho)\ J_1(2\pi D_s \rho)\, d\rho\ , \quad (2.2)$$

where ρ is the spatial frequency in the detector plane, *OTF* stands for the optical transfer function, and OTF_{optics}, $OTF_{turbulence}$ represents the *OTF*s of the receiving optics and atmospheric turbulence, respectively. Assuming an ideal annular optical collecting aperture with an obscuration ratio Γ, and a Kolmogorov model for the atmospheric turbulence structure with a Fried parameter r_o, the mean fraction of the signal energy is given by [55,89]

$$\eta_{FOV}(D_s) = 2\pi D_s \int_0^1 \frac{2}{\pi\left(1-\Gamma^2\right)}\left[\cos^{-1}\rho - \rho\left(1-\rho^2\right)^{1/2}\right]\exp\left[-3.44\left(\frac{D\rho}{r_o}\right)^{5/3}\right] J_1(2\pi D_s \rho)\, d\rho, \quad (2.3)$$

where J_1 is the first-order Bessel function of the first kind.

2.8. Signal Photons Model

Using the standard communications link budget analysis [55], the average received power at the receiver end is given by

$$P_r = P_t\ G_t G_r\ \eta_t\ \eta_r\ \eta_{atm} L_s\left(\sigma_{tr}^2, \sigma_{syn}^2\right)\left(\frac{\lambda}{4\pi Z}\right)^2, \tag{2.4}$$

where P_t is the average transmitted power; η_t and η_r are the transmitter and the receiver telescope optical efficiencies at the wavelength λ, respectively, which represent the optical (coupling, truncation, polarization and vignetting) losses in these telescopes; η_{atm} represents the atmospheric attenuation; and Z is the distance between the transmitter and the receiver. G_t and G_r are transmitting and receiving antenna (telescope) gains, respectively, which depend upon telescope aperture diameters [17]. $L_s(\sigma_{tr}^2, \sigma_{syn}^2)$ represents the tracking and synchronization losses. The typical PPM slot-widths ($\approx ns$) are quiet small compared to the characteristic time scales of the atmospheric turbulence ($\approx ms$), hence, atmospheric turbulence is considered to be frozen over a PPM slot-width, and the received signal intensity is taken as a constant during a PPM slot. Using this model, the average number of signal photons in a PPM signal slot is given by

$$K_s = P_r\ M\ T_s\ \eta_{det}\,\eta_{FOV}(D_s)\left(\frac{\lambda}{hc}\right) \text{ photons/ PPM slot}, \tag{2.5}$$

where P_r is the received optical power as given in Eq. (2.4); T_s is the PPM slot-width and MT_s represents the PPM frame-length; and η_{det} is the photodetector optical to electrical conversion quantum efficiency. $\eta_{FOV}(D_s)$ is given in Eq. (2.3) and represents the fraction of the received optical energy encompassed by the detector in the focal (detector) plane; Finally, hc/λ is the single photon energy at the carrier wavelength.

2.9. Background Photons Model

Background noise, emanating from the diffused sunlight from the sky during daytime, and stars, planets, etc. during nighttime, enters the receiver FOV along with the desired signal power [39-43]. This noise degrades the performance of an optical receiver. The background power (P_{bo}) collected in the diffraction-limited case (absence of atmospheric turbulence) is a constant and is independent of the receiving aperture diameter. For a radiation source with an area greater than the receiver FOV (e.g., diffuse light from sky), it is given by [17]

$$P_{bo} = L(\lambda)\, \Delta\lambda_{NBPF}\ \ \Omega_{DL}\, A_R = L(\lambda)\, \Delta\lambda_{NBPF}\ \ \lambda^2, \tag{2.6}$$

where $L(\lambda)$ is the spectral radiance function, representing the background source, in the units of μW/(cm^2-sr-nm), $\Delta\lambda_{NBPF}$ is the full width at half maximum (FWHM) bandwidth of the front-end optical filter, and A_R is the area of the receiving telescope aperture. Ω_{DL} is the solid angle representing the diffraction-limited FOV of the receiver that depends on the collecting aperture diameter , and is given by $\Omega_{DL} \approx \lambda^2 / A_R$ [17].

In the presence of atmospheric turbulence, the background power collected by the receiver is given by [55]

$$P_b = P_{bo}\ \frac{\Omega_{FOV}}{\Omega_{DL}}\ = P_{bo} \times N_r, \tag{2.7}$$

where Ω_{FOV} is the solid angle representing the receiver FOV in the presence of atmospheric turbulence and depends upon the detector size used in the focal plane to encompass the distorted PSF. N_r represents the number of random modes into which the

incoming optical field is broken up by the atmospheric turbulence. The average number of background photons per PPM slot is given by

$$K_b = P_b\ \eta_r^*\ \eta_{det}\ T_s\ \frac{\lambda}{hc} \quad \text{photons/PPM slot,} \tag{2.8}$$

where η_r^* is the receiver optical efficiency for background noise.

2.10. Communications System Performance

2.10.1. Probability of Error

In the *M*-ary PPM format, $log_2 M$ data bits are encoded by the position of a laser pulse in one of *M* possible slots. The photon-counting detectors are employed whose output counts in each PPM slot are compared to decode the received symbol. The output of photon-counters obeys the Poisson statistics [17,85]. For an average received signal count of K_s photons/slot and an average background noise count of K_b photons/slot, the output of photon-counters in a signal-slot is modeled as a random variable with the Poisson probability distribution function (PDF) given as

$$Pos(k, K_b + K_s) = \frac{(K_b + K_s)^k}{k!} e^{-(K_b + K_s)}. \tag{2.9}$$

In a non-signal-slot, only the background photons are received, and the output is modeled by the following Poisson PDF

$$Pos(k, K_b) = \frac{K_b^{\ k}}{k!} e^{-(K_b)}. \tag{2.10}$$

For a telescope array receiver, average K_s and K_b in Eqs. (2.8) and (2.9) are given by the sum of signal and background photons received by all the individual telescope elements in the array, respectively.

$$K_{s)Array} = \sum_{i=1}^{N} K_s^i \quad , \quad K_{b)Array} = \sum_{i=1}^{N} K_b^i \ , \tag{2.11}$$

where i represents the *i-th* telescope and N is the number of telescopes in the array receiver. It is important to mention that in the presence of detector dark current, a constant DCR is also added in each PPM slot. In PPM, a detection error is made whenever any one of the non-signal-slot photon count exceeds that of the signal-slot photon count. In case of a tie, a random choice is made between slots with equal counts. For a Poisson channel model employing PPM modulation, the uncoded probability of symbol error (PSE) is given as [17]

$$\begin{aligned} PSE \ = 1 - & \ \frac{\exp[-(K_{s)Array} + MK_{b)Array})]}{M} \\ & - \sum_{k_1=1}^{\infty} Pos\,(k_1, K_{s)Array} + K_{b)Array})\,[\sum_{k_2=1}^{k_1-1} Pos\,(k_2, K_{b)Array})\,]^{\,M-1} \\ & - \sum_{r=1}^{M-1} \frac{(M-1)!}{r!(M-1-r)!(r+1)} \sum_{k=1}^{\infty} Pos\,(k, K_{s)Array} + K_{b)Array})\,[Pos(k, K_{b)Array})]^{\,r} \\ & \times [\sum_{j=0}^{k-1} Pos(j, K_{b)Array})]^{\,M-1-r} \ . \end{aligned} \tag{2.12}$$

Eq. (2.12) can be approximated by [7]

$$PSE \ = 1 - \sum_{k=0}^{\infty} \left(1 + \frac{K_{s)Array}}{K_{b)Array}}\right)^k \times \frac{e^{-K_{s)Array}}}{M} \times \left(F_{Y|X}\,(k\,|\,0)^M - F_{Y|X}\,(k-1\,|\,0)^M\right), \tag{2.13}$$

where

$$F_{Y|X}\left(k\,|\,0\right) = \sum_{m=0}^{k} \left(\frac{K_{b)Array}^k \times e^{\,-K_{b)Array}}}{k!}\right). \tag{2.14}$$

Probability of bit error (PBE) is given by [17]

$$PBE = \frac{M}{2(M-1)}\, PSE\,. \tag{2.15}$$

2.10.2. Channel Capacity

The ultimate goal of any communications system is to transfer the information at the maximum possible data rate. Hence, the performance of the optical communications link is evaluated in terms of the achievable throughput. The channel capacity in units of bits/PPM symbols depends on the PSE and PPM order *M*. Using the hard-decision decoding strategy, the capacity (*C*) of a PPM channel is given by [7,55,90]

$$C = \log_2 M + (1-PSE)\,\log_2(1-PSE) + PSE \times \log_2\left(\frac{PSE}{M-1}\right) \text{ bits/PPM symbol.} \tag{2.16}$$

In terms of PBE, the channel capacity can be expressed as

$$\begin{aligned} C = {} & \log_2 M + \left(1-\frac{2(M-1)\times PBE}{M}\right)\times \log_2\left(1-\frac{2(M-1)\times PBE}{M}\right) \\ & + \frac{2(M-1)\times PBE}{M}\times \log_2\left(\frac{2\times PBE}{M}\right) \text{bits/PPM symbol.} \end{aligned} \tag{2.17}$$

The maximum achievable link data rate depends on the channel capacity and PPM parameters, and is given by [7]

$$R = \frac{C}{M\,T_s} \text{ bits/s} \tag{2.18}$$

It is important to mention that probabilities of errors considered in this thesis are uncoded one. However, as shown in Refs. [7,91], several error correcting codes can be applied to PPM signals to reduce the relatively high uncoded error probabilities. One coding scheme is to combine a Reed-Solomon code with PPM. Another is to use a convolutional code and a soft-decision decoder that iteratively decodes the convolutional code and the PPM

modulation, thus attaining error rates that can support high-performance deep- space optical communications

2.11. Chapter Summary

In this chapter, I have presented the definitions and system models that are employed in all the analyses presented in this thesis. Specifically, basics of optical communications systems, direct-detection communications systems, and PPM are introduced. Assumptions about the specifications of a transmitter in deep-space and system detectors are given. A deep-space optical communications link is introduced; important systems and subsystems are presented; and major limiting factors are identified. Details of the impact of atmospheric turbulence, Fried parameter and its effect on the detected optical energy are given. The performance of an optical communications receiver depends upon the relative number of received signal and background photons and detector DCR. I also developed the models for the received signal and background photons. In the end, analytical models to evaluate the performance of optical communications receivers (in terms of probability of error and achievable data rates) are presented.

CHAPTER 3

OPTIMIZATION OF SYSTEM PARAMETERS

Background noise and atmospheric turbulence phenomenon drastically affect the performance of deep-space optical communications systems. For the given channel conditions, the purpose of the optimization is to choose system parameters to minimize the background noise and turbulence effects and to maximize the communications system throughput. In this chapter, I first present the optimization of detector sizes (i.e., receiver FOV) to minimize the PBE, and then I present the optimization of PPM parameters (i.e., PPM slot-width T_s and PPM order *M*) to maximize the achievable data rates. Although, many other system parameters can be considered for optimization, the most important ones are addressed here. The examples that follow in this chapter assume Earth-Mars conjunction phase and an aggregate receiving aperture diameter of 10 m.

3.1. Dependence of Received Signal and Background Photons on Detector Size

In a direct-detection optical communications system, the receiver FOV is determined by the detector size [17,55]. Typically, the detector size is chosen just large enough to encompass the extent of the focused spot size in the image plane. The number of received signal and background photons, besides other factors, depends on the detector size, however, in different ways. The methodology of calculations of signal and background photons under turbulence conditions is given in Chapter 2. Using Eqs. (2.2 – 2.8), the numbers of received signal and background photons as functions of the detector size are calculated and plotted in Figure 3.1. In this example, the background spectral

radiance is 10 μW/(cm^2-sr-nm) and Fried parameter r_o = 4 cm. It is evident from the figure that the number of signal photons increases initially with an increase in the detector size and then saturates after a certain limit (i.e., after the complete encapsulation of the turbulence-degraded PSF). On contrary, the number of background photons continues to increase linearly on a log scale with an increase in the detector size. As the performance of the receiver mainly depends upon the relative number of signal and background photons, Figure 3.1 dictates that the detector size needs to be selected to optimize the receiver's performance.

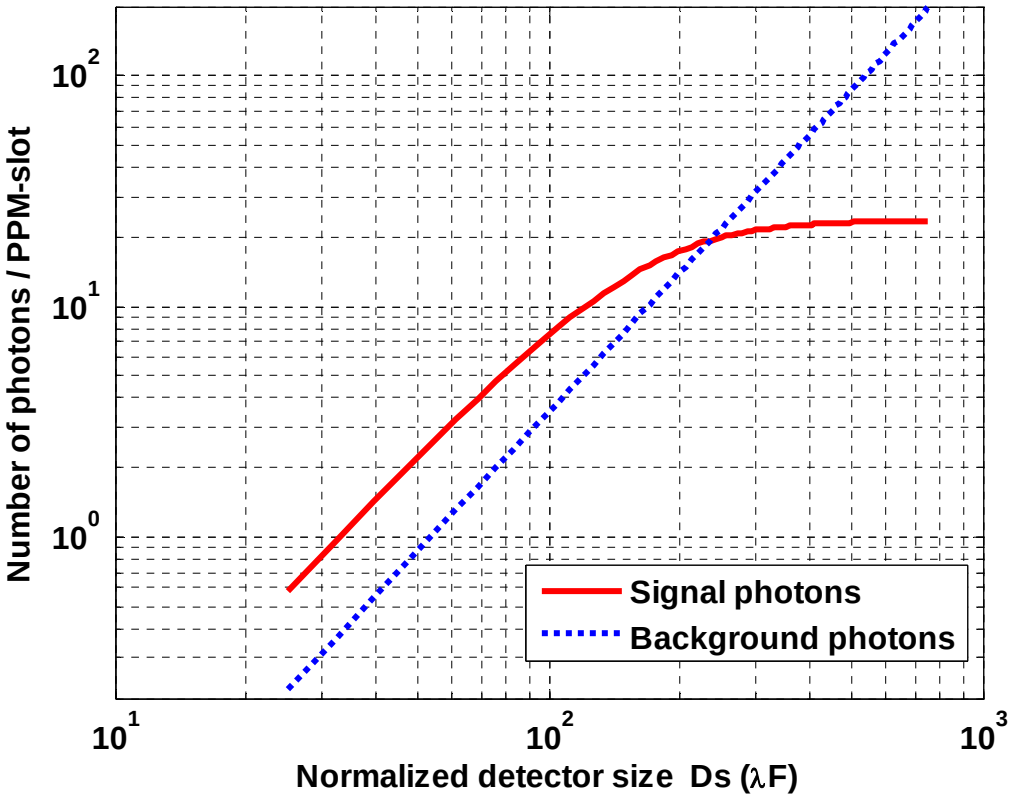

Figure 3.1. Number of received signal and background photons versus normalized detector size. M = 256, telescope aperture diameter D = 10 m, and Fried parameter r_o is 4 cm.

3.2. Optimization of Detector Sizes to Minimize the Probability of Bit Error (PBE)

The PBE as given by Eqs. (2.12–2.15) is the cost function that we want to minimize. PBE depends on the number of received signal and background photons, which in turn depend on the detector size (Figure 3.1). For the given system parameters, background noise, and turbulence conditions, the aim is to find the optimum detector size (D_s) that minimizes the PBE. Mathematically, the goal of optimization can be stipulated as to

$$\textbf{Minimize} \qquad PBE = PBE\left(K_s,\, K_b, D_s, r_o\right), \tag{3.1}$$

$$\textbf{subject to} \qquad K_s = K_s\left(P_s, D_s, r_o\right) \text{ photons / PPM slot}, \tag{3.2}$$

$$K_b = K_b\left(P_{bo}, D_s, r_o\right) \text{ photons / PPM slot}. \tag{3.3}$$

The optimization process is described as follows: All the given system parameters and channel conditions are plugged in the algorithm. The algorithm runs the link budget analysis, searches over a wide range of detector sizes (normalized with respect to the diffraction-limited spot size), and calculates the signal and background photons and the uncoded PBE for each data point using Eqs. (2.2–2.15). The detector size that minimizes the PBE is selected as the optimal one through this exhaustive search. Figure 3.2 shows the result of this procedure for a Fried parameter of $r_o = 4$ cm, and three different values of background spectral radiance *L*, i.e., 175, 10 and 3 μW/(cm^2-sr-nm). To compare the performances of the telescope array receiver and a single telescope receiver, I calculated the PBE for the two cases under these different background noise conditions. The set of curves on the right in Figure 3.2 corresponds to a single telescope with an aperture diameter of 10 m, and the curves on the left correspond to a telescope array-based

receiver consisting of 100 telescopes with individual aperture diameters of 1 m. It is evident from Figure 3.2 that for the given channel conditions, there is a unique detector size that minimizes the PBE in each case, and the optimum detector size vary with different link conditions. The optimum detector sizes for a single telescope are 177.25, 230, and 250, all in the units of (λF), corresponding to three background cases. Whereas, the optimum detector size for individual telescopes in the telescope array receiver are 17, 23, and 26, in the units of (λF), for three background cases. For stronger background noise conditions, the optimum detector size is relatively smaller, i.e., FOV of the receiver is reduced to reject more background noise (spatially). The reduction in the receiver FOV results in the loss of signal photons, but the rejection of background noise is more significant, which results in the better receiver performance. As the background spectral radiance L decreases from 175 to 10 and 3 μW/(cm^2-sr-nm), the optimum detector sizes and the corresponding FOV increases to collect more signal photons due to low background noise conditions. It is also obvious that the optimum detector sizes in the telescope array case are considerably smaller than those in the single (large) telescope due to the large disparity between the sizes of the telescopes in the two architectures. Nevertheless, the optimum PBEs achieved by the single telescope and the telescope array-based architectures are almost equal for similar background noise conditions.

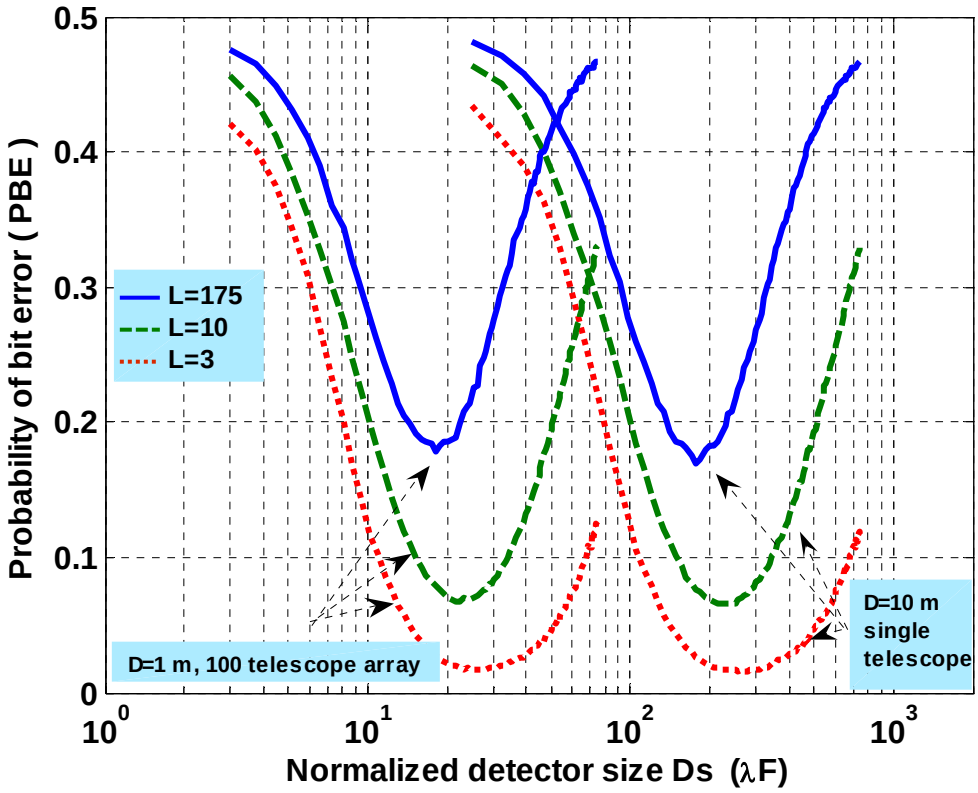

Figure 3.2. PBE vs. normalized detector size for a deep-space optical communications link. The set of curves on the left is for a telescope array receiver consisting of 100, 1 m diameter telescopes. The set of curves on the right is for a single telescope with 10 m aperture diameter. Fried parameter r_o is 4 cm and M = 256. Background noise radiance L is in units of μW/(cm^2-sr-nm).

Figure 3.3 represents the optimization of the detector sizes for the same channel conditions as those of Figure 3.2, but with a different Fried parameter of r_o = 20 cm, which represents the best turbulence conditions during the daytime. The background spectral radiance values in Figure 3.3 correspond to L = 175, 60, and 10, all in units of μW/(cm^2-sr-nm). Due to better turbulence conditions in this case, I tested slightly higher background noise as compared to Figure 3.2. The optimal detector sizes for a single telescope case are 50, 52, and 60, in the units of (λF), corresponding to three

background values. The optimal detector sizes for each telescope in the array are 5, 5.2, and 6, in the units of (λF), for three background values. Comparing the PBE data for the single telescope and the telescope array case shown in Figure 3.3, we get similar conclusions to what obtained from Figure 3.2. The optimum detector size in the array receiver case is much smaller than that in a single telescope case while the optimum PBE in both cases are similar.

More importantly, comparison of Figures 3.2 and 3.3 shows that in better turbulence conditions, (i.e., larger r_o) the optimum detector sizes and PBE at a given background noise level are considerably smaller (Figure 3.3) then those in the strong turbulence conditions (Figure 3.2). Furthermore, Figure 3.3 shows that the optimization curves are generally broader at lower background spectral radiance levels (i.e., for L = $10\,\mu$W/(cm^2-sr-nm)). This means that the optimum detector size is not too sensitive to the system parameters in best channel conditions (i.e., when background noise and turbulence are very weak). Nevertheless, the range of optimal detector sizes is much wider in case of strong turbulence and background conditions. Hence, the need and impact of optimization is more profound in case of strong turbulence and background noise conditions.

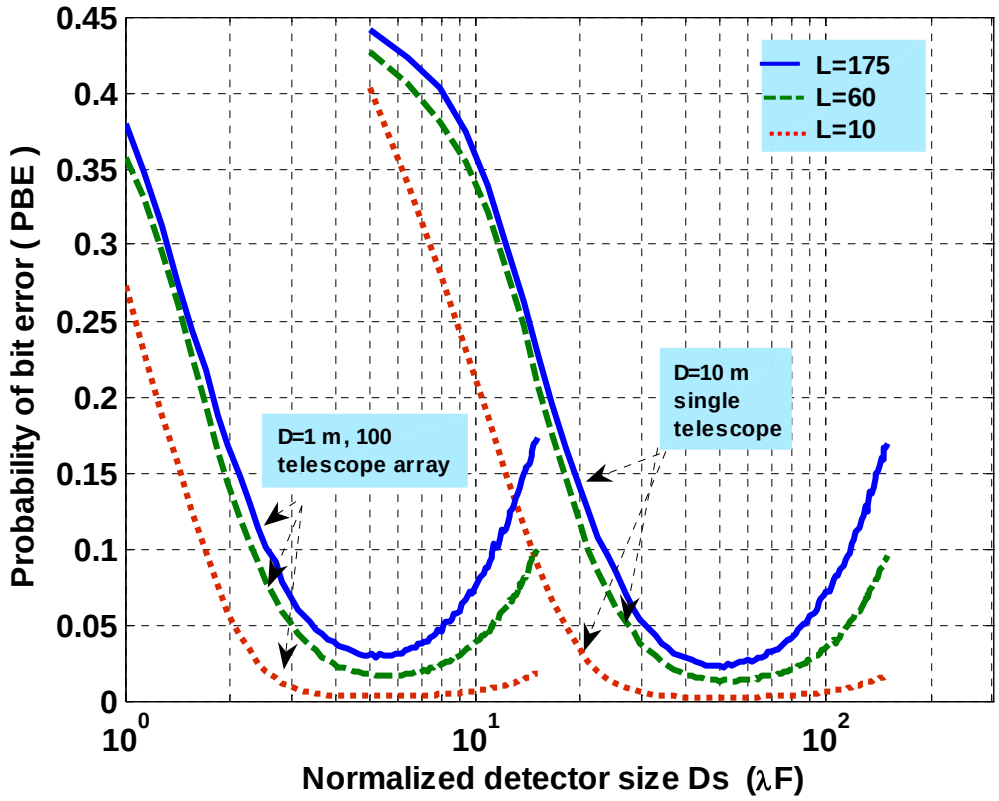

Figure 3.3. PBE versus different detector sizes for a deep-space optical link with Fried parameter $r_o = 20$ cm. All the other system parameters are same as those in the caption of Figure 3.2.

3.3. Optimization of PPM Parameters and Detector Size to Maximize the Data Rate

The achievable link data rate depends on the PPM order M, slot width T_s, and the PBE, as given in Eqs. (2.15–2.18). In this section, I present the simultaneous optimization of the detector size, PPM slot-width T_s, and PPM order M to maximize the achievable data rate. This optimization procedure will be used in the performance analysis of the telescope array receivers in subsequent sections. The cost function to maximize is the achievable data rate given by Eq. (2.18). Mathematically, the goal of the optimization is to

Maximize Data rate $R = R(C, M, T_s)$ bits/s, (3.4)

subject to Channel Capacity $C = C(PBE, K_s, K_b, M, D_s, r_o)$ bits/symbol, (3.5)

$$\text{Average power} = (P_{avg}) = E_{peak} \times PRF = E_{peak} \times \frac{1}{T_s \times M} = \frac{P_{peak}}{M} \text{ W}, \quad (3.6)$$

$$\text{Average power} = 5 \text{ W, Peak power} \leq 1.3 \text{ KW}, \quad 2ns \leq T_s \leq 20ns. \quad (3.7)$$

Eq. (3.7) represents the constraints on the specifications of the state-of-the-art space qualified transmitting laser [81,88]. The lower bound on the PPM slot-width is set to 2 *ns*, as a slot-width narrower than this value will render the synchronization and tracking tasks at the receiver very difficult. Slot-widths greater than 20 *ns* will result in very low data rates. Hence, the optimization of T_s is performed over the range given in Eq. (3.7). The optimization algorithm starts with the input of the system and the link parameters. It runs the link budget analysis to calculate the received signal and background photons, PBE, and the achievable data rate for different detector sizes and PPM parameters (T_s and M). It then selects the parameters, which maximize the channel capacity.

3.3.1. Strong Background Noise Conditions

The results for the Fried parameter of r_o = 4 cm and background spectral radiance of 175 μW/(cm^2-sr-nm), which represent the most stressing channel conditions, are given in Figure 3.4 and Figure 3.5. The achievable data rates are plotted as a function of the normalized detector sizes and PPM slot widths in the figures. Although, the optimization is performed over three parameters namely, T_s, M, and detector sizes D_s, the results are shown only for two parameters due to the limitations on plotting the 3D data. Corresponding one-dimensional results of Figure 3.4 are given in Figure 3.5. It is obvious

from these figures that the data rate is maximized at 2.1 Mbits/s when the design parameters are optimized and selected as follows: normalized detector size D_s = 177.25 (λF), T_s = 9 *ns*, and M =*256*.

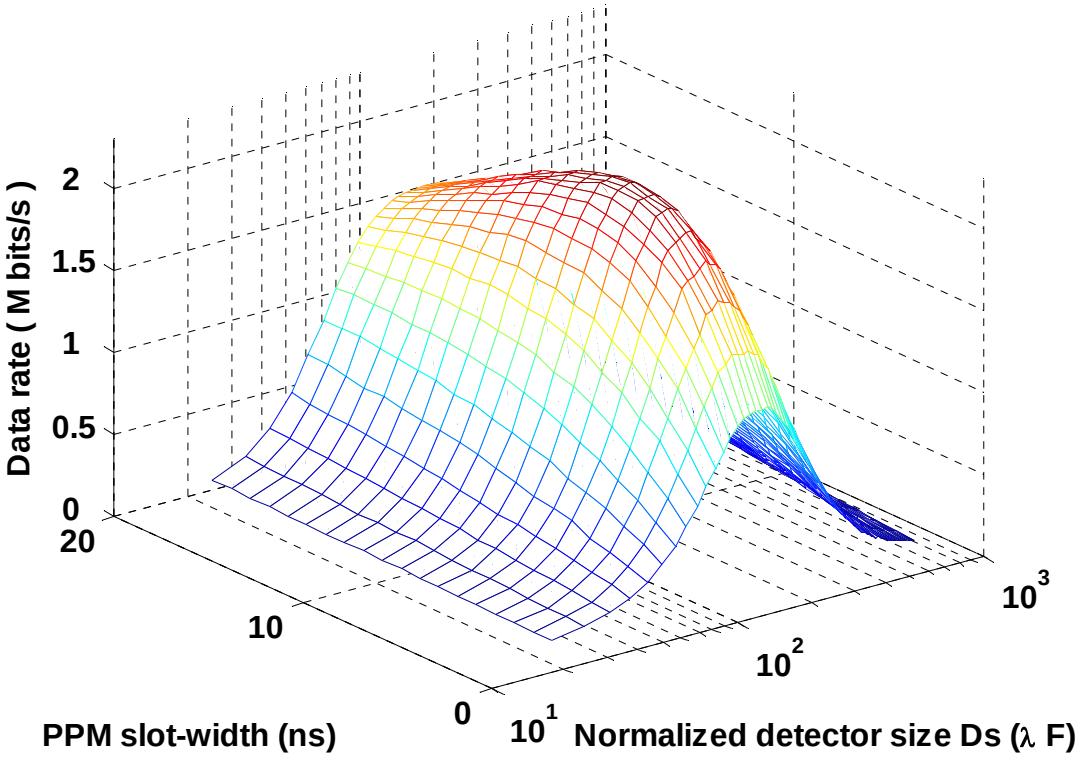

Figure 3.4. Achievable data rates versus different PPM slot-widths and normalized detector sizes D_s for a deep-space optical communications link between Earth and Mars. Background noise radiance is fixed at L = 175 μW/(cm^2-sr-nm), Fried parameter r_o = 4 cm, and optimal M = 256.

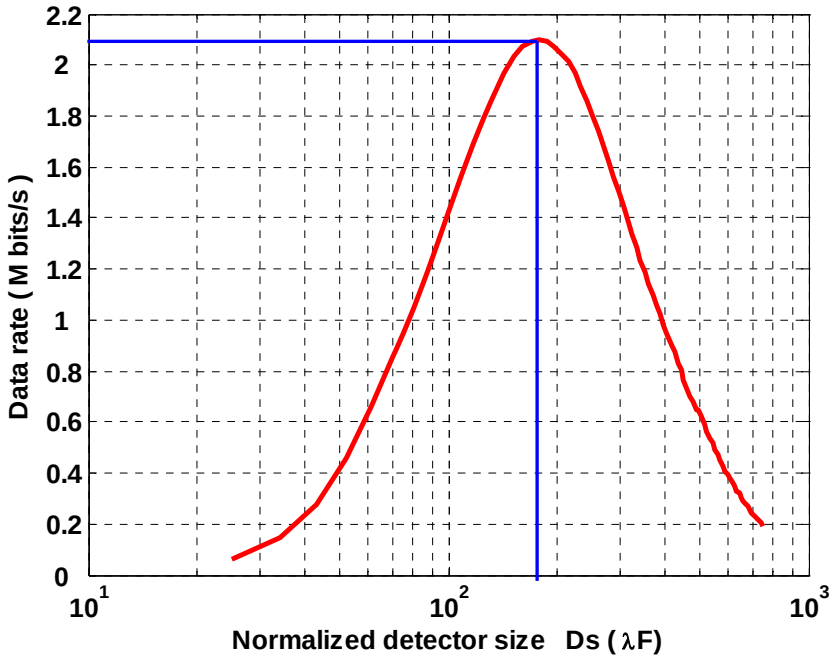

(a)

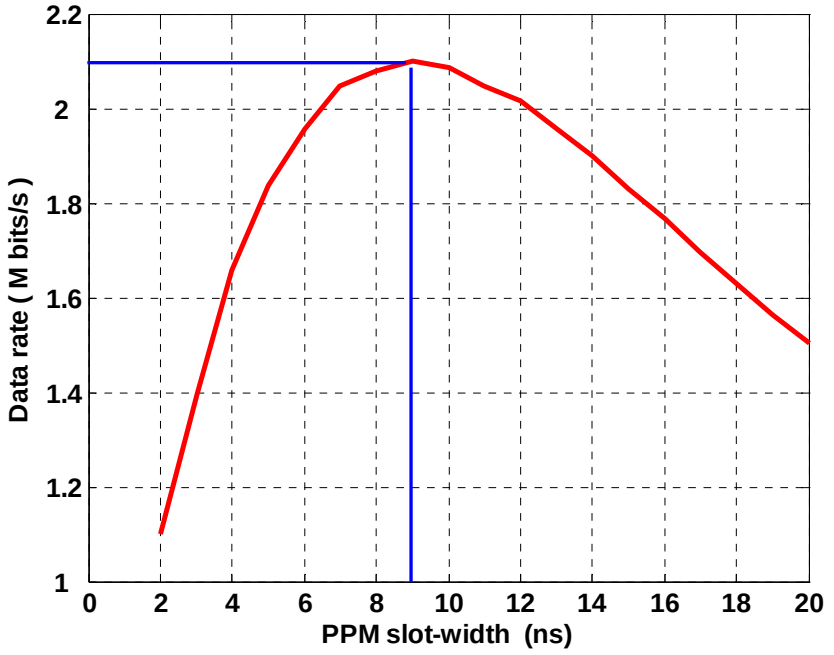

(b)

Figure 3.5. One-dimensional representation of the data in Figure 3.4. Optimization of (a) the detector size, and (b) the PPM slot-width to maximize the achievable data rate. All the other system parameters are same as those in the caption of Figure 3.4.

3.3.2. Weak Background Noise Conditions

The optimization algorithm is repeated for weak background condition with a radiance of 10 μW/(cm^2-sr-nm), and the results are shown in Figure 3.6 and Figure 3.7. It is shown that in these conditions, a data rate of 12.35 Mbits/s is achievable with an optimized detector size of D_s = 220 (λF), T_s = 2 *ns*, and M = 256. Hence, in better channel conditions (i.e., less background noise) the optimum detector size is increased, and the optimum slot-width is reduced, i.e., the power efficiency is traded for the bandwidth efficiency. It is important to mention that all the above-mentioned results have been verified through the Monte-Carlo simulations and the analytical techniques. The above-mentioned results underscore the importance of running the optimization algorithm for the specific link conditions, and selecting the optimal system parameters to maximize the communications system throughput.

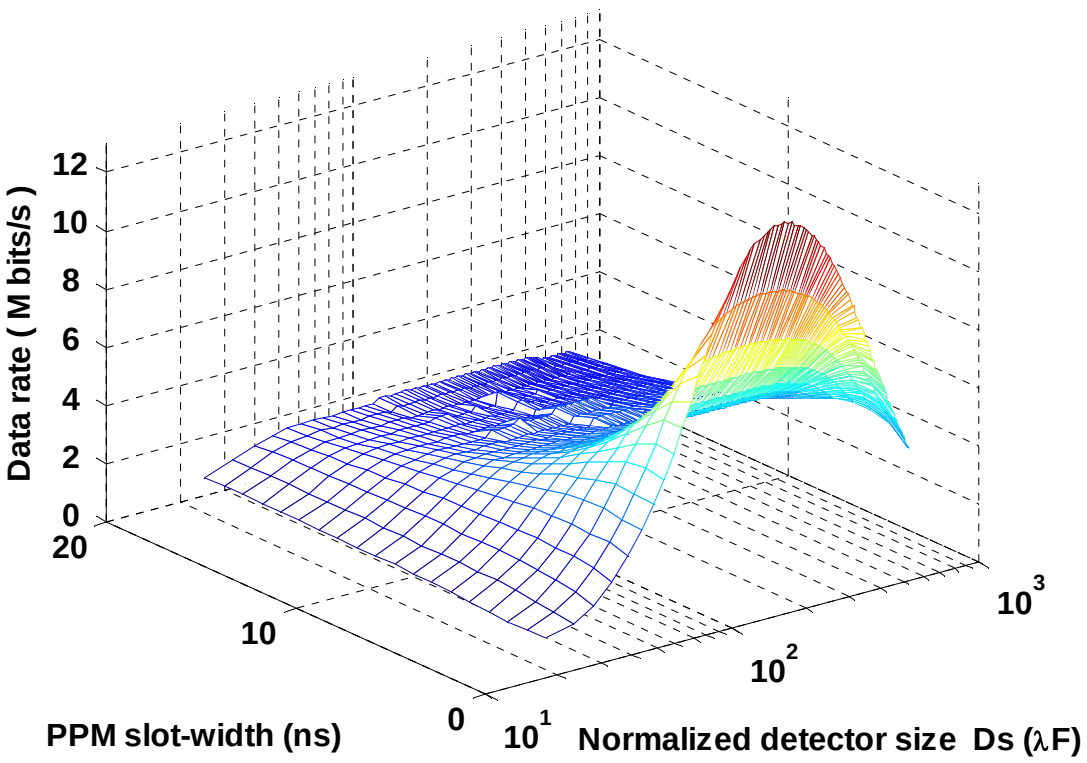

Figure 3.6. Achievable data rates vs. different PPM slot-widths and normalized detector sizes D_s for a deep-space optical communications link between Earth and Mars. Background radiance is fixed at $L = 10\,\mu\text{W/(cm}^2\text{-sr-nm)}$, Fried parameter $r_o = 4$ cm, and optimal $M = 256$.

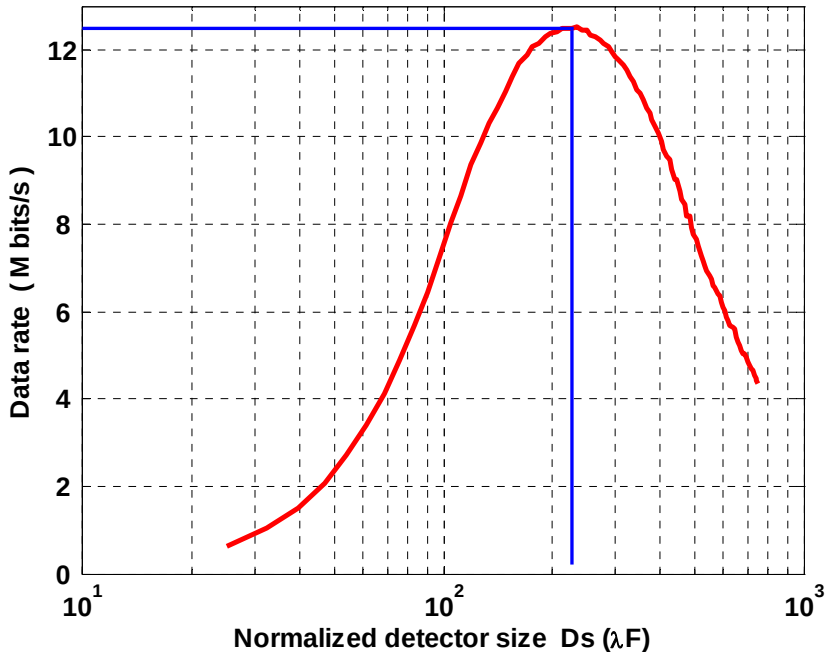

(a)

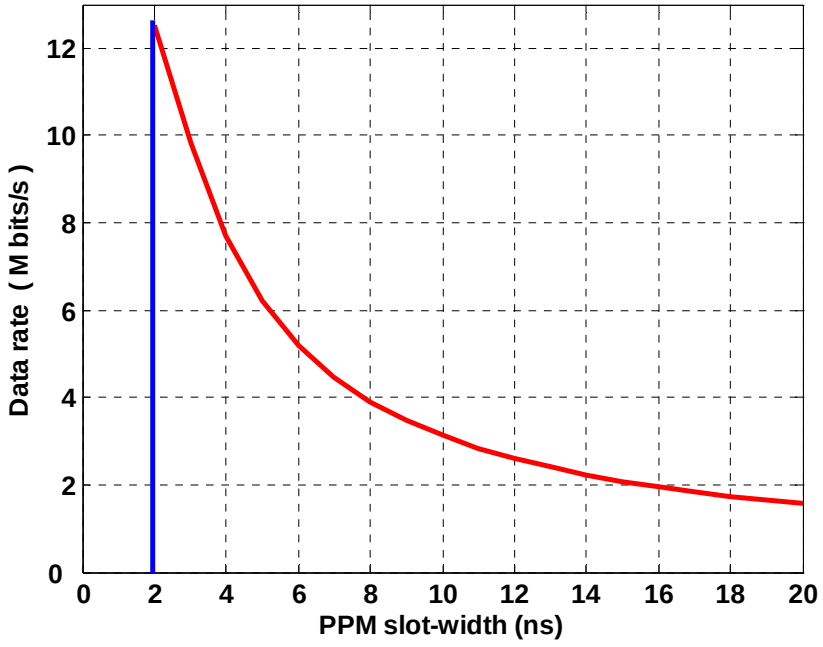

(b)

Figure 3.7. One-dimensional representation of the data in Figure 3.6. Optimization of (a) the detector size, and (b) the PPM slot width to maximize the achievable data rate. All the other system parameters are same as those in the captions of Figure 3.6.

3.4. Chapter Summary

Atmospheric turbulence and background noise are the major limiting factors in a deep-space optical communications link. In this chapter, I presented the optimization of the important system parameters, i.e., detector size, PPM order *M*, and PPM slot-width T_s, to minimize these deleterious effects subject to the constraints of the currently available space-qualified laser technology. Although, several other parameters can also be considered for optimization, I targeted the most significant ones. I showed examples of the optimization for different background and turbulence conditions. In an actual deployment of the optical receiver at a specific location on Earth, the local background and turbulence conditions can be measured a priori, and statistical analysis and estimation of these parameters can be done easily. The incorporation of this knowledge into the optimization algorithms can further simplify the optimization process and improve the performance of the system.

CHAPTER 4

ANALYSIS OF TELESCOPE ARRAY-BASED RECEIVERS FOR DEEP-SPACE OPTICAL COMMUNICATIONS BETWEEN EARTH AND MARS

In this chapter, performance analysis of telescope array-based receivers for a deep-space interplanetary optical communications link between Earth and Mars is presented. In optical communications receivers, telescopes act as antennas. Their purpose is to collect the transmitted communications signals and to focus the collected optical signals onto detectors in the focal plane. First, the conceptual design of a telescope array-based receiver is presented. Next, performance analyses of telescope array receivers are given for a broad range of operational scenarios, such as: Earth-Mars conjunction, Earth-Mars opposition, a wide range of atmospheric turbulence and background noise conditions. The link budgets for these channel conditions are also delineated. The performance of a single telescope is compared to different array architectures (having the equal aggregate aperture area) and upper and lower bounds on achievable data rates are determined. It is shown that compared to current RF-based communications network, telescope array-based optical communications can support orders of magnitude greater data rates.

4.1. Conceptual Design of a Telescope Array-based Receiver

Deep-space optical communications involve distances on the order of hundreds of millions of kms. As a result, the received communications signal becomes very weak when received at Earth. Moreover, presence of many other limiting factors such as background noise and atmospheric turbulence further complicate the communications operations. Due to constraints on the power and size of a transmitter at a spacecraft in deep-space, one of the solutions in hand is to use a large aperture diameter telescope (antenna) at the receiver location. It has been shown by us in Ref. [57,61] that for a deep-space optical communications link, a 10 m aperture diameter telescope is required for providing acceptable communications throughput during worst-case channel conditions. However, a single large telescope has the limitations of high cost, single-point failure in case of malfunction, difficulty in maintenance, enormous weight, substantial gravitational effects, and difficulty in manufacturing the high quality optics. In addition, the communications operations with a large telescope for small Sun-Earth-Probe (SEP) angles are very difficult, as a single big lens acts as a formidable solar energy concentrator.

An array of relatively smaller-sized telescopes is a viable alternative to a single large monolithic telescope receiver. Telescope arrays have advantages of lower cost, improved diffraction-limited performance, less gravitational effects, scalability, ease of maintenance, and redundancy in operations [25]. A telescope array is an aggregation of a number of relatively smaller-sized telescopes whose outputs are connected (in the electrical domain) to form a larger effective photon-collecting area. The number and sizes of the individual telescopes are selected so that the collective aperture of the array gives

the same combined gain as that required from a single large telescope. Conceptual design of a telescope array-based receiver is given in Figure 4.1. Individual telescope elements have an optical front-end consisting of focusing optics and optical filters to reject the ever-present background noise. Each telescope collects a portion of the incoming optical signal and in-band background noise, and focuses it onto its detectors. In my design, I incorporate direct-detection technique and photon-counters with the capability of single-photon detection. The details of detectors have been given in Chapter 2. The sizes of the focal plane detectors are optimized for the specific link conditions, as explained in Chapter 3.

Each telescope has its own clock, acquisition, and pointing control subsystems. The telescopes are also equipped with the synchronization, tracking, and AO systems. Detected signals and photon-counts from all telescopes are sent to a central combining unit via a high-speed digital network. In case of a large number of telescopes in the array, partial signal combination is also performed at different cluster control centers to reduce the central network load. The central combing unit combines photon counts from all of the telescopes after delay compensation and synchronization. The decision statistics for a PPM frame are formed in the central combining unit and are sent to the digital decoder for data extraction and information recovery purposes. Finally, the decoded data and information is transferred to the end user. The vital concept in a telescope array receiver is that signals are first optically detected at different array elements and then combined electrically for decoding purposes. In this chapter, synchronization, tracking, and AO subsystems are shown as block diagrams. The detailed analysis and design of these subsystems will be presented in following chapters. It is also important to mention that

for a highly specialized application such as a deep-space optical communications link, photodetectors and other associated electronic circuitry in the receiver are enclosed in a cryogenic module, which greatly suppresses the receiver thermal noise and photodetector dark current count.

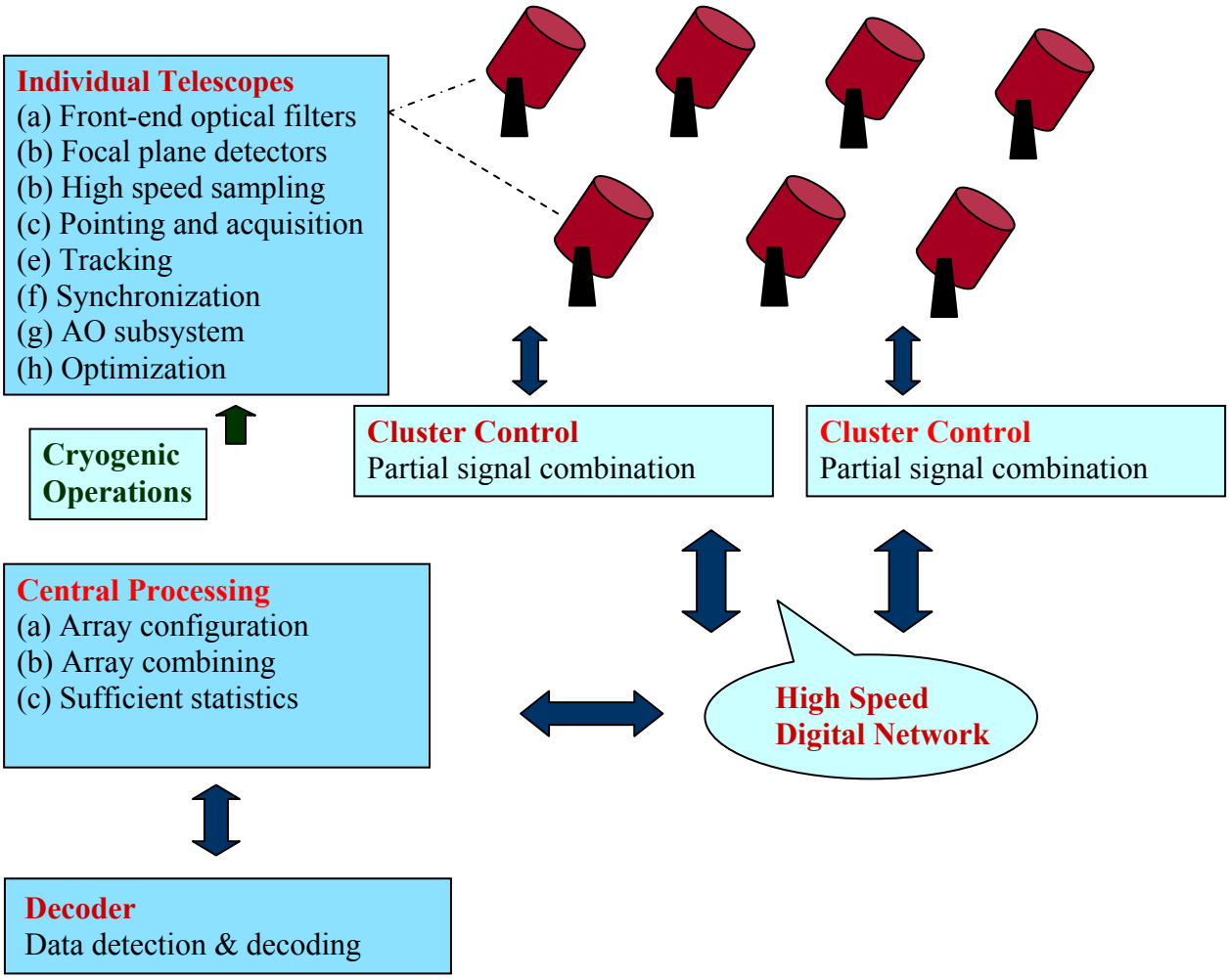

Figure 4.1. Conceptual design of a telescope array-based optical communications receiver.

4.2. Performance Analysis

In this section, the performance of telescope array-based optical receivers is evaluated for a deep-space optical communications link between Earth and Mars. It is important to highlight that one of the aims of this study is to find the upper and lower bounds on achievable data rates. Hence, the link is tested for both the worst-case and the best-case channel conditions. The main design parameters of the array architecture are the sizes of individual telescopes and the number of telescopes in the array. However, for comparison purposes, the total photon-collecting aperture of the complete telescope array receiver remains constant in different architectures (10 m in this case). I start with a monolithic, telescope with 10 m aperture diameter, i.e., the $(1\times 10\text{ m})$ configuration. Then, I increase the number of telescopes in the array by breaking down the single aperture into 2, 4, 8, 16, 32, 100, 135, and 150 etc. telescopes with 7.07 m, 5 m, 3.53 m, 2.5 m , 1.76 m, 1 m, 0.866 m, and 0.815 m (further on) aperture diameters, respectively. These cases correspond to the $(2\times 7.07\text{ m})$, $(4\times 5\text{ m})$, $(8\times 3.53\text{ m})$, $(16\times 2.5\text{ m})$, $(32\times 1.76\text{ m})$, $(100\times 1\text{ m})$, $(135\times 0.866\text{ m})$, $(150\times 0.815\text{ m})$, and so on, configurations.

Performance of telescope array receivers are evaluated using the following steps: given the specific channel conditions (link budget specifications, background noise, and turbulence parameters), signal and background photons are calculated and system parameters are optimized using the techniques described in Chapters 2 and 3. The Poisson distributed counts from individual telescopes are sent to the central processor where data is combined and sufficient statistics are formed for each PPM slot within a symbol. The PBE and the achievable data rate are evaluated using the analytical techniques discussed in Chapter 3. To further substantiate the analytical results, Monte-

Carlo simulations are preformed and the simulation results are compared with the analytical results. In Monte-Carlo simulations, 1 million PPM frames of order M are transmitted. A portion of the transmitted signal and background noise is received by each telescope in the array. The output photon counts for each PPM slot are modeled as Poisson random variables and slot counts from each telescope are summed up in the central station. The individual slot counts are compared and the slot containing the largest count is selected as the signal slot in each PPM frame, and then PBE is evaluated after averaging over 1 million symbols. The results of the analysis for different link conditions are presented in the next sections.

4.2.1. Earth-Mars Conjunction

Earth-Mars conjunction phase represents the most stressing case for the communications link between Earth and Mars. During this phase, the distance between Earth and Mars is at the maximum, i.e., 2.5 astronomical units (AU), where 1 AU $=1.49598\times10^{11}$ m. In addition, the Sun-Earth-Probe (SEP) angles can be very small; the link operates during daytime when both the background noise and the atmospheric turbulence are at their respective peaks.

4.2.1.1. Link Budget

The link budget parameters for this scenario are given in the Table 1. The specifications of the transmitter, receiver, optical losses, and front-end filters are chosen based on the state-of-the-art, space-qualified lasers and other optical devices [55,81,88]. The average power of the transmitter laser is fixed at 5 W. The PPM parameters, detector size and the peak power are optimized for specific link conditions. The Kolmogorov atmospheric turbulence model is employed in simulations. The background noise,

atmospheric turbulence represented by Fried parameter values, and telescope architecture parameters (number and size of individual telescopes) are treated as the variable entities in the analysis.

Table 4.1. Link budget for Earth-Mars conjunction.

Transmitter	**Description**	**Value**
Average transmitter power, $P_{avg.}$	5 W	6.98 dBW
PPM order , M		16-256 (optimized)
Slot width , T_s		2-20 *ns* (optimized)
Peak transmitter power, P_{peak}	$P_{avg.} \times M$, 80-1300 Watts	(19.03-31.12) dBW (optimized)
Transmitter antenna gain	30 cm telescope at λ =1060 nm	117 dBi
Transmitter losses	Optical and vignetting losses	1.43 dB
Pointing losses		1.25 dB
Channel		
Free space loss	2.5 AU (1AU =1.49598×10^{11} m)	372.48 dB
Atmospheric loss	Absorption and scattering	1.75 dB
Background spectral radiance	μW/(cm^2-sr-nm)	1-175
Fried parameter	Best conditions	20cm
	Worst conditions	4cm
Receiver (Cryogenic)	Cryogenic operations	
Receiver antenna gain	(1-10 m) Telescope diameter	(129.3 - 149.3) dB
Receiver losses (signal)	Optical, truncation, polarization	4.58 dB
Receiver losses (background)		5.01 dB
Front end filer optical bandwidth		0.1 *nm*
Photodetector efficiency	Quantum detection efficiency	45 %
Photodetector dark current rate		4×10^4 count/s
Link margin		3 dB

4.2.1.2. Results: Achievable Data Rates

First, the link is tested for the worst channel conditions, i.e., when the SEP angle is as low as 3º, the background sky radiance is very strong at 175 μW/(cm^2-sr-nm), and turbulence is at its peak with the Fried parameter r_o = 4 cm [55,88]. The achievable data rates are calculated for different array architectures and are plotted in Figure 4.2 as a function of individual telescope diameters in the array. Figure 4.2 shows that as the diameter of individual telescopes decreases from 10 m to 1 m, the achievable data rate decreases only slightly from 2.10 Mbits/s to 2.04 Mbits/s. However, as we further reduce the telescope diameters until these reach 3.78 cm, a considerable degradation in the performance is observed as the data rates reduce to just 460 Kbits/s.

It is important to mention that this particular condition can occur for only about 5 % of the time in a deep-space optical communications link between Earth and Mars. However, the analysis is presented to establish the lowest bound on achievable data rates for Earth-Mars optical link based on the technological considerations in this thesis.

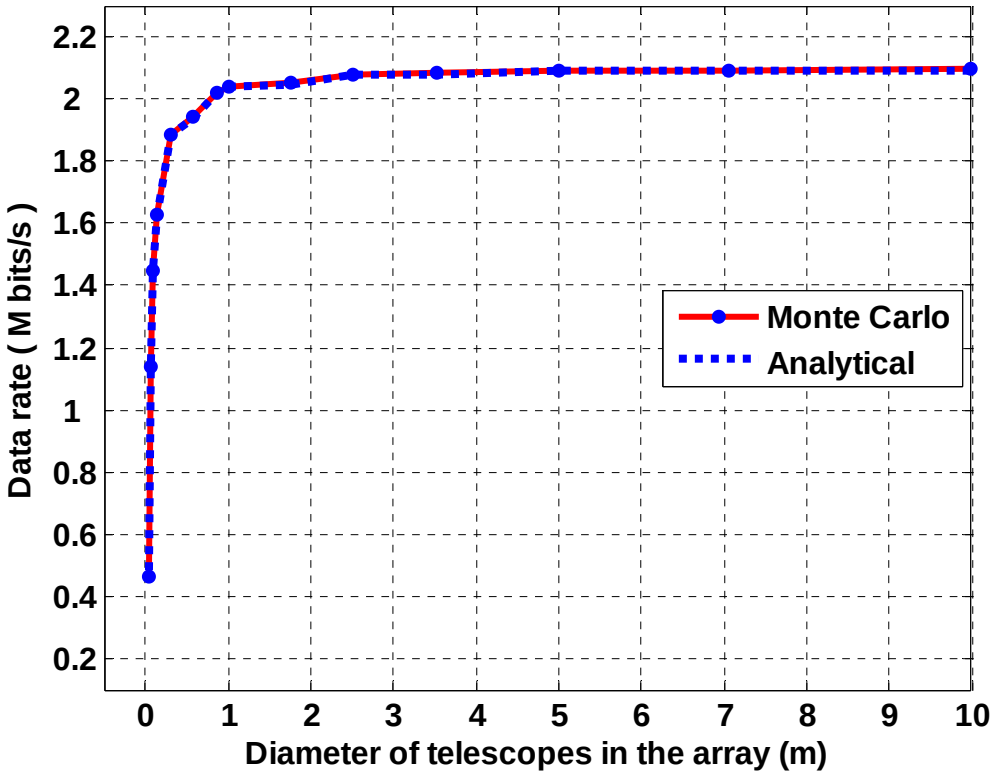

Figure 4.2. Achievable data rate vs. the diameter (D) of individual telescopes in the array receiver. The aggregate aperture area in each case is 10 m. Background noise radiance is fixed at $L = 175\,\mu\text{W/(cm}^2\text{-sr-nm)}$, Fried parameter $r_o = 4$ cm, optimal $M = 256$, and optimal $T_s = 9$ *ns*. Excellent agreement between the analytical results and Monte-Carlo simulations is evident.

The results given in Figure 4.2 are redrawn in Figure 4.3 in the form of achievable data rate as a function of the number of telescopes in the array receiver. Figure 4.3 shows that the achievable data rates degrade from 2.10 Mbits/s to 2.04 Mbits/s as the number of telescopes is increased from 1 to 100. This performance degradation is negligible and the performance of an array of up to 100 telescopes elements is almost equivalent to a single telescope-based receiver. However, as the number of telescope increases beyond 100 (and correspondingly the individual telescope diameter decreases below 1 m), the performance degradation is more profound. As the number of telescopes approaches

70,000 (i.e., corresponding individual diameters of 3.78 cm), the performance loss is about an order of magnitude that is unacceptable

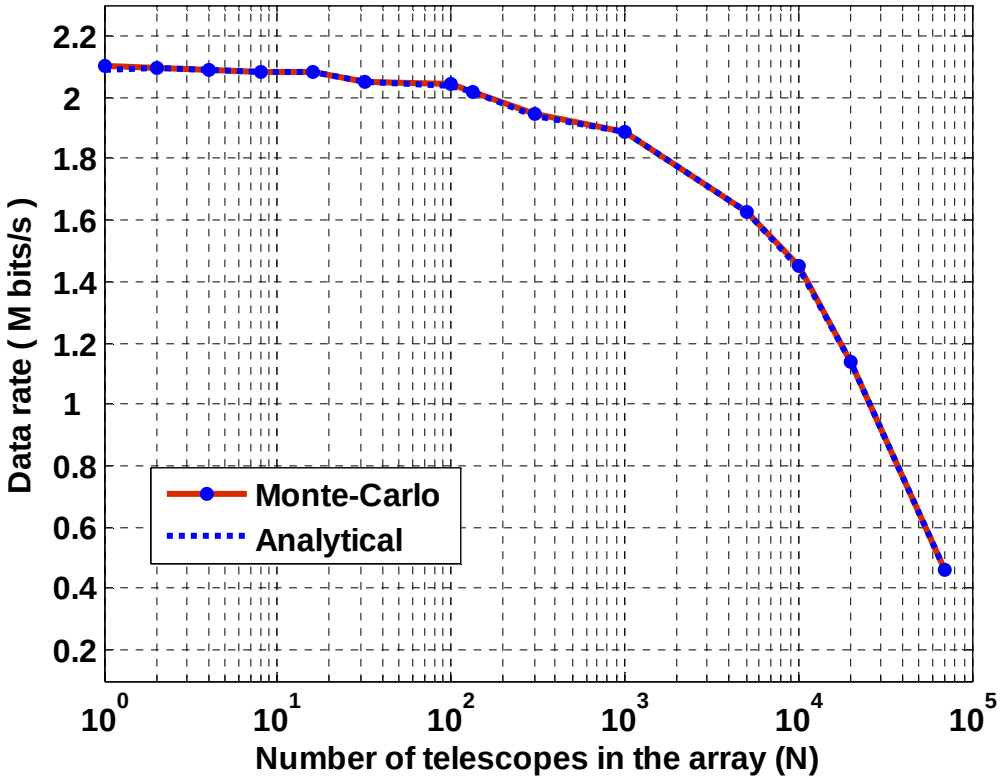

Figure 4.3. Achievable data rate vs. the number of telescopes (N) in the array receiver. All the parameters are similar to those listed in the caption of Figure 4.2.

To further explore the impact of atmospheric Fried parameter on array receivers' performance degradation and to find the relationship between the Fried parameter and individual telescope diameters, the analysis presented in Figures 4.2 and 4.3 is repeated for a Fried parameter of 20 cm (the best value that can occur during the daytime [34,36,88]). All the other link parameters (including background radiance of L=175 μW/(cm^2-sr-nm) are same as those in Figure 4.2. The results are depicted in Figure 4.4. It is shown that achievable data rates degrade from 13.37 Mbits/s to 12.88

Mbits/s as the number of telescopes is increased from 1 to 100. In this case also, this performance degradation is negligible and the performance of an array of up to 100 telescopes elements is almost equivalent to a single telescope-based receiver. However, as diameters of individual telescopes approach 14 cm and corresponding the number of telescopes in the array receiver approaches 5000, significant performance degradation is observed.

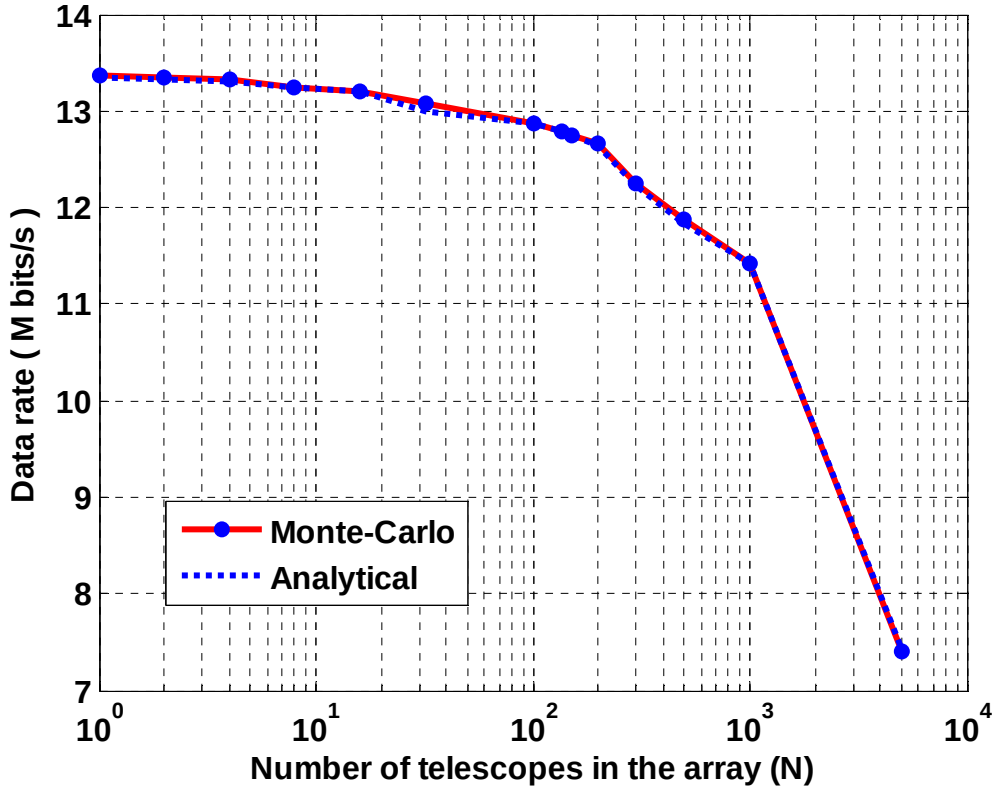

Figure 4.4. Achievable data rate versus the number of telescopes (N) in the array receiver. Fried parameter r_o = 20 cm. All other parameters are similar to those listed in the caption of Figure 4.2.

Based on the results presented in Figures (4.2–4.4), it is established that compared to a monolithic telescope, the performance degradation in telescope array

receivers is quite significant as the individual telescope diameters approach the Fried parameter, i.e., (4 cm and 20 cm in the above cases). These results also verify the conclusion made in Ref. [34] that an array of telescopes performs similar to a single large telescope as long as the individual element diameters exceed the atmospheric Fried parameter. The main reason of this degradation is that as the individual telescope diameters approach the Fried parameter, the background noise collected by the array receiver increases compared to a monolithic equivalent aperture, whereas, the total signal power remains the same. In addition, for smaller telescopes the turbulence-induced scintillation effects become more prominent. All of these effects result in the degradation of the performance of the receiver.

Based on the results in Figures (4.2-4.4), the further analysis of telescope arrays will be restricted to architectures with up to 100 telescope elements (with 1 m individual aperture diameters), i.e., from $(1\times 10 \text{ m})$ to $(100\times 1 \text{ m})$ configuration. This configuration has the benefits of practicality (as many commercial telescopes are available around 1 m diameter size) and the ease of operations (due to less computational and network load). The scintillation effects are negligible for telescopes with these sizes due to the aperture-averaging phenomenon [36].

Next, the performance of different array architectures is evaluated for the background noise spectral radiance values of L = 175, 60, 10, and 1, in the units of $\mu\text{W}/(\text{cm}^2\text{-sr-nm})$. These values typically represent the variations of the background noise during the daytime optical link operations [88]. Fried parameter r_o is fixed at 4 cm. The results are plotted in Figure 4.5. The optimized PPM parameters are also shown for the specific background conditions. The results for all the four cases show that the

performance of the $(100\times1$ m) configuration array receiver is almost equivalent to that of a single telescope based receiver, i.e., $(1\times10$ m) configuration. The data rates achieved by the $(100\times1$ m) configuration are 2.04 Mbits/s, 4.59 Mbits/s, 12.34 Mbits/s, and 20.54 Mbits/s corresponding to the four background noise values mentioned above. The optimal values of *M* for these link conditions are 256, 256, 256, and 128, respectively, whereas the optimal slot widths are 9 *ns*, 5 *ns*, 2 *ns*, and 2 *ns*, respectively, for the four background cases. Hence, during the Mars-Earth conjunction phase in the worst atmospheric turbulence conditions, the range of achievable data rates is from 2 Mbits/s to 20 Mbits/s, as background noise vary from very strong to nominal values.

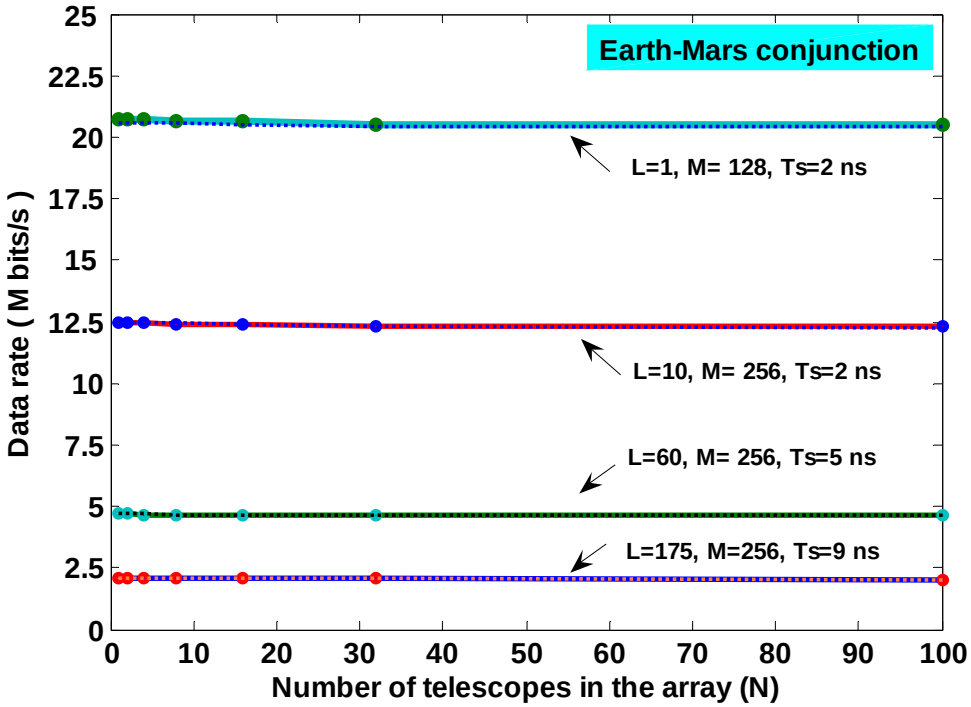

Figure 4.5. Achievable data rates for different array architectures for an optical communication link between Mars and Earth operating in various background conditions during the conjunction phase. Fried parameter $r_o = 4$ cm and background radiance *L* is in units of μW/(cm^2-sr-nm). The aggregate aperture diameter for the telescope array receiver in each case is 10 m. The PPM parameters *M* and T_s are optimized in each case.

During daytime, the turbulence conditions change from weak to strong conditions. In the weak turbulence conditions, the Fried parameter value increases to r_o = 20 cm [34]. Performance of telescope array receivers is also evaluated for this Fried parameter value and the results for four different background noise values of L =175, 60, 10, and 1 μW/(cm^2-sr-nm) are depicted in Figure 4.6. Once again, the performance of different array configurations is almost equivalent to a single telescope. The data rates achieved by the $(100\times1$ m) telescope array configuration are 12.88 Mbits/s, 17.92 Mbits/s, 22.03 M bits/s, and 32.26 Mbits/s corresponding to the above-mentioned background values. The optimal values of M for these link conditions are 256, 128, 64, and 64 respectively; whereas, the optimal slot-widths are 2 *ns* in all cases. It can be inferred from Figure 4.6 that during Earth-Mars conjunction (i.e., when Mars is farthest from Earth) data rates between 12.79 Mbits/s and 32 Mbits/s are possible during the daytime, when the strength of atmospheric turbulence is at its minimum.

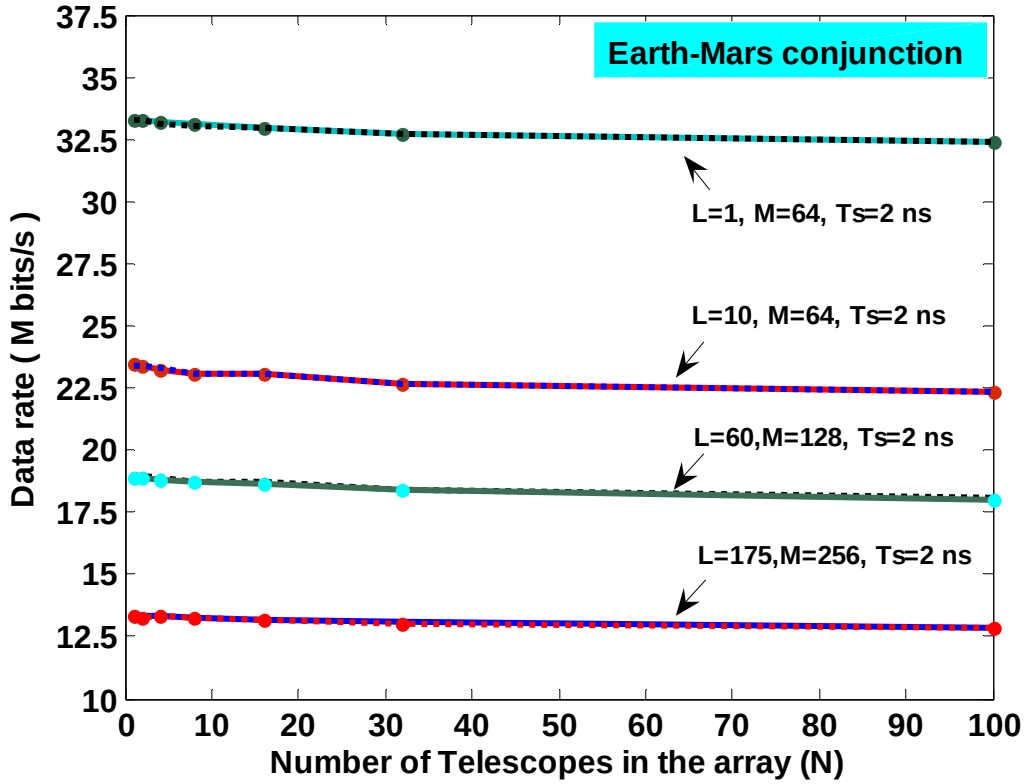

Figure 4.6. Achievable data rates for different array architectures for an optical communications link between Mars and Earth operating in various background noise conditions. Fried parameter is r_o = 20 cm. Other parameters are similar to those used in Figure 4.4.

4.2.2 Earth-Mars Opposition

The best optical channel condition between Earth and Mars occurs during the Earth-Mars opposition phase, when Mars is closest to the Earth (i.e. the distance is 0.75 AU), and the link operates during nighttime when the background noise and atmospheric turbulence values are quite low. During this phase, the major source of the background noise is Mars itself. The number of background photons from Mars depends on the planet's irradiance, the angular size of the Mars relative to the detector FOV, the Mars

geometric albedo [7], and atmospheric turbulence. The background noise from Mars is calculated as per the procedure given in [7,55].

4.2.2.1. Link Budget

The link budget parameters for this phase are given in Table 2. The free space loss is smaller by about 11 dB compared to the conjunction phase and the optimal values for the PPM order *M* are relatively low (i.e., 16, 32) due to better signal to background count ratios.

4.2.2.2. Results: Achievable Data Rates

The performance of telescope array receivers is evaluated and results are given in Figure 4.7 for two different turbulence conditions. During nighttime, the Fried parameter values range from 30 cm (best conditions) to 6 cm (worst conditions) [88]. For r_o = 6 cm, the data rates decrease from 117.88 Mbits/s to 116.5 Mbits/s as the number of telescopes is increased from 1 to 100. For r_o = 30 cm, the data rates range from 123.28 Mbits/s to 121.40M bits/s as the array dimensionality is increased to $(100 \times 1$ m$)$. However, this small (1.5%) performance degradation is negligible as compared to several benefits of the telescope array architecture discussed earlier.

Table 4.2. Link budget for Earth-Mars opposition.

Transmitter	**Description**	**Value**
Average transmitter power, $P_{avg.}$	5 W	6.98 dBW
PPM order , M		16-32 (optimized)
Slot width , T_s		2 *ns* (optimized)
Peak transmitter power, P_{peak}	$P_{avg.} \times M$, 80-160 Watts	(19.03-22.04) dBW
Transmitter antenna gain	30 cm telescope at λ =1060 nm	117 dBi
Transmitter losses	Optical and vignetting losses	1.43 dB
Pointing losses	Transmitter mispointing	1.25 dB
Channel		
Free space loss	0.75 AU (1AU =1.49598×10^{11} m)	361.5 dB
Atmospheric loss	Absorption and scattering.	1.75 dB
Background noise photons	*photons / (nsec-A°)*	0.04-1
Fried parameter	Best conditions	30cm
	Worst conditions	6cm
Receiver	Cryogenic operations	
Receiver antenna gain	(1-10 m) telescope aperture	(129.3 - 148.5) dBi
Receiver losses (signal)	Optical, truncation, polarization	4.58 dB
Receiver losses (background)		5.01 dB
Front end filer optical bandwidth		0.1 *nm*
Photodetector efficiency	Quantum detection efficiency	45 %
Photodetector dark current rate		4×10^4 count/s
Link margin		3 dB

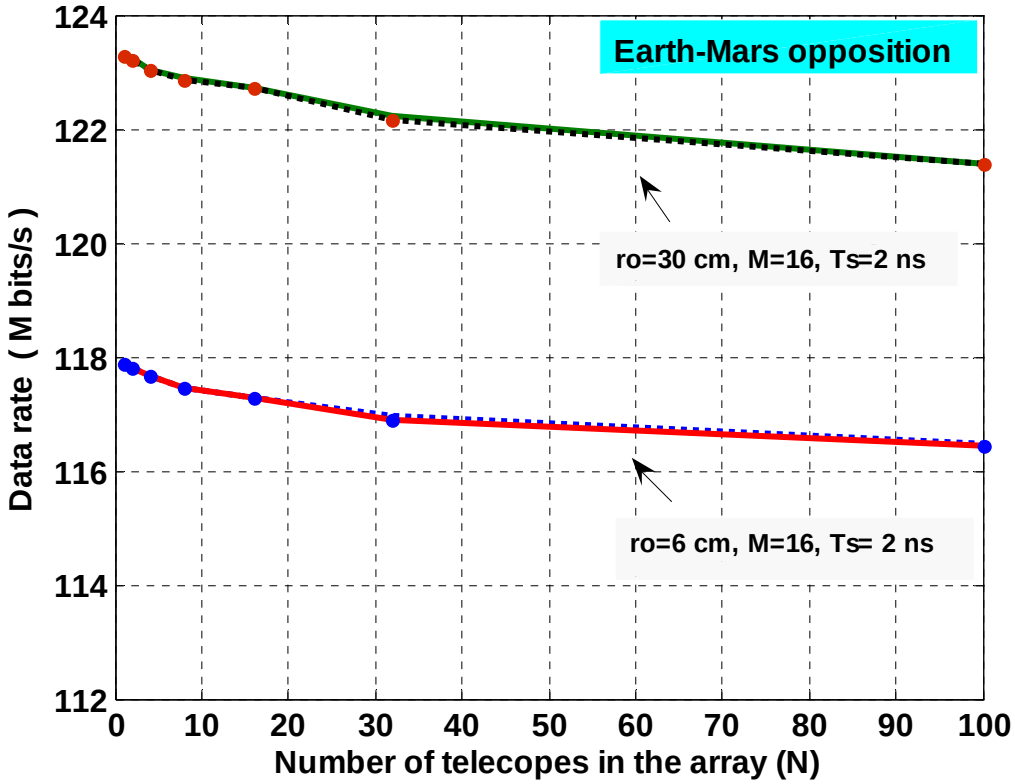

Figure 4.7. Achievable data rates for different array architectures for an optical communications link between Mars and Earth operating at night during Earth-Mars opposition. The link parameters used in the analysis and simulations are listed in Table 4.2. The aggregate aperture diameter for the telescope array receiver in each case is 10 m. The PPM parameters M and T_s are optimized.

4.3. Discussion of Results

In the research presented in this chapter, the main purpose was three fold: (a) the analysis and performance evaluation of telescope array-based receivers for an inter-planetary optical communications link between Earth and Mars, (b) the performance comparison of a single telescope receiver with different array architecture receivers to solidify theoretical equivalence, (c) establish the lower and upper bounds on achievable data rates between Earth and Mars with the given specifications.

I evaluated the performance of different optical arrays architectures in terms of the achievable data rates. I showed that the performance of a telescope array receiver consisting of 100 telescopes with 1 m individual diameters was almost similar to that of a single large telescope receiver. I also showed that the performance of the telescope array receiver degrades eventually as the individual telescope diameters approach the Fried parameter (i.e., 4 cm, 20 cm). In the further analysis, I restricted myself to the $(100 \times 1 \text{ m})$ configuration. This configuration limit has the benefits of practicality (as low-cost commercial telescopes are available near 1 m diameter), the ease in implementation due to a manageable number of telescopes in the array, and comparable performance to a single large telescope. I showed that during Earth-Mars conjunction the data rates range between 2 Mbits/s to 32 Mbits/s, as the link conditions vary from the worst to the best. Hence, in the most stressing case (SEP angle as low as 3º), 2 Mbits/s are achievable. However, this specific condition occurs only for 5 % of a Martian year [88]. The other results reveal that during the conjunction phase, on the average 25 Mbits/s can be achieved, and 32 Mbits/s are possible during the best conditions. In the Earth-Mars opposition phase, the achievable data rates range between 117 Mbits/s and 121 M bits/s, which represents the upper bound on the achievable data rates, under the assumed transmitter and receiver specifications. In addition, it was found that the un-coded PBE values tend to be high in strong background and turbulence conditions. However, as shown in [7,90,91], the incorporation of error correcting codes and a soft-decision decoder can significantly reduce the un-coded error probabilities in the presence of turbulence-degraded signals.

It is important to highlight that these data rates are not exhaustive. The analysis presented in this chapter was based on the power and modulation limits of the currently available space-qualified lasers and an assumption of an aggregate aperture of 10 m diameter. However, in future, with the availability of more sophisticated, high-powered and ultra-fast lasers, and optical array receivers with considerably larger aggregate aperture diameters (i.e., 15 m to 30 m), optical communications technology has the potential to achieve data rates in the Gbits/s range between Earth and Mars. Hence, telescope array-based optical communications systems have the potential to fulfill the large bandwidth demands of future deep-space exploration missions pursued by the international community. Finally, although the Earth-Mars link was evaluated here, the similar analysis and insight can be extended to any other inter-planetary deep-space optical communications link, i.e., Earth-Jupiter, Earth-Neptune links etc.

4.4. Chapter Summary

In this chapter, I evaluated the performance of telescope array-based receivers for a deep-space optical communications link between Earth and Mars in the presence of atmospheric turbulence and background noise radiation under different operational link scenarios, such as the Earth-Mars opposition, the Earth-Mars conjunction, and various background and turbulence conditions to determine the upper and lower bounds on achievable data rates. Different system parameters were optimized to minimize the effects of turbulence and background noise and to maximize the communications throughput. The performance of different array architectures was compared to a single 10 m telescope-based receiver. It was shown that during Earth-Mars opposition phase, data rates of 121 Mbits/s can be achieved by a telescope array receiver consisting of 100

telescopes with 1 m aperture diameter each. The RF-based DSN stations operating at the experimental Ka band can achieve a maximum of 6 Mbits/s in this scenario [9,12]. I also showed that during Earth-Mars conjunction phase, data rate of 32 Mbits/s could be achieved by a telescope array receiver with $(100 \times 1 \text{ m})$ configuration. All the results were verified by Monte Carlo simulations and analytical techniques. It is also very interesting to note the excellent agreement between the analytical model and Monte-Carlo simulation results in all the figures presented in this chapter. Hence, the analysis and results presented in the chapter show that a deep-space optical communications link based on the telescope array receivers is a viable architecture that can provide broadband data support to future universe exploration ventures in deep-space.

CHAPTER 5

DESIGN AND ANALYSIS OF A KALMAN FILTER-BASED SYNCHRONIZATION SCHEME FOR TELESCOPE ARRAY RECEIVERS

In this chapter, the impact of random synchronization errors on the performance of ground-based telescope array receivers operating in an inter-planetary optical deep-space communications (ODSC) link is presented. An adaptive method based on Kalman filters is developed for the synchronization and combination of different telescope signals in the array. An end-to-end simulation platform for ODSC link between Earth and planet Mars is implemented. The effects of atmospheric turbulence and background noise are also modeled. The performance of array receivers is evaluated in terms of the achievable data rates. The Monte-Carlo simulation results show that the Kalman filter-based synchronization scheme keeps the synchronization losses within acceptable limits. The analysis also shows that in difficult operational scenario and presence of random synchronization errors, an array consisting of 100, 1 m telescopes perform almost similar to a single 10 m telescope. Hence, the degradation in the combined signal due to synchronization errors places a minor limitation on the number of telescopes in a telescope array receiver consisting of up to one hundred telescope elements.

5.1. Statement of the Synchronization Problem

Each PPM symbol consists of M slots with a slot-width of T_s seconds and encodes $log_2 M$ data bits. In an array receiver, each telescope detects a portion of the incoming

transmitted signal and photon counts are estimated after slot integrations. The count data from individual telescopes are sent to a central processing station for information extraction purposes. Accurate decoding operation requires the precise synchronization of the incoming signal slot boundaries with the receiver clock and the accurate alignment of slot counts from individual telescopes during the signal combination process. The timing offset errors arise due to a number of reasons, such as clock drift and jitter, atmospheric turbulence, and variations in laser pulsing timings. In an array-based receiver, each telescope receives only a fraction of the total transmitted power. Therefore, less power is available for synchronization and clock tracking compared to a single large telescope, which can lead to the performance degradation.

We presented a Kalman filter-based synchronization scheme in Ref. [63] to solve this problem. Following our work, several synchronization schemes for telescope arrays have also been proposed [65-68]. A synchronization scheme based on the insertion of the periodic pilot symbols and incorporation of a fixed-coefficient first-order loop filter was analyzed for an array consisting of 4 telescopes in [65,66]. Comparison of pilot symbol insertion and inter-symbol guard time insertion techniques was carried out in [68]. It is shown in [68] that the pilot symbol insertion technique is more computationally intensive and both techniques perform well for timing errors less that 1 ppm (part per million). However, these techniques reduce the bandwidth and data throughput by inclusion of several overhead symbols in the transmitted data stream. Also, for the highly random and non-stationary channels the adaptive filters perform much better than the fixed coefficients, first and second-order filters [64,92].

Nevertheless, our synchronization scheme as presented in Refs. [63,64] and in this chapter still stands out in numerous advantages. Here, I present an adaptive Kalman filter-based signal synchronization method for telescope arrays, which uses the received data itself for synchronization and does not need overhead symbols. Hence, the developed scheme does not reduce the communications throughput. Moreover, a robust adaptive (Kalman) filter is designed, which performs much better than the first and second order fixed coefficients filters. The performance of the receiver in this research is evaluated in the presence of timing errors of 4 ppm, which is greater than the errors of 1 ppm analyzed previously [65-68]. The analysis shows that the Kalman filter successfully tracks the timing errors dynamics and keeps the synchronization and combination losses within acceptable limits, i.e., < 1 dB, for array architectures consisting of up to 100 telescopes. Hence, synchronization errors are a not a major limiting factor for arrays consisting of up to 100 telescope elements with 1 m aperture diameter each.

5.2. Telescope Array Synchronization

The sources of synchronization errors in each telescope are transmitter/receiver clock drift and jitter, atmospheric turbulence, and variations in laser pulsing timings. Each telescope is equipped with its own clock to perform slot integrations at individual telescopes. Therefore, synchronization errors for individual telescopes in an array are modeled as the uncorrelated random variables and each telescope is outfitted with the independent closed-loop synchronization system. The incorporation of the individual clock and tracking system reduces the data processing load on the distribution network and central station for an array receiver consisting of a large number of telescopes.

5.2.1. Delay Dynamics Model

The random timing delay variations between the system clock and the received PPM symbols for each telescope are modeled by the following difference equations:

$$\Delta t^{i}[n+1] = \Delta t^{i}[n] + \Delta f^{i}[n]\, T + \delta t^{i}_{Dopp}[n] + w^{i}_{t}[n], \tag{5.1}$$

$$\Delta f^{i}[n+1] = \Delta f^{i}[n] + + \delta f^{i}_{Dopp}[n] + w^{i}_{f}[n], \tag{5.2}$$

where $\Delta t^{i}[n]$ and $\Delta f^{i}[n]$, respectively, represent the delay and frequency fluctuations at the *i-th* telescope in the array at the *n-th* time step, and *T* is the equation update time-step that is equal to the duration of a PPM symbol. δt^{i}_{Dopp} and δf^{i}_{Dopp} , respectively, represent the delay and frequency variations due to the Doppler frequency shift and relative movement of the transmitter spacecraft and receiver telescopes on the Earth; w^{i}_{t} and w^{i}_{f}, respectively, represent the cumulative stochastic delay and frequency variations due to all the other sources and are modeled as Gaussian white noise processes.

The above-mentioned system can be represented by a second order state-space system, given as

$$\mathbf{x}^{i}[n+1] = \mathbf{A}\,\mathbf{x}^{i}[n] + \mathbf{Q}_{Dopp}[n] + \mathbf{w}^{i}[n], \tag{5.3}$$

$$y^{i}[n+1] = \mathbf{C}\,\mathbf{x}^{i}[n] + v^{i}[n], \tag{5.4}$$

where $\mathbf{x}^{i}[n] = \begin{bmatrix} \Delta t^{i}[n] & \Delta f^{i}[n] \end{bmatrix}^{\mathrm{T}}$ is the state vector for the *i-th* telescope, $\mathbf{A} = \begin{bmatrix} 1 & T \\ 0 & 1 \end{bmatrix}$ is the state transition matrix, $\mathbf{C} = \begin{bmatrix} 1 & 0 \end{bmatrix}$, $\mathbf{w}^{i}[n] = \begin{bmatrix} w^{i}_{t}[n] & w^{i}_{f}[n] \end{bmatrix}^{T}$ is the vector noise process representing the frequency and timing jitter experienced at the *i-th* telescope,

$\mathbf{Q}_{Dopp}[n] = \left[\delta t^{i}_{Dopp}[n] \quad \delta f^{i}_{Dopp}[n] \right]^{T}$, $y^{i}[\mathrm{n}]$ is the timing-error measurement (observation), and $v^{i}[\mathrm{n}]$ represents the measurement noise. $\mathbf{w}^{i}[n]$ and $v^{i}[\mathrm{n}]$ are modeled as the uncorrelated Gaussian white noise processes with zero mean, i.e.,

$$E(\mathbf{w}[n]) = \mathbf{0}, \quad E(\mathrm{v}[n]) = 0, \tag{5.5}$$

$$E\left(\mathbf{w}^{(i)}[n]\, \mathbf{w}^{(\mathrm{j})H}[k]\right) = \begin{cases} \mathbf{Q}_{w}[n] & k = n,\ i = j \\ \mathbf{0} & k \neq n,\ i \neq j \end{cases}, \tag{5.6}$$

$$E\left(v^{(i)}[n]\, v^{\mathrm{T}(\mathrm{j})}[k]\right) = \begin{cases} R_{v}[n] & k = n,\ i = j \\ 0 & k \neq n,\ i \neq j \end{cases}. \tag{5.7}$$

with $\mathbf{Q}_{w}[n]$ being the process noise covariance matrix. $R_{v}[n]$ represents the measurement (observation) noise variance and $E(.)$ represents the expectation operator. It is worth-mentioning that the pair (**A, C**) is both *observable* and *controllable*.

5.2.2. Design of a Closed-Loop Synchronization System

Synchronization of the telescope signals is done in two steps. In the first step (called acquisition), the system initially finds a coarse estimation of the start of a PPM symbol. After acquisition, the second step (called the fine synchronization or tracking) starts. The fine synchronization algorithm is used to minimize the residual delay error and to track the random delay fluctuations. Independent closed-loop synchronization subsystems are employed at each telescope in the array for this purpose. The block diagram of the synchronization system is shown in Figure 5.1.

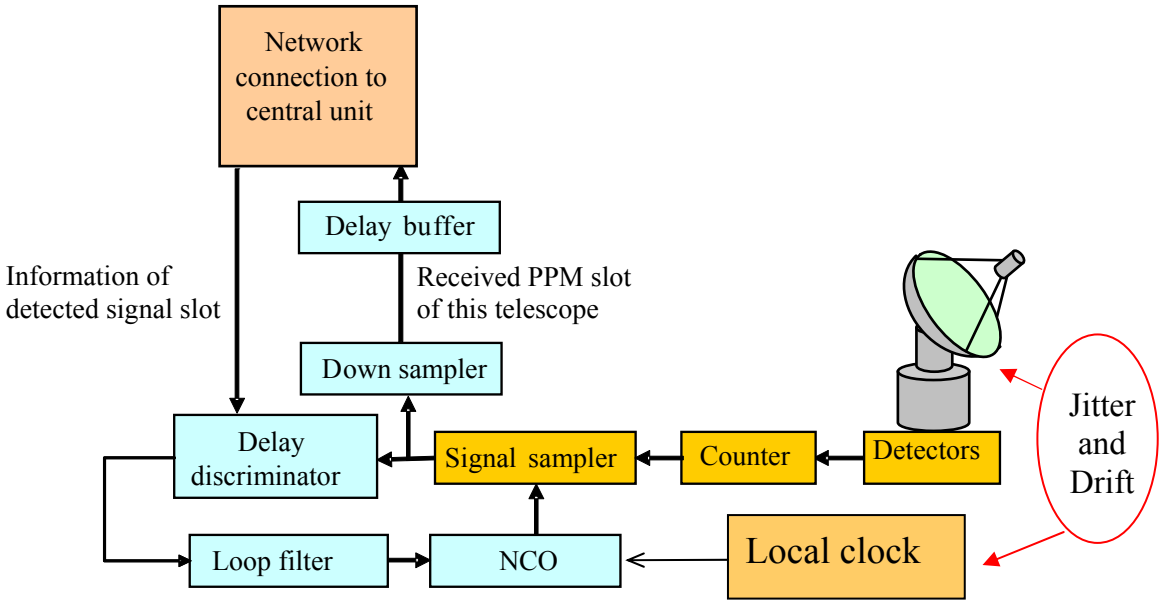

Figure 5.1. Block diagram of the closed-loop synchronization system employed at each telescope.

In the synchronization subsystem (as shown in Figure 5.1), the output pulses of the GMAPD are counted by a counter and a new sample is generated every fraction of a slot time. A numerically controlled oscillator (NCO) is used to control the sampling rate. This NCO receives the system clock as input and the NCO clock rate is controlled with a feedback from the synchronization system. In this algorithm, the synchronization system needs to have an estimation of the position of the signal-slot in the PPM symbol. Each telescope accumulates the samples corresponding to each PPM slot according to the last synchronization data and sends the results to the signal combination unit in the central station. After combining signals from all the telescopes in the array, a decoder in the central station finds an estimate of the signal slot by comparing all the slot counts in the PPM symbol. According to the maximum likelihood (ML) decoding strategy, the slot containing the largest count is selected as the signal slot and in case of a tie, a random

choice is made between the equal count slots. The central station returns the estimated signal slot position and other required information back to the telescopes to be used for the delay synchronization within the next symbol. A delay discriminator (a mask) is used as the error sensor in the synchronization system. The functionality of the sensor is shown in Figure 5.2.

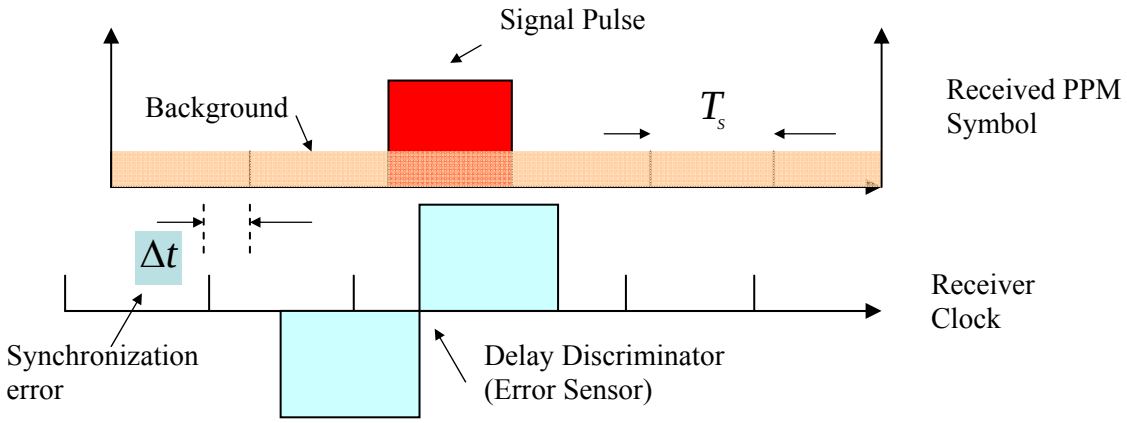

Figure 5.2. Timing-error sensor is a delay discriminator (a mask) that employs early-late slot correlation of the signal-slot to calculate the error.

As shown in above figure, the delay discriminator uses an early-late correlator (integration) of the signal slot to estimate the signal timing error. Background noise power is uniformly distributed in all the slots whereas the received signal power (count) depends upon the correct slot-integration. The dynamic range of the delay estimator is only one slot. Therefore, the tracking errors should remain less than one slot in order to ensure that the tracking system remains locked to the delay fluctuations. The output of the delay discriminator (timing error Δt) in the *j-th* slot (signal slot) of the *i-th* telescope

is the difference of the received power between the first and the second halves of the signal slot, given by

$$e_j^i(\Delta t) = \left[\int_{(j+1/2)T_s}^{(j+1)T_s} \left(s_j^i(t) + b_j^i(t) \right) dt - \int_{jT_s}^{(j+1/2)T_s} \left(s_j^i(t) + b_j^i(t) \right) dt \right], \qquad (5.8)$$

where T_s is the PPM slot-width, $b^i(t)$ and $s^i(t)$, respectively are the received background and signal photons rates impinged upon the *i-th* telescope pupil, given as

$$s^i(t) + b^i(t) = \frac{\eta_{det}}{h\nu} \int_{A_d} \left(I_s^i(t,\mathbf{r}) + I_b^i(t,\mathbf{r}) \right) d\mathbf{r} \ , \quad \text{counts/s}, \qquad (5.9)$$

where η_{det} is the detector's quantum efficiency, A_d is the photodetector (optimized) area, $h\nu$ is the single photon energy, and I_s and I_b are the signal and background intensities, respectively. Corresponding mean value of photon count over a signal slot period is found as

$$K_s^i + K_b^i = \frac{\eta_{det}}{h\nu} \int_o^{T_S} \int_{A_d} \left(I_s^i(t,\mathbf{r}) + I_b^i(t,\mathbf{r}) \right) d\mathbf{r} \ dt, \quad \text{count/slot.} \qquad (5.10)$$

The output of the photon-counter is modeled by the Poisson probability distribution. The probability of receiving *m* photons for an average of $(K_s + K_b)$ photons in a single slot is given by

$$Pos(m, K_s + K_b) = \frac{(K_s + K_b)^m \exp[-(K_s + K_b)]}{m!} \ . \qquad (5.11)$$

The output of the delay discriminator given in Eq. (5.8), for the *i-th* telescope in the *k-th* signal slot, in the discrete domain is given by

$$e^i[k] = \left[\sum_{j \in kth\ slot/2}^{kth\ slot\ end} \left(K_s^i(\Delta t) + K_b^i \right) - \sum_{j \in kth\ slot\ start}^{kth\ slot/2} \left(K_s^i(\Delta t) + K_b^i \right) \right], \qquad (5.12)$$

where T_s is the PPM slot-width, and j is the photon arrival time of a single photon in the *k-th* slot that is selected as the signal slot after the decision from the decoder in the central station. $K_s^i(\Delta t)$ is the number of signal photons in the signal slot in the presence of timing offset Δt. In Eq. (5.12), the midpoint of the *k-th* slot is represented by *k-th* slot/2. The error signal output of the discriminator in Eq. (5.12) is converted to the timing delay error by

$$\Delta t^i[k] = e^i[k] \times \frac{T_s}{2\left\langle K_s^i \right\rangle} \quad , \qquad (5.13)$$

where K_s^i is the average number of received signal photons at the *i-th* telescope, in the absence of any timing error. From Eqs. (5.12) and (5.13), the measurement error variance for the *i-th* telescope is given by

$$R_v^i = \left(\sigma_{meas}^i(\Delta t^i) \right)^2 = T_s^2 \times \frac{\left[\left(1 - \Delta t^i\right) K_s^i + K_b^i \right]}{4\left[K_s^i \right]^2} = \frac{T_s^2}{4 \times SNR^i\left(\Delta t^i\right)}, \qquad (5.14)$$

where

$$SNR^i\left(\Delta t^i\right) = \frac{\left[\left(1 - \Delta t^i\right) K_s^i \right]^2}{\left[\left(1 - \Delta t^i\right) K_s^i + 2K_b^i \right]}. \qquad (5.15)$$

$SNR^i\left(\Delta t^i\right)$ represents the signal to background count ratio at the *i-th* telescope in the presence of the instantaneous timing error $\left(\Delta t^i\right)$. The measured timing delay is fed to a loop-filter that controls the NCO to track the delay fluctuations. Figure 5.4 shows a model for the synchronization loop. The loop-filter in Figure 5.4 should be designed to

simultaneously suppress the delay measurement noise and to track random clock fluctuations.

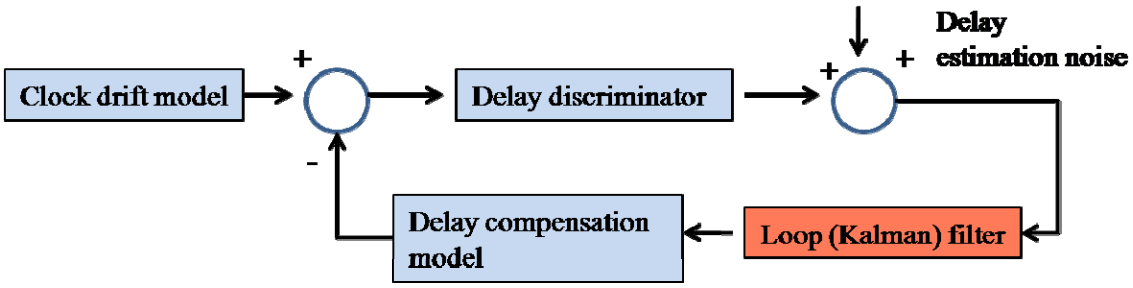

Figure 5.3. Simulation model of the synchronization system.

5.2.3. Kalman Filter-based Synchronization/Tracking

It is common in the synchronizer designs to assume time invariant loop-filters and to approximate timing disturbances by static unknown parameters. In our case, the deep-space optical channel is highly random due to atmospheric turbulence and variations in optical link conditions. Hence, in this work, I introduce the use of a Kalman (recursive) filter for the synchronization and delay tracking. The Kalman filtering approach naturally accommodates both time-varying loop-filters [92] and the dynamic model (as given in Eqs. 5.1 and 5.2).

The primary purpose of the Kalman filter is to estimate and track the state $\mathbf{x}^i[n]$ (i.e., timing and synchronization errors) from the noisy measurements $y^i[n]$. The Kalman filter gives the optimum linear recursive estimate of the state $\mathbf{x}^i[n]$ for the *i-th* telescope, and each telescope employs the independent Kalman filter-based closed-loop system to track the delay dynamics. The Kalman filter minimizes the mean square estimation error, i.e.,

$$\min\ E\left\{ \|e[n]\|^2 \right\}, \tag{5.16}$$

where $$\mathbf{e}[n] = \mathbf{x}[n] - \hat{\mathbf{x}}[n], \tag{5.17}$$

and $\hat{\mathbf{x}}[n]$ is the filtered estimate of the state $\mathbf{x}[n]$. The Kalman filter (recursive) equations for the *i-th* telescope according to the delay dynamics model defined in the previous section are given as:

Initialization

$$\hat{\mathbf{x}}^i[0\,|\,0] = E\,[\,\mathbf{x}^i(0)\,] \tag{5.18}$$

$$\mathbf{P}^i[0\,|\,0] = E\,[\,\mathbf{x}^i(0)\;\mathbf{x}^{(i)\;H}(0)\,] \tag{5.19}$$

For n = 1, 2, …….. compute

Prediction equations

$$\hat{\mathbf{x}}^i[n\,|\,n-1] = \mathbf{A}\,\hat{\mathbf{x}}^i[n-1\,|\,n-1] + \mathbf{Q}_{Dopp}[n] \tag{5.20}$$

$$\mathbf{P}^i[n\,|\,n-1] = \mathbf{A}\,\mathbf{P}^i[n-1\,|\,n-1]\,\mathbf{A}^H + \mathbf{Q}_w^i[n] \tag{5.21}$$

Update equations

$$\mathbf{K}^i[n] = \mathbf{P}^i[n\,|\,n-1]\;\mathbf{C}^H\left[\;\mathbf{C}\;\mathbf{P}^i[n\,|\,n-1]\;\mathbf{C}^H + R_v^i[n]\;\right]^{-1} \tag{5.22}$$

$$\hat{\mathbf{x}}^i[n\,|\,n] = \hat{\mathbf{x}}^i[n\,|\,n-1] + \mathbf{K}^i[n]\left[\,y^i[n] - \mathbf{C}\,\hat{\mathbf{x}}^i[n\,|\,n-1]\,\right] \tag{5.23}$$

$$\mathbf{P}^i[n\,|\,n] = \left[\mathbf{I} - \mathbf{K}^i[n]\mathbf{C}\right]\mathbf{P}^i[n\,|\,n-1] \tag{5.24}$$

In above equations, the choice of initial conditions as given in Eqs. (5.18) and (5.19) ensures the un-biased estimate $\mathbf{x}[n]$ for all n. $\mathbf{K}[n]$ is the time-varying Kalman gain matrix (measurement feedback gain) that minimizes the cost function, i.e., mean square estimation error given in Eqs. (5.16), (5.17), and (5.24). $\mathbf{P}[n]$ is the estimation error covariance matrix defined as

$$\mathbf{P}[n\,|\,n] = E\left[\mathbf{e}[n\,|\,n].\,\mathbf{e}^{H}[n\,|\,n]\right]. \tag{5.25}$$

For a Kalman time-varying gain matrix $\mathbf{K}^{i}[n]=\left[K_1^i[n] \quad K_2^i[n]\right]$, Eq. (5.23) gives the following expression for the signal delay estimation for the *i-th* telescope:

$$\Delta\hat{t}^{\,i}[n+1\,|\,n] = \Delta\hat{t}^{\,i}[n\,|\,n-1]+T\,\hat{f}^{\,i}[n\,|\,n-1]+ K_1^i[n]\varepsilon^i[n]+K_2^i[n]\varepsilon^i[n]\,, \tag{5.26}$$

where $\varepsilon^i[n]=y^i[n]-\mathrm{C}\,\hat{\mathrm{x}}^i[n\,|\,n-1]\,.$ (5.27)

The Kalman filtering operation (Eq. 5.26) is shown in Figure 5.4. The block diagram in the figure is similar to a second order digital phase-locked loop (DPLL). However, Kalman filter gains are time varying as oppose to the fixed gains in DPLLs.

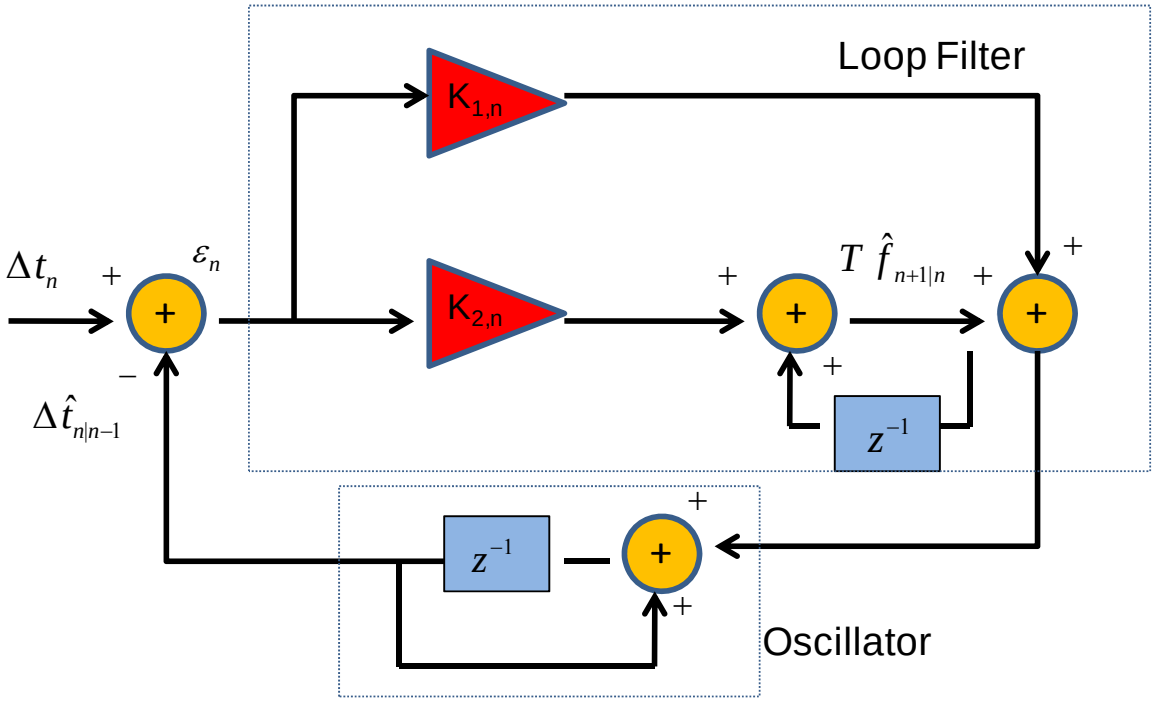

Figure. 5.4. Block diagram of the Kalman filter operations.

5.3. Performance Analysis

In this section, the performance of different telescope array architectures is evaluated through Monte-Carlo simulations in the presence of random synchronization errors for an inter-planetary deep-space optical communications link between Earth and Mars, after the incorporation of Kalman filters-based closed-loop synchronization systems.

5.3.1. Link Parameters

The number of received signal and background photons for a communications link between Earth and Mars are calculated according the channel model given in Chapter 2 (Eqs. 2.2 - 2.8). The worst-case channel conditions are considered: Earth-Mars conjunction when the distance between Earth and Mars is at the maximum, i.e., 2.5 astronomical units (AU), where $1\text{AU}=1.49598\times10^{11}$ m. In addition, the Sun-Earth-Probe (SEP) angles are very small and the link operates during daytime, when both the background noise due to the diffused sunlight from sky and the atmospheric turbulence are at their respective peaks. Atmospheric turbulence represented by the Fried parameter of r_o= 4 cm is incorporated and three different background conditions ranging from worst to best are analyzed in the simulations. The other link budget parameters are same as those given in Table 4.1.

5.3.2. Simulation Results

In this section, the performance of telescope array-based optical receivers is evaluated in terms of achievable data rates using Monte-Carlo simulations. It is important to highlight that this study is aimed at testing the performance of array receivers in the presence of synchronization errors in the most stressing channel conditions when the

signal photon count is very small at the individual telescopes in the array. The main design parameters of the array architecture are the sizes of individual telescopes and the number of telescopes in the array. However, the total photon-collecting aperture of the complete telescope array receiver is kept constant in different architectures. I start with a monolithic large telescope of 10 m diameter, i.e., the $(1\times 10\,\mathrm{m})$ configuration. Then, I increase the number of telescopes in the array by breaking down the single aperture into 2, 4, 8, 16, 32, and 100 telescope elements of 7.07 m, 5 m, 3.53 m, 2.5 m, 1.76 m, and 1 m telescope diameters respectively. These cases correspond to $(2\times 7.07\,\mathrm{m})$, $(4\times 5\,\mathrm{m})$, $(8\times 3.53\,\mathrm{m})$, $(16\times 2.5\,\mathrm{m})$, $(32\times 1.76\,\mathrm{m})$, and $(100\times 1\,\mathrm{m})$ array configurations, respectively.

Performances of array receivers are evaluated using the following steps: For each array architecture and link scenario, Monte-Carlo simulations are repeated for 1 million symbols. Given the specific channel conditions (link budget specifications, background noise, and turbulence parameters), the signal and background photons are calculated and system parameters are optimized for each telescope in the array receiver as per the procedures given in Chapters 3 and 4. The outputs of the photon-counters are modeled by the Poisson distribution and photon-counts are generated for each PPM slot at individual telescopes. It is assumed that each telescope has an independent clock and an artificial random timing error with 4 ppm (i.e. part per million), that is a relatively large clock drift [63-66] is injected into the system in the simulations to evaluate the efficacy of the synchronization system. The clock errors due to the Doppler shifts are calculated pre-hand based upon the spacecraft ephemeris data and the information is incorporated in the timing system for the correction purposes. The propagation of timing errors and clock

jitters dynamics from other sources are modeled according to Eqs. (5.1) and (5.2). It is assumed that an acquisition algorithm is used before the delay tracking to bring the synchronization errors within single slot duration.

A Kalman filter based closed-loop synchronization system as explained in the previous section is employed at each telescope for synchronizing the PPM slot boundaries with the receiver clock, tracking the delay dynamics, and suppressing the measurement noise. After the delay compensation and synchronization, the Poisson counts from the individual telescopes are sent to the central processor where the data is combined and sufficient statistics are formed for each PPM slot within a symbol for decoding purposes. The slot containing the largest count is selected as the signal slot in each frame. Information about the signal slot is also forwarded to each telescope to be used in the future synchronization process. When the decoder in the central station makes a false detection, a wrong slot is selected as the signal slot and forwarded to all telescopes. This degrades the performance of the synchronization and tracking system. However, this degradation in overall performance of synchronization system is not considerable as evident from the results shown in next paragraphs. The probability of symbol error is calculated as the ratio of the number of false detections to the total number of received symbols after averaging over 1 million symbols and PSE is plugged in Eqs. (2.16 – 2.18, Chapter 2) to evaluate the achievable data rates.

An example of Kalman filter delay synchronization and tracking for an array of 16 telescopes with 2.5 m diameter each is depicted in Figure 5.4 by plotting the *root mean square* (RMS) tracking/synchronization error (as a fraction of PPM slot-width) of the complete array versus the received PPM symbols, as the communications operation

progresses. The background noise radiance of $L = 60\,\mu$W/(cm^2-sr-nm) is assumed. Figure 5.5 shows that an initial large timing error (i.e., $0.5T_s$) is injected at $t = 0$. It is clear from Figure 5.5 that the Kalman filter-based synchronization system quickly brings the timing error down by about an order of magnitude after initial 1000 symbols, i.e., just 9 μ sec. This time period is normal for the adaptive Kalman filter as it searches for the optimal solution to acquire and track the system dynamics. After this phase, the filter successfully tracks the timing errors dynamics and keeps the RMS tracking errors within a very small fraction of the slot-width, i.e., less than 1.5 %. This figure emphasizes the importance and robustness of the designed Kalman filter-based tracking in the telescope array receiver for worst-case deep-space communication channel conditions.

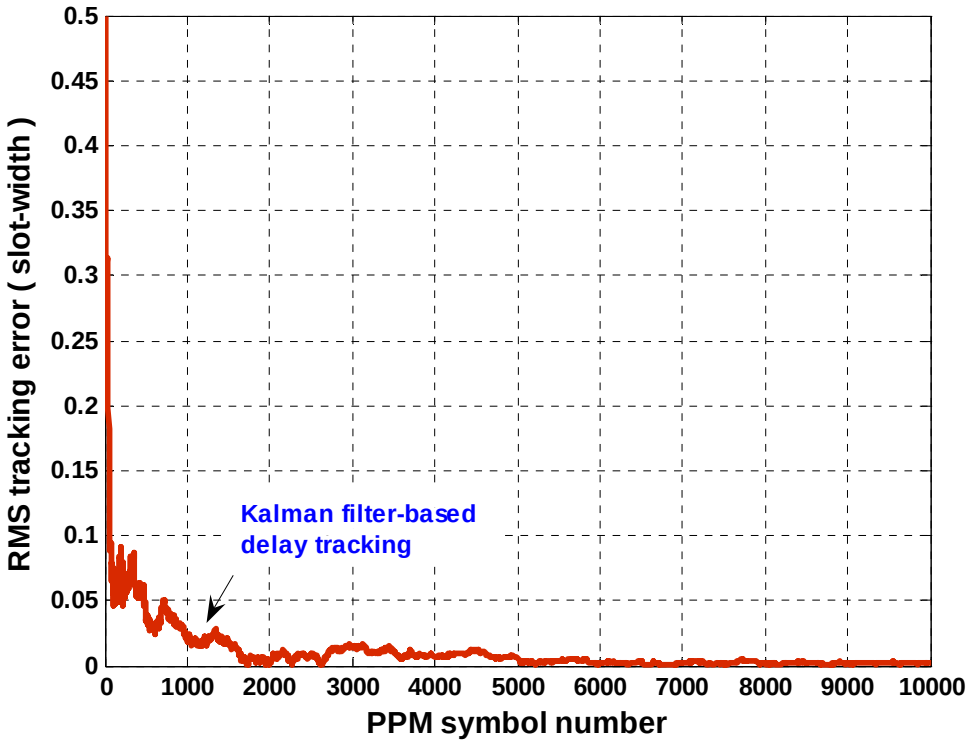

Figure 5.5. RMS delay tracking error for a telescope array consisting of 16 telescopes with 2.5 m aperture diameter each. Background noise radiance is 60 μW/(cm^2-sr-nm) . A Kalman filter is employed for synchronization and tracking.

Figure 5.6 shows the operations without Kalman filter-based synchronization and tracking. It is obvious that the initially injected synchronization error grows, without bounds, according to the delay dynamics and after just 600 symbols, the RMS synchronization error reaches to almost 95 % of the PPM slot-width that would lead to a substantial degradation in the performance of the receiver ultimately leading to a virtual shutdown of the communications link. Figures 5.5 and 5.6 emphasize the significance and robustness of the designed Kalman filter-based tracking in telescope array receivers for deep-space communications operations.

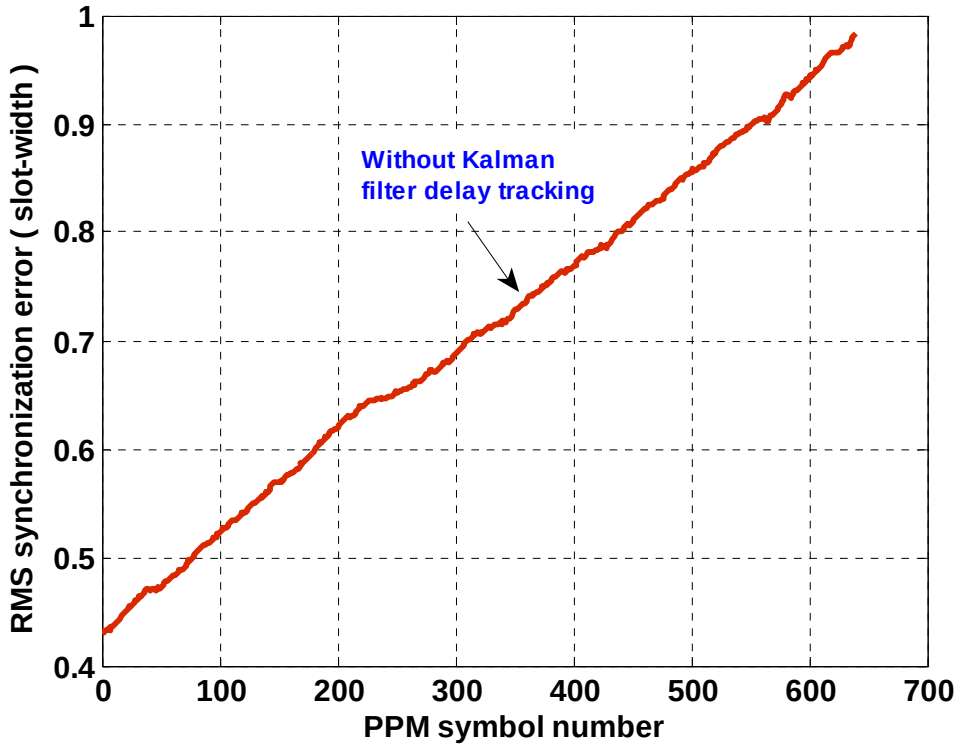

Figure 5.6. RMS delay tracking error for a telescope array consisting of 16 telescopes with 2.5 m aperture diameter each without closed-loop synchronization and tracking. Background noise radiance is 60 μW/(cm^2-sr-nm) .

Next, simulations for different array architectures are carried out for the strong background noise conditions of L =175 μW/(cm^2-sr-nm) . In each case, the Kalman filter-based synchronization system was able to track and minimize the timing errors, as depicted in Figure 5.5. However, the residual tracking errors always resulted in some combination power loss. It was found that as the array dimensionality and the number of telescopes in the array was increased from 1 to 100, the power loss due to the residual tracking errors increased from 0.38 dB to 0.81 dB. However, this power loss is quite nominal in the wake of extreme channel conditions. The calculated PBE also increased by a small amount with the number of telescopes. The achievable data rates are calculated based upon the PBE using Eqs. (2.16-2.18). Figure 5.7 plots the achievable data rates as a function of the number of telescopes in the array, while the diameter of each telescope in the array is properly selected to keep the overall collecting aperture equivalent to a single 10 m telescope. Figure 5.7 shows that as the number of telescopes in the array is increased from 1 to 100, the achievable data rate decrease from 2.05 Mbits/s to 1.70 M bits/s, which is equivalent to a 17 % performance loss.

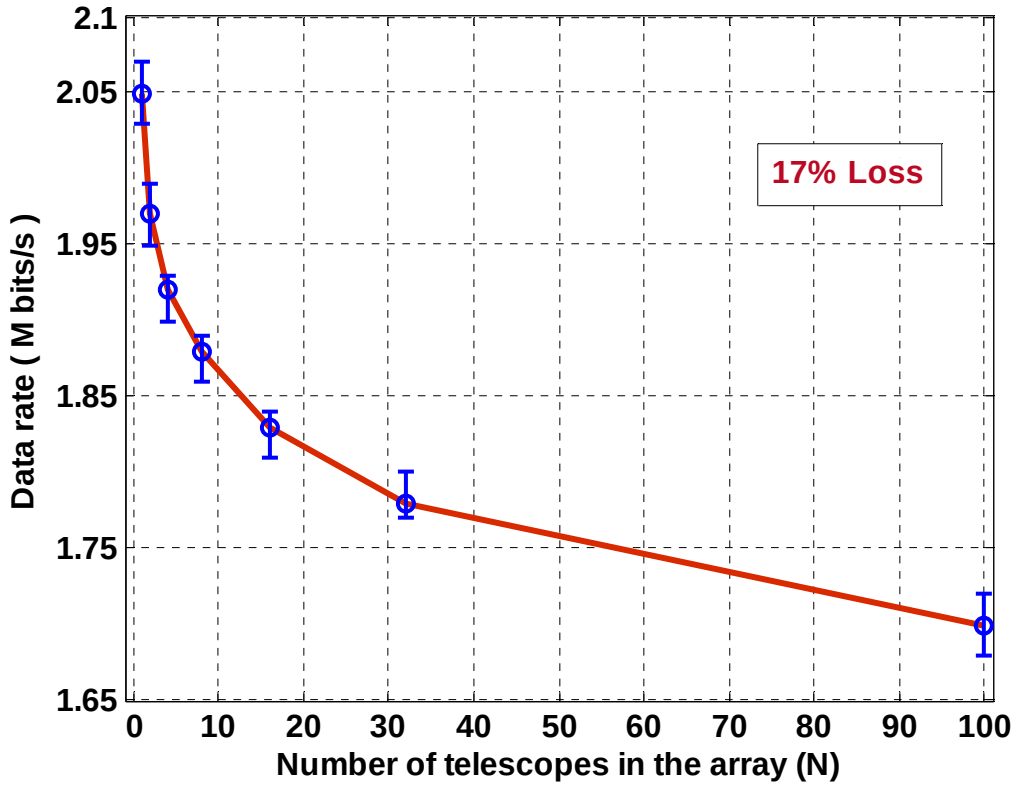

Figure 5.7. Achievable data rates as a function of number of telescopes in the array receiver in the presence of synchronization errors. Extreme background noise conditions with L=175 μW/(cm^2-sr-nm) and a Fried parameter of 4 cm is employed.

Next, simulations are repeated for background noise radiance values of L = 60 and 10 μW/(cm^2-sr-nm), which correspond to the moderate and weak background noise conditions. However, the turbulence conditions are still kept at the peak value represented by a Fried parameter of 4 cm. The achievable data rates for these channel conditions are plotted in Figures 5.8 and 5.9. Figure 5.8 shows that in moderate background conditions, the achievable data rates decrease from 4.64 Mbits/s to 4.18 Mbits/s as the telescope array dimensionality is increased from 1 to 100. This corresponds to a 9.8 % performance loss. The results for the nominal background conditions are shown in Figure 5.9. It is obvious that when a single telescope is replaced by a N =100 element array receiver, the

achievable data rates decrease from 12.41 M bits/s to 11.65 Mbits/s that correspond to a very nominal 6 % performance loss. The performance losses of the smaller array architectures ($N \leq 32$) are much lesser. These figures (i.e., Figures 5.7-5.9) verify the efficacy of the Kalman filter in successfully tracking and minimizing the random synchronization and tracking errors. In addition, the performance loss of the array architecture is quite nominal. As explained in the Chapter 1, the array architectures have numerous advantages, i.e., cost, redundancy, ease of manufacturing, maintenance, operations, and ability to provide a near diffraction-limit performance. Keeping in view these advantages, the small loss in the performance due to residual synchronization errors is acceptable, and is not a major limitation in the viability of the array-based receiver up to N =100 elements for a deep-space optical communications link.

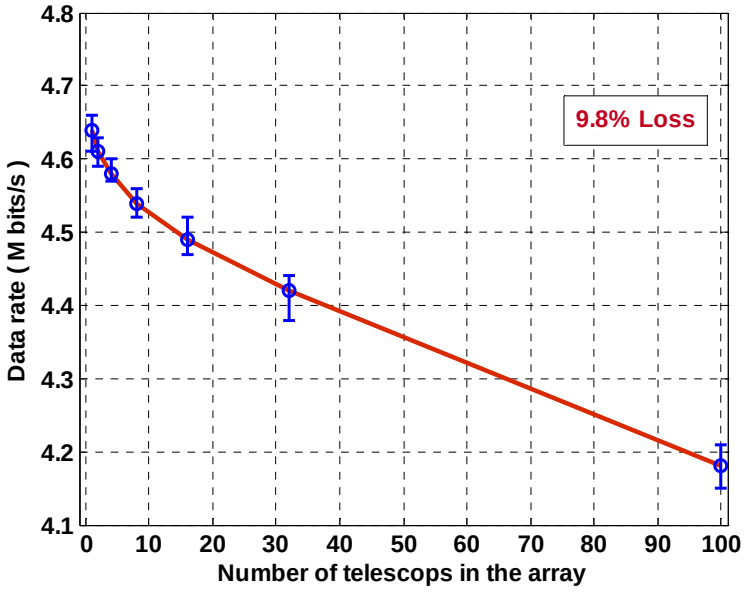

Figure 5.8. Achievable data rates as a function of number of telescopes in the array receiver in the presence of synchronization errors. Moderate background noise conditions with L = 60 μW/(cm^2-sr-nm) and r_o = 4 cm is incorporated.

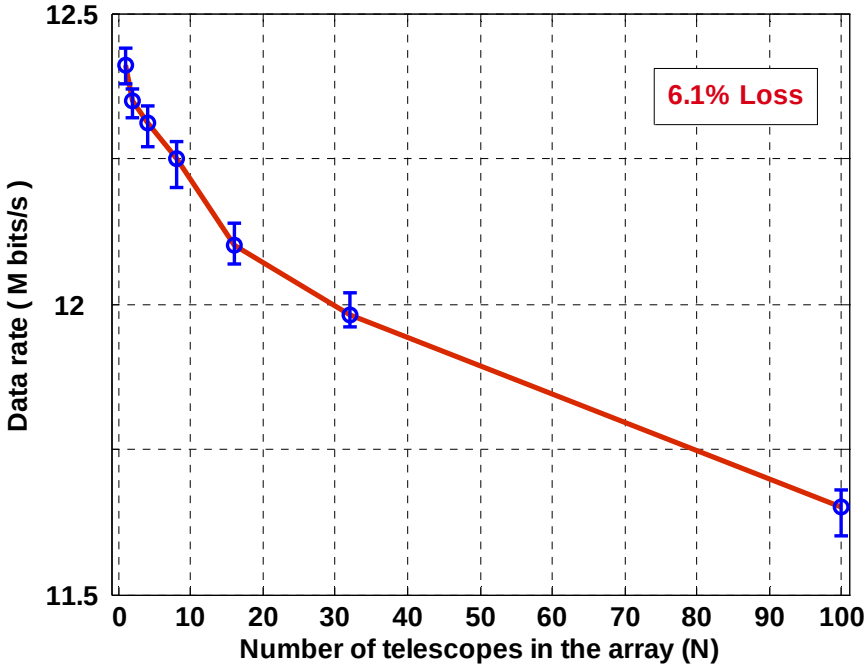

Figure 5.9. Achievable data rates as a function of number of telescopes in the array receiver in the presence of synchronization errors. Nominal background noise conditions with L = 10 μW/(cm^2-sr-nm) and r_o = 4 cm is incorporated.

5.4. Chapter Summary

In this chapter, I presented a design of a Kalman filter-based closed-loop synchronization system for a telescope array-based optical communications receiver. The performance of closed-loop systems and different array architectures are evaluated for a deep-space optical communications link between Earth and Mars during the Mars conjunction phase. The analysis presented in this chapter solidifies the theoretical foundations of the telescope arrays-based receivers for deep-space optical communications links. The results presented here show that the Kalman filter-based synchronization system in individual telescopes efficiently tracks the time-varying delay fluctuations even during worst channel conditions, i.e., when Mars is farthest from Earth, atmospheric turbulence is at its peak, and background noise is very intense. The

performance evaluation of different array architectures reveal that in the presence of the synchronization errors, the performance degradation of an array consisting of 100, 1 m telescopes is small ($\leq$ 9 % for most operating conditions) as compared to a monolithic 10 m telescope. The performance degradation increase to about 17 % in the extreme background noise conditions, however, this particular condition occurs only for less then 5 % of the time during a complete Mars-Earth orbital cycle [88]. The advantages of the array architecture are numerous and this analysis shows that even in low signal to background noise scenarios, by incorporating a robust adaptive synchronization system, synchronization errors do not pose a major limitation in the deployment of the array architecture. Hence, for direct detection arrays, for architectures with a large number of telescopes (N = 100), synchronization errors are not a major limitation.

CHAPTER 6

PERFORMANCE ANALYSIS OF TELESCOPE ARRAYS IN THE PRESENCE OF TRACKING ERRORS

In this chapter, the effect of random tracking errors on the performance of the ground-based telescope array receivers for an inter-planetary optical deep space communications (ODSC) link is investigated. This chapter has two major parts. In the first part, the statistical analysis and mathematical modeling of the impact of tracking errors on the operation of general direct-detection optical communications receivers employing PPM is presented. In the second part, the design of a closed-loop tracking subsystem for telescope array receivers operating in deep-space optical communications is presented. An end-to-end simulation platform for ODSC link between Earth and planet Mars is implemented that incorporates closed-loop tracking subsystems for individual telescopes in array receivers to mitigate the effects of random tracking errors. The results of simulations show that the closed-loop tracking systems keep the tracking errors within acceptable limits. Comparison of the achievable data rates show that in the presence of random tracking errors, an array of smaller-size telescopes can replace a costly monolithic telescope with negligible performance degradation.

6.1. Statement of the Tracking Problem

As mentioned in previous chapters, major advantages of optical communications are the narrow beam divergence that allows the transmitted power to be concentrated on the receiving location, small diameter, large gain transmitting and receiving antennas, and much smaller component (e.g., photodetector) sizes. However, due to the narrow beam

divergence and small detector FOVs (about 10s of μ radians); the received signal power is extremely sensitive to the pointing and tracking errors. Pointing errors arise because of imperfect pointing of transmitter towards the receiver. The effect of beam pointing error on the optical receiver's performance has been analyzed previously [93]. However, after the initial spatial acquisition, the receiver should track and maintain the line-of-sight (LOS) with the transmitter, and stabilize the focused spot on the focal plane detectors to avoid power losses. Nevertheless, tracking errors arise as a result of random phenomenon like beam-wander due to atmospheric turbulence and platform and structural jitters at the receiving telescopes [36,94]. Large tracking errors can lead to intolerable signal fades at the receiver and can result in significantly degraded performance. In the next section, I carry out the statistical analysis of the impact of random tracking errors on general direct-detection optical receivers employing PPM modulation.

6.2. Statistical Analysis of the Impact of Tracking Errors

6.2.1. Tracking Errors-Induced Power Losses

A telescope in an optical receiver collects the incoming light and focuses it onto the detectors placed at its focal plane. The amplitude of the electric field distribution in the plane of detector (in the absence of any loss) is given by [17]

$$E(\rho,\gamma) = \frac{E_o D}{2\rho}\left[\, J_1(\gamma\rho)\,\right], \tag{6.1}$$

where ρ is the radial coordinate in detector plane; E_o is the peak amplitude of the wave impinging on the telescope entrance and D represents the diameter of the telescope's aperture. $\gamma = k/2F$ with F being the telescope *F*-number (given by f/D), f being the telescope's focal length, and *k* being the wave number. By using the diffraction

theory, the focal plane intensity pattern for a circular aperture of diameter D results in the famous Airy pattern, given by [17]

$$I(\rho,\gamma) = \frac{\pi D^2/4}{\lambda f_c}\left[\frac{2J_1(\gamma\rho)}{\gamma\rho}\right]^2. \tag{6.2}$$

Instantaneous tracking errors arise when there is an angular (in azimuth/elevation) difference between the transmitter LOS and optical axis of the receiver, as depicted in Figure 6.1. If ψ_{el} and ψ_{az} represent the angular errors in the elevation and azimuth directions respectively, then the radial tracking error ψ_r, at the receiver is given by

$$\psi_r = \sqrt{\psi_{el}^2 + \psi_{az}^2}\,. \tag{6.3}$$

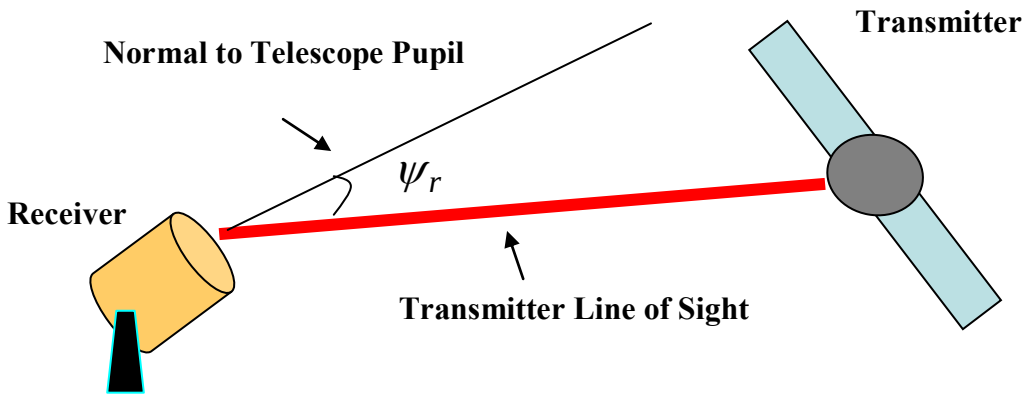

Figure 6.1. Instantaneous angular tracking error (ψ_r) in the telescope pupil plane.

The angular tracking errors ψ_r in the telescope aperture plane result in the focal spot tracking (position) error r_r in the detector plane, given by $r_r = \psi_r f$, as shown in Figure 6.2. In the figure, f is the focal length of receiving lens, $r_r = \sqrt{x_e^2 + y_e^2}$, and x_e

and y_e represent the PSF shift in the respective axis in the detector plane. This phenomenon results in power losses at the receiver end.

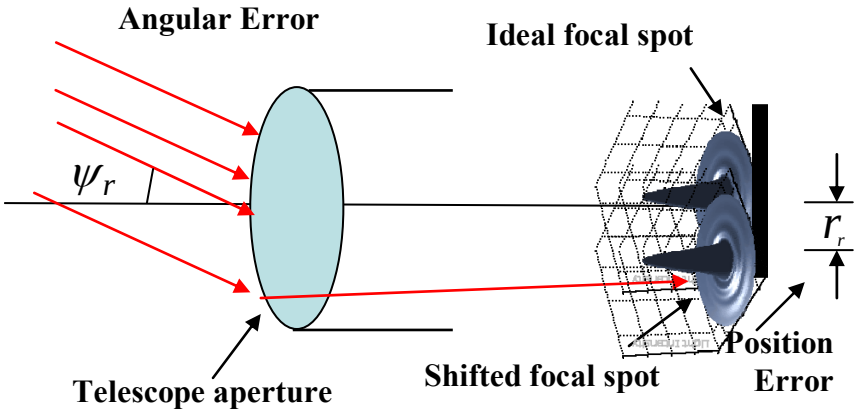

Figure 6.2. Angular tracking errors induce tracking (position) errors in detector plane.

In a direct-detection system, the overall signal power received at the detector is an important quantity. To quantify the power losses because of tracking errors, let us refer to the detector geometry depicted in Figure 6.3.

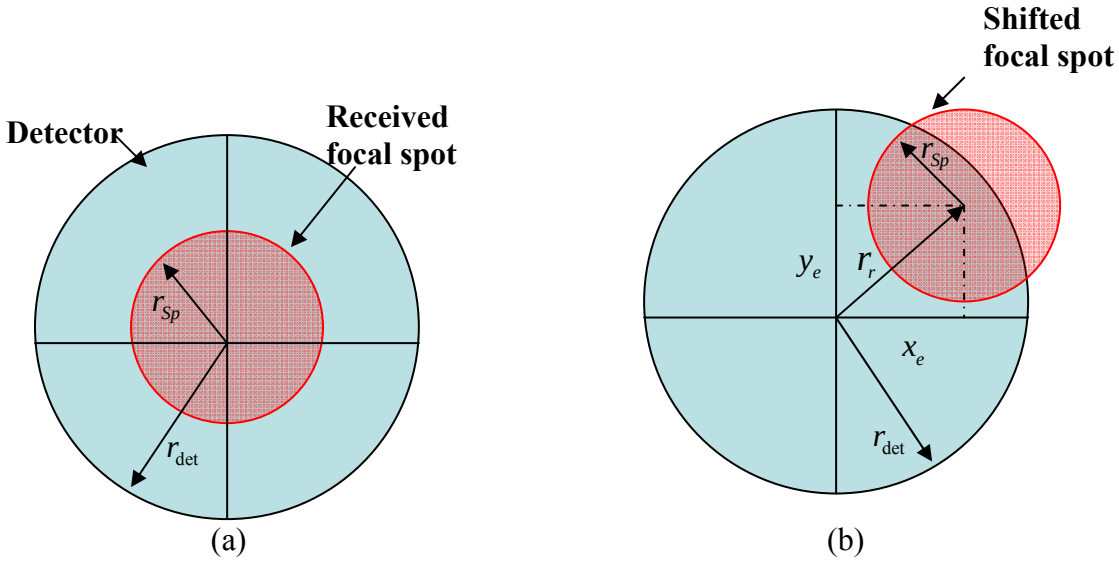

Figure 6.3. Detector and focal spot geometry. (a) In the absence of angular errors, the diffracted focal spot is exactly at the center. (b) Angular tracking errors result in the shifted focal spot and power losses.

Figure 6.3(a) represents an ideal case, when there is no tracking error and incoming light fields are exactly normal to the receiver telescope aperture (or aligned with the receiver's optical axis). It is important to mention that for simplification purposes, a diffraction-limited limited system and circular detectors are considered here. The actual PSF and detector may vary from system to system. Nevertheless, the analysis presented here is valid for a general direct-detection diffraction-limited system. In a diffraction-limited system, the focal spot radius is given by $r_{sp} \cong \pi / \gamma$. The r_{sp} represents the size of the central halo of the Airy disk where most of the energy (84 %) is concentrated [17]. It is assumed that $r_{\det} > r_{sp}$ for collection of the maximum energy. Figure 6.3(b) depicts the case of a shifted PSF due to the tracking errors. When the tracking error r_r is such that some portion of the focal spot slides off the detector area, the received power reduces due to spillover losses. The power fraction detected in a direct detection system due to tracking errors is given by

$$\eta\ (r_r, r_{\det}, \gamma) = \frac{\iint\limits_{Detecor\ Area} I\ (r_r, r_{\det}, \gamma)}{\iint\limits_{Detector Area} I\ (r_{\det}, \gamma)}, \tag{6.4}$$

where the denominator represents the ideal case of zero tracking error. Let us define $\varsigma = (r_{\det} - r_{sp}) = (r_{\det} - \pi / \gamma)$ as the relative size of the detector and the focal spot. It is clear that the power loss results only when the instantaneous tracking (position) error r_r is greater than ς. As long as r_r is less than or equal to ς, the focal spot remains completely on the detector area and there is no power loss. Using Eqs. (6.2) and (6.4) and

the geometry given in Figure 6.3, instantaneous power loss due to tracking errors is given by

$$L\left(r_r\,\gamma\,,\,r_{\text{det}}\right) = \frac{\iint\limits_{\text{Detector Area}} \left[\frac{J_1\left(\gamma\sqrt{\left(x-x_e\right)^2+\left(y-y_e\right)^2}\right)}{\gamma\sqrt{\left(x-x_e\right)^2+\left(y-y_e\right)^2}}\right]^2 dx\;dy}{\iint\limits_{\text{Detector Area}} \left[\frac{J_1\left(\gamma\sqrt{\left(x\right)^2+\left(y\right)^2}\right)}{\gamma\sqrt{\left(x\right)^2+\left(y\right)^2}}\right]^2 dx\;dy} \quad \text{when} \quad r_r \geq \varsigma = \left(r_{\text{det}} - r_{sp}\right),$$

$$= \qquad 0 \qquad\qquad\qquad\qquad \text{when} \quad r_r \leq \varsigma = \left(r_{\text{det}} - r_{sp}\right) \tag{6.5}$$

where the numerator represents the integration of the shifted intensity diffraction pattern over the detector area in the presence of tracking errors and the denominator represents the ideal received power (i.e. without any tracking error). The loss given in Eq. (6.5) depends on many factors such as telescope *F*-number and respective detector and focal spot sizes. To generalize the analysis, a normalized error variable ξ is introduced and is given by

$$\xi = \frac{r_r - \varsigma}{r_{sp}} = \frac{\sqrt{x_e^2 + y_e^2} - \varsigma}{r_{sp}}. \tag{6.6}$$

The ξ represents the tracking error normalized with respect to the focal spot and detector sizes. Numerical techniques are employed to estimate the instantaneous power loss in Eq. (6.5) as a function of ξ. The results are given in the Figure 6.4. It is obvious from the figure that the power loss drastically increases with the increase of normalized tracking error. After a certain limit ($\xi \geq 2$), the spot slides off the detector area, and the received signal completely vanishes resulting in the complete shutdown of the optical communications link.

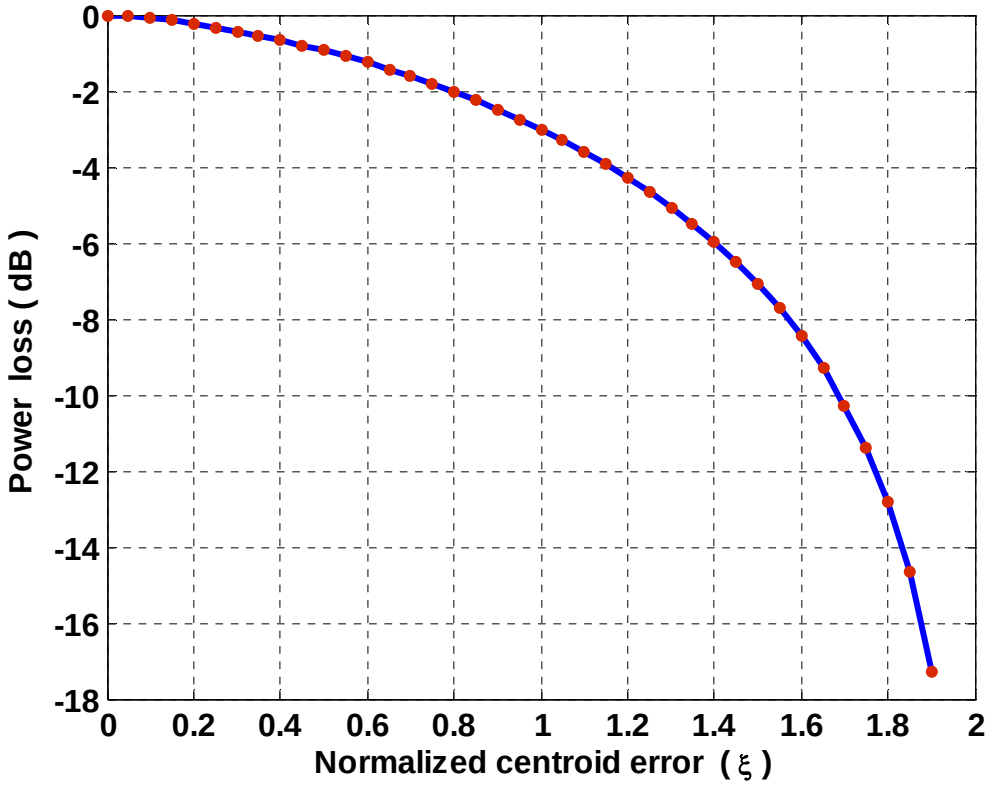

Figure 6.4. Power loss due to tracking errors in direct-detection optical receivers.

6.2.2. Impact on Receiver's Performance

Tracking errors arise from a number of different phenomena like telescope platform jitter and beam wander due to turbulence, wind etc. Tracking errors in both the azimuth and elevation are modeled as independent Gaussian random variables [93]. The azimuth and elevation tracking errors have the PDFs

$$P(\psi_{Az}) = \frac{1}{\sqrt{2\pi}\sigma_{Az}} \exp\left[-\frac{(\psi_{Az} - \mu_{Az})^2}{2\sigma_{Az}^2}\right], \tag{6.7a}$$

$$P(\psi_{El}) = \frac{1}{\sqrt{2\pi}\sigma_{El}} \exp\left[-\frac{(\psi_{El} - \mu_{El})^2}{2\sigma_{El}^2}\right], \tag{6.7b}$$

where ψ_{Az} (ψ_{El}) is the instantaneous azimuth (elevation) tracking error; and μ_{Az} (μ_{El}) and σ_{Az}^2 (σ_{El}^2) are the mean value and the variance of the azimuth (elevation) tracking error, respectively. As both the azimuth and elevation errors evolve as independent identically distributed (i.i.d.) random variables, the PDF of the aperture plane tracking error $\psi_r = \sqrt{\psi_{el}^2 + \psi_{az}^2}$ and the detector plane tacking error $r_r = \sqrt{x_e^2 + y_e^2}$, is given by the Rayleigh distribution [16] as

$$P(\psi_r) = \frac{\psi_r}{\sigma_{\psi_r}^2} \exp\left[-\frac{\psi_r^2}{2\sigma_{\psi_r}^2} \right], \tag{6.8a}$$

$$P(r_r) = \frac{r_r}{\sigma_r^2} \exp\left[-\frac{r_r^2}{2\sigma_r^2} \right], \tag{6.8b}$$

with $\sigma_{\psi_r}^2$ and σ_r^2 being the variances of ψ_r and r_r, respectively. $\sigma_r^2 = f^2 \sigma_{\psi_r}^2$ and it represents the cumulative variance of the tracking errors from all the sources, i.e.

$$\sigma_r^2 = \sigma_{platform\ jitter}^2 + \sigma_{beam\ wander}^2 + \sigma_{wind}^2 + ... \tag{6.9}$$

Random tracking errors cause the random excursion of received intensity in the focal plane. As a result, the received power and the number of signal photons also fluctuate randomly, inflicting random power losses. Incorporating the tracking loss factor Eq. (6.5) in Eq. (2.5), the number of received photons is given by

$$K_s\left(r_r\, \gamma,\, r_{\text{det}}\right) = P_r\ M\ T_s\ \eta_{det}\, \eta_{FOV}\,(D_s) \left(\frac{\lambda}{hc} \right) L\left(r_r\, \gamma,\, r_{\text{det}}\right) \text{ photons/ PPM slot}, \tag{6.10}$$

In contrast, the received background photon count remains constant, even in the presence of random tracking errors, as the diffuse sky background noise is an extended source and

background photon intensity is distributed uniformly over the receiver FOV and the detector plane [17]. This phenomenon results in the degradation of the overall signal to noise ratio (SNR), which in turn affects the receiver performance. For a background noise limited photon-counting channel employing PPM, the SNR is defined as [17]

$$SNR = \frac{K_s^2}{\left(K_s + 2K_b\right)}, \tag{6.11}$$

where K_b is the sum of background photon count and detector dark current count. The random fluctuations of the instantaneous number of signal photons result in the random variation of the probability of error PSE. In the further analysis, we assume that the detector size is selected to encircle the complete receiver FOV for maximum power detection, i.e. $r_{\text{det}} \cong \lambda / D \cong 1/\gamma$. Using the properties of random variables [95] and incorporating Eqs. (6.7) and (6.10) into Eq. (2.17), the average PSE is given by

$$E\left[PSE\right] = \int_0^\infty PSE\left(K_s(r_r\,\gamma), K_b, M\right) \frac{r_r}{\sigma_r^2} \exp\left(-\frac{r_r^2}{2\sigma_r^2}\right) dr\,. \tag{6.12}$$

Eq. (6.12) is simplified by inserting the change of variables $u = r_r / \sigma_r$ and $v = \sigma_r \gamma$, and getting

$$E\left[PSE\right] = \int_0^\infty PSE\left(K_s(uv), K_b, M\right) u \exp\left(-\frac{u^2}{2}\right) du\,. \tag{6.13}$$

It is evident that the average PSE as given in Eq. (6.13) is a function of $v = \sigma_r \gamma \cong \sigma_r (D/\lambda) \cong \sigma_r / FOV_{DL}$, i.e. ratio of root-mean-square (RMS) tacking error to the receiver diffraction-limited FOV. In a typical optical communications link, the tracking error RMS value needs to be bounded to a small fraction (e.g. 5% - 10%) of the receiver's FOV for minimal loss and maximum link availability. The average PSE as

given in Eq. (6.13) is numerically integrated and results are shown in Figure 6.5. PSE is plotted as a function of SNR for $M = 4$ and different values of normalized variable ν . It is obvious that as the normalized RMS tracking error increases and becomes a significant fraction of the receiver's FOV (i.e. 0.1 % - 20 %), the performance of the receiver degrades drastically. For example, if the receiver is required to maintain an average PSE of at least 1×10^{-6}, 2-15 dB more SNR is needed as ν increases from 0.01 to 0.20. This power loss in power-starved optical communications link drastically degrades the performance of the receiver and results in reduction in the overall link capacity.

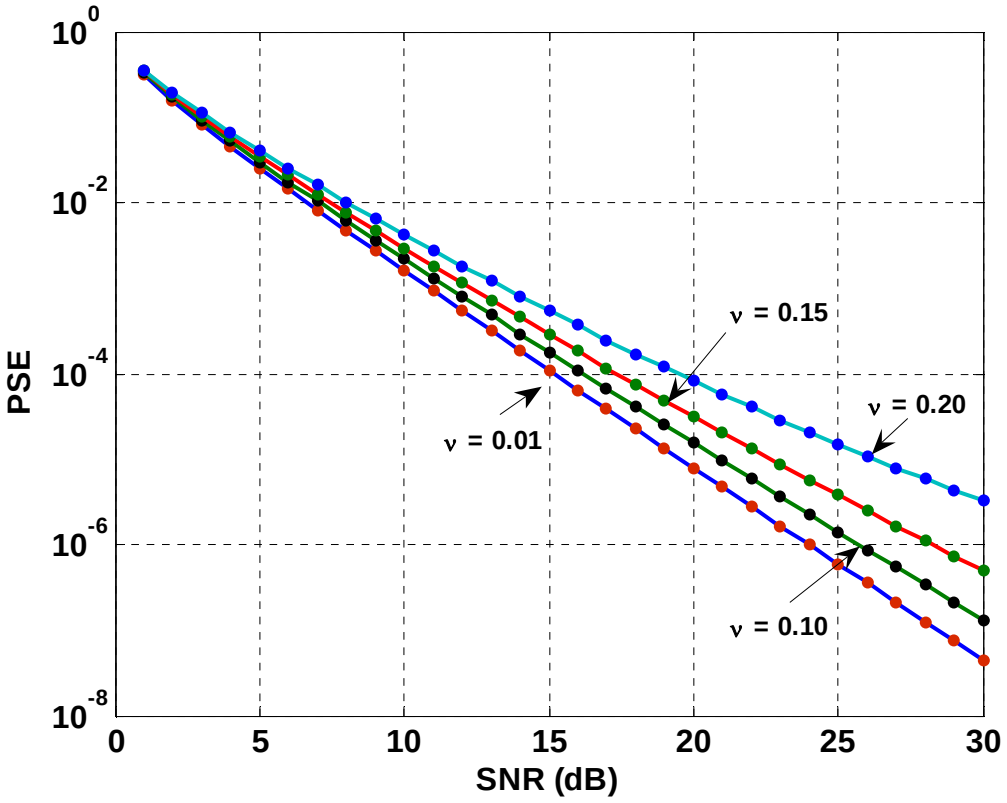

Figure 6.5. PSE as a function of SNR and normalized tracking error RMS values.

6.3. Design of a Closed-Loop Tracking Subsystem

As explained in the previous section, the uncompensated tracking errors can severely degrade the performance of an optical communications receiver. In this section, I present the design and incorporation of a closed-loop tracking subsystem for each telescope in the array receiver to mitigate the deleterious effects of tracking errors on the receiver performance. An array of GMAPDs arranged in four quadrants followed by the photon counters in the focal plane of each telescope act as the tracking error sensor, as shown in Figure 6.6. The received optical field is focused onto the detector array. The output counts from the four quadrants are spatially compared to generate the tracking error signals in both the azimuth and elevation dimensions. At the same time, the photon counts from all the detectors are added and sent to the central combing station for the symbol decoding purposes. In the absence of an error, the incoming signal fields are normal to the receiver and aligned with the optical axis. The focused spot is exactly at the center and all quadrants receive equal amount of signal intensities resulting in zero output error signal, as depicted in Figure 6.6(a). In case of an angular error in either the azimuth or the elevation or both, the PSF is displaced on the detector array. Each quadrant receives a different portion of the received intensity and the output error signal is proportional to the position error. This case is shown in Figure 6.6(b). For a simple optical design (to the first order approximation), the position errors x_e and y_e are related to the azimuth and elevation errors (ψ_{Az}, ψ_{El} respectively) through the focal length f of the receiving aperture, i.e., $x_e = \psi_{Az} f$ and $y_e = \psi_{El} f$.

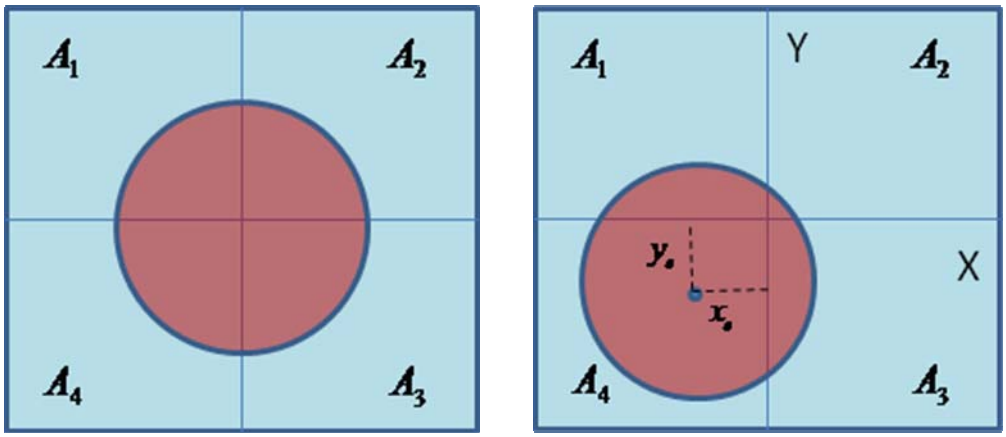

(a) (b)

Figure 6.6. The tracking error sensor in quadrant array configuration. (a) In the absence of tracking errors, all the quadrants receive equal amount of energy. (b) Tracking errors cause shift in the center of the PSF and different quadrant areas receive different amount of energy.

The average error signals (in azimuth/elevation) are calculated by comparing the illuminated areas of each detector element within a quadrant array and are given by

$$E_{Az}\left(\psi_{Az},t\right)=\alpha\left[\int_{A_1+A_4}\left(I_s(\psi_{Az},t)+I_b\right)dx\,dy-\int_{A_2+A_3}\left(I_s(\psi_{Az},t)+I_b\right)dx\,dy\right], \quad (6.14)$$

$$E_{El}\left(\psi_{El},t\right)=\alpha\left[\int_{A_1+A_2}\left(I_s(\psi_{El},t)+I_b\right)dx\,dy-\int_{A_3+A_4}\left(I_s(\psi_{El},t)+I_b\right)dx\,dy\right], \quad (6.15)$$

where $I_s\left(\psi,t\right)$ is the distribution of the received signal intensity over respective quadrant areas (i.e., A_1, A_2, A_3, and A_4), I_b is the background field intensity that is assumed to be uniform across the telescope FOV [17], and $\alpha=\eta_{\det}\lambda/hc$. During a PPM frame, the error sensor produces the azimuth and elevation error counts ($K_{Az}\left(\tau_i\right)$ and $K_{El}\left(\tau_i\right)$, respectively) as

$$K_{Az}(\tau_i) = \frac{\sum_{j=1,4}\left(K_{s(i,j)} + K_b\right) - \sum_{j=2,3}\left(K_{s(i,j)} + K_b\right)}{\sum_{j=1,2,3,4}\left(K_{s(i,j)} + K_b\right)}, \tag{6.16}$$

$$K_{El}(\tau_i) = \frac{\sum_{j=1,2}\left(K_{s(i,j)} + K_b\right) - \sum_{j=3,4}\left(K_{s(i,j)} + K_b\right)}{\sum_{j=1,2,3,4}\left(K_{s(i,j)} + K_b\right)}, \tag{6.17}$$

where $K_{s(i,j)}$ is the average signal photon count in the *i-th* slot of the PPM symbol and *j-th* quadrant detector, and K_b is the sum of the average background photon and detector dark current count in a single PPM slot. Note that within each received PPM frame, tracking error signals are generated during the signal slot τ_i only, where $i \in \{1, 2.....M\}$ and M is the order of PPM. In non-signaling slots, the near uniform background noise over all the quadrants is averaged out and the output tracking error signal is almost zero. The angular tracking errors (ψ_{Az}, ψ_{El}) in the aperture plane are converted to two-dimensional spatial errors (x_e, y_e) in the focal plane, as shown in Figure 6.6(b). The relationship between the output tracking errors counts in Eqs. (6-16), (6-17) and the spatial tracking error (x_e, y_e) is found by referring to the detector geometry given in Figure 6.6 (b), and determining the areas under an offset diffracted spot that falls within symmetrically located quadrants, as given in Eqs. (6-14) and (6.15). The result is given in Eqs. (6.18) and (6.19) referred commonly in tracking terminology as loop *S-curve* [62]

$$K_{Az}(\tau_i) = 1 - \frac{2}{\pi}\left[\arccos\left(\frac{x_e D}{1.2\lambda f}\right) - (0.53)\frac{x_e D}{\lambda f}\sqrt{1 - \left(\frac{x_e D}{\lambda f}\right)^2}\right], \tag{6.18}$$

$$K_{El}(\tau_i) = 1 - \frac{2}{\pi}\left[\arccos\left(\frac{y_e D}{1.2\lambda f}\right) - (0.53)\frac{y_e D}{\lambda f}\sqrt{1-\left(\frac{y_e D}{\lambda f}\right)^2}\right], \qquad (6.19)$$

where D and f are the diameter and focal length of the receiving telescope, respectively.

The complete closed-loop system based on the above-mentioned quadrant error sensor is shown in Figure 6.7. The collective noise from different sources (i.e. tracking sensor noise) is shown as an additive noise source in the tracking loop. Second order low-pass filters are used to estimate and filter the noisy tracking error signals [62]. The output of the filters are used to control and maneuver a high-speed steering tip-tilt mirror, which compensates for the tracking errors and tries to keep the PSF in the center of focal plane detectors. At the same time, the photon counts from all the detectors are added and sent to the central combining station for the symbol decoding purposes.

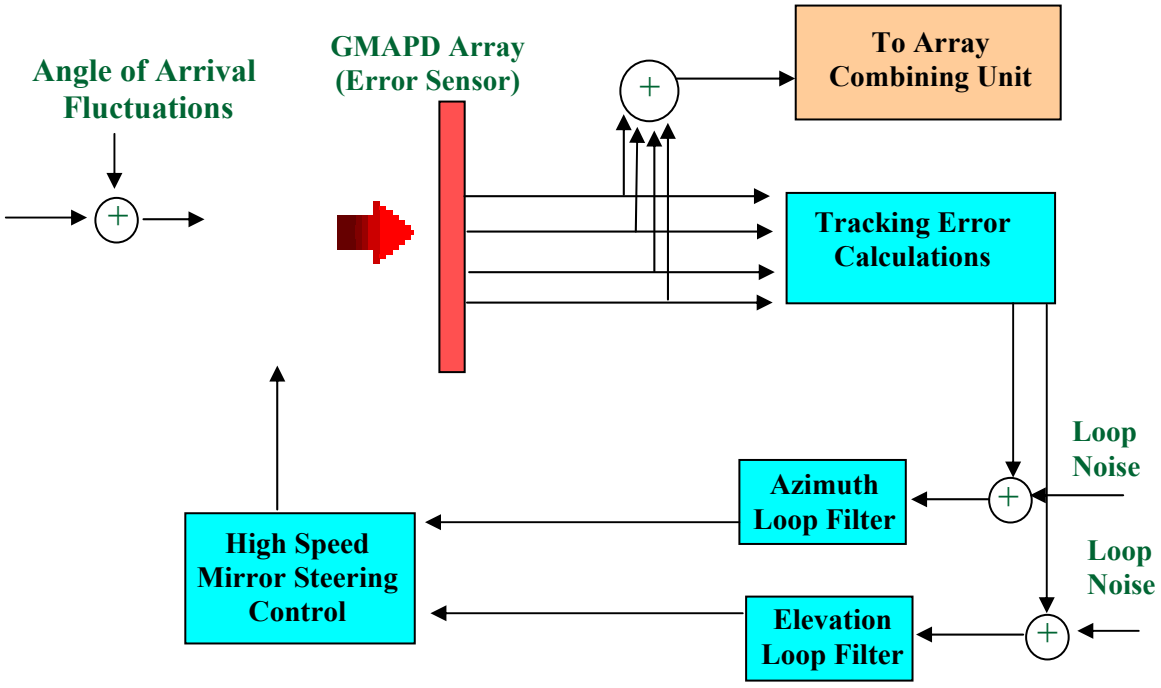

Figure 6.7. Closed-loop tracking subsystem to measure and correct the tracking errors in the telescope LOS.

6.4. Performance Analysis

To evaluate the performance of telescope array receivers in the presence of random tracking errors, Monte-Carlo simulations of an end-to-end optical communications link between Earth and Mars are carried out.

6.4.1. Link Parameters

The aim of the study is to evaluate the tracking performance in extreme operating conditions. Hence, the link is tested for worst-case scenario, i.e. when Mars is at the farthest distance from Earth and during daytime conditions, when the background noise and atmospheric turbulence are at the peak conditions. The parameters summarized in Table 4.1 are used for link budget calculations. The number of received signal and background photons for a communications link between Earth and Mars are calculated according the channel model given in Chapter 2 (Eqs. (2.2-2.8)). Atmospheric turbulence represented by the Fried parameter of r_o = 4cm is incorporated and three different background conditions ranging from worst to best are analyzed in the simulations. Specifically, the background noise radiance values of L = 175, 60, and 10 (all in units of μW/(cm^2-sr-nm) are incorporated in simulations.

6.4.2. Simulation Results

The main design parameters of the array architecture are the sizes of the individual telescopes and the number of telescopes in the array. However, the total photon-collecting aperture of the complete telescope array receiver remains constant in each case. I start with a monolithic, large telescope of 10 m diameter, i.e., the $(1\times10\,\mathrm{m})$ configuration. Then, the number of telescopes in the array is increased by breaking down

the single aperture into 2, 4, 8, 16, 32, and 100 elements of 7.07 m, 5 m, 4 m, 3.53 m, 2.5 m, 1.76 m, and 1 m telescope diameters, respectively. These array architectures correspond to $(2\times 7.07\text{m})$, $(4\times 5\,\text{m})$, $(8\times 3.53\,\text{m})$, $(16\times 2.5\,\text{m})$, $(32\times 1.76\,\text{m})$, and $(100\times 1\,\text{m})$ receiver configurations.

Performances of array receivers are evaluated using the following steps: For each array architecture and link scenario, Monte-Carlo simulations are repeated for 1 million symbols. Given the specific channel conditions (link budget specifications, background noise, and turbulence parameters), the signal and background photons are calculated and system parameters are optimized for each telescope in the array receiver as per the procedures given in Chapters 2 and 3. Artificial tracking errors modeled by zero mean Gaussian random variables are injected in the simulations to represent the LOS and PSF jitter. These tracking errors arise from various sources like atmospheric turbulence, wind, and telescope platform vibrations. As mentioned previously, tracking errors are normally described in terms of their RMS values that should remain bounded to few percent of the receiver FOV for satisfactory operations. For uniformity in the comparison of the results and to test the link in the presence of relatively large tracking errors, the RMS tracking error for individual telescopes in different array architectures is fixed at 20 % of the telescopes' FOV.

Tracking is done in two phases at the receiver-end. In the first stage, the spacecraft ephemeris data is used along with the coarse acquisition algorithms to acquire the transmitter LOS. In the second stage, closed-loop tracking system as explained in Section 5.3 is employed to compensate for the tacking errors and to maintain the focal spot on the detectors for minimization of power losses. The output of the quadrant

photodetectors are modeled by the Poisson distribution and photon-counts are generated for each PPM slot at individual telescopes. The photon-counts from four quadrants are compared to generate the tracking errors signals in azimuth and elevation dimensions (Eqs 6.14-6.17). The error counts are converted to corresponding tracking errors using Eqs. (6.18) and (6.19). The output counts from the four quadrants are also summed for forming the sufficient statistics at each telescope.

As the number of telescopes in the array is increased, the combined residual tracking error of the array also increases inflicting power losses. While the tracking system in each telescope mitigates the tracking errors effects, outputs from all telescopes are combined in a central combining unit for decoding and symbol detection. As per Maximum Likelihood (ML) detection strategy for PPM demodulation [7], the signal slot is selected as the slot containing the largest number of photons after comparison of all slot statistics in the decoder. The system PSE is calculated as the ratio of the number of false detections to the total number of received symbols. PSE is plugged in Eqs. (2.16 – 2.18, Chapter 2) to evaluate the achievable data rates in the presence of tracking errors.

Figure 6.8 shows the effect of increasing the number of elements in the array on the achievable data rates in the worst-case channel conditions. As the number of telescopes increase from 1 to 100, the achievable data rate decrease from 2.07 Mbits/s to 1.79 Mbits/s that correspond to a 13 % performance loss. This performance degradation can be attributed to the fact that as a result of reducing the size and increasing the number of telescopes in the array, the performance of closed-loop tracking system decreases due to lesser received signal power and an increase in measurement noise. Consequently, the RMS value of the residual tracking error of the combined array increases. This results

into power losses and a decrease in achievable data rates. However, it is obvious that in the worst-case channel conditions and presence of large tracking errors, the degradation in performance is not substantial.

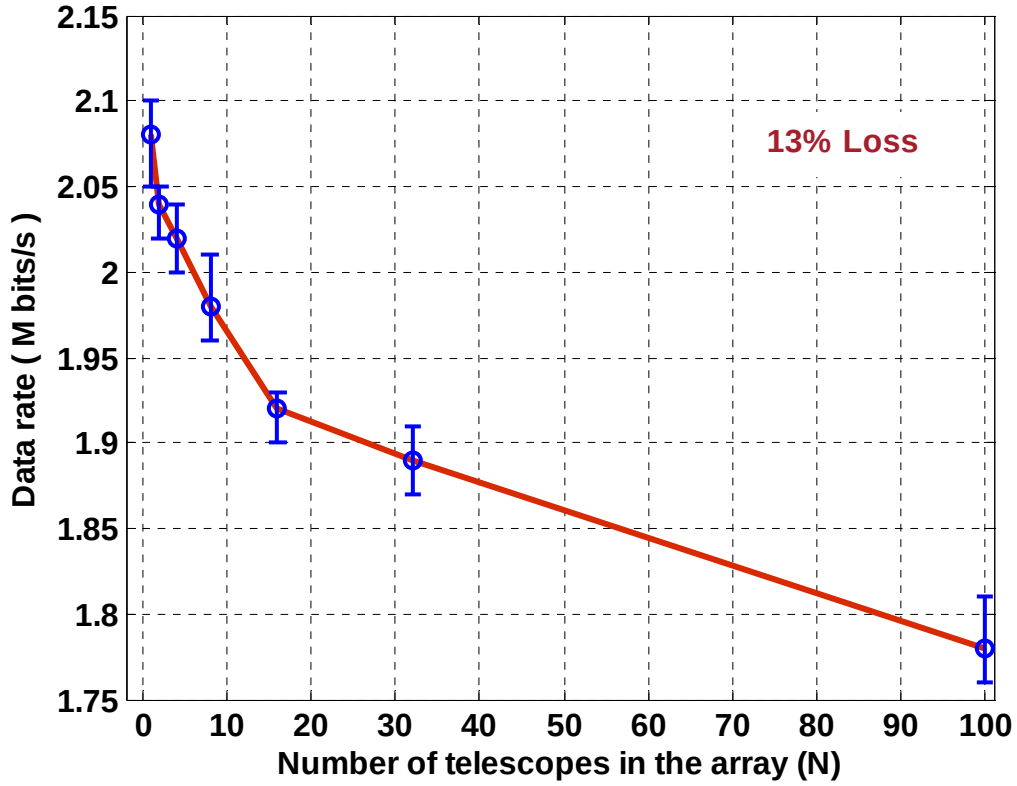

Figure 6.8. Achievable data rates as a function of number of telescopes in the array receiver in the presence of random tracking errors. Extreme background noise with L=175 μW/(cm^2-sr-nm) and a Fried parameter of 4 cm is employed.

Next, simulations are repeated for background noise radiance values of L = 60 and 10 μW/(cm^2-sr-nm), which correspond to the moderate and weak background noise conditions. However, the turbulence conditions are still kept at the peak value represented by a Fried parameter of 4 cm. The achievable data rates for these channel conditions are plotted in Figures 6.9 and 6.10. Figure 6.9 shows that in the moderate background conditions, the achievable data rates decrease from 4.62 Mbits/s to 4.15 Mbits/s as the

telescope array dimensionality is increased from 1 to 100. This corresponds to about 10 % performance loss. The results for the nominal background conditions are shown in Figure 6.10. It is obvious that when a single telescope is replaced by a N =100 element array receiver, the achievable data rates decrease from 12.30 M bits/s to 11.35 Mbits/s that correspond to about 7.7 % performance loss. The performance losses in smaller array architectures ($N \leq 32$) are much less. Figures (6.8-6.10) demonstrate the efficacy of the closed-loop tracking subsystem in successfully tracking and minimizing the effects of tracking errors. As explained in the Chapter 1, the array architectures have numerous advantages, i.e., cost, redundancy, ease of manufacturing, maintenance, operations, and ability to provide a near diffraction-limit performance. Keeping in view these advantages, the small loss in the performance due to residual tracking errors seems to be acceptable, and is not a major limitation in the viability of array-based receivers up to N =100 telescope elements for a deep-space optical communications link.

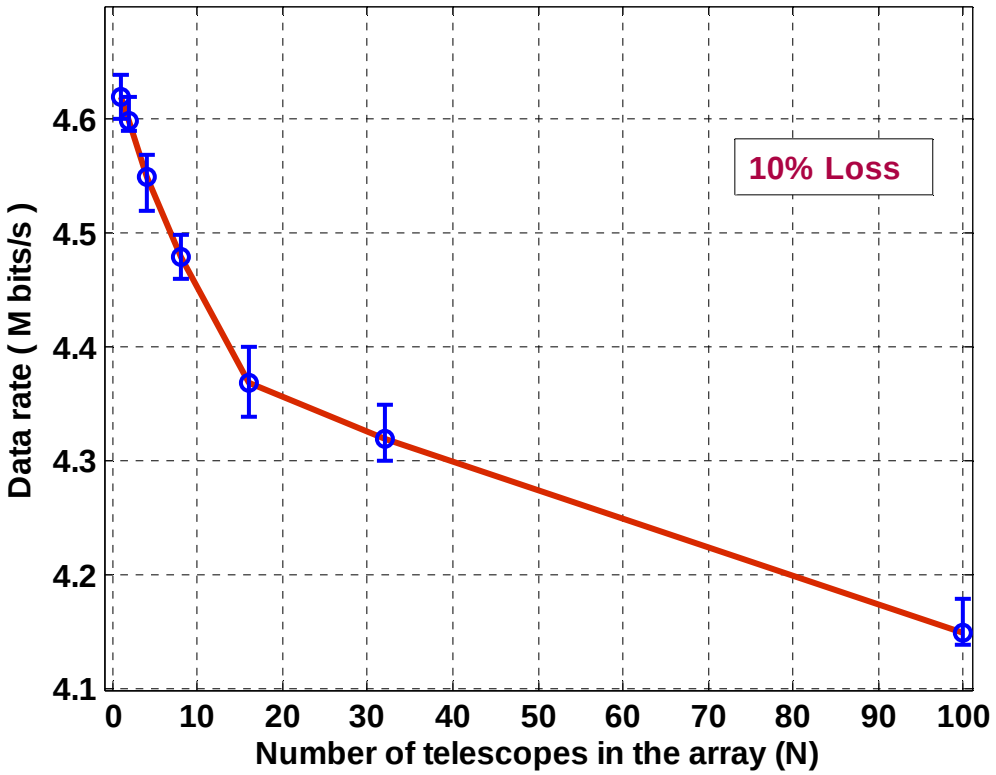

Figure 6.9. Achievable data rates as a function of number of telescopes in the array receiver in the presence of random tracking errors. Moderate background noise with L = 60 μW/(cm^2-sr-nm) and a Fried parameter of 4 cm is employed.

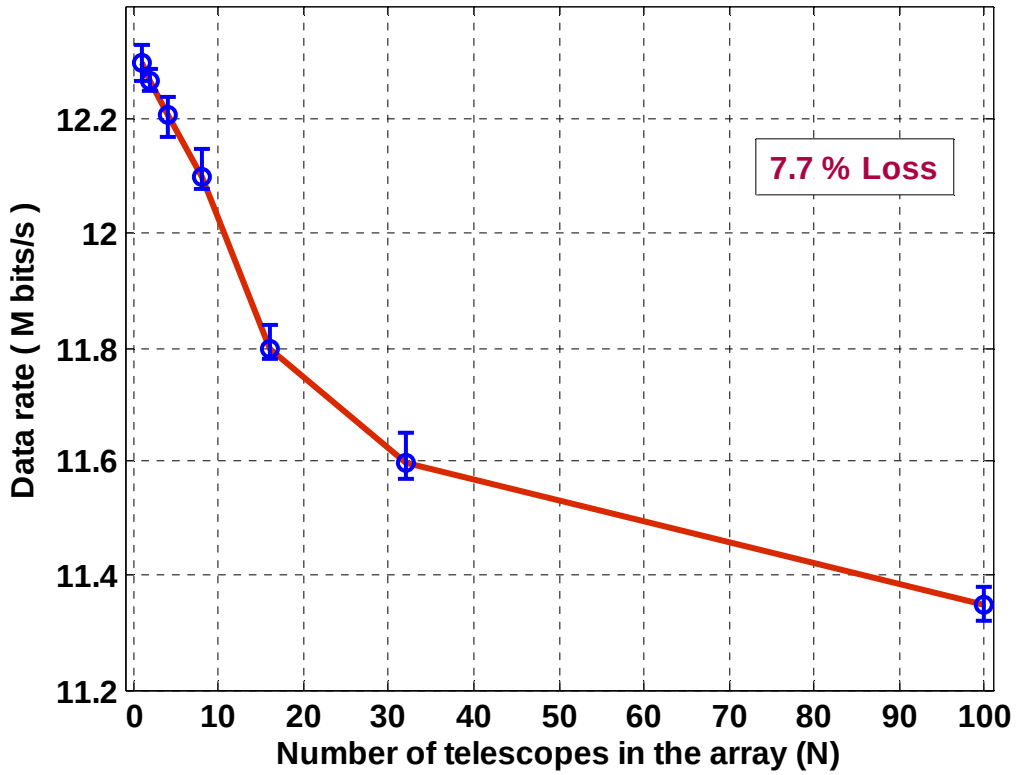

Figure 6.10. Achievable data rates as a function of number of telescopes in the array receiver in the presence of random tracking errors. Nominal background noise conditions with $L = 10\ \mu$W/(cm^2-sr-nm) and a Fried parameter of 4 cm is employed.

6.5. Chapter Summary

In this chapter, I first presented a statistical analysis to evaluate the performance of general direct-detection receivers in the presence of random tracking errors. The analysis showed that the tracking errors resulted in considerable degradation in the performance of optical receivers. Next, I presented the design of a closed-loop tracking subsystem for mitigation of the tracking errors to avoid power losses. Finally, I analyzed and compared the performance of different telescope arrays configurations with a monolithic aperture, for an optical communications link between Earth and Mars, after incorporating the designed closed-loop tracking subsystem. The results show that as the

number of elements in the telescope array receiver is increased from 1 to 100, the overall performance (evidenced by achievable data rates) degrades slightly (i.e. about 10 % for most conditions of interest) compared to single large telescope architecture. Therefore, tracking errors (if compensated) do not pose a big limitation as far as the replacement of a telescope with the telescope arrays is concerned. Taking into account the cost factor and several other benefits of telescope arrays (e.g. scalability, operational ease, and redundancy) this performance loss is acceptable.

CHAPTER 7

DESIGN OF ADAPTIVE OPTICS (AO)-BASED TELESCOPE ARRAY RECEIVERS FOR COMPENSATION OF ATMOSPHERIC TURBUELNCE EFFECTS

In this chapter, investigation and design of the use of adaptive optics (AO) subsystems are presented for the compensation of the coupled effects of optical turbulence and background noise in telescope array-based receivers. An end-to-end simulation platform for an ODSC between Earth and planet Mars is implemented. AO subsystems are incorporated at individual telescopes in the array receiver to compensate for turbulence effects. The performance of array receivers is evaluated in terms of achievable data rates. The analysis presented in this chapter shows that in worst-case atmospheric turbulence and background noise conditions, the incorporation of AO systems in an array receiver consisting of 100, 1 m telescopes results in 8.48 dB of performance improvement in achievable data rates. The performance improvement of 5.59 dB is possible during moderate channel conditions. The performance comparison of array receivers with a single large telescope reveals that the incorporation of AO systems is more feasible in array receivers consisting of relatively smaller sized telescopes.

7.1. Statement of the Problem

Atmospheric turbulence is a major limiting factor in a deep-space optical communications link. Atmospheric turbulence gives rise to *optical turbulence*. Optical turbulence distorts the phase of the propagating optical fields thus limiting the focusing

capabilities of telescopes; it induces beam-wander and a random excursion of the focused spot in the detector plane; and it inflicts intensity fluctuations called scintillations [36]. The effect of beam wander can be compensated by incorporating an active tracking subsystem in the receiver, as shown in Chapter 6. The scintillation effects are negligible for relatively larger telescope, with aperture diameter $\geq$ 1 m, due to aperture-averaging phenomenon [36]. Hence, the dominant effect of random phase perturbations is considered in this chapter. The random phase distortions result in a larger point spread function (PSF), compared to a diffraction-limited system, in the focal (detector) plane of the receiving system. Hence, comparatively, a large size detector is required to encompass the signal energy in the focal-plane. In a direct-detection optical communications system, the receiver field-of-view (FOV) depends upon the detector size [17]. In a deep-space optical link, some background light (from the Sun, the sky etc.) always enters the receiver FOV along with the desired optical signal fields [40-45]. As the detector dimensions and receiver FOV are increased to capture the larger PSF in the detector plane, the amount of background noise also increases. This phenomenon results in a substantial degradation in the overall signal to background noise photon count ratio and performance of the optical receiver. Unfortunately, both the atmospheric turbulence and background noise are at their respective peaks during daytime, and is the foremost challenge for optical communications systems.

In this chapter, I present a solution to this problem by incorporating adaptive optics (AO) subsystems in telescope array-based receivers for compensation of optical turbulence and background noise effects in a deep-space optical communications link between Earth and Mars. The use of AO systems is very common in astronomical

applications [70] and many modern telescopes around the globe are equipped with AO subsystems for mitigation of atmospheric turbulence effects [70-73]. However, the domain of deep-space optical communications is different from astronomical applications. Astronomical systems mostly operate during nighttime, whereas, deep-space optical communications systems would operate during daytime also when turbulence and background noise are at their respective peaks. Hence, the use AO system in telescope array receivers for deep-space optical communications is a new challenge, which is addressed here.

Specifically, the results for a communication link between Earth and Mars presented in this chapter show that the incorporation of AO systems in extreme turbulence and background condition results in performance improvements of 9.24 dB, 8.74 dB, 8.67 dB, and 8.48 dB in telescope array-based receivers with $(8\times 3.53\text{ m}), (16\times 2.5\text{ m}), (32\times 1.76\text{ m})$, and $(100\times 1\text{m})$, respectively, configurations. During moderate background conditions, performance improvements of 6.25 dB, 5.69 dB, 5.72 dB, and 5.59 dB, respectively, are possible in the same architectures. The performance of AO subsystems in above-mentioned architectures is also compared to the use of AO systems in $(1\times 10\text{ m})$ and $(4\times 5\text{ m})$ configurations and it is shown that the use of high-complexity AO systems is more feasible in array receivers with smaller-sized (i.e., $\leq$ 3.53 m) telescopes.

7.2. Impact of Atmospheric Turbulence

Atmospheric turbulence, generated by the pressure and temperature differentials in the atmosphere, creates random fluctuations in the atmospheric refractive index called the *optical turbulence*. The major effect of optical turbulence is the loss of spatial

coherence of the laser beam as it propagates through the atmosphere [36]. The loss of spatial coherence limits the extent of focusing capabilities of the collecting aperture. As a result, PSF in the focal plane deviates from the ideal diffraction-limited performance. In the diffraction-limited case, the incoming plane waves from a distant point source are focused into a spot size, limited only by the size of the collecting-aperture D, i.e., $\cong(2.44\lambda f/D)$ [17,76], where f is the focal length of the telescope. In this regime, the background noise is not dependent upon the aperture size [17]. Hence, the aperture size can be increased to increase the received signal energy. However, in the presence of turbulence the focused spot size is limited by the atmospheric Fried parameter r_o (which varies from 20 cm to 4 cm with the turbulence strength), i.e., $(\cong 2.44\lambda / r_o)$ [17,76]. For deep-space applications typically $D >> r_o$; hence, the turbulence-limited spot size is much larger than the ideal diffraction-limited one. An increase in the detector size is needed to capture the signal energy spread over a wider area. Increasing the detector size results in an increase in the received background noise, which degrades the performance of the receiver.

The behavior of a sub-portion of optical turbulence is described in a statistical manner and forms the basis of most propagation theories. For optical wave propagation, the associated power spectral density for refractive index fluctuations is widely described by the Kolmogorov spectrum in the literature given as [7,36,45,69,88,105],

$$\Phi_n(\kappa) = 0.033 C_n^2 \, \kappa^{-11/3}, \qquad 1/L_o << \kappa << 1/l_o, \tag{7.1}$$

where κ is the spatial frequency in the telescope aperture plane, L_o is the turbulence outer-scale, and l_o is the inner-scale of turbulence. The atmospheric turbulence effects

are simulated by generating a phase screen on the telescope aperture by using the methods described in Ref. [96]. The aperture-plane signal distribution is Fourier transformed to get the focal-plane intensity distribution of the received signal. An example of the simulated turbulence effects on a telescope with D = 1 m and r_o = 4 cm is shown in Figure 7.1. The aperture-plane phase distribution in Figure 7.1(a) clearly deviates from an ideal plane wave. Figure 7.1(b) shows the focal plane distribution as a function of the diffraction-limited spot size, which deviates from the ideal Airy pattern. It is obvious from Figure 7.1(b) that the PSF is about 25 (i.e., D / r_o) times larger than the diffraction-limited Airy disc in a single dimension.

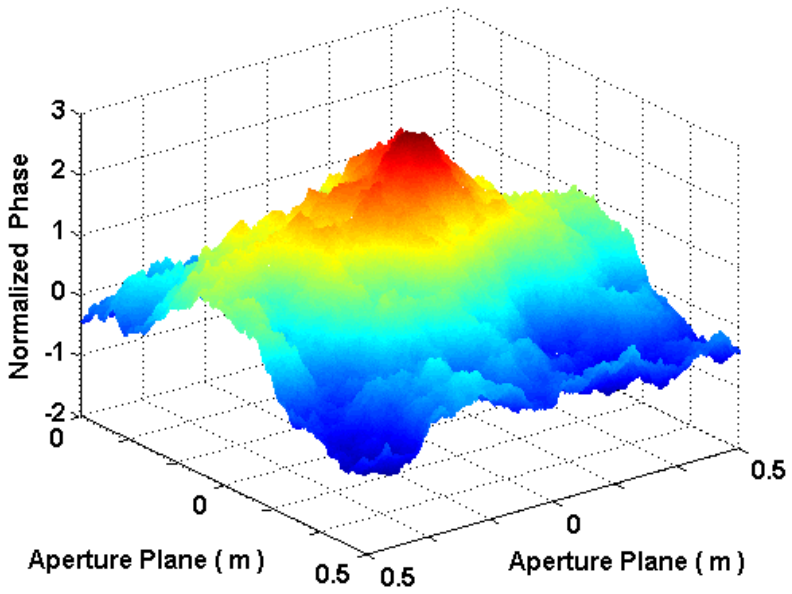

7.1(a)

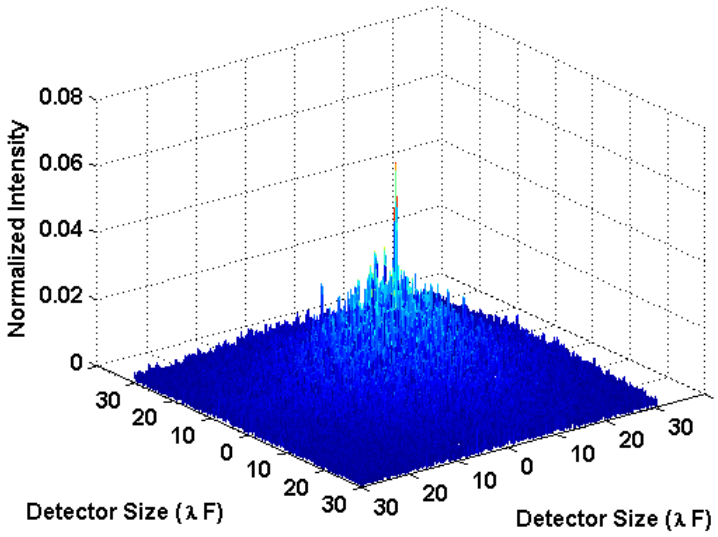

7.1(b)

Figure 7.1. (a) Random phase distribution in the aperture-plane of the telescope, (b) corresponding focal plane distribution. Telescope aperture diameter is 1 m and Fried parameter r_o is 4 cm.

7.3. Adaptive Optics (AO) Systems

7.3.1. Functional Description

A generic AO system consists of three principal elements: a wavefront sensor, a deformable element, and a feedback scheme. Typically, these components are a Shack-Hartmann sensor, a deformable mirror, and a control computer [69]. The wavefront sensor measures the phase distortion of the incoming optical beam; the control computer is a signal processor that reconstructs the phase of the beam and translates the wavefront sensor output into deformable mirror actuator commands. The deformable mirror consists of many actuators, which deform the mirror to a specified shape and try to apply the conjugate of the phase aberrations (measured by the wavefront sensor) to the distorted

optical beam. After the correction, the received PSF approaches the ideal Airy pattern; a smaller detector is used in the focal plane to encompass the concentrated energy thus spatially rejecting most of background noise energy.

Since the received optical signal power in a deep-space optical communications link is not enough to estimate and correct the wavefront error and a suitable natural guide star may not always be available in the receiver's FOV, an artificial laser guide star (LGS)-based AO system is employed. Specifically, the resonant excitation of the sodium layer at the 94 km altitude by a laser with λ=589 nm is used as the LGS in this research [69]. LGS-based AO systems are commonly used in the astronomical application [69,73]. The main difference of the AO in astronomy and communications is that the latter requires a much smaller FOV and operates during daytime. This makes LGS-based AO for deep space communications even more efficient than those for astronomical applications as the rejection of background noise during daytime is substantial (as will be shown in Section 7.5).

7.3.2. AO Systems Performance Criterion

Due to many spatial and temporal constraints, it is very difficult for an AO system to compensate the turbulence-induced phase distortions completely. Even the most advance AO systems are able to compensate the distortions partially, and some residual wavefront (phase) error σ_{φ}^2 is always left. An example of the partial phase compensation is given in Figure 7.2. The figure shows the phase fluctuations of an input wavefront over a telescope pupil-plane (1 m aperture diameter) before and after wavefront corrections by an arbitrary AO system with a twelve-actuator deformable mirror. The Fried parameter r_o is 4 cm. It is evident that the AO system compensates phase-fluctuations with low

spatial frequencies but high-frequency components of the random phase cannot be compensated.

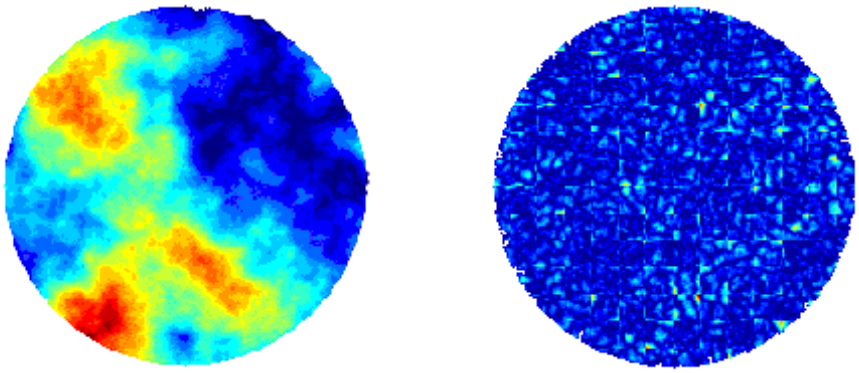

(a) (b)

Figure 7.2. Distribution of the phase of a received wavefront on a telescope pupil with 1 m aperture diameter and a Fried parameter of 4 cm, (a) before AO correction, (b) after AO correction.

There are many criterions to estimate the performance of an AO system. In this research, the efficiency of an AO system and improvement in the beam quality after phase-correction is represented by the Strehl ratio (*SR*). *SR* is defined as the ratio of the peak intensity in the aberrated PSF to the peak intensity in a diffraction-limited PSF (Airy disk). Using the Marechal approximation (valid for *SR* > 0.2) and for large aperture diameter telescopes ($D >> r_o$), the SR_φ after AO correction is given as [69]

$$Strehl\ ratio\ SR = \exp(-\sigma_\varphi^2), \tag{7.2}$$

where σ_φ^2 is the total residual mean square wavefront error after AO correction.

7.3.3. Sources of Residual Wavefront Errors

There are four main sources of errors inherent in a closed-loop LGS-based AO system, which contribute to the total wavefront error. To the first order, the errors from each of the four sources can be treated as uncorrelated. Therefore, the mean square wavefront error is given by the following quadrature sum [69]:

$$\sigma_{\varphi}^2 = \sigma_{FA}^2 + \sigma_{WFS)pd}^2 + \sigma_{fit}^2 + \sigma_{time}^2 . \tag{7.3}$$

In Eq. (7.3) σ_{FA}^2 is the "focus anisoplanatism (*FA*)" error that arises because of the cone shape of the artificial LGS. $\sigma_{WFS)pd}^2$ is the wavefront phase-difference error arising due to slope measurement errors in the wavefront sensor. σ_{fit}^2 is the wavefront fitting error that arises because of the limited number of wavefront actuators. σ_{time}^2 represents the temporal error arising due to a time delay in the AO system control loop. A detailed description of these error sources is given next.

7.3.3.1. Focus Anisoplanatism (FA) Error

Artificial laser guide star (LGS)-based AO systems face a fundamental error called "focus anisoplanatism (*FA*)" or the cone effect. This error arises because the rays of light from the beacon to a receiving telescope trace out a cone rather than the desired cylindrical volume of air above the telescope. The mean square *FA* error variance for a single beacon per telescope is defined as [69]

$$\sigma_{FA}^2 = \left(\frac{D}{d_o}\right)^{5/3}, \tag{7.4}$$

where D is the telescope aperture diameter and d_o is a parameter that depends only on wavelength and the turbulence profile at the telescope site. The value of d_o at a beacon altitude of 94 km and a communications wavelength of 1.06 μm is 10 m [69]. It is shown in the design examples in Tables 7.1 and 7.2 that σ_{FA}^2 is a major source of residual wavefront error in larger telescopes (D $\geq$ 5 m) at the wavelength of 1.06 μm. Due to the *FA* error, achieving higher *SR* is extremely difficult for telescopes with (D $\geq$ 5 m). A solution to this problem is the use of multiple beacons at individual telescopes [69]. However, in this research we restrict ourselves to the use of a single beacon per telescope.

7.3.3.2. Fitting Error

Fitting error arises because of the limited number deformable mirror actuators. It is given by [69]

$$\sigma_{fit}^2 \cong 0.3\left(\frac{r_s}{r_o}\right)^{5/3}, \tag{7.5}$$

where r_o is the Fried parameter and r_s is the mirror inter-actuator spacing. For a total number of N independently controlled actuators in the deformable mirror, r_s is given by

$$r_s = D/\sqrt{N} \tag{7.6}$$

7.3.3.3. Temporal Error

The temporal error arises because of the limited closed-loop bandwidth of an AO system. For a servo-control system with a time delay of τ seconds, it is defined as [69]

$$\sigma_{time}^2 = \left(\frac{\tau}{\tau_o}\right)^{5/3}, \tag{7.7}$$

where τ_o is the Greenwood time delay given by [69]

$$\tau_o = 0.314 \times \frac{r_o}{\bar{\upsilon}} . \tag{7.8}$$

r_o is the Fried parameter and $\bar{\upsilon}$ is the modulus of the mean propagation velocity of turbulent layers.

7.3.3.4. Wavefront Sensor Phase Difference Error

The wavefront sensor (WFS) phase difference error arises because of WFS photon-noise error. WFS photon-noise error occurs due to a finite photon return rate per WFS sub-aperture and finite beacon image size. It is given as [69]

$$\sigma^2_{WFS)\,pd} \cong \left(\frac{2\pi\,\alpha\,\gamma\,w}{N_{ph}} \left(1 + \frac{4n_d^2}{N_{ph}} \right)^{1/2} \frac{\lambda_b}{\lambda_i} \right)^2 . \tag{7.9}$$

λ_b = 589 nm for the sodium LGS, λ_i = 1060 nm, n_d is the detector readout noise, γ is the noise reduction factor for the closed-loop system, w is the image width factor, and α =0.65. N_{ph} is the number of photons received at each wavefront sensor subaperture and is given by [69]

$$N_{ph} = F\, d^2_{WFS}\, \tau\, \eta_{\text{det}} , \tag{7.10}$$

where F is the stellar flux (photons/area/time). η_{det} is the detector quantum efficiency, τ is the integration time, and d_{WFS} is the diameter of the wavefront subaperture.

7.3.4. Design of Laser Guide Star (LGS)-Based AO System

It is common for the current state-of-the-art astronomical AO systems to achieve a *SR* > 0.50. However, due to the *FA*-induced error, it becomes difficult for relatively large

telescopes ($D \geq 5\,\text{m}$) to achieve a high *SR* at the communications wavelength of $1.06\,\mu\text{m}$. The examples of the design of LGS-based AO systems for telescopes with different aperture sizes in array receivers are given in this section. Section 7.3.4.1 describes the designs of AO systems that can achieve a *SR* = 0.30. Sections 7.3.4.2 describes the AO systems that can achieve a *SR* = 0.75. A single laser-beacon is assumed in AO subsystems employed at each telescope. Different telescope architectures are analyzed. These architectures range from a single 10 m diameter telescope to an array of 100, 1 m telescopes. The design parameters for telescopes with different aperture diameters are given next.

7.3.4.1. Strehl Ratio (SR) =0.30

Following parameters are fixed in the analytical calculations to achieve a *SR* of 0.30: $d_o = 10\,\text{m}$, $\bar{\upsilon} = 5\,\text{m/s}$, $r_o = 4\,\text{cm}$, $\tau = 0.3$ ms, $\alpha = 0.65$, $w = 0.3$, $\gamma = 0.78$, $n_d = 1e^4$ count/s, $\eta_{\text{det}} = 0.80$, and $F = 0.07$ photon/ms/cm^2. Beacon source = 10 W (CW) sodium LGS. Detailed descriptions of these parameters are given in Ref. [69]. Following parameters change with different telescopes: Diameter *D* vary with different array configurations and is given in the following tables. The number of actuators across the telescope pupil is $2n$. $d_{WFS} = D/10$ and a (10×10) Shack-Hartman sensor is employed in each case.

Table 7.1. Design of AO systems to achieve *SR*=0.30.

D (m)	*n*	σ^2_{FA}	σ^2_{fit}	σ^2_{time}	$\sigma^2_{WFS)pd}$	$\sigma^2_{\phi)tot}$	*SR*
1	12	0.0215	1.0195	0.0290	0.0532	1.1232	0.3252
1.76	20	0.0553	1.1164	0.0290	0.0092	1.2099	0.2982
2.5	30	0.0992	1.0195	0.0290	0.0036	1.1513	0.3162
3.53	44	0.1763	0.9570	0.0290	0.0016	1.1638	0.3123
5	68	0.3150	0.8275	0.0290	0.0007	1.1722	0.3097
10	300	1	0.2214	0.0290	0.0001	1.2504	0.2864

7.3.4.2. Strehl Ratio (SR) =0.70

In this example, all the constant parameters are same as those in section 7.3.4.1. The beacon in this case is a 25 W (CW) sodium LGS [106]. The other significant change compared to Table 7.1 is the use of a large number of actuators to achieve a higher *SR*.

Table 7.2. Design of AO systems to achieve *SR*=0.75.

D (m)	n	σ^2_{FA}	σ^2_{fit}	σ^2_{time}	$\sigma^2_{WFS)pd}$	$\sigma^2_{\phi)tot}$	*SR*
1	30	0.0215	0.2214	0.0290	0.0126	0.2845	0.7524
1.76	56	0.0553	0.2007	0.0290	0.0028	0.2877	0.7500
2.5	92	0.0992	0.1575	0.0290	0.0012	0.2869	0.7506
3.53	180	0.1763	0.0915	0.0290	0.0006	0.2973	0.7428
5	300	0.3150	0.0697	0.0290	0.0003	0.4140	0.6610
10	350	1	0.1712	0.0290	0.0001	1.2003	0.3011

It is evident from Table 7.1 that a *SR* of 0.3 can be achieved in the telescopes of all sizes. However, the last two rows in Table 2 show that a *SR* = 0.75 could not be achieved in telescopes with diameters of 10 m and 5 m. The major limiting factor in these two cases is the *FA* error at the communications wavelength of $1.06\,\mu$m . A solution to

this problem is to either change (increase) the operating wavelength or the use of multiple beacons at individual telescopes [69]. However, in this thesis, the analysis is restricted to the use of a single beacon at each telescope. Hence, for telescopes with diameters of 10 m and 5 m, only a correction achieving $SR = 0.30$ is assumed.

7.4. Background Noise Compensation

As explained in Section 7.2, the turbulence-limited PSF in a telescope focal-plane is much larger than the diffraction-limited PSF. A large-size detector is needed in direct-detection communications systems to capture the optical energy spread over a wider area. The use of a large detector results in an increase in background noise. Incorporation of an AO system results in the correction of the distorted wavefront and generation of a smaller and more concentrated PSF. However, as explained in previous sections, the distortions cannot be compensated completely. As a result of the partial compensation, the PSF in the focal-plane is a sum of the two terms: an Airy disc due to the partial correction plus a halo around the disc due to the light diffracted by the uncompensated wavefront errors. The size of the Airy disc depends upon the telescope D ($i.e., \cong 2.44\lambda/D$) and the extent of the halo is limited by the Fired parameter r_o ($i.e., \cong 2.44\lambda/r_o$) [69,105]. The *SR* value represents the fraction of the total received energy in the Airy disc, whereas the remaining fraction of the total energy (i.e., (1 - *SR*)) is distributed in the encircling halo. The use of a small detector (i.e., with the size equivalent to the central Airy disc) results in a substantial reduction in the detected background noise.

It is important to mention that because of this reduction in the detector size; only *SR* fraction of the signal energy is detected. However, the reduction in the background noise is more significant, which results in an overall improvement in the performance of

the communications system, as shown in Section 7.5. As an example, Figure 7.3 shows the received power distributions in the focal-planes of a 1 m telescope after incorporation of different AO systems with varying complexity levels. The atmospheric turbulence strength is represented by a Fried parameter value of 4 cm. The normalized intensity is drawn versus the detector dimensions in the focal-plane for different cases. Figure 7.3(a) represents an ideal diffraction-limited case when most of the energy is concentrated in the Airy disc with the full-width at half-maximum (FWHM) of $\approx \lambda / D$. Figure 7.3(b) represents a turbulent-limited case where the received energy is spread over an area with FWHM of $\approx \lambda / r_o$. Figure 7.3(c) shows the result of the incorporation of an AO system, which partially compensates the phase distortions and achieves a *SR* of 0.3. In this case, 30 % of the total received energy is concentrated in the FWHM extent of the Airy disc and the rest is spread over the surrounding halo. Reducing the size of a photodetector to FWHM size of the Airy disc results in the reduction of the signal energy to 30 % of its maximum value. However, the background noise in this case reduces to less than 5 % of its original value. This phenomenon results in a considerable improvement in the performance of a direct-detection optical communications receiver operating in strong background and turbulence conditions, as prevalent in deep-space optical communications links.

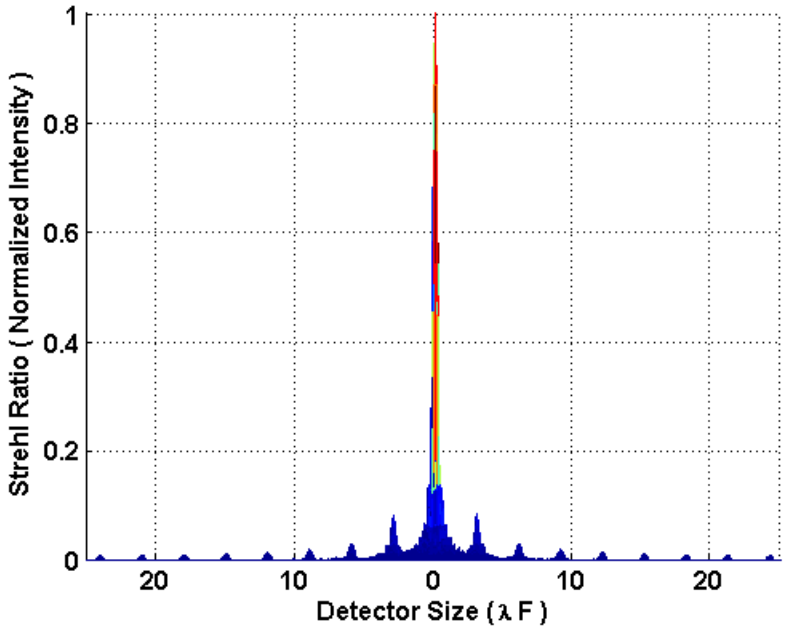
Strehl Ratio (Normalized Intensity)
1
0.8
0.6
0.4
0.2
0
20
10
0
10
20
Detector Size (λ F)

7.3(a)

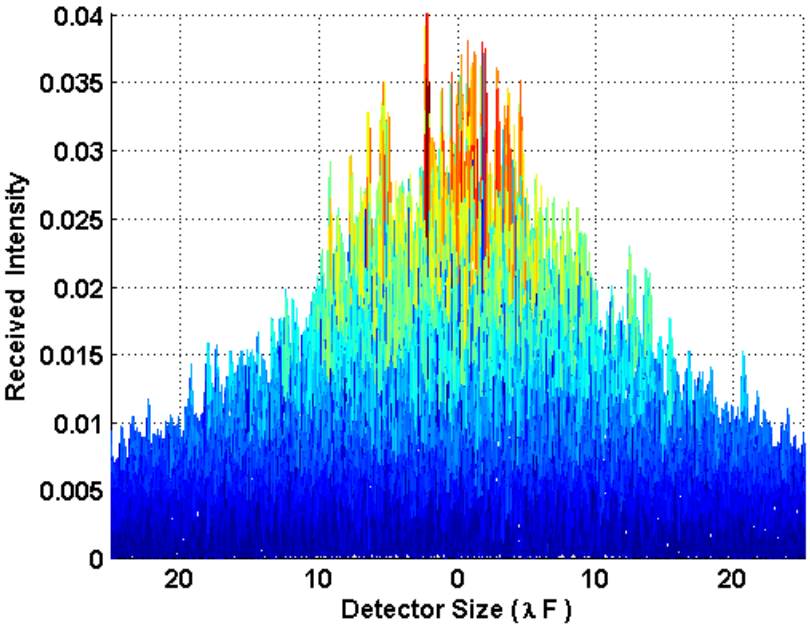
Received Intensity
0.04
0.035
0.03
0.025
0.02
0.015
0.01
0.005
0
20
10
0
10
20
Detector Size (λ F)

7.3(b)

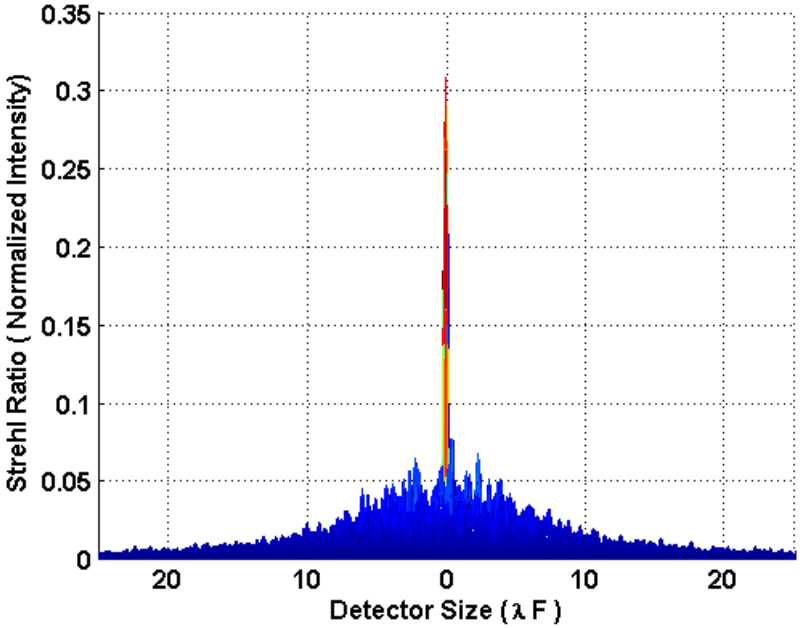

7.3(c)

Figure 7.3. Normalized intensity distributions in focal plane of a 1 m telescope: (a) Ideal distribution without optical turbulence, (b) turbulence-induced distribution without AO system, (c) distribution after AO-based compensation achieving a SR = 0.30. The Fried parameter r_o = 4 cm in (b) and (c).

7.5. Performance Analysis of AO-based Telescope Array Receivers

In this section, the performance of AO-based telescope array receivers for a deep-space optical communications link between Earth and Mars is evaluated. PPM along with direct-detection techniques are employed in the subsequent analysis. It is assumed that AO systems that can achieve a SR of 0.30 and 0.75 (as designed in Section 7.3.4) are employed at each telescope element in array receivers for mitigation of turbulence-induced phase distortions.

7.5.1. Link Parameters

It is important to highlight that the aim of this study is to find the effect of AO-induced corrections on achievable data rates in extreme channel conditions. Hence, the efficacy of AO systems is tested in worst-case channel conditions. These channel conditions correspond to Earth-Mars conjunction (i.e., Mars is farthest from the Earth) and very strong turbulence conditions represented by a Fried parameter value of 4 cm. The link is tested for background radiance values of $175\,\mu\text{W/(cm}^2\text{-sr-nm)}$ representing extreme background noise and $60\,\mu\text{W/(cm}^2\text{-sr-nm)}$ representing moderate background noise conditions. Details of other link budget parameters are same as those given in Table 4.1. The numbers of received signal and background photons are calculated according the channel model given in Chapter 2 (Eqs. (2.2-2.8)).

7.5.2. Numerical Results

The main design parameters of array architecture are the size of individual telescopes and the number of telescopes in the array. However, for comparison purposes, the total photon-collecting aperture of the complete telescope array receiver remains constant (i.e., 10 m) in different architectures. I start with a monolithic, large telescope with 10 m diameter, i.e., the $(1\times10\,\text{m})$ configuration. Then, I increase the number of telescopes in the array by breaking down the single aperture into 4, 8, 16, 32, and 100 telescopes with 5 m, 3.53 m , 2.5 m , 1.76 m, and 1 m aperture diameters, respectively. These cases correspond to $(4\times5\,\text{m})$, $(8\times3.53\,\text{m})$, $(16\times2.5\,\text{m})$, $(32\times1.76\,\text{m})$, and $(100\times1\,\text{m})$, respectively, configurations.

Performance of telescope array receivers are evaluated using the following steps: given the specific channel conditions (i.e., link budget specifications, background noise radiance, and turbulence Fried parameter), signal and background photons are calculated using models given in Chapter 2. System parameters (detector size, PPM slot-width T_s, and PPM order *M*) are optimized employing the methodology described in Chapter 3. For a particular array architecture, turbulence-induced optical fields are generated in the aperture planes of individual telescopes using the techniques mentioned in Section 7.2. The AO systems as designed in Section 7.3.4 are incorporated at each telescope and phase-corrections are applied to the distorted fields received at each telescope. The signal and background photons are scaled according to the achievable *SR* and the smaller detector sizes are employed in the focal-plane. The resultant output signal and background photon counts in PPM slots are modeled as Poisson random variables. The Poisson distributed counts from individual telescopes are sent to the central processor where the data is combined and sufficient statistics are formed for each PPM slot within a symbol. The PSE, PBE, and achievable data rates are evaluated using Eqs. (2.13-2.18). Achievable data rates (after different levels of AO compensation) are compared to the uncompensated data rates.

Figure 7.4 shows the results of AO compensation for the background noise radiance of 175 μW/(cm^2-sr-nm) and a Fired parameter r_o = 4 cm during Earth-Mars conjunction. These values represent the most stressing channel conditions that can occur for an optical communications link between Earth and Mars. Figure 7.4 draws the achievable rates versus different telescopes architectures. Different curves correspond to

different levels of AO corrections, i.e., no correction and corrections achieving SR = 0.30 and 0.75, respectively.

It is shown that the achievable data rates without any correction range between 2.10 Mbits/s and 2.04 Mbits/s, as the array dimensionality is increased from $(1\times10\,\mathrm{m})$ configuration to $(100\times1\mathrm{m})$ configuration. After an AO correction achieving SR = 0.30, an improvement in achievable data rates is observed. Specifically, the data rates range between 8.90 Mbits/s and 5.70 Mbits/s as the number of telescopes is increased from 1 to 100. The achievable data rates are also shown for an AO correction of SR = 0.75. As it was mentioned in Section 7.3, it is very difficult to achieve a SR = 0.75 for telescopes with aperture diameters > 5 m at the communications wavelength of $1.06\,\mu\mathrm{m}$. Hence, the results are shown for smaller telescopes (i.e., $D \le 3.53$ m), which can achieve a SR = 0.75, as shown in Table 7.2. The substantial improvement in the performance of communications systems is evident from these plots. The data rate for the $(8\times3.53\ \mathrm{m})$ configuration increases to 17.50 Mbits/s compared to 2.08 Mbits/s in the uncorrected case. The improvement in the $(100\times1\ \mathrm{m})$ configuration is also evident as the partial AO-based correction results in 14.40 Mbits/s compared to 2.02 Mbits/s in the uncorrected case.

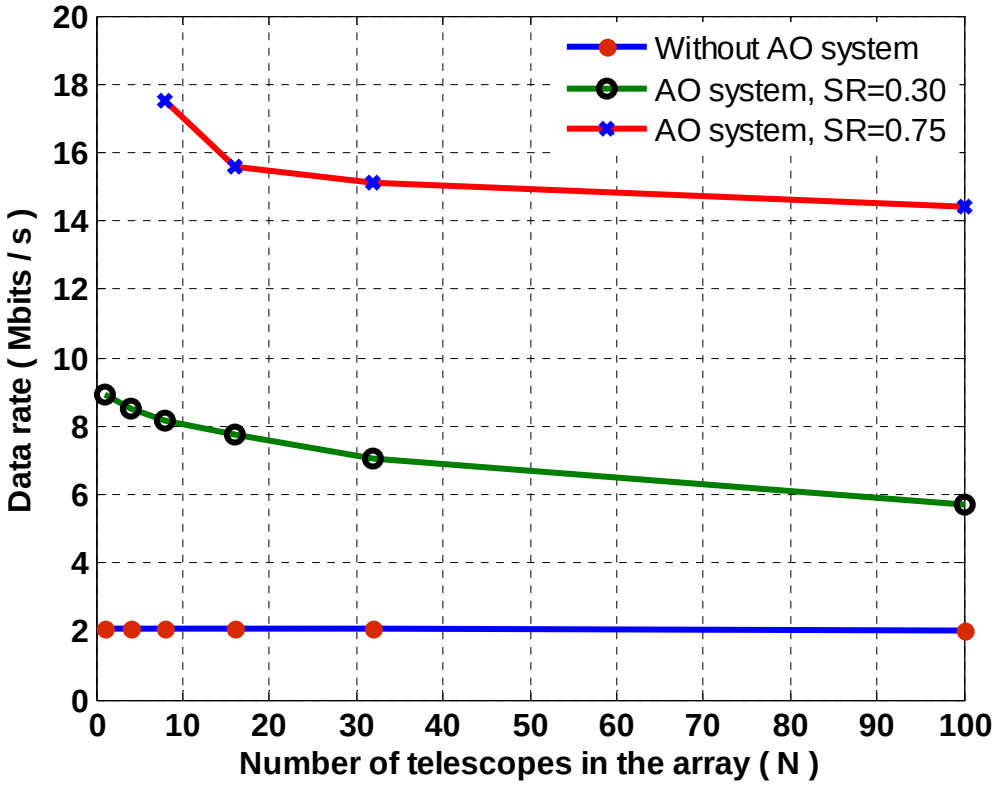

Figure 7.4. Achievable data rates versus the number of telescopes in the array (different array configurations). Different curves correspond to different levels of AO-induced correction. Earth-Mars conjunction phase is assumed with a background radiance of L=175 μW/(cm^2-sr-nm) and the value of Fried parameter $r_o = 4$ cm.

The analysis is repeated for the moderate background noise radiance of 60 μW/(cm^2-sr-nm). The results are shown in Figure 7.5. The achievable data rates without any correction range between 4.70 Mbits/s and 4.60 Mbits/s, as the array dimensionality is increased from (1×10 m) configuration to the (100×1 m) configuration. After AO correction with SR = 0.30, the achievable data rates increase to 9.03 Mbits/s for a single 10 m telescope, and to 7.02 Mbits/s for an array with 100, 1 m telescopes. For an AO correction of SR = 0.75, results are shown for smaller telescopes (i.e., $D \leq 3.53$ m). The substantial performance gains in this case are evident and similar to the ones shown

in Figure 7.4. The achievable data rate for the $(8\times3.53\text{ m})$ configuration increases to 19.62 Mbits/s compared to 4.66 Mbits/s in the uncompensated case. The improvement in $(100\times1\text{ m})$ configuration is also noteworthy as 16.70 Mbits/s is achieved as compared to 4.60 Mbits/s in the uncompensated case.

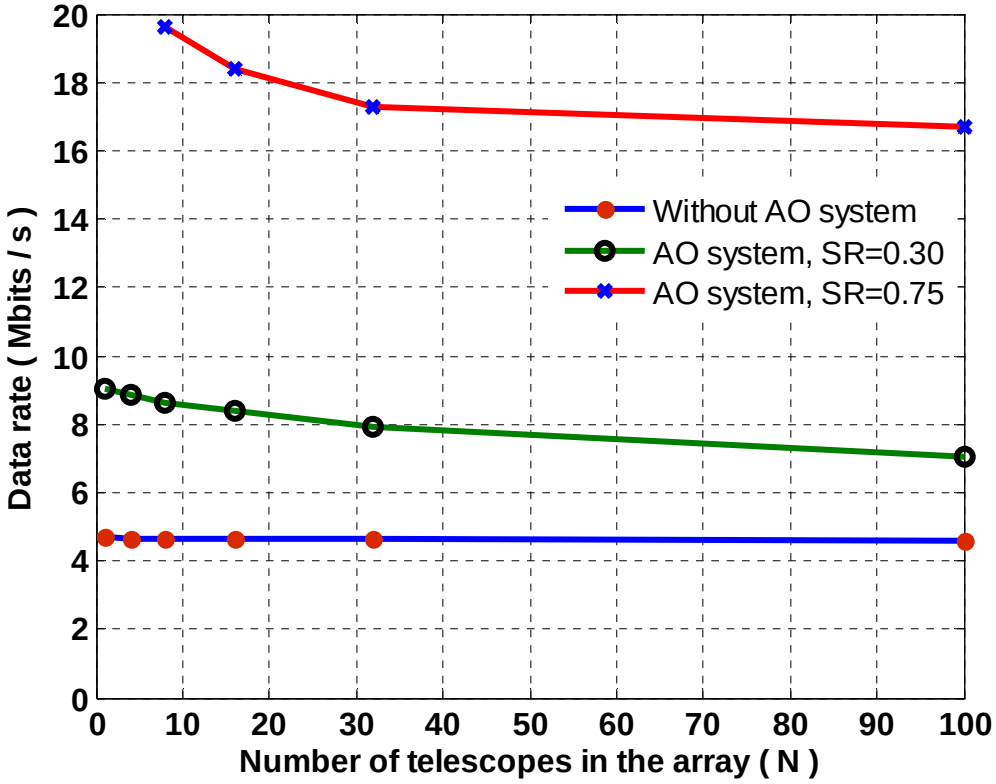

Figure 7.5. Achievable data rates versus the number of telescopes in the array (different array configurations). Different curves correspond to different levels of AO-induced correction. Earth-Mars conjunction phase is assumed with a background radiance of L = 60 μW/(cm^2-sr-nm) and a Fried parameter $r_o = 4$ cm.

The comparison of analysis presented in Figures 7.4 and 7.5 reveals that the improvement in the performance of communication systems is more profound in strong background noise conditions. This phenomenon is logical as the AO-based correction

results in more background noise rejection in extreme background conditions. The performance improvements in achievable data rates in dB for different array architectures and different *SR* values are given in Table 7.3, for extreme and moderate background conditions. It is evident that the performance improvements in array configurations with smaller number of telescopes (larger diameters) are a bit higher. It is because after AO correction, the background noise increases with the number of telescopes in the array.

However, it is also obvious that for an array consisting of up to 100, 1 m telescopes, the difference in performance gains is not very significant (i.e., < 1.45 dB). It is important to mention that the implementation of AO subsystems is easier in smaller telescope, as the *FA* error is low and the required number of deformable mirror actuators is less (Table 7.1 and Table 7.2). Keeping in view the availability of many commercial telescopes with aperture diameters around 1 m, the performance gains presented in this research, and relative ease of AO subsystems implementation in telescopes with this size, (100×1m) configuration seems to be a good choice. However, the actual selection of the array configuration will be driven by specific objectives and confronting constraints.

Table 7.3. AO subsystems-induced performance improvements in achievable data rates (in dB) for different array configurations.

Background radiance μW/(cm^2-sr-nm)	*SR*	1×10 m (dB)	5×4m dB	8×3.53 m dB	16×2.5 m dB	32×1 m dB	100×1 m dB
175	0.3	6.28	6.10	5.90	5.69	5.34	4.47
	0.75	-	-	9.24	8.74	8.67	8.48
60	0.3	2.84	2.78	2.68	2.54	2.33	1.82
	0.75	-	-	6.25	5.96	5.72	5.59

Figure 7.6 emphasizes the performance improvements (in achievable data rates) in dB for the $(100\times1\text{m})$ configuration. The results are drawn for different background noise conditions represented by 175 and 60 μW/(cm^2-sr-nm). For moderate background noise conditions, the performance improvements correspond to 1.82 dB and 5.59 dB for SR = 0.30 and 0.75 respectively. The performance improvements in strong background noise conditions are more significant as 4.47dB and 8.48 dB improvements are achieved with SR = 0.30 and 0.75, respectively.

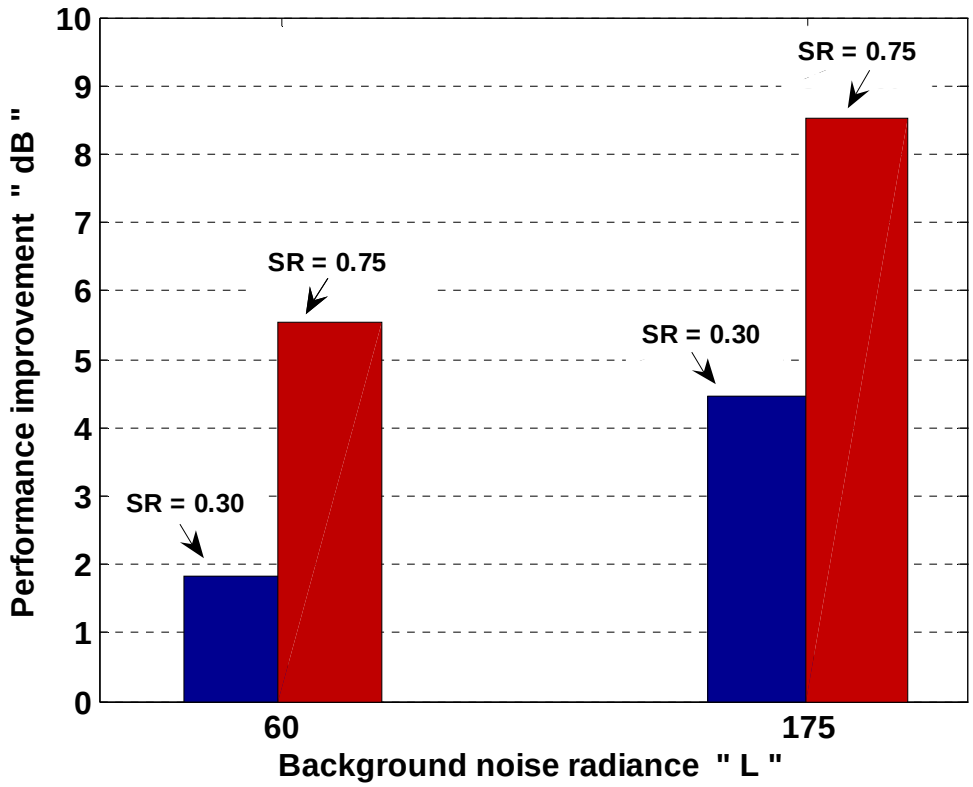

Figure 7.6. AO-induced performance improvements (in achievable data rates) in dB for a telescope array receiver consisting of 100, 1 m telescopes operating in different background conditions. Earth-Mars conjunction phase is assumed with a Fried parameter value of r_o = 4 cm. The background radiance L is in units of μW/(cm^2-sr-nm).

7.6. Discussion of Results

In this part of the research, the main purpose was the analysis and performance evaluation of AO subsystems in telescope array-based receivers for compensation of atmospheric turbulence and background noise effects in a deep-space optical communications link. Atmospheric turbulence and background noise are the major limiting factors in such links. I first simulated the effects of atmospheric turbulence on the received optical fields using Kolmogorov turbulence model. The design of LGS-based AO systems is presented next, which can achieve a SR = 0.30 in telescopes with diameters ranging from 1 m to 10 m in an array. It is also found that achieving a SR = 0.75 seems possible for telescopes with diameters ranging between 1 m and 3.73 m at a communications wavelength of $1.06\,\mu\text{m}$. For larger telescopes (i.e., $D \geq 5$ m), FA-induced effect is the major error source that prevents achieving higher SRs. In this case, the use of multiple laser beacons in each telescope is a solution to achieve a higher SR [69]. However, for the analysis presented in this thesis, we restrict ourselves to the use of a single LGS beacon in each telescope.

The performance of different array architectures is evaluated in terms of achievable data rates. It is shown that the incorporation of AO system results in substantial performance improvement in the communications system throughput. The performance improvements are more profound in strong background noise conditions as a substantial amount of noise is rejected in these circumstances. The deployment of AO systems is easier in smaller telescopes but the number of individual AO systems increases with the number of telescopes in an array receiver. The actual deployment of AO systems at individual telescopes, the complexity of AO systems, and the selection of a particular

array architecture (number and size of the telescopes) will be driven by many constraints. For instance, budget limitations, turbulence and seeing conditions at a specific receiver site, the overall requirements, constraints, and goals of a particular mission will drive a specific design. However, the analysis presented here establishes that performance improvements of many dB are possible by incorporating AO subsystems in telescope array-based receivers operating in deep-space optical communication links.

7.7. Chapter Summary

In this chapter, I analyzed and evaluated the performance of AO subsystems in mitigating the coupled effects of atmospheric turbulence and background noise in telescope array-based receivers operating in a deep-space optical communications link between Earth and Mars. It is shown that in extreme turbulence conditions (i.e., Fried parameter r_o = 4 cm) during Earth-Mars conjunction, a telescope array receiver consisting of 100, 1 m telescopes can achieve data rates of 5.7 Mbits/s after an AO-based correction achieving a *SR* = 0.30. Further, it is shown that 14.40 Mbits/s are achievable with the *SR* = 0.75. During moderate background conditions, the same array configuration can achieve data rates of 7 Mbits/s and 16.7 Mbits/s corresponding to the *SR* = 0.30 and 0.75, respectively. It is also revealed that compared to the uncorrected case in the same architecture, the use of AO systems results in a performance improvement of 8.48 dB for *SR* = 0.75, and 4.47 dB for *SR* = 0.30, in extreme background noise conditions. The performance improvements in moderate background noise conditions are 1.82 dB and 5.59 dB corresponding to *SR* = 0.30 and 0.75, respectively. The performance improvements in other array configurations are also reported and found to be substantial. Hence, the use of AO subsystems is quite effective in mitigating the atmospheric

turbulence and background noise effects that are faced by telescope array-based receivers while operating in deep-space optical communications links.

CHAPTER 8

EXPERIMENTAL EVALUATION OF THE USE OF ADAPTIVE OPTICS SYSTEMS FOR COMPENSATION OF TURBULENCE EFFECTS

In this chapter, I will demonstrate and evaluate the effectiveness of AO systems in mitigating the turbulence-induced wavefront errors. I will give an overview of the experimental setup, the functionality and specifications of each individual component in the AO subsystem, methodology of calculations, and experimental results. It has been established in Chapter 7 that the essence of AO-induced performance improvement in deep-space optical communications link lies in the phase-compensation. The results in this chapter demonstrate that AO systems can effectively compensate the random phase errors and result in the concentration of received energy in much smaller sized PSFs.

8.1. System Description

The schematic of a generic AO system in shown in Figure 8.1. The output of a laser source is distorted by the atmospheric turbulence. The distorted beam is impinged upon a deformable mirror and re-imaged onto a wavefront sensor. The wavefront sensor samples the distorted input beam and measures the local tilts, which are representative of the wavefront distortions. A processor calculates the input wavefront distortions employing the output local tilts of the sensor. A closed-loop feedback controller employs the output of the wavefront sensor to generate the control voltages that are applied to the deformable mirror. The voltages are calculated so as to apply the (distorted) phase

conjugation to the incoming beam. Ideally, the output of an AO system should be a plane wave. However, the system limitations bound the performance away from the ideal. A snapshot of the experimental setup is given in Figure 8.2. Next, I will discuss the functionality of individual subcomponents.

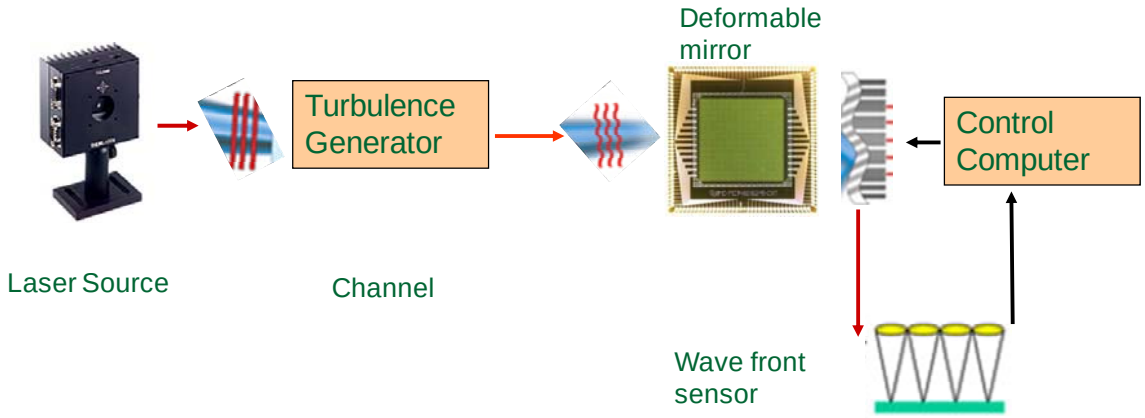

Figure 8.1. Schematic of an AO system.

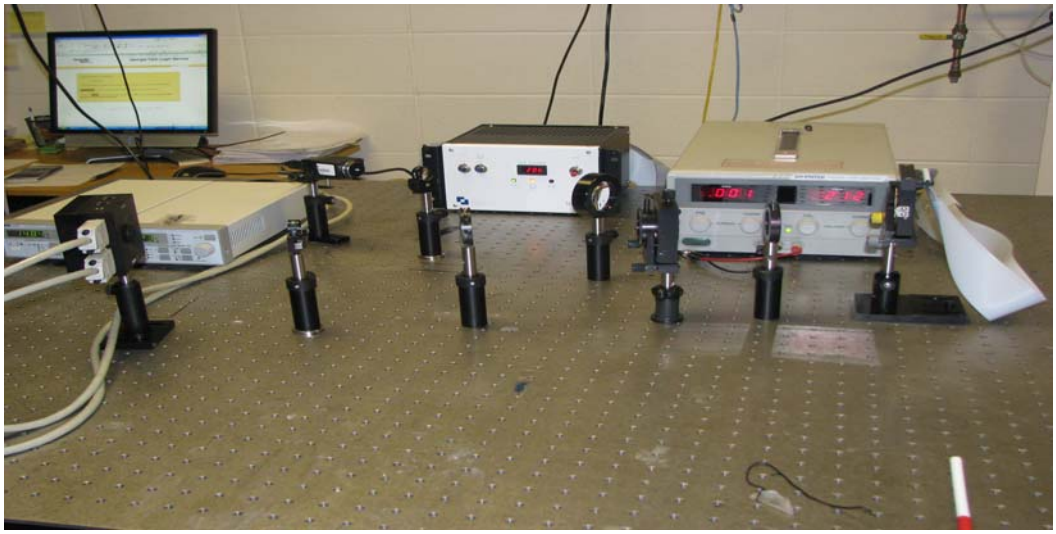

Figure 8.2. Snapshot of AO experimental setup

8.1.1. Wavefront Sensing

For the experimental setup shown in Figure 8.2, a set of laser diodes (L850P010 and L850P030 from the Thorlabs Inc., emitting at 850 nm) was procured. The laser diode is mounted on the TEC-cooled TCLDM9 mount and is controlled using the laser current and temperature controller package (LTC100-B). This control package consists of LDC 205C laser diode controller and TED200C temperature controller. Different type of lenses are used for collimation, alignment, and reimaging the plane of the deformable mirror on the optical conjugate plane of the wavefront sensor. The wavefront of the output beam is distorted by passing it through a distorted phase screen, which simulates the effect of turbulence-induced phase distortions.

Next, the wavefront sensing and reconstruction part is implemented. The wavefront sensor is a Shack-Hartman lenslet array (a hexagonal array of 127 micro-lenses with a focal distance of 15 mm and a pitch of 300 μm, mounted on a C-mount from OKO Tech. [109]), a 0.5 inch digital CMOS camera (model A602f by Basler). The output Hartmangram is captured by the camera and transferred to the PC through a firewire interface. A sample Hartmangram is shown in Figure 8.3. Figure 8.3(a) represents the output of the Shack-Hartman sensor for an ideal plane wave (without any distortion). Figure 8.3 (b) shows the output of an artificially distorted beam. The wavefront sensing code in the PC employs the Hartmangram and measures the individual spot positions to estimate the local wavefront tilts at each lenslet array. The set of wavefront tilts are used for the wavefront reconstruction and for controlling the deformable mirror [109].

In the wavefront construction process the modal reconstruction technique is used [100,101,105]. This technique requires that the wavefront is represented by a series expansion over a system of linearly independent basis functions, and the coefficients of expansion are calculated in terms of this basis (Zernike polynomials). The reconstructed wavefront is then defined continuously throughout the whole aperture of the sensor. The further details about this technique can be found in [45,105]. The coefficients of Zernike polynomials are also employed to calculate the wavefront error variance. We use the following Zernike polynomials for wavefront reconstruction [45,105,109]

$$Z(n,-m) = R_n^m(\rho)Cos(m\theta), \tag{8.1}$$

$$Z(n,m) = R_n^m(\rho)Sin(m\theta), \tag{8.2}$$

where R_n^m are radial polynomials

$$R_n^{\pm m}(\rho) = \sum_{s=0}^{\frac{n-m}{2}} (-1)^s \frac{(n-s)!}{s!\left(\frac{n+m}{2}-s\right)! \times \left(\frac{n-m}{2}-s\right)!} \rho^{n-2s}. \tag{8.3}$$

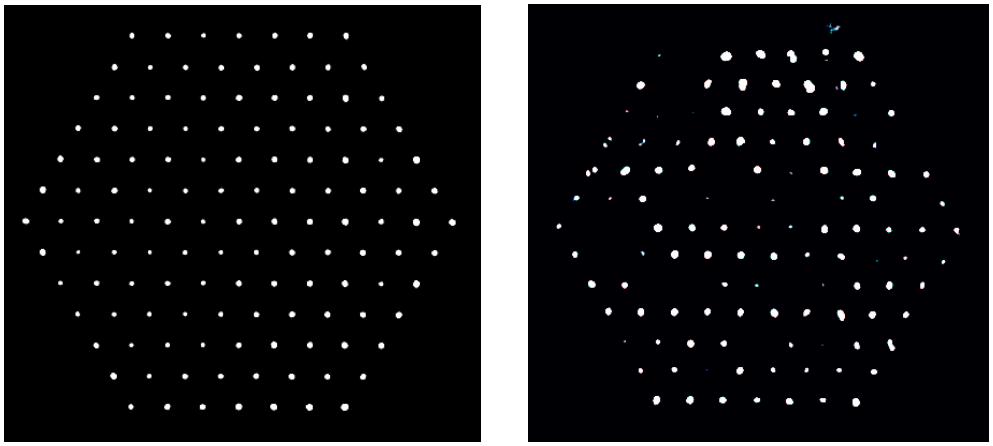

(a) (b)

Figure 8.3. Sample output of Shack-Harman sensor consisting of 127 lenslet arrays. (a) Ideal wavefront, (b) distorted wavefront.

8.1.2. Deformable Mirror

A deformable mirror (μCDM 1.5 μm) was procured from Boston Micromachines Corporation. The silver-coated deformable mirror has 32 actuators and an active area of 1.5 mm. The deformable mirror is connected to the PC through a PCI-based DIO-24 digital acquisition (DAQ) card procured from Measurement Computing (MC) Inc. Mirror control feedback software was developed for the wavefront correction in *C*++ language and integrated to the wavefront sensing system.

The feedback control of the deformable mirror falls in the realm of the multivariate control theory. For a given set of mirror actuator command signals $\mathbf{x}_a$, the effect of the mirror deformation on the reflected wavefront is given by [105]

$$\boldsymbol{\varphi}_m = \mathbf{A}_m \mathbf{x}_a , \tag{8.4}$$

where $\mathbf{A}_m$ is the influence matrix of the mirror, which is measured before the start of the control operations. Conversely, the set of actuator voltages that gives the best least-square fit to a required wavefront correction $\boldsymbol{\varphi}_r$ are given by

$$\mathbf{x}_a = \mathbf{A}_m^{-1} \boldsymbol{\varphi}_r , \tag{8.5}$$

where $\mathbf{A}_m^{-1}$ is the pseudo-inverse of $\mathbf{A}_m$ given by

$$\mathbf{A}_m^{-1} = \mathbf{V}\mathbf{S}^{-1}\mathbf{U}^T , \tag{8.6}$$

where $\mathbf{U}$, $\mathbf{S}$, and $\mathbf{V}$ are the singular value decomposition of $\mathbf{A}_m$ given by [102]

$$\mathbf{A}_m = \mathbf{U}\mathbf{S}\mathbf{V}^T \tag{8.7}$$

The columns of $\mathbf{U}$ and $\mathbf{V}$ make up orthonormal sets of the mirror deformation and can be thought of spatial modes of the system. The values of the diagonal matrix $\mathbf{S}$ are the

singular values and represent the gains of the modes and the controllability of the mirror. The singular values and SVD decomposition is performed before the start of the feedback operations. The measured singular values of the deformable mirror corresponding to the 32 actuators are given in Figure 8.4.

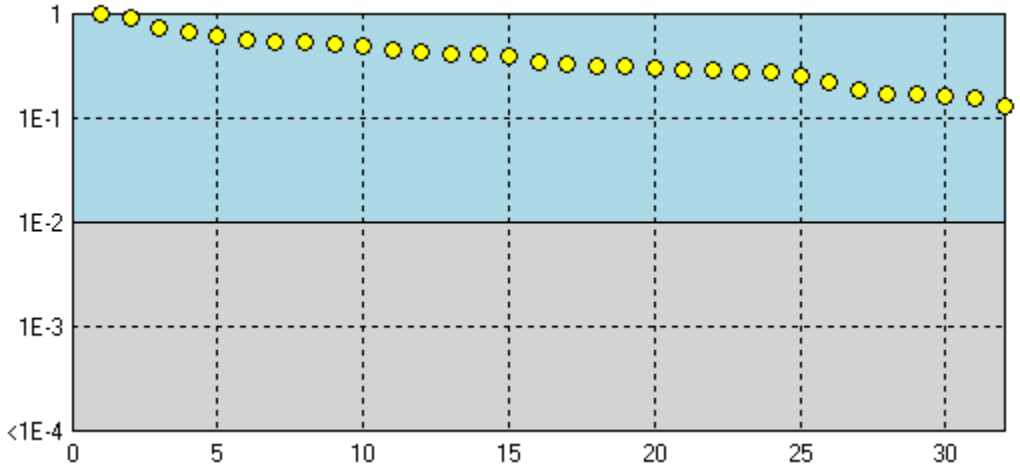

Figure 8.4. Singular values of the influence matrix of the deformable mirror.

8.2. AO System Operations

In the feedback loop operation mode, a set of measured influence functions of the mirror is employed for the fitting of the desired phase aberration. If the residual aberration $\boldsymbol{\varphi}_r[n]$ at the *n-th* iteration corresponds to the set of actuator signals $\mathbf{x}_a[n]$, then the signals at the next step $\mathbf{x}_a[n+1]$ are determined by the expression

$$\mathbf{x}_a[n+1] = \mathbf{x}_a[n] - \mathbf{g}\,\mathbf{A}_m^{-1}\,\boldsymbol{\varphi}_r[n] \tag{8.8}$$

where $\mathbf{A}_m^{-1}$ is the pseudo-inverse given in Eq. (8.6) and $\mathbf{g}$ is the feed-back parameter that can be adjusted.

8.3. Experimental Results

The experimental setup as explained previous sections is employed to test the efficiency of AO system. In this section, I will explain some of the experimental results. Specifically, I will report the following four results: the ideal wavefront; wavefront distortion equivalent to a Fried parameter of 4 cm; AO-induced partial compensation achieving a SR of 0.30; and AO-induced partial compensation achieving a SR of 0.75.

Figure 8.5 shows the case of an ideal wavefront (in the absence of any wavefront distortion). Figure 8.5(a) shows the reconstructed wavefront profile in the sensor aperture plane and the PSF in the focal plane is shown in Figure 8.5 (b). It is evident from both the figures that the wavefront profile is (almost) an ideal plane wave. Some little distortions are observed due to imperfections in the imaging optics (that would be present in most of the systems). The PSF in this case is also equivalent to the Airy pattern. The local tilts (measured from wavefront sensor) are decomposed over the Zernike polynomials and the total wavefront variance is calculated after summing the Zernike coefficients. The wavefront error variance in this case is calculated to be just ($0.025\,rad^2$) corresponding to a *SR* of 0.976. It is obvious that a small size detector can be placed in the focal plane to capture almost all of the focused optical energy. In a deep-space optical communications link, this will correspond to the case of a diffraction-limited system in the absence of atmospheric turbulence.

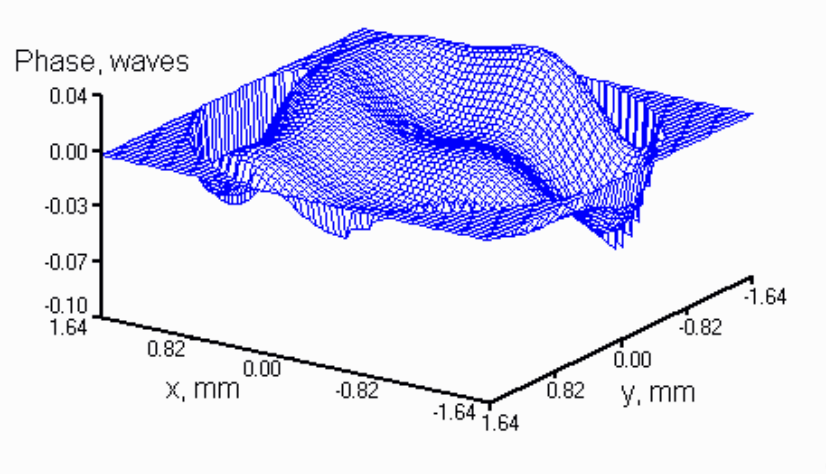

(a)

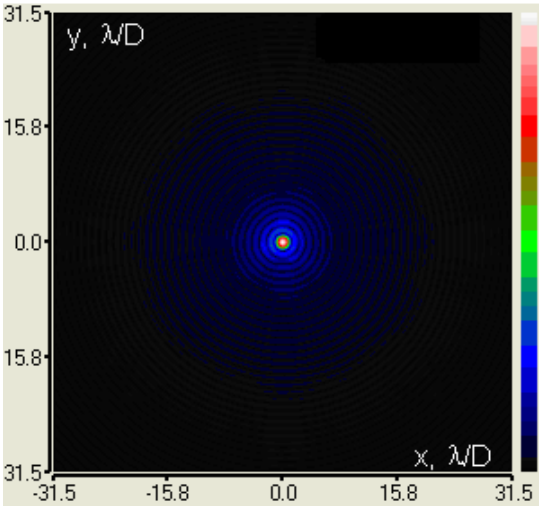

(b)

Figure 8.5. Ideal wavefront (without any distortion). (a) Aperture plane wavefront profile, (b) PSF in the focal plane.

Figure 8.6 shows the case of a distorted wavefront (in the absence of any AO correction). Figure 8.6(a) shows the reconstructed wavefront profile in the aperture plane and the PSF in the focal plane is shown in Figure 8.6 (b). It is evident that the wavefront is highly distorted and the PSF is spread over a much wider area (almost 50 times larger than the ideal case) in the focal plane. Based upon the wavefront spread, this distortion corresponds to a Fried parameter of $r_o = 4$ cm, which represents the worst-case turbulence conditions. To capture this widespread energy in an actual deep-space operation, a large

detector area (FOV) would be required. The use of a large FOV will result in a substantial increase in the background noise. The wavefront error variance in this case is calculated to be 2.40 rad^2, corresponding to a *SR* of about 0.091.

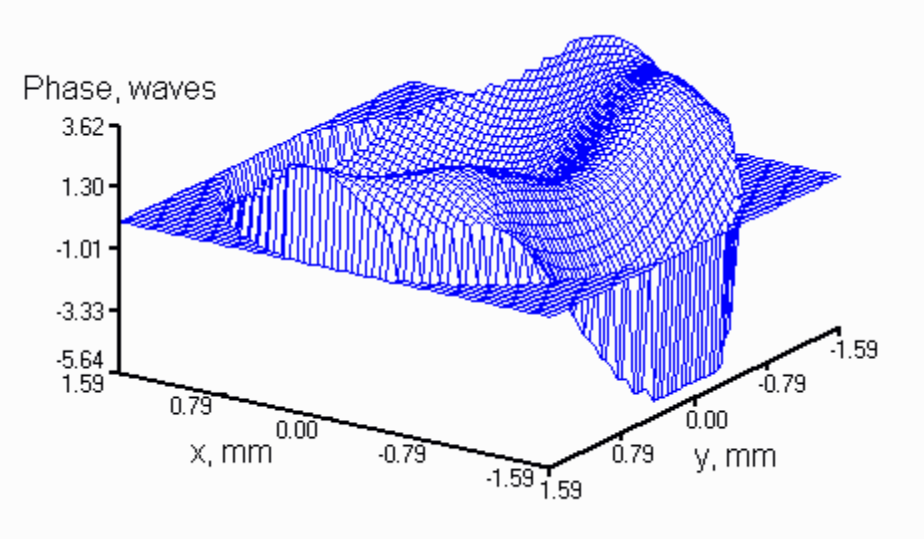

(a)

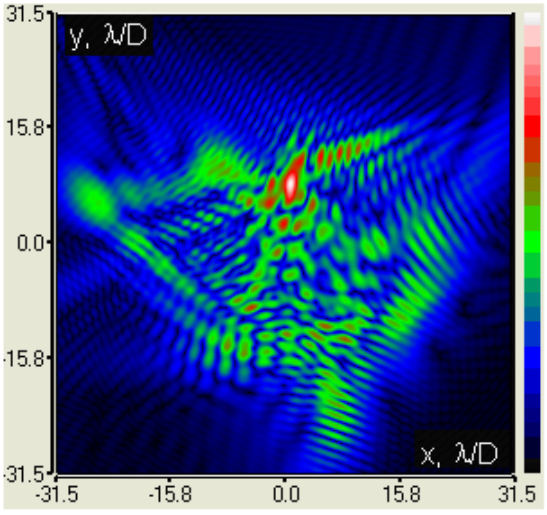

(b)

Figure 8.6. Wavefront in strong turbulence conditions (without AO compensation). (a) Aperture plane wavefront profile, (b) PSF in the focal plane.

Figure 8.7 shows the case of a partial AO-based compensation (of the distortion in Figure 8.6) achieving a residual wavefront error variance of $1.14\,rad^2$, which corresponds to a *SR* of 0.32. Figure 8.7(a) shows the reconstructed wavefront profile in the aperture plane and the PSF in the focal plane is shown in Figure 8.7(b). It is evident that after the partial AO-induced compensation, the wavefront profile has improved and more energy is (about 30 %) concentrated in the central portion (equivalent to the Airy disc) of the PSF. As explained in Chapter 7, by employing a smaller detector in this case, more than 95 % of the background noise can be rejected. This phenomenon improves the overall performance of an optical communications system.

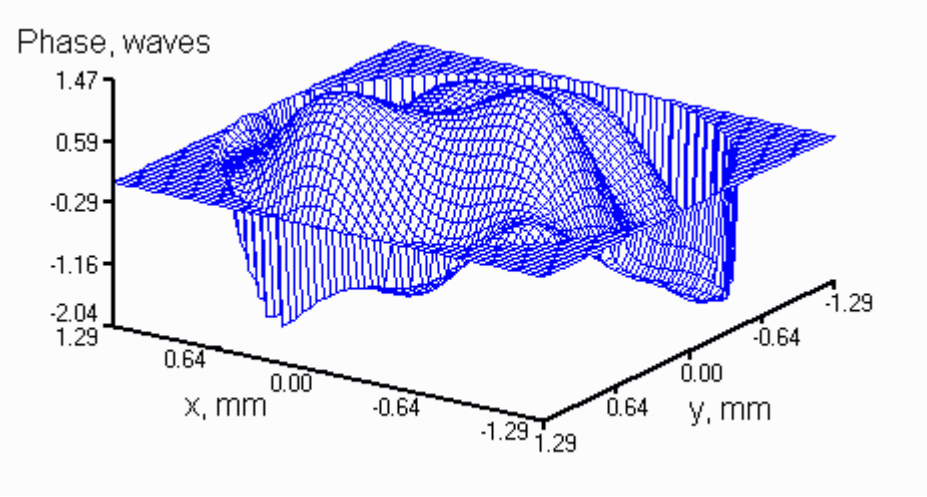

(a)

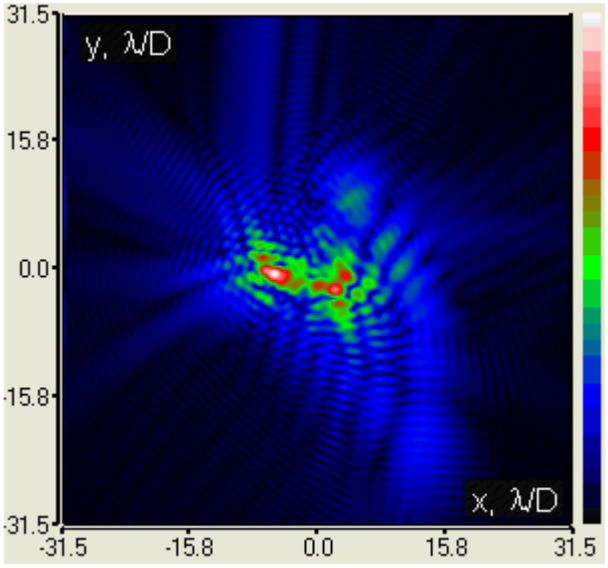

(b)

Figure 8.7. Wavefront in strong turbulence conditions (after AO compensation achieving a *SR* = 0.30). (a) Aperture plane wavefront profile, (b) PSF in the focal plane.

Figure 8.8 shows the case of an almost perfect AO compensation (of the distortion in Figure 8.6) achieving a residual wavefront error variance of $0.29\,rad^2$, which correspond to a *SR* of 0.75. Figure 8.7(a) shows the reconstructed wavefront profile in the aperture plane and the PSF in the focal plane is shown in Figure 8.7 (b). It is evident that after partial AO-based compensation, the wavefront profile has improved a lot and almost 75 % of the energy concentrated in the central portion (equivalent to airy disc) of the PSF. By employing a small detector size in this case, more than 95 % of the background noise can be rejected while the loss in signal energy is just 25 %. This phenomenon will drastically improve the overall performance of an optical communications system.

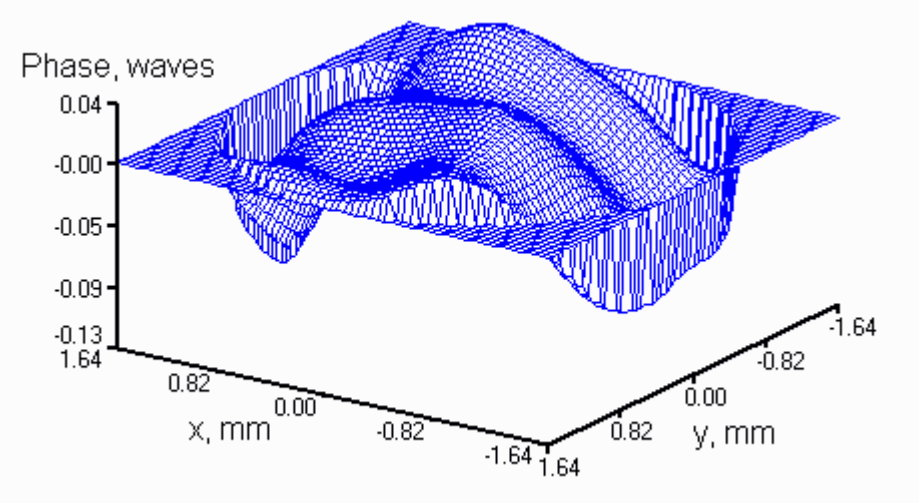

(a)

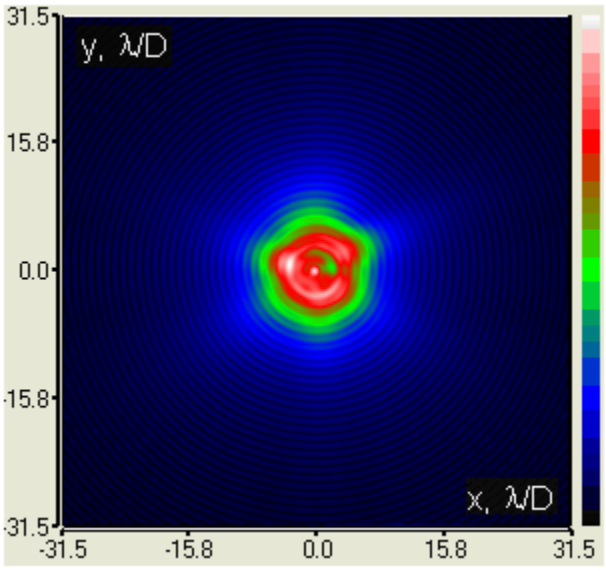

(b)

Figure 8.8. Wavefront in strong turbulence conditions (after AO compensation achieving a *SR* = 0.80). (a) Aperture plane wavefront profile, (b) PSF in the focal plane.

8.4. Chapter Summary

In the research outlined in this chapter, experimental implementation of an AO system is explained. This economical system can be thought of as an abridged version of the more sophisticated AO systems designed for large telescopes arrays as delineated in Chapter 7. However, the experimental setup was capable enough to demonstrate and substantiate the AO-induced performance improvements as simulated in Chapter 7.

CHAPTER 9

DESIGN OF A NOVEL SPACE-TIME ADAPTIVE PROCESSOR (STAP) FOR MITIGATION OF ATMOSPHERIC TURBULENCE EFFECTS

As emphasized in previous chapters, atmospheric turbulence along with the background noise is a major limiting factor in a typical deep-space optical communications link. In this chapter, I design and develop a novel space-time adaptive processor (STAP), which employs 2D adaptive filters-based practical algorithms for the mitigation of turbulence and background noise effects. In this design concept, a photon-counting focal plane detector array (FPA) is employed at the receiver and the STAP processes the output of the FPA before decoding operations. It is shown through simulations that for photon-counting receivers observing Poisson statistics, performance improvements of 4-7 dB can be achieved under adverse channel conditions. This performance improvement is not only significant but the implementation of the processor is also cost effective and practical.

9.1. Motivation and Statement of the Problem

I presented the design of AO systems in Chapters 7 and 8 as a solution to the problems of atmospheric turbulence and background noise, which are faced by a deep-space optical receiver. It was also shown in these chapters that the incorporation of AO systems results in a substantial improvement in the performance of an optical receiver. AO systems are based on the active optics technology (i.e., deformable mirrors,

wavefront sensors etc.). In literature, another suggested solution to the problem of the turbulence in optical receivers is based on the use of adaptive detector arrays (focal plane arrays) together with signal processing algorithms [77]. It is reported in Ref. [77] that by employing the photon-counting detector arrays, a performance improvement of nearly 5 dB is possible. However, the signal processing algorithms developed in Ref. [77] needs an instantaneous estimation of the number of signal and background photon at each detector element of the FPA, and it was assumed that signal and background intensities at each detector elements are known a priori. The instantaneous estimation of signal intensities in a time-varying environment is a difficult task and can be inaccurate, which can degrade the performance of the processing algorithm in Ref. [77].

In this chapter, I present the design of a novel STAP processor for processing the output counts of focal plane arrays. The processor does not need an estimation of the number of signal and background photons. The turbulence-degraded signals are generated in the aperture plane of an optical receiver using Kolmogorov statistics (Eq. 7.1). The incoming optical signals and in-band background noise are focused by the receiving telescope aperture onto photon-counting focal plane detector arrays. The output of the FPA is processed by the STAP and processed counts are then sent to the decoder assembly for data decoding purposes. It is important to mention that in a typical optical deep space communications link, the main challenge is the diffused sunlight from the sky background during the daytime when the optical turbulence is also at its peak. The designed processor exploits the fact that the average background radiation intensity have a uniform distribution over the focal plane detector array, whereas the focal plane signal intensity distributions are dominated by the turbulence effects. Hence, the signal

component of the incoming field has high spatial frequency contents on the focal plane array as compared to a near uniform (DC) level of the additive background noise. The processor employs adaptive algorithms to dynamically scan the focal plane array; suppress the intensity fluctuation, detector noise, and near-uniform background noise fields; and extract the embedded random signal fields. Simulation results are presented for the pulse-position modulation (PPM) scheme and direct-detection receivers. A Poisson probability model is used for the calculation of the received signal and background photon counts in the receiver. Analysis of probability of bit error (PBE) shows that for high background noise conditions, performance improvements of 6.6 dB are achieved at the probability of error (PBE) of 0.01. Improvements of more than 7 dB are also achieved at lower bit error rates. The algorithm developed here is not only practical but also makes no assumptions about the a-priori knowledge of the signal and background intensities. However, it is also important to mention that the STAP processor developed here is more effective in mitigating the background noise emanating from an extended source (compared to receiver FOV). For example, the diffused sunlight from the sky during daytime. The strong background noise from these kinds of sources appears as a flat (near uniform) distribution on FPA, and STAP processor exploits this fact. For the background noise emanating from point sources (e.g., planets and stars) at night, the STAP processor is not very effective. Nevertheless, the major limiting factor in a deep-space optical communications link is during daytime when atmospheric turbulence is also very high. During nighttime, the sources of background noise are not that strong and strength of atmospheric turbulence is also low. Hence, the STAP processor is very useful for mitigating a major limiting factor during daytime operations.

9.2. Optical Field Expansions

In a typical Earth-Space optical link, the turbulence distorted incoming fields can be treated as stochastic fields; the incoming optical fields consist of the sum of a randomly distributed optical signal component that is broken up by the atmospheric turbulence, and the diffused background light originated from the sky during daytime, and stars and planets during nighttime. Let the general received optical field be represented by

$$f_r(t,\vec{r}) = f_s(t,\vec{r}) + f_b(t,\vec{r}), \tag{9.1}$$

where $f_s(t,\vec{r})$ is the random optical signal component and $f_b(t,\vec{r})$ is the additive background noise; $\vec{r}$ is the spatial vector in the receiver aperture plane. In communications systems analysis, it is suitable to expand the incoming random signals into different modes. Using the spatial orthogonal expansions, the incoming optical fields can be expressed as [17]

$$f_r(t,\vec{r}) = \sum_{i=1}^{\infty} a_i(t)\, \exp(j\omega_o t)\ \mathbf{\Phi}_i(\vec{r}), \tag{9.2}$$

where the component functions $\{a_i(t)\}$ are the random time processes, ω_o is the optical radian frequency of the transmitter, and $\{\mathbf{\Phi}_i(\vec{r})\}$ are a set of complex two-dimensional orthogonal spatial basis functions defined over the collecting aperture or in the focal plane. $\{a_i(t)\}$ are given by

$$a_i(t) = \frac{\int_A a(t,\vec{r})\ .\ \Phi_i^*(\vec{r})\ d\vec{r}}{\int_A \left|\Phi_i^*(\vec{r})\right|^2 d\vec{r}}. \tag{9.3}$$

Eq. (9.2) represents a stochastic field whose spatial mode functions have a random time envelope variations imposed on them. The convergence of sum in Eq. (9.2) is in the mean square sense. If the random field is Gaussian and uncorrelated, then $\{a_i(t)\}$ are independent processes and the field is said to have independent random modes. When the spatial basis functions $\{\mathbf{\Phi}_i(\vec{r})\}$ are selected as constant amplitude plane waves arriving from directions $\vec{z}_i$, corresponding to a set of arrival angles properly spaced over an aperture area *A*, as given below [17]

$$\mathbf{\Phi}_i(\vec{r}) = \exp\left(-j(z_i . \vec{r})\right) \quad , \quad \vec{r}\,\varepsilon\, A \tag{9.4}$$

then the expansion in Eq. (9.2) corresponds to the plane wave expansion given as

$$f_r(t,\vec{r}) = \sum_{i=1}^{\infty} a_i(t)\, \exp\left(j(\omega_o t)\right) \exp\left(-j(z_i . \vec{r})\right) \tag{9.5}$$

As each off-normal arriving plane wave transforms to a shifted Airy pattern, the resulting focal plane expansion of the diffracted field corresponds to separated Airy patterns over the focal plane. This permits us to consider the stochastic focused field as a set of time-varying Airy patterns distributed over the focal plane [17]. Each Airy pattern mode has a time varying signal energy component and a near uniform background noise component (in strong background noise conditions such as diffused background light from sky during daytime). This model is employed in the design of the STAP processor.

9.3. Space-Time Adaptive Processor (STAP)

The block diagram of the decoding scheme at the optical receiver employing the FPAs and adaptive filters based-STAP is given in Figure 9.1. The incoming optical fields impinge upon the receiving aperture, which focuses the optical fields onto the focal

plane. Photons counting FPAs are used instead of one large detector element for detection purposes. The size of each detector is chosen to be equivalent to the diffraction-limited spot size. The incident fields are modeled using the Kolmogorov spectrum and expanded into different random modes using the plane wave expansions given in Section 9.2. Each mode (detector) receives a random portion of the transmitted optical intensity and (almost) constant background average intensity from the diffused skylight. The outputs of the photon-counting detector elements have a Poisson distribution. The output photon counts are fed to the STAP that filters out the near uniform (spatial) background noise and extracts the random signal counts. The processed data is sent to the data decoder where photon counts are summed in each PPM slot to form the decision statistics.

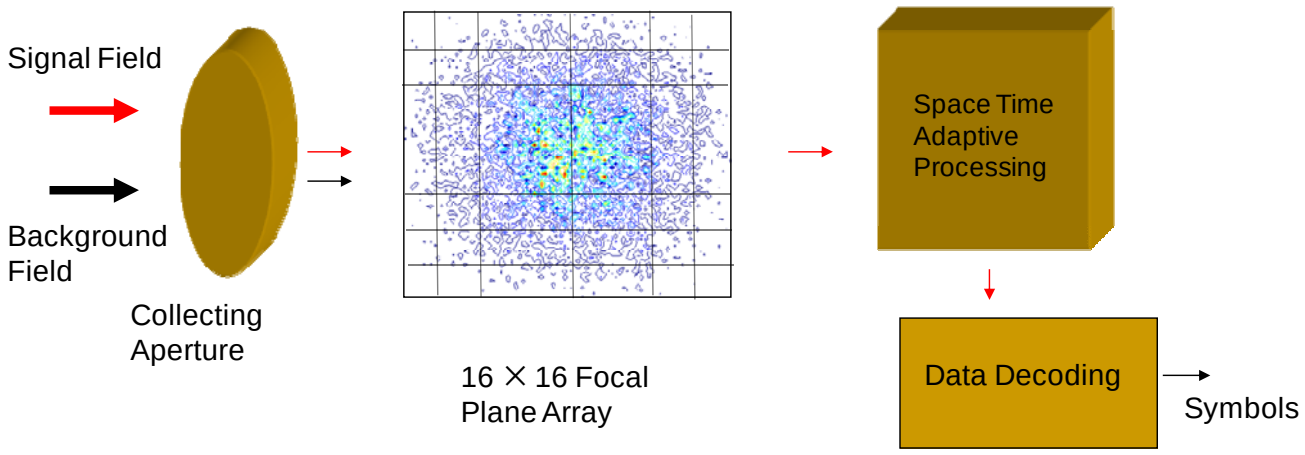

Figure 9.1. Conceptual diagram of focal plane array-based Space-Time Adaptive Processor (STAP) for an optical communications receiver.

9.3.1. Principle of Operations

The principle of operation of the STAP is as follows. In a transmitter employing *M-ary* pulse position modulation (PPM) technique, digital data is encoded by the position

of a pulse slot within a frame of *M* possible slots. In the optical PPM, a single optical pulse is transmitted as the carrier in the desired slot in each frame. After the reception at the receiving optics, the temporal modulated PPM signal is transformed into a space-time intensity random distribution in the detector plane. The output counts of the detector array are randomly distributed in the space-time domain. Hence, the processor processing this distribution is termed as the space-time adaptive processor (STAP). As the temporal bandwidth of the turbulence (few *milli*-seconds) is small as compared to a typical PPM slot width (*nano*-seconds), the distribution of the input optical signals remains constant during a PPM slot. During a non-signal slot within a PPM frame, the input fields consist of the background noise only. According to the previously discussed model in section 9.2, the resultant intensity distribution is (almost) spatially uniform on the focal plane array, as the background noise originates from an extended source (the sky) compared to the receiver's field of view. In case of an optical signal slot, the incoming field intensity consists of the randomly distributed signal modes due to atmospheric turbulence plus uniform background intensity in each mode. Hence, in the 2D spatial Fourier domain of the FPA output counts, the non-signal slot spatial spectrum is a near DC output. Whereas, for the signal slot, the background noise is concentrated at the near zero frequency, and the transmitted signal has both the low and high frequency contents depending upon the distortions induced by the turbulence. A simple 2D high pass filter could ideally suppress the DC background in both the signal and non-signal slot, and pass the signal counts in the pulse slot. However, the presence of intensity fluctuations and detector noise induce deviations from the ideal operation. To mitigate these effects, a 2D adaptive Wiener filter is employed in the STAP. This filter applies a rectangle window on the 2D input data,

which scans through the focal plane 2D outputs to estimate and suppress different noise sources. The output of the 2D adaptive Wiener filter is further processed through a 2D high-pass filter to suppress the background noise. The internal block diagram of STAP is given in Figure 9.2.

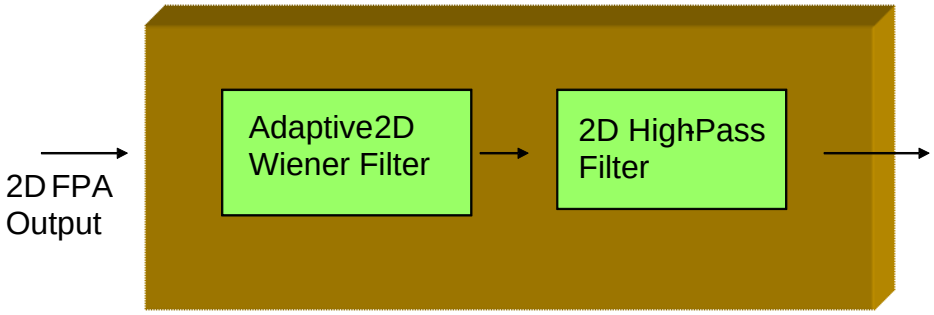

Figure 9.2. Internal block diagram of the STAP processor. 2D adaptive Wiener filter followed by a 2D HPF.

9.3.2. Design of Adaptive Filters for Background Noise Suppression

The core of the designed space-time adaptive processor (STAP) consists of an adaptive 2D Wiener filter followed by a 2D high-pass filter. In adaptive filters theory, Wiener filtering is one of the robust approaches in solving problems in which a signal is degraded by the additive noise [92]. In our case, 2D Wiener filter is designed to process the received signal distribution that is degraded by different noise sources (i.e., additive background noise, detector noise, intensity fluctuations). The input to the Wiener filter is a two-dimensional array of FPA output counts $c(n_1, n_2)$, where (n_1, n_2) represent the spatial dimensions in the detector plane. During the *i-th* slot in a PPM frame, The adaptive Wiener filter uses a $(N \times M)$ 2D window around each detector (pixel) $(n_1 \times n_2)$ element to estimate the local mean and variance as follows [107]:

$$\mu^{i}(n_1,n_2)=\frac{1}{N\times M}\sum_{n_1,n_2\,\varepsilon\,D} c^{i}(n_1,n_2). \tag{9.6}$$

$$\sigma^{2\,(i)}(n_1,n_2)=\frac{1}{N\times M}\sum_{n_1,n_2\,\varepsilon\,D} c^{2(i)}(n_1,n_2)-\mu^{i}(n_1,n_2). \tag{9.7}$$

The coefficients of the space-variant 2D Wiener filter are determined by using the estimates in Eqs. (9.6) and (9.7) as [107]

$$\mathrm{W}^{i}(n_1,n_2)=\mu^{i}(n_1,n_2)+\left[\frac{\sigma^{2(i)}(n_1,n_2)-\upsilon^{2\,(i)}}{\sigma^{2(i)}(n_1,n_2)}\times\left(c^{i}(n_1,n_2)-\mu^{i}(n_1,n_2)\right)\right], \tag{9.8}$$

where $\upsilon^{2(i)}$ is the average of all the local estimated variances (i.e., $\sigma^{2(i)}(n_1,n_2)$). The output of the filter is given by

$$p^{i}(n_1,n_2)=\mathrm{W}^{i}(n_1,n_2)\ **\ c^{i}(n_1,n_2), \tag{9.9}$$

where $(**)$ is the 2D convolution operator. The block diagram of the Wiener filter operations is given in Figure 9.3.

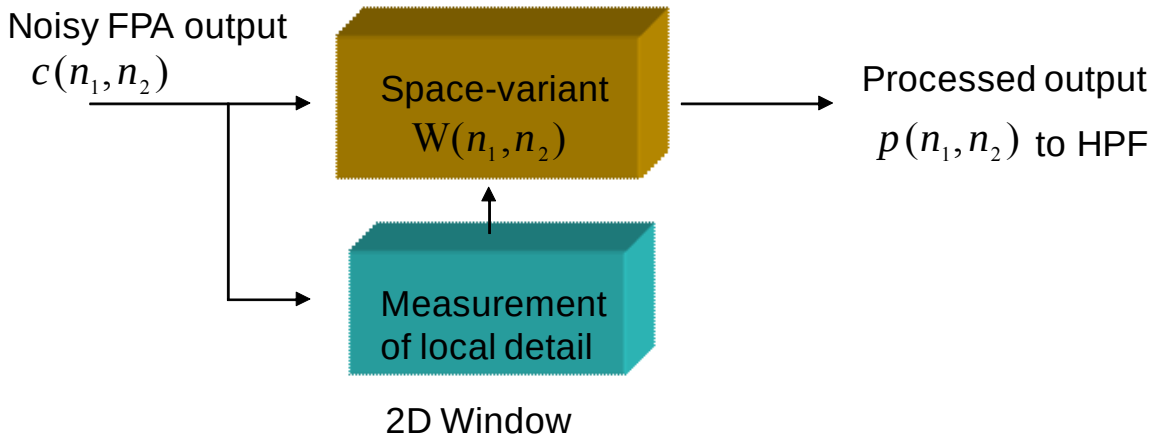

Figure 9.3. Functional block diagram of the adaptive 2D Wiener filter in the STAP processor.

The output of the adaptive Wiener filter is high-pass filtered to suppress the uniform background noise and extract the signal portion. It is important to mention that some portion of the signal is also suppressed in this way, but as the noise suppression is dominant, hence, overall signal to background count increases considerably as shown in the simulation results presented in the next section. The impulse response representation of a 2D HPF that is designed and used in the simulations is given in Figure 9.4. The spatial frequency response of the HPF is given in Figure 9.5.

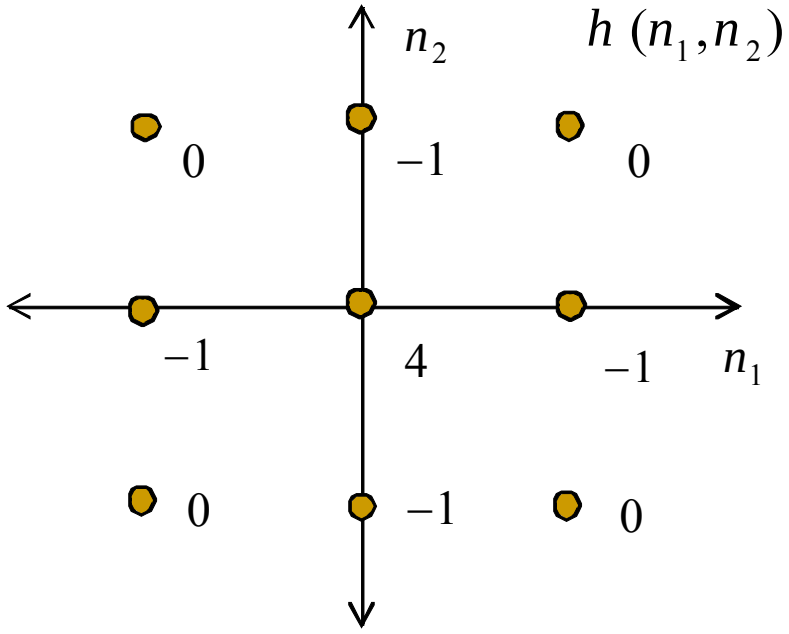

Figure 9.4. Impulse response of the 2D high-pass filter (HPF).

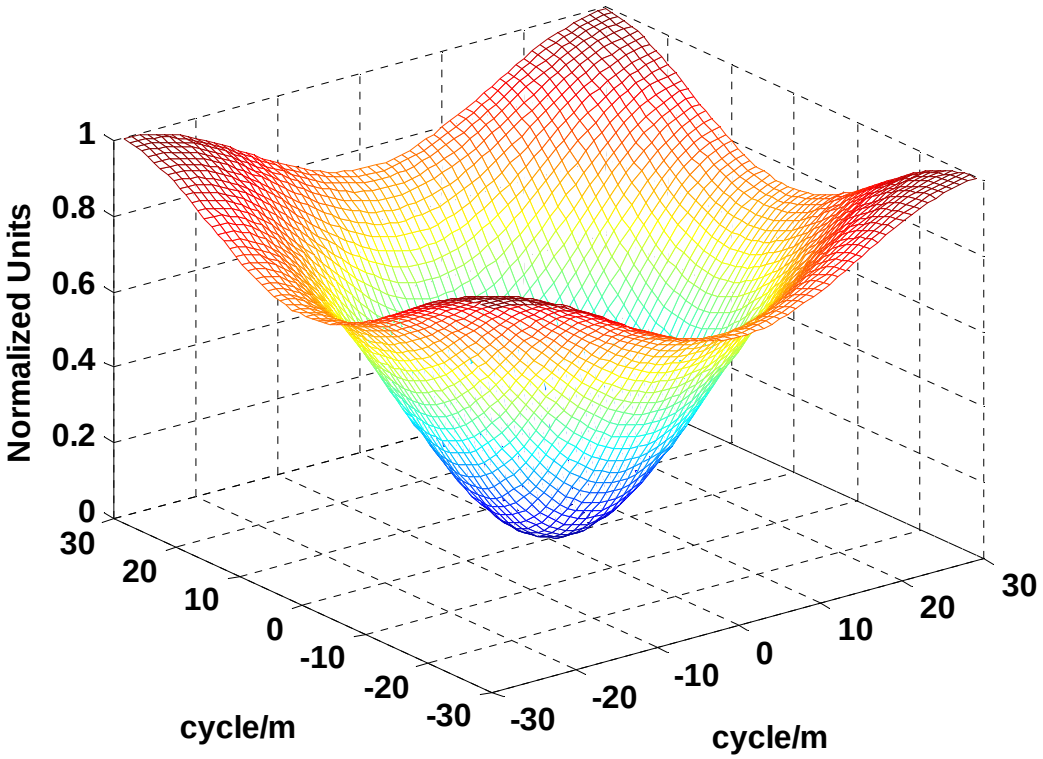

Figure 9.5. Frequency response of the 2D high-pass filter (HPF).

The final relationship between the input and the output of the STAP processor for the *i-th* PPM slot can be stipulated as

$$y^i(n_1,n_2) = h(n_1,n_2) ** \left[\mathrm{W}^i(n_1,n_2) ** c^i(n_1,n_2) \right]. \tag{9.10}$$

Slot-statistics in each PPM frame are formed by summing the output of all the individual detector elements in FPA and decoding is performed by selecting the slot containing the largest count. i.e., $\mathbf{max}\left(Y(iT_s)\right)$, where

$$Y(iT_s) = \sum_{i=1}^{L} y^i(n_1,n_2). \tag{9.11}$$

9.4. Simulation Results

In this section, I will present the Monte-Carlo simulations carried out using the STAP processor. The performance of the complete receiver is evaluated by calculating the probability of bit error (PBE) versus the total number of incoming signal photons in the presence of background noise sources. PPM modulation format is used with $M = 2$. The turbulence degraded intensity distributions are generated using the Kolmogorov spectrum in both the aperture and focal planes. A telescope aperture diameter of 1 m and a Fried parameter of 4 cm (strong turbulence conditions) are assumed. The total number of received signal photons are scaled according to the random (turbulence-induced) distributions and then detected by the individual detector elements in the focal plane array. The size of each detector element is made (approximately) equal to the diffraction limited spot size. I use a 16×16 focal plane array consisting of 256 detector elements to encompass the complete signal distribution. Hence, each detector element receives a (near) diffraction-limited mode, which contains both the random signal and background distributions. The output counts of the individual detector elements are modeled as the Poisson random variables. The output counts of each PPM slot are then processed by the STAP processor and then sent to the decoder assembly (according to methodology explained in Section 9.3). The decoder forms the decision statistics for each PPM slot and then selects the symbol corresponding to the greatest slot count. The PSE is the probability that any one of non-signal slots photon count exceeds the signal slot count.

Monte-Carlo simulations are run for 1 million symbols each and the performance is evaluated for two different background scenarios. These cases represent the moderate and high background values of $K_b = 0.1$ and 1 photons/detector/PPM slot corresponding

to 25.6 and 256 total background photons/slot received at the receiver. These specific values are chosen to compare the performance of the STAP processor to the previously reported results in Ref. [77] in similar conditions. Probability of symbol error (PSE) and probability of bit error (PBE) are evaluated after averaging over 1 million symbols. The calculated PBE versus the number of received signal photons and simulation results for K_b = 0.1 photons/detector/PPM slot are given in Figure 9.6. The performance of the STAP processor is compared to three other cases. First, when the turbulence is absent (ideal case) and the incoming fields are in the form of a plane wave. This condition is equivalent to the reception of a single diffraction-limited mode. Second case represents the use of a large single detector in the presence of the turbulence for collection of all the signal energy distributed in different random modes (the un-compensated case). Previously reported performance results in Ref [77] are also simulated and shown in the figure. It is obvious from Figure 9.6 that the STAP process performs much better than the un-compensated case and the previously reported results. Specifically, a performance gain of ($\times 2.22$) is achieved corresponding to a 3.47 dB improvement at the PBE of $1\times e^{-2}$. It is also shown that the STAP processor achieves a substantial 4.25 dB performance improvement at the PBE of $1\times e^{-5}$. A Fried parameter value of r_o = 4 cm is employed in these simulations. The PBE presented in these results is the un-coded PBE.

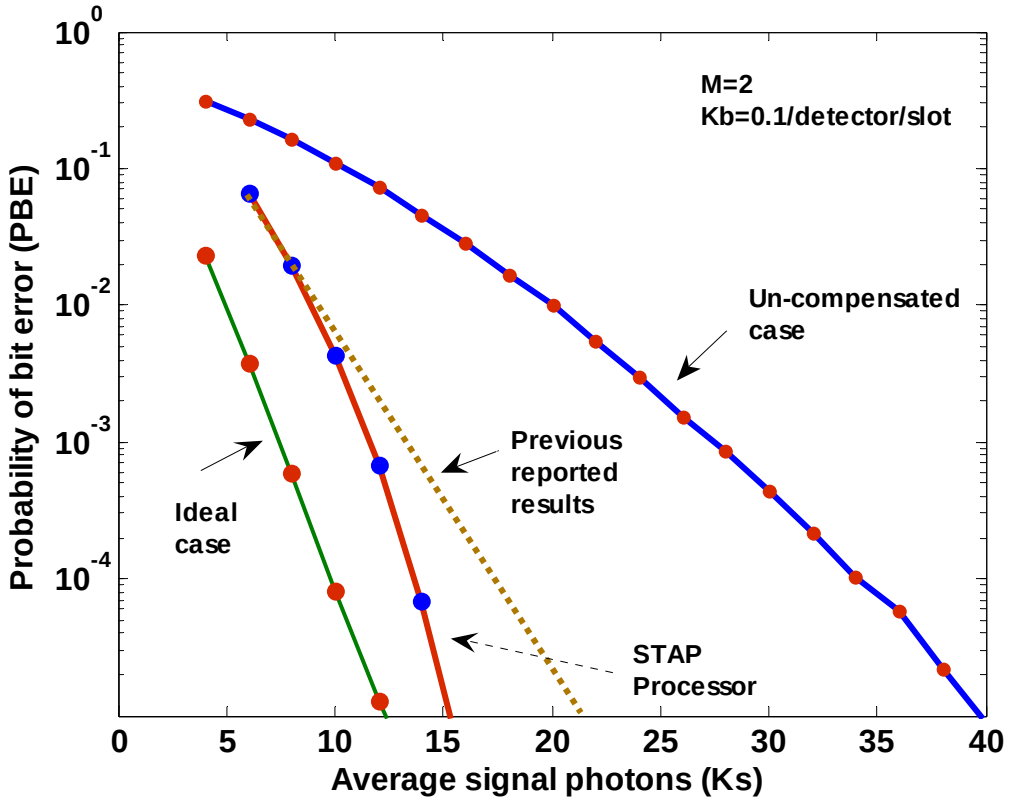

Figure 9.6. PBE vs. the number of input signal photons. Different curves correspond to the un-compensated case, STAP processor, and an ideal case. The performance of previous reported results are also shown for comparison purposes. The background noise is K_b = 0.1/detector/slot and M =2. The performance gains by the STAP processor are evident.

Next, the simulations are repeated for a strong background noise condition represented by the K_b = 1 photon/detector/PPM slot and the results are depicted in Figure 9.7. It is evident that the performance gain of (×4.58), i.e., 6.3 dB is achieved at the PBE of $1\times e^{-2}$. The performance gains in excess of 7 dB are achieved at the PBE of $1\times e^{-5}$. It is evident that performance gains by the STAP processor are more profound in the strong background noise case. This is because in the high background environment, a large amount of background noise is filtered out by the processor and performance gains

are substantial. It is also evident that the STAP processor performs much better than the un-compensated case and the previously reported results. It is also important to mention that the STAP processor does not need a priori knowledge of the signal and background intensities at individual detector elements (as required in the previous techniques [77]).

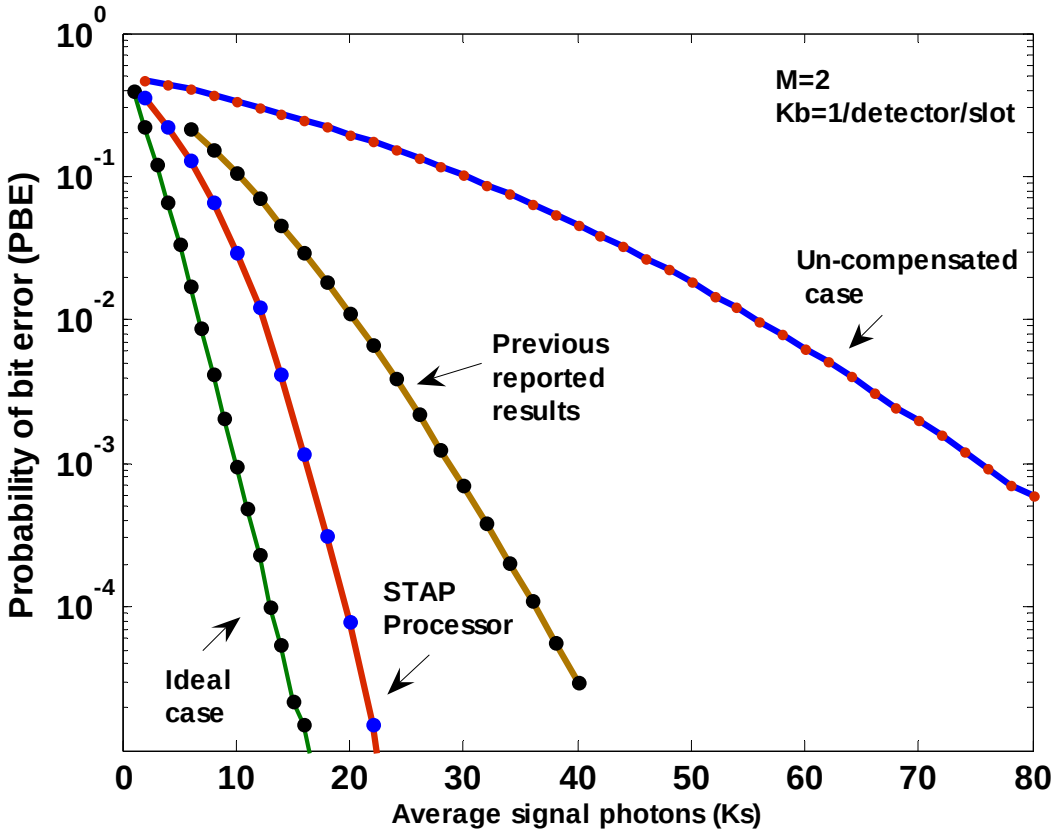

Figure 9.7. PBE vs. the number of input signal photons. Different curves correspond to un-compensated case, STAP processor, and an ideal case. The performance of previous reported results are also shown for comparison purposes. The background noise is K_b = 1/detector/slot and M = 2. The performance gains achieved by the STAP processor are evident.

9.5. Chapter Summary

In this chapter, I introduced the concept of a 2D adaptive filters-based STAP processor for processing the output of FPAs in an Earth-Space optical communications receiver to mitigate the coupled effects of atmospheric turbulence and background noise. Efficient and practical algorithms have been developed for the STAP processor. Monte-Carlo simulations were performed to evaluate the performance of the STAP-based optical receiver. I considered the worst-case scenario, when the background noise is generated from an extended source (i.e., diffused light from the daytime sky) and atmospheric turbulence strength is at its peak. Simulation results show that the STAP processor performs much better than the un-compensated case and previously reported results. It is further revealed that 4-7 dB performance improvements in moderate to high background noise and turbulence conditions are attainable. The new approach is simple, cost-effective, implementable, and does not need a-priori knowledge about the signal and background intensities.

CHAPTER 10

DEVELOPMENT OF A GENERAL PUPORSE SIMULATION TOOL FOR SHORT-RANGE TERRESTRIAL FREE-SPACE OPTICAL (FSO) COMMUNICATIONS SYSTEMS

Free-space optical (FSO) systems can provide a line-of-sight, wireless, and high bandwidth communications link between remote sites [74]. The performance of FSO systems is degraded by the atmospheric turbulence. In this chapter, I will explain the development of an efficient simulation software tool for prediction of the parameters of interest of a communications laser beam propagating through atmospheric turbulence. The software has the added functionality to analyze and predict the performance of an optical receiver's performance in the presence of atmospheric turbulence. The incorporation of AO systems in short-range terrestrial FSO systems is also modeled in the simulation tool.

10.1. Motivation

10.1.1. Free-Space Optical (FSO) Communications Systems

Free-space laser communications (lasercom) or free-space optical (FSO) communications systems can provide a line-of-sight, wireless, and high bandwidth communications link between terrestrial sites [74]. Laser communications has many advantages over other wireless technologies, such as microwave or RF spread spectrum. These advantages include much higher data rates; increased security because of the laser's narrow beam width, which makes detection, interception, and jamming very difficult; and the lower cost. Because of its superior security, lasercom/ FSO is suitable

for the wireless transfer of financial, legal, military, and other sensitive information. Another major advantage of lasercom/FSO over RF is that no Federal Communications Commission (FCC) licensing or frequency allocation is required. However, FSO communications is one of the least-deployed broadband technologies so far despite its tremendous potential for solving several long-standing problems, such as “the last mile connectivity”; “broadband internet access in rural areas”; “disaster recovery”; and many others. The widespread deployment of FSO communications systems has been hampered by the reliability or availability issues related to atmospheric variations. Atmospheric turbulence is a major limiting factor in the terrestrial, short-range FSO communications systems.

10.1.2. Software Development

Software development and simulations are a basic part of communications system research. By performing a good modeling and simulation of the entire link, the performance bounds and the proof of concept for the working mechanism of the system is provided; and many errors in the design can be avoided or corrected before going through the very costly process of the development and testing of the actual system. Having that in mind, a small part of my research effort is devoted to the development of efficient simulation tools for FSO systems operating in terrestrial, turbulence-degraded links. One software package is available in the commercial market for the analysis of laser beam parameters [108]. However, the software developed in this research has much more functionality and is sufficiently modular. Specifically, the first module of the developed software code calculates the most of the parameters of interest of a laser beam propagating through the randomly varying atmosphere. The second module can be

employed to analyze the performance of a direct-detection optical receiver operating in the presence of atmospheric turbulence. The third module simulates the incorporation of AO systems in short-range, terrestrial FSO systems and calculates the impact of AO-induced compensation. A brief functionality of each module and sample outputs are given in next sections.

10.2. Laser Beam Parameters Estimation

10.2.1. Flow Chart

The first module of the developed software code is able to calculate most of the parameters of interest of a laser beam propagating through the randomly varying atmosphere. The main challenge was to have a flexible code that can be employed to calculate parameters of interest for any link conditions, i.e., different transmitter/receiver specifications, different link distances and varying turbulence conditions ranging from weak fluctuations to strong fluctuations regimes. It is a well-known fact that atmospheric turbulence is a severely limiting factor in a typical free-space optical communication system [45]. Turbulence induces beam spreading (beyond that due to diffraction), random variations of the position of beam-centre called beam wander, and a random distribution of the beam energy within a cross section of the beam leading to irradiance fluctuations. The entire phenomenon results in significant power reduction of the received optical signal, which affects the performance of optical communications systems. However, intensity fluctuation is the major limiting factor in short-range FSO systems.

The major difference between fiber optics and FSO communications is that as an optical wave traverses through a random media like atmospheric turbulence, the wave propagation is governed by a “Stochastic Wave Equation.” Several approximations exist

in the literature for the calculations of statistical moments. The statistical moments are further employed to calculate the parameters of interest of a laser beam. In this research, I have incorporated the "Rytov approximation" for the solution of the stochastic wave equation and "Kolmogorov power law spectrum" (Eq. 7.1) to model the turbulence. A detailed treatment of the Rytov approximation, Kolmogorov spectrum and statistical moments of interest is given in Ref. [36]. Figure 10.1 shows a flowchart of the steps used in the developed software to calculate the statistical moments and various beam parameters of interest in the presence of turbulence [36].

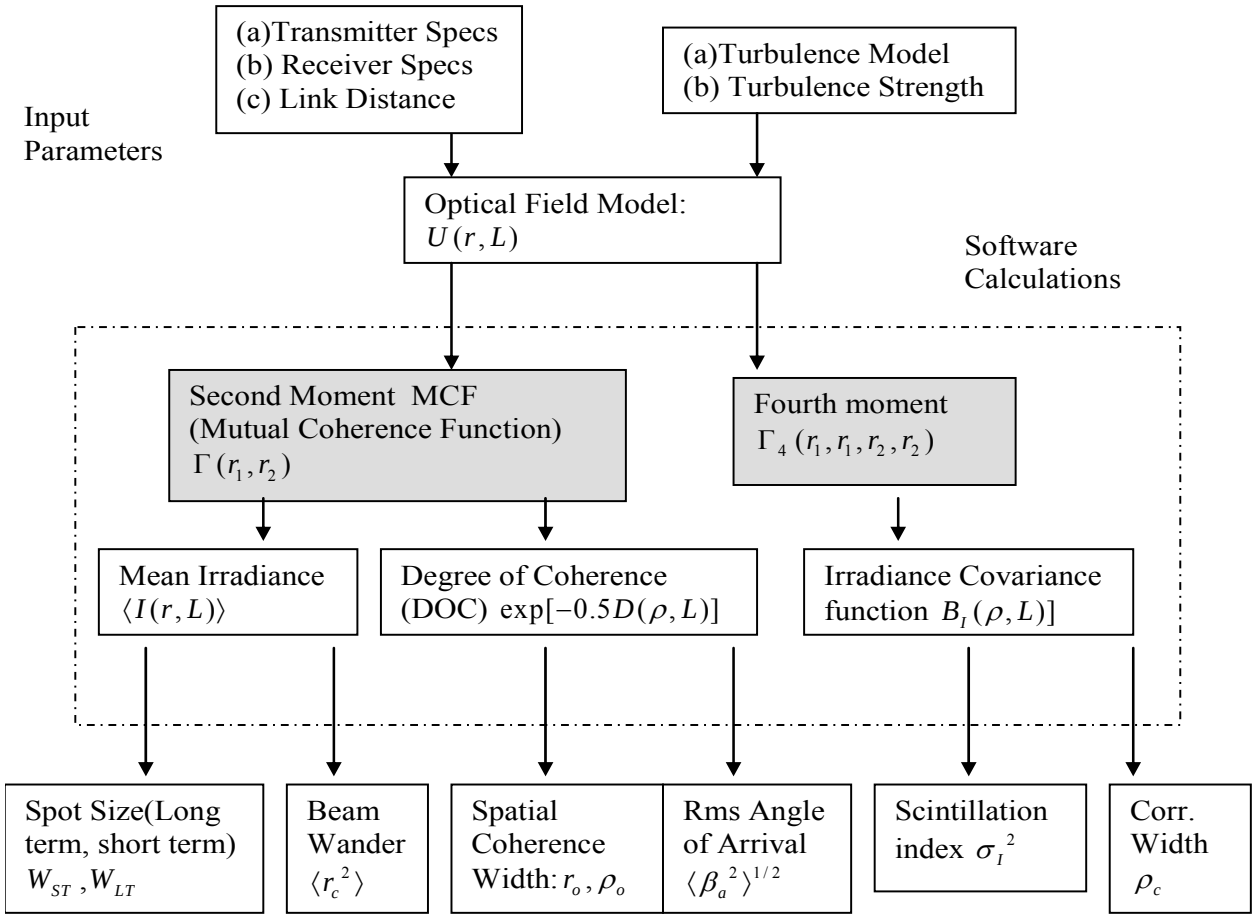

Figure 10.1. Flowchart of steps involved in calculations of beam parameters in the presence of turbulence [36].

10.2.2. Design Control Table

The output beam parameters (as given in Figure 10.1) are quite useful and can be used as elements of a design control table (DCT) for designing FSO communications systems. Values of spot sizes (both the short term W_{ST} and long term W_{LT}) are used to select the proper receiver lens and detector sizes to receive and detect maximum power. The beam-wander $\langle r_c^2 \rangle$ and angle-of-arrival (AOA) variances $\langle \beta_a^2 \rangle$ help in designing the appropriate beam-tracking system for the link. A suitable adaptive optics system can be designed based on the irradiance scintillation index σ_I^2 and spatial coherence-widths (r_o, ρ_o). An example of the calculation of these parameters is given in Table 10.1. The calculations are performed for different link conditions. The link distances are chosen to be 500 m, 1 Km and 2 Km. The strength of atmospheric turbulence is represented by the atmospheric structure constant C_n^2. Different conditions of turbulence (weak, moderate, and strong) are simulated using the values of C_n^2 as $1\times10^{-15}\, m^{-2/3}$, $7\times10^{-14}\, m^{-2/3}$ and $5\times10^{-13}\, m^{-2/3}$, respectively. The transmitting aperture diameter is chosen to be 3 cm. The examples in this chapter are given for a wavelength of 850 nm. However, since this is a general-purpose tool, the parameters can be calculated for any other wavelength such as 1550 nm. It is obvious from the values in Table 1 that as the turbulence conditions change from weak to strong regimes, the impact on beam parameters gets adverse. Specifically, the values in the last row in Table 10.1 are pretty high.

Table 10.1. Laser beam parameters calculated according to the flow-chart given in Figure 10.1. The turbulence conditions vary from the weak to strong fluctuations regime as the link distance and the value of C_n^2 increase.

Gaussian beam Parameters		W_{ST} Short term spot size (cm)	W_{LT} Long term spot size (cm)	$\langle r_c^2 \rangle$ Beam Wander variance	ρ_o Spatial Coherence (cm)	$\langle \beta_a^2 \rangle^{1/2}$ rms angle of arrival μ rad	$f\langle \beta_a^2 \rangle$ image jitter μ m	σ_R^2 Rytov variance	σ_I^2 Scintillation index	σ_B^2 Gaussian beam Rytov variance
	500 m	3.02	3.04	0.099	11	1.58	0.473	0.0133	0.0085	0.0085
C_n^2	1.0 Km	3.16	3.24	0.274	7.42	2.23	0.667	0.0401	0.0025	0.6692
1×10^{-15}	2.0 Km	3.67	3.75	0.782	5.26	3.15	0.946	0.1430	0.0649	0.0649
	500 m	3.24	3.34	0.825	0.856	13.19	3.96	0.7883	0.4957	0.05948
C_n^2	1.0 Km	4.11	4.73	2.33	0.583	18.66	5.59	2.81	0.9480	1.7501
7×10^{-14}	2.0 Km	7.16	9.74	6.60	0.423	26.39	7.918	10.01	1.26	4.54
	500 m	3.58	3.84	1.395	0.45	22.30	6.69	2.252	0.9259	1.695
C_n^2	1.0 Km	5.48	6.75	3.95	0.31	31.54	9.46	8.02	1.22	5
2×10^{-13}	2.0 Km	11.11	15.75	11.16	0.22	44.61	12.26	28.60	29.4	12.97

10.3. Performance Evaluation of FSO Receivers

The second module of the developed software uses the beam parameters developed in the previous table to investigate several key performance characteristics of a FSO communications system operating in a terrestrial link for which the index of refraction structure parameter C_n^2 can be treated as essentially constant. The calculations are limited to direct-detection receivers and the OOK modulation technique. Threshold detection is employed. Scintillations along with other noise sources in the receiver (shot noise, circuit, and electronic thermal noise) limit the performance of optical receivers [45]. The intensity fluctuations in an optical wave are described by the scintillation index

$$\sigma_I^2 = \frac{\left\langle I^2 \right\rangle}{\left\langle I \right\rangle^2} - 1, \tag{10.1}$$

where I is the intensity of the optical wave and the angle brackets $\langle\ \rangle$ denote an ensemble average. In literature, intensity fluctuations are modeled by many probability distributions. In this software, two well-known PDFs, i.e., lognormal and gamma-gamma distributions are incorporated.

10.3.1. Lognormal Distribution

The lognormal PDF for intensity fluctuations is given as [45]

$$p_I(I) = \frac{1}{I\sqrt{2\pi\sigma_I(0,L)}} \exp\left\{ -\frac{\ln(\frac{I}{\langle I(0,L)\rangle}) + \left(\frac{1}{2}\right)\sigma_I{}^2(0,L)}{2\sigma_I{}^2(0,L)} \right\}, \tag{10.2}$$

where $\langle I(0,L)\rangle$ is the on-axis mean irradiance and $\sigma_I{}^2(0,L)$ is the scintillation index at the link distance L.

10.3.2. Gamma-Gamma Distribution

Lognormal PDF is suitable for weak fluctuations regime. However, as the strength of the turbulence increases, multiple self-interference effects should be taken into account, and the irradiance statistics of the measured data deviate from the lognormal distribution [103]. The more complex gamma-gamma PDF model tallies well with the experimental data in the strong fluctuations regime. The gamma-gamma model is a two-parameter distribution that is based on a doubly stochastic theory of scintillations that assumes that the small-scale irradiance fluctuations are modulated by large-scale irradiance fluctuations of the propagating waves, both governed by independent gamma

distributions [103]. The resulting irradiance PDF takes the form of a generalized K distribution, termed as gamma-gamma PDF.

$$\begin{aligned} p_I(I) &= \int_0^\infty p_y\left(I \mid x\right) p_x(x)\, dx \\ &= \frac{2\left(\alpha\,\beta\right)^{\left(\alpha+\beta/2\right)}}{\Gamma\left(\alpha\right)\Gamma\left(\beta\right)} I^{(\alpha+\beta)/2-1} K_{\alpha-\beta}\left[2\left(\alpha\beta I\right)^{1/2}\right],\ I>0 \end{aligned} \quad . \tag{10.3}$$

The positive parameter α represents the effective number of large scale cells and β represents the effective number of small scale cells given by

$$\alpha = \frac{1}{\sigma_x^2}\ ,\ \beta = \frac{1}{\sigma_y^2}\,, \tag{10.4}$$

and the total scintillation index is related to the above mentioned parameters by

$$\sigma_I^2 = \frac{1}{\alpha} + \frac{1}{\beta} + \frac{1}{\alpha\beta} \tag{10.5}$$

10.3.3. Fade Statistics

Scintillations can lead to power losses at the receiver and eventually to fading of the received signal below a prescribed threshold. Hence, we quantify the performance characteristics of an optical receiver in terms of various fade statistics (the probability of fade, the expected number of fades per second, and the mean fade time). Fade statistics can be further used to predict the PBE of the receiver system. The probability of fade as a function of a prescribed threshold value I_T is defined by the cumulative probability [36]

$$p_{fade}(I) = 1 - \Pr_{(\det)} = 1 - \left(\int_0^\infty \int_{i_T}^\infty p_I(s)\, p_{s+n}(i \mid s)\, di\, ds \right), \tag{10.6}$$

where $p_{s+n}(i \mid s)$ is the PDF of the detector output current in the absence of turbulence containing both the signal and the receiver's noise. In the current analysis, Gaussian

statistics are assumed for all noise sources, hence, $p_{s+n}(i \mid s)$ represents a Gaussian PDF. $p_I(I)$ is given by Eq. (10.2) or Eq. (10.3). Other quantities of interest in FSO systems are the frequency of surges and frequency of fades of the photodetector output current. For a stationary process, Rice [97] has shown that the frequency of either positive or negative crossings of the threshold value i_T by the output current is given by the expected number of crossings per second defined by

$$\langle n(i_T) \rangle = \frac{1}{2} \int_{-\infty}^{\infty} \left| I' \right| \; p_I(I_T, I') \; dI', \tag{10.7}$$

where $p_{I,I'}(I, I')$ is the joint PDF of the intensity and its time derivative. Knowing the probability of fade and the expected number of fades per second, the mean fade time is simply the ratio of these quantities and is defined by [36]

$$\langle t(I_T) \rangle = \frac{\Pr(I \le I_T)}{\langle n(I_T) \rangle}. \tag{10.8}$$

If the receiving aperture in an FSO system is larger than the irradiance correlation width, the receiver sees several correlation patches and the scintillation levels measured by the detector in the image-plane begin to decrease. This effect, known as *aperture averaging*, is intentionally used in direct-detection systems to reduce scintillations and consequently it improves the receiver performance by decreasing the fade statistics. The aperture averaging factor (or co-efficient) A for a circular aperture of diameter D_G is defined by the ratio [104]

$$A(D_G) = \frac{\sigma_I^2(D_G)}{\sigma_I^2(0)} = \frac{16}{\pi} \int_0^1 x \, b_I(xD_G, L) \left(\cos^{-1} x - x\sqrt{1-x^2} \right) dx, \tag{10.9}$$

where $b_I(\rho, L) = B_I(\rho, L) / B_I(0, L)$ is the normalized covariance function and the terms in brackets arise from the modulation transfer function (MTF) of the circular aperture.

As an example, Figures 10.2 and 10.3 show various fade statistics as calculated using the equations (10.1) to (10.10) as a function of Fade threshold parameter F_T. The fade parameter F_T, given in decibels (dB) represents the dB level below the on-axis mean irradiance that the threshold current I_T is set. It is defined by

$$F_T = 10 \log_{10} \left(\frac{\langle I \rangle}{I_T} \right) \text{(dB)}. \tag{10.10}$$

In Figure 10.2, the probability of fade associated with a Gaussian beam wave versus fade threshold parameter is shown for a link distance of L= 3 Km. This case belongs to the strong turbulence regime. Other parameters are fixed at $C_n^2 = 10^{-13}\, m^{-2/3}$, $l_o = 0$, $L_o = \infty$, $\lambda = 850\, nm$, and transmitter aperture radius at 1 cm. The probability of fade is also parameterized by the receiver lens size (diameter). Mean Fade time (MFT) as a function of F_T is shown in Figure 10.3. Aperture averaging effects are evident and considerable performance improvement is possible by using larger aperture receivers. Given the fixed link budget specifications and the detector/decoder characteristics, the plots in these figures can be used to properly select the optimal receiver diameter to achieve the prescribed fade statistics. It is also evident that the lognormal model overestimates the receiver performance in strong turbulence regimes. Gamma-gamma model is the appropriate choice in these regimes.

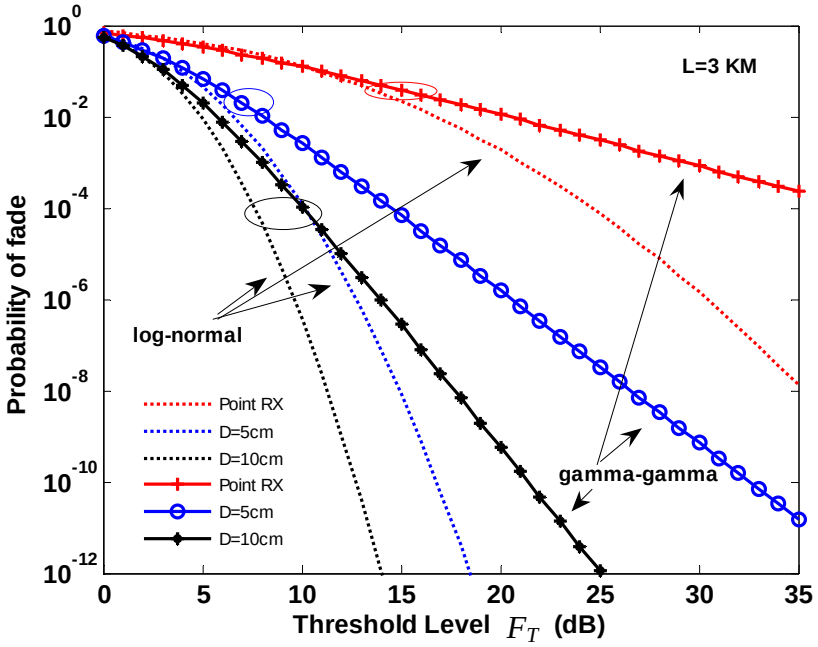

Figure 10.2. Probability of fade as a function of the threshold parameter F_T. D is the receiver lens diameter. Link distance is 3 Km and this case represents the moderate turbulence regime.

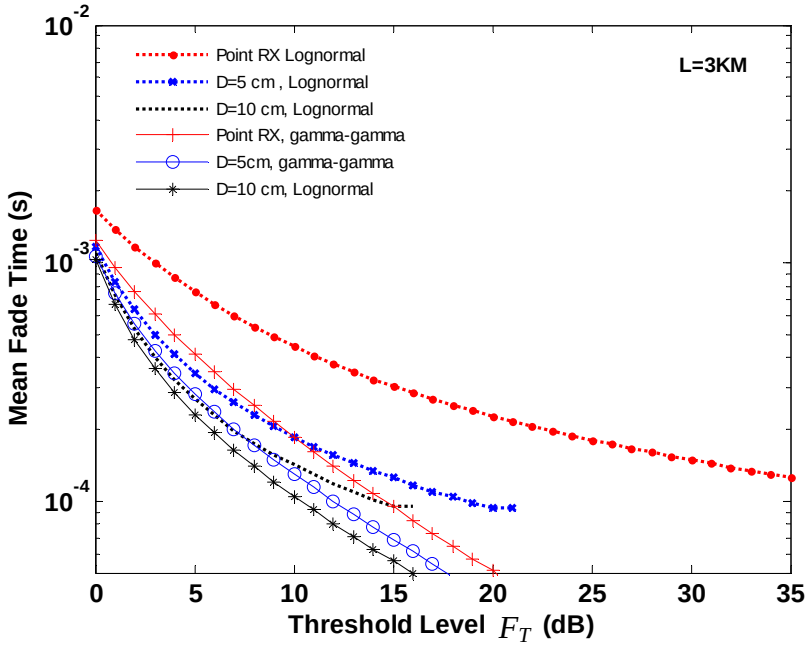

Figure 10.3. Mean fade time vs. the threshold parameter F_T, link distance is 3 Km.

For OOK systems operating in atmospheric turbulence, PBE is given by [36]

$$PBE = \frac{1}{2}\int_0^{\infty} p_I(u)\, erfc\left(\frac{< SNR > u}{2\sqrt{2}}\right) du \qquad (10.11)$$

where $p_I(I)$ is given in Eqs. (10.2) and (10.3), and Gaussian statistics are assumed for the noise sources in the receiver. An example of PBE calculations is given in Figure 10.4. OOK keying with direct-detection is employed. The other parameters are λ=1.55 μm and $C_n^2 = 1\times10^{-13}\, m^{-2/3}$. The turbulence-induced deleterious effects are evident and similar conclusions, as that of previous figures in this chapter, about aperture-averaging effects can be drawn. However, the receiver size can be increased to a certain limit. Beyond that some other technique such as AO systems shall be employed for turbulence mitigation.

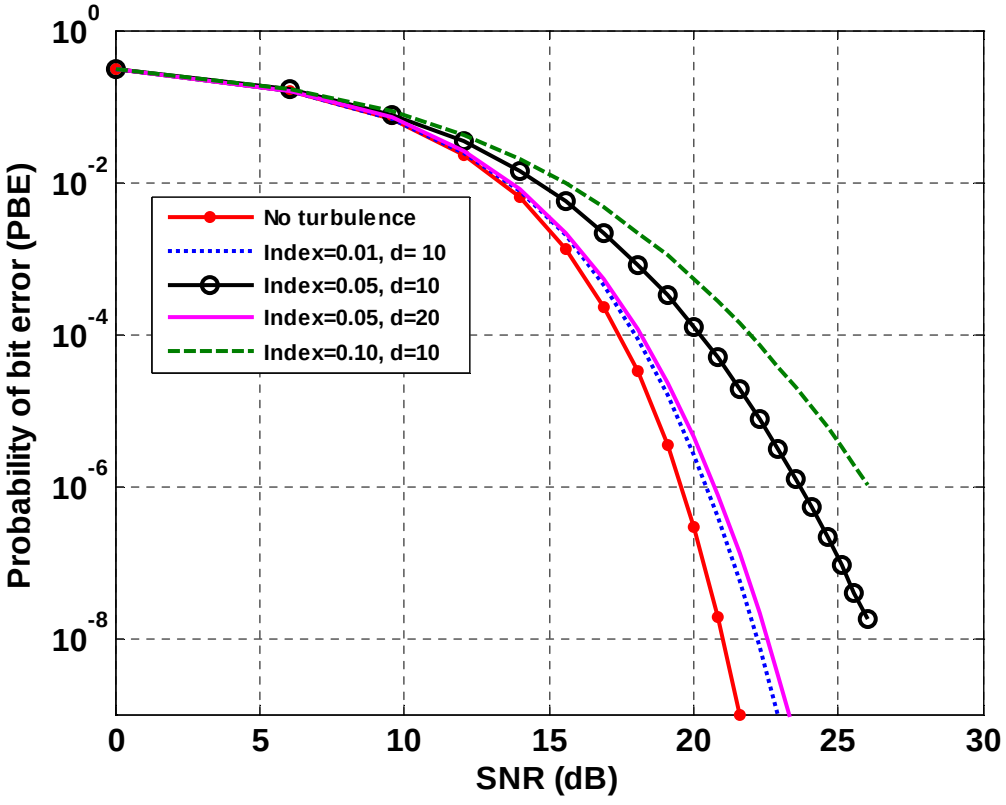

Figure 10.4. PBE as a function of the mean SNR for different receiver configurations.

10.4. Incorporation of AO systems

Adaptive Optics (AO) systems are employed to mitigate the atmospheric turbulence effects. A conventional closed-loop adaptive optics system for the FSO link consists of the following components: a deformable mirror, a wavefront sensor and a control processor. The cost of such an adaptive-optics system is directly proportional to its complexity, i.e., degrees of freedom, which mainly depend upon the number of actuators in the deformable mirror and the control-loop bandwidth. Each FSO system link design requires optimization of the AO system parameters. The third software module is developed to simulate the effects of AO system on the receiver performance as quantified by the PBE. In literature, the Zernike polynomials are used to describe the turbulence-induced aberrations on the optical beam [98]. By removing an increasing number of Zernike modes (equivalent to degrees of freedom of the adaptive optics system), the improvement in PBE can depict the performance improvement of the receiver. The scintillation index after the AO-induced correction is given by [36,105]

$$\sigma_I^{\,2}(L) = \frac{2.606}{2\pi} C_n^{\,2} k^2 L \int_0^{2\pi}\int_0^{\infty} \kappa^{-8/3} \left[1 - \frac{k}{L\kappa^2}\sin\left(\frac{L\kappa^2}{k}\right)\right]\left[1 - \sum_{i=1}^{N} F_i(\kappa, D_G, \phi\right] d\kappa \, d\varphi, \tag{10.12}$$

where the term $\left[1 - \sum_{i=1}^{N} F_i(\kappa, D_G, \phi\right]$ represent the adaptive optics filter functions that operates on the transverse spatial spectrum (κ dependence) and represents the removal of spatial modes by adaptive optics phase conjugation [105]. The adaptive optics filter functions are derived from the Fourier transforms of Zernike polynomials. D is the receiving lens aperture diameter and the filter functions are given by [99,105]

$$F_i(\kappa, D_G) \qquad\qquad 1(m=0)$$

$$F_{i,even}(\kappa, D_G, \varphi) \quad = \quad (n+1)\left[\frac{2J_{n+1}(\kappa D_G/2)}{\kappa D_G/2}\right]^2 \quad 2\cos^2 m\varphi$$

$$F_{i,odd}(\kappa, D_G, \varphi) \qquad\qquad 2\sin^2 m\varphi$$

(10.13)

Figure 10.5 shows the expected PBE improvement after incorporating an AO subsystem in a FSO communications link using a receiver lens of 15 cm diameter and operating at 850 nm wavelength. Results are shown for three different link distances of 500 m, 1 Km, and 2 Km. The atmospheric structure constant is $C_n^2 = 10^{-14}\, m^{-2/3}$. PBE for different link conditions (as calculated in Eq. 10.11 after AO correction) are shown versus different number of Zernike modes removed (the degree of freedom or number of actuators in a deformable mirror in the AO subsystem). It is evident from the figure that the removal of 30-40 modes results in several orders of magnitude improvement in receiver performance. This simulations platform can be employed to calculate the optimum number of Zernike modes removal (degrees of freedom or complexity level of an AO system) required to achieve a specified PBE in the design of a FSO communications system.

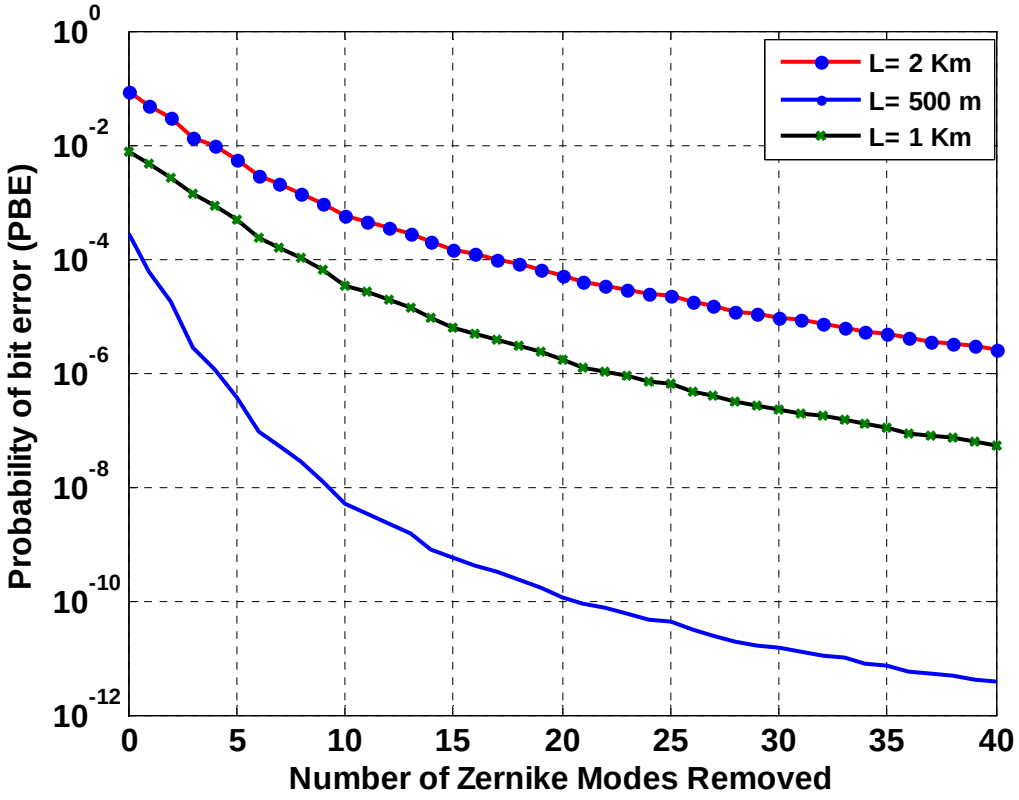

Figure 10.5. PBE improvement with the varying complexity of AO system. Three link distance ranges capture weak, moderate, and strong turbulence conditions.

10.5. Chapter Summary

In this chapter, I explained the development of efficient and robust software tools for the following functionality: (a) to calculate most of the parameters of interest of a laser beam propagating through atmospheric turbulence; (b) to quantify the performance of optical receivers in the presence of turbulence; and (c) to estimate and optimize the impact of AO subsystems in FSO systems receiving the turbulence-degraded laser signal. The code is flexible and can be used for different atmospheric conditions ranging from week to strong refractive index fluctuation regimes over any link distance. The output parameters of the code can be very helpful for designing the complete FSO link and the

adaptive optics subsystem. The developed code is modular and can serve as a starting platform for any further research related to the free-space optical communications systems in the Optics and Photonics research group.

CHAPTER 11

CONCLUSIONS AND FUTURE DIRECTIONS

The need for a broadband and high-speed communications infrastructure that can satisfy the ever-growing data requirements of future deep-space exploration missions, which are launched by the international scientific community, was the driving force behind the initiation of this research. The research presented in this thesis has been focused towards the design, analysis, simulations, and evaluation of novel architectures and subsystems that can provide and support the communications throughput and data rates, which are substantially greater than the current state-of-the-art RF-based NASA Deep-Space Network (DSN). Optical communications technology has revolutionized the modern-era telecommunications. In this research, I have designed and evaluated different architectures and subsystems for an optical communications receiver operating in a deep-space optical communications link. However, the core of this research has been around the design and analysis of telescope array-based optical receivers. The major contributions and outcomes of this research can be divided into following parts.

11.1. Analysis of Telescope Array-based Receivers and Optimization

I evaluated the performance of telescope array receivers for a deep-space optical communications link between Earth and Mars for different operational scenarios, such as Earth-Mars opposition, Earth-Mars conjunction, and various background and turbulence conditions. Various system parameters were optimized to maximize the communications system throughput. The performance of different array architectures was compared to a single 10 m telescope-based receiver. It was found that the performance of an array

receiver consisting of 100, 1 m telescopes was almost similar to a monolithic telescope. The performance of array-based receiver degraded drastically as the individual telescope diameters approach the atmospheric Fried parameter. It was shown that during Earth-Mars opposition phase, data rates of 121 Mbits/s can be achieved by a telescope array receiver consisting of 100 telescopes with 1 m aperture diameter each. The RF-based DSN stations operating at the experimental Ka band can achieve a maximum of 6 Mbits/s in this scenario. I also showed that during Earth-Mars conjunction phase, data rate of 32 Mbits/s could be achieved by a telescope array receiver with $(100 \times 1\ \text{m})$ configuration. All the results were verified by Monte-Carlo simulations and analytical techniques. Hence, the analysis and results presented in this phase showed that a deep-space optical communications link based on telescope array receivers is a viable architecture, which can provide broadband data support for future universe exploration ventures in deep-space. It was also shown that the optimization of important system parameters, such as detector's FOV, PPM slot-width, and PPM order greatly enhanced the performance of the receiver.

11.2. Design and Evaluation of Adaptive Subsystems

After the first phase, it was determined that synchronization errors, tracking errors, atmospheric turbulence, and background noise are among major limiting factors for a deep-space optical communications link. Hence, in the next phase of the research, various subsystems and adaptive algorithms were developed for mitigation of these effects in telescope array-based receivers.

11.2.1. Compensation of Synchronization and Tracking Errors

First, I designed a Kalman filter-based closed-loop synchronization system for a telescope array-based optical communications receiver. The performance of the closed-loop systems and different array architectures were evaluated for a deep-space optical communications link between Earth and Mars during the Mars conjunction phase in the presence of substantial synchronization errors. The simulation results showed that the Kalman filter-based synchronization system in individual telescopes efficiently tracked the time-varying delay fluctuations even during worst channel conditions, i.e., when Mars is farthest from Earth, atmospheric turbulence is at its peak, and the background noise is very intense. The performance evaluation of the array architecture revealed that in the presence of the synchronization errors, the performance degradation of an array consisting of hundred 1 m telescopes was small ($\leq$ 9 % for most operating conditions) compared to a monolithic 10 m telescope. The performance degradation increased to about 17 % in the extreme background noise conditions; however, this particular condition occurs only for about ($<$ 5 %) of the time during the complete Mars-Earth orbital cycle [88].

Next, I developed a statistical analysis to evaluate the performance of general direct-detection receivers in the presence of random tracking errors. The analysis showed that the tracking errors result in considerable degradation in the performance of optical receivers. Then, I presented the design of a closed-loop tracking subsystem for the mitigation of the tracking errors to avoid power losses in telescope array receivers. I analyzed and compared the performance of different telescope array configurations with a monolithic aperture, for an optical communications link between Earth and Mars, after

incorporating the proposed closed-loop tracking subsystem. The results show that as the number of elements in the telescope array receiver increased from 1 to 100, the overall performance (evidenced by achievable data rates) degraded slightly (i.e., about 10 % for the most conditions of interest) compared to a single large telescope architecture.

The design and analysis of synchronization and tracking subsystems solidify the theoretical foundations of the telescope arrays-based receivers for deep-space optical communication links. It is concluded that tracking and synchronization errors (if compensated) do not pose a big limitation as far as the replacement of a large telescope (10 m diameter) with the optical arrays (consisting of smaller 100, 1 m telescopes) is concerned. Keeping in view the benefits of practicality (as many low-cost commercial telescopes are available near 1 m diameter), the ease in implementation due to a manageable number of telescopes in the array, and comparable performance to a single large telescope in the presence of major limiting factors, an array receiver consisting of 1 m telescopes is a viable array architecture.

11.2.2. Compensation of Atmospheric Turbulence and Background Noise

In this phase, I first designed and evaluated adaptive optics (AO) subsystems for the mitigation of the coupled effects of atmospheric turbulence and background noise in telescope array-based receivers operating in a deep-space optical communications link. It was shown that in extreme turbulence conditions (i.e., Fried parameter r_o = 4 cm) during Earth-Mars conjunction, a telescope array receiver consisting of 100, 1 m telescopes could achieve data rates of 5.7 Mbits/s after an AO-based correction achieving the SR = 0.30. Further, it was shown that 14.40 Mbits/s are achievable with the SR = 0.75. During moderate background conditions, the same array configuration could achieve data rates of

7 Mbits/s and 16.7 Mbits/s corresponding to the *SR* = 0.30 and 0.75, respectively. It was also revealed that compared to the uncorrected case in the same architecture, the use of AO systems resulted in a performance improvement of 8.48 dB for *SR* = 0.75, and 4.47 dB for *SR* = 0.30 in extreme background noise conditions. The performance improvements in moderate background noise conditions were 1.82 dB and 5.59 dB corresponding to the *SR* = 0.30 and 0.75, respectively. The performance improvements in other array configurations was also evaluated and found to be substantial. Hence, it was concluded that the use of AO subsystems is quite effective in mitigating the atmospheric turbulence and background noise effects that are faced by telescope array-based receivers while operating in deep-space optical communications links.

Experimental investigation of the use of AO subsystems was also carried out. A closed-loop system based on a deformable mirror was implemented experimentally in the lab. The experimental results proved the efficacy of AO systems in correcting various phase and wavefront errors and concentration of the received energy into a much smaller PSF. The narrower PSF would require the use of smaller detectors and spatial rejection of the background noise.

In the second part of this phase, I introduced the concept of a 2D adaptive filters-based STAP processor for processing the output of FPAs in an Earth-Space optical communications receiver to mitigate the coupled effects of atmospheric turbulence and background noise. Efficient and practical algorithms were developed for the STAP processor. Monte-Carlo simulations were performed to evaluate the performance of the STAP-based optical receiver. Simulation results for strong background conditions showed that STAP processor performs much better than the un-compensated case and the

previously reported results in the literature. It is further revealed that 4-7 dB performance improvements in moderate to high background and strong turbulence conditions are attainable. The new approach is simple, cost-effective, implementable, and does not need a priori knowledge about the signal and background intensities.

In summary, I demonstrated the robustness and effectiveness of two techniques in mitigating the effects of atmospheric turbulence and background noise in deep-space optical communications receivers. AO is an active optics technology whereas the STAP-based processing can be regarded as an electronic-counterpart of the AO systems.

Summarizing the research in the deep-space optical communications part, the telescope array-based receiver is a viable architecture that can provide orders of magnitude greater data rates than the current RF-based DSN. Optimization of important system parameters has been performed to maximize the communications throughput. Various subsystems have been designed and analyzed to mitigate the synchronization and tracking errors. Incorporation of AO subsystems and STAP processor can further enhance the performance of optical receivers operating in the worst-case channel conditions.

It is important to highlight that the data rates presented in this thesis are not exhaustive. The analysis was based on the power and modulation limits of the currently available space-qualified lasers and an assumption of an aggregate aperture of 10 m diameter. However, in future, with the availability of more sophisticated, high-power and ultra-fast lasers and detectors, and optical array receivers with considerably larger aggregate aperture diameters (i.e., 15 m to 30 m), optical communications technology has the potential to achieve data rates in the Gbits/s range between Earth and Mars. Finally, although the Earth-Mars link was evaluated here, the analysis, insight, and conclusions of

this thesis can be easily extended to any other inter-planetary deep-space optical communications link, i.e., Earth-Jupiter, Earth-Neptune links, etc.

11.3. Development of Analysis Tools for Terrestrial FSO Systems

In the last part of the thesis, a small part of research effort is dedicated to short-range, terrestrial, free-space optical (FSO) communications links also. It is believed that FSO systems can solve the last mile connectivity problem faced by the current commercial telecom market. An efficient general-purpose simulation tool was developed that can model and predict the parameters of interest of a laser beam propagating through a turbulent channel in FSO systems. This simulation tool can also be employed to analyze the performance of a short-range FSO communications system employing OOK modulation format, and operating in any link condition. The developed code also has the option of incorporating a closed-loop adaptive optics subsystem for mitigation of turbulence effects and estimating the resultant performance improvement.

A brief summary of the contributions of this research are as follows:

- Design, analysis, and performance comparison of different telescope array-based receiver architectures for a deep-space optical communications link between Earth and Mars. The performance analysis is carried out for a wide range of atmospheric turbulence, background noise, and channel conditions to estimate the upper and lower performance bounds [55-57].
- Optimization of important system parameters such as detector size, receiver FOV, PPM order M, and PPM slot-width T_s to maximize the optical communications system performance between Earth and Mars [55,58].

- Statistical modeling of the impact of random tracking errors on direct-detection optical communications systems; design of a tracking subsystem; and analysis of telescope array-based receivers for deep-space communications in the presence of tracking errors [60-62].
- Design and analysis of a Kalman filter-based synchronization scheme for telescope array receivers operating in a deep-space optical communications link [63,64].
- Design and analysis of a laser guide star (LGS)-based adaptive optics (AO) system in telescope array receivers for mitigation of atmospheric turbulence and background noise effects in deep-space optical communications links [75,76]. Experimental evaluation and demonstration of the use of AO systems to mitigate turbulence-induced phase errors is also performed.
- Design and analysis of a novel 2D Wiener filter-based space-time adaptive processor (STAP) for mitigation of the atmospheric turbulence and background noise effects in a deep-space optical communications link [78,79] .
- Development of a general-purpose software code to simulate and predict the parameters of a laser beam travelling through atmospheric turbulence. The code has the options to calculate the performance of FSO communications systems in turbulence, and to simulate the effects of AO systems on FSO receivers [74].

11.4. Future Directions

The pursuit of human research has no boundaries. The meaning of "from quantum to cosmos" is truly realized when we think about using telescope arrays to receive few signal photons that have travelled hundreds of millions of kms from deep-space. The research efforts on deep-space optical communications started about 30 years back at NASA [7]. The analysis of telescope arrays and design of subsystems is an important milestone. There are many avenues that need to be explored. Specifically, the following research efforts are perceived that may follow this research:

(a) The analysis presented in this thesis is based on the un-coded bit error rates and hard-decision decoders. A lot of research effort is being dedicated for the development of efficient and robust codes and soft-decision decoding [7]. As a next step, the analysis of telescope array receivers may be carried out after incorporation of efficient error-correcting techniques.

(b) The optimization examples presented in this thesis are based upon the background noise and turbulence data that is observed at CA, USA [88]. The optimization algorithms can be hard-wired in a receiver for specific locations. Substantial research efforts have been dedicated to identify the use of multiple sites that can collectively provide a cloud-free line-of-sight (CFLOS) operation [7]. The computation and estimation of the local background and turbulence parameters should be carried out and pre-wired into optimization algorithms for the specific receiver locations.

(c) Many robust adaptive filtering techniques and algorithms have been designed and evaluated in this thesis. However, the areas of statistical DSP and adaptive filters

continue to grow. In future, robust adaptive techniques such as genetic algorithms, artificial intelligence-based neural networks, and Particle filters can be incorporated and evaluated for the potential performance improvement

(d) The prospect of optical communications is very bright. Recently, it has been reported in Ref [80,87] that with the current growth in the optical technology (detectors, lasers, and optics) the substantial increase in data rates is possible. In addition, the aggregate aperture diameter in this thesis is fixed at 10 m. Many ventures to build much larger telescopes are underway. With the commercialization and availability of low cost telescopes, telescope arrays with much larger aggregate apertures are possible. All these developments should be incorporated in any future analysis and the milestone of Gbits/s data over deep-space distances is not very far.

(e) The concept of hybrid RF-Optical communications is evolving rapidly in the commercial, military, and government arenas. The feasibility of hybrid architectures should be explored for providing a reliable and large bandwidth deep-space optical communications link.

(f) The communications wavelength of choice in this thesis has been 1.06 μm due to the limitations on the available technology for the space-qualified transmitter and single photon detectors [81]. However, with the current pace of technology evolution, switching to the telecom wavelength of 1.55 μm seems possible in near future. A detailed analysis to find out the impact of switching to 1.55 μm should be carried out.

(g) In this thesis, telescope arrays have been analyzed for deep-space optical communications applications. The results in this thesis are also helpful in analyzing telescope array receivers for several "lightscience" measurements. In a manner analogous to the traditional radio-science measurements, "lightscience" measurements are possible using the laser beam transmitted from a space-borne laser-communications terminal for positional reference and light propagation experiments. Several preliminary studies have been made into viable scientific applications of laser communications [7]. Some of these are (1) Laser ranging of Lunar and other celestial objects; (2) light-propagation experiments that include occultation investigations of probe planetary limbs and scattering from the medium throughout interplanetary space; (2) enhanced knowledge of Solar-System body (e.g., planet, moon asteroid, or comet) properties; (3) tests of fundamental theories of physics; and (4) improved knowledge of Solar-System ephemerides. Some of these measurements are unique to optical communications technologies and the application of today's state-of-the-art tracking capability [7]. Many science measurements can be made with incoherent systems (which may include pulsed laser sources), while others require (or are more precise with) coherent systems.

REFERENCES

[1] K. Clark *et al*., "Return to Europa: overview of the Jupiter Europa orbiter mission," in *Proc. IEEE Aerospace Conference'09*, 2009, pp. 1-20.

[2] M. Williamson, "EXOMARS: Europe rises to the challenge," *Aerospace America*, vol. 47, no. 5, May, pp. 38-45, 2009.

[3] L. Colangeli *et al*., "MEDUSA: the ExoMars experiment for in-situ monitoring of dust and water vapour," *Planetary and Space Science*, vol. 57, no. 8-9, July, pp. 1043-1049, 2009.

[4] H. Zhao, "YingHuo-1- Martian space environment exploration orbiter," *Chinese Journal of Space Science*, vol. 28, no. 5, Sept., pp. 395-401, 2008.

[5] R. S. Grammier, "A look inside the Juno mission to Jupiter," in *Proc. IEEE Aerospace Conference'09*, 2009, pp. 1-10.

[6] W. J. Weber *et al*., "Transforming the deep space network into the interplanetary network," *Acta Astronautica*, vol. 58, no. 8, Apr., pp. 411-421, 2006.

[7] H. Hemmati, Ed., *Deep Space Optical Communications.* New Jersey: John Wiley and Sons, 2006.

[8] J. Taylor, M. M. Fernández, A. I. B. Alamanac, and K. M. Cheung, "Deep space 1 telecommunications," in *Design and Performance Summary Series DESCANSO*, J. H. Yuen, Ed. Pasadena, CA: Jet Propulsion Laboratory, California Institute of Technology, 2001.

[9] Jet Propulsion Laboratory, CA. Communications with Earth. [Online]. Available: http://mars.jpl.nasa.gov/mro/mission/communications/

[10] S. Shambayati, J. S. Border, D. D. Morabito, and R. Mendoza, "MRO Ka-band demonstration: cruise phase lessons learned ," in *Proc. IEEE Aerospace Conference*, 2007, pp. 1-17.

[11] S. Shambayati, "The struggle for Ka-band: NASA's gradual move towards using 32-GHz Ka-band for deep space missions," in *Proc. IEEE Aerospace Conference'07*, 2007, pp. 1-21.

[12] Jet Propulsion Laboratory, CA. Telecommunications. [Online]. Available: http://mars.jpl.nasa.gov/mro/mission/spacecraft/parts/telecommunications/

[13] Wikipedia. Electromagnetic-spectrum. [Online]. Available: http://en.wikipedia.org/wiki/File:Electromagnetic-Spectrum.png

[14] J. Kliore *et al*., "S band radio occultation measurements of the atmosphere and topography of Mars with Mariner 9: extended mission coverage of polar and intermediate latitudes," *Journal of Geophysical Research*, vol. 78, no. 20, July, pp. 4331-4351, 1973.

[15] P. D. Potter, "NASA/JPL deep space network 64-meter-diameter antenna dual-frequency feed system," *JPL Quarterly Technical Review*, vol. 3, no. 2, July, pp. 23-26, 1973.

[16] J. Kliore *et al*., "Cassini radio science," *Space Science Reviews*, vol. 115, no. 1-4, Nov., pp. 1-70, 2004.

[17] R. M. Gagliardi and S. Karp, *Optical Communications.* 2nd ed., New York: John Wiley and Sons, 1995.

[18] W. D. Williams *et al*. "RF and optical communications: A comparison of high data rate returns from deep space in the 2020 timeframe," in *Proc. 12th Ka and Broadband Communications Conference*, 2006, pp. 1-9.

[19] National Aeronautics and Space Administration, *2003 Strategic Plan.* Washington, DC: Strategic Investment Division, 2003.

[20] National Aeronautics and Space Administration. Fiscal Year 2010 Budget Estimates. [Online]. Available: http://www.nasa.gov/pdf/345225main_FY_2010_UPDATED_final_5-11-09_with_cover.pdf

[21] M. Bertero and P. Boccacci, "Image restoration methods for the Large Binocular Telescope (LBT)," *Astronomy & Astrophysics Supplement Series*, vol. 147, no. 2, Dec., pp. 323-333, 2000.

[22] W. M. Keck Observatory. [Online]. Available: http://www.keckobservatory.org/

[23] Large Binocular Telescope Observatory. [Online]. Available: http://medusa.as.arizona.edu/lbto/

[24] D. A. H. Buckley *et al*., "Commissioning of the Southern African Large Telescope (SALT) first-generation instruments," in *Proc .of SPIE*, 2008, vol. 7014, pp. 1-15.

[25] D. M. Boroson, R. S. Bondurant, and D. V. Murphy, "LDORA: a novel communication receiver array architecture," in *Proc. of SPIE,* 2004, vol. 5338, pp. 56-64.

[26] T. A. ten Brummelaar *et al*., "First results from the CHARA Array. II. A description of the instrument," *Astrophysical Journal*, vol. 628, no. 1, pt. 1, July, pp. 453-465, 2005.

[27] M. M. Colavita *et al*., "The Keck Interferometer," in *Proc. of SPIE*, 1998, vol. 3350, pp. 776-784.

[28] P.M. Hinz *et al*., "Status of the LBT interferometer," in *Proc. of SPIE*, 2008, vol. 7013, pp. 1-9.

[29] G. Leto *et al*., "VLA observation of dMe stars," *Astronomy and Astrophysics*, vol. 359, no. 3, July, pp. 1035-1041, 2000.

[30] G. M. Dubner, P. F. Velazquez, W. M. Goss, and M. A. Holdaway, "High-resolution VLA imaging of the supernova remnant W28 at 328 and 1415 MHz," *Astronomical Journal*, vol. 120, no. 4, Oct., pp. 1933-1945, 2000.

[31] M. R. Sankarararnan and S. Ananthakrishnan, "Giant metrewave radio telescope and VLBI observations," *MAPAN-Journal of Metrology Society of India*, suppl. issue, no. 2, Feb., pp. 344-351, 2001.

[32] G. Polatidis, J. E. Conway, R. Parra, and Y. M. Pihlstrom, "Continuum EVN and MERLIN observations of ultra luminous infrared galaxies," in *Proc. of AIP Conference*, 2005, no. 783, pp. 361-364.

[33] V. Vilnrotter, C. W. Lau, M. Srinivasan, K. Andrews, and R. Mukai, "An optical array receiver for deep-space communication through atmospheric turbulence," Jet Propulsion Laboratory, Pasadena, CA. Tech. Rep. IPN 42-154, Aug. 2003.

[34] V. Vilnrotter, C. W. Lau, M. Srinivasan, K. Andrews, and R. Mukai, "Optical array receiver for communication through atmospheric turbulence," *Journal of Lightwave Technology*, vol. 23, no. 4, Apr., pp. 1664-1675, 2005.

[35] J.D. Barry and G.S. Mecherle, "Beam pointing error as a significant design parameter for satellite-borne free space optical communication systems," *Opt. Eng.,* vol. 24, no. 6, Nov., pp. 1049-1054, 1985.

[36] L. C. Andrews and R. L. Phillips, *Laser Beam Propagation through Random Media.* Bellingham, WA: SPIE Press, 2005.

[37] J. R. Lesh, "Capacity limit of the noiseless, energy-efficient optical PPM channel," *IEEE Transactions on Communications*, vol. COMM-31, no. 4, Apr., pp. 546-548, 1983.

[38] D. Zwillinger, "Maximizing throughput over an average-power-limited and band-limited optical pulse-position modulation channel," Jet Propulsion Laboratory, Pasadena, CA. Tech. Rep. TDA 42-62, pp. 81-86, 15 Apr. 1981.

[39] V. Vilnrotter, "Background sources in optical communications," Jet Propulsion Laboratory, Pasadena, CA. Tech. Rep. 83-72, 15 Nov. 1983.

[40] E. E. Bell, L. Eisner, J. Young, and R. A. Oetjen, "Spectral radiance of sky and terrain at wavelengths between 1 and 20 microns. II. Sky measurements," *Journal of the Optical Society of America*, vol. 50, no. 12, Dec., pp. 1313-1320, 1960.

[41] L. Eisner, E. E. Bell, J. Young, and R. A. Oetjen, "Spectral radiance of sky and terrain at wavelengths between 1 and 20 microns. III. Terrain measurements," *Journal of the Optical Society of America,* vol. 52, no. 2, Feb., pp. 201-209, 1962.

[42] R. C. Ramsey, "Spectral irradiance from stars and planets, above the atmosphere, from 0.1 to 100 microns," *Applied Optics*, vol. 1, no. 4, July, pp. 465-471, 1962.

[43] J. Katz, "Planets as background noise sources in free space optical communications," Jet Propulsion Laboratory, Pasadena, CA, Tech. Rep. TDA 42-85, pp. 13-24. Mar. 1986.

[44] K. Lumme and E. Bowell, "Radiative transfer in the surfaces of atmosphereless bodies. I. Theory," *Astronomical Journal*, vol. 86, no. 11, Nov., pp. 1694-1704, 1981.

[45] L. C. Andrews and R. L. Phillips, *Laser Beam Propagation through Random Media.* Bellingham, WA: SPIE Press, 1998.

[46] I. Tatarski, *Wave Propagation in a Turbulent Medium,* R. A. Silverman, Trans., New York: McGraw-Hill, 1961.

[47] A. Ishimaru, *Wave Propagation and Scattering in Random Media.* Piscataway, New Jersey: IEEE Press, 1997.

[48] J. Stroebehn, Ed., *Laser Beam Propagation in the Atmosphere.* New York: Springer, 1978.

[49] R. L. Fante, "Wave propagation in random media: a systems approach," in *Progress in Optics XXII*, E. Wolf, Ed. New York: Elsevier, 1985, pp. 341-398.

[50] R. R. Beland, "Propagation through atmospheric optical turbulence," in *The Infrared & Electro-Optical Systems Handbook*, vol. 2, F. G. Smith, Ed. Bellingham, WA: SPIE Optical Engineering Press, 1993.

[51] B. E.-K. Souw, “Coherent telescope array with self-homodyne interferometric detection for optical communications,” *Opt. Eng*., vol. 42, no. 11, Nov., pp. 3139-3157, 2003.

[52] L. C. Andrews and R. L. Phillips, “Free space optical communication link and atmospheric effects: single aperture and arrays,” in *Proc .of SPIE*, 2004, vol. 5338, pp. 265–275.

[53] V. Vilnrotter, C. -W. Lau, K. Andrews and M. Srinivasan, “Two-element optical array receiver concept demonstration,” in *Proc. of SPIE*, 2005, vol. 5712, no.1, pp. 225-239.

[54] A. A. Eftekhar, S. Khjorasani, A. Adibi, and S. Piazzolla “Analysis of telescope arrays for deep space optical communications,” in *Proc. IEEE Aerospace Conference*, 2005, pp. 1589-1597.

[55] A. Hashmi, A. A. Eftekhar, A. Adibi, and F. Amoozegar, “Analysis of telescope array receivers for deep-space inter-planetary optical communication link between Earth and Mars,” *Optics Communications*, vol. 283, no. 10, May, pp. 2032-2042, 2010.

[56] A. Hashmi, A. A. Eftekhar, A. Adibi, and F. Amoozegar, “Analysis of telescope arrays based receiver for deep-space optical communications with Mars,” in *Proc. IEEE LEOS Annual Meeting*, 2009, pp. 831-832.

[57] A. Hashmi, A. A. Eftekhar, A. Adibi, and F. Amoozegar, “Deep-space optical communication with Mars: achievable data rates,” presented at IEEE Southeast Conf. Atlanta, GA, 2009.

[58] A. Hashmi, A. A. Eftekhar, A. Adibi, and F. Amoozegar, “Optimization of focal plane detectors for mitigation of atmospheric turbulence effects in deep space optical communication,” in *Proc. Conf. on Lasers and Electro-Optics (CLEO)*, 2009.

[59] A. Biswas et al., “Approach for acquiring and tracking downlink from mars using the hale telescope,” in *Proc .of SPIE*, 2005, vol. 5712, no.1, pp. 60-71.

[60] A. Hashmi, A. A. Eftekhar, A. Adibi, and F. Amoozegar, “Statistical evaluation of an optical array receiver for deep-space laser communications under random pointing and tracking errors,” presented at Optics in the Southeast Conf. Charlotte, NC, 2006.

[61] A. Hashmi, A. A. Eftekhar, A. Adibi, and F. Amoozegar, “Effect of tracking errors on performance of telescope array receiver for deep-space optical communication,” in *Proc. IEEE Aerospace Conference*, 2007, pp. 1362-1369.

[62] A. Hashmi, A. A. Eftekhar, A. Adibi, and F. Amoozegar, "Telescope array receivers for deep-space laser communications: evaluation and statistical analysis of the performance under random tracking errors," *in preparation.*

[63] A. A. Eftekhar, A. Hashmi, A. Adibi, and F. Amoozegar, "The effect of synchronization errors on the performance of telescope arrays for optical deep space communications," in *Proc. IEEE Aerospace Conference*, 2006, pp. 1-7.

[64] A. Hashmi, A. A. Eftekhar, A. Adibi, and F. Amoozegar, "A Kalman filter-based synchronization scheme for telescope array receivers in deep-space optical communication links," *submitted*.

[65] J. A. Mendenhall *et al*., "Design of an optical photon counting array receiver system for deep-space communications," *Proceedings of the IEEE*, vol. 95, no. 10, Oct., pp. 2059-2069, 2007.

[66] G. Zogbi and L. M. Candell, "Signal acquisition and timing for a free space laser communications receiver," in *Proc. of SPIE*, 2007, vol. 6457, pp.1-14.

[67] F. I. Khatri, G. Zogbi, and D. M. Boroson, "Telescope divisibility limitations due to synchronization of array-based photon counting receivers in laser communications links," in *Proc. of SPIE*, 2008, vol. 6877, pp. 1-8.

[68] K. J. Quirk, J. W. Gin, and M. Srinivasan, "Optical PPM synchronization for photon counting receivers," in *Proc. IEEE Milcom. Conf.*, 2008, pp.1-7.

[69] F. Roddier, Ed., *Adaptive Optics in Astronomy*. United Kingdom: Cambridge University Press, 1999.

[70] M. L. Louarn, N. Hubin, M. Sarazin, and A. Tokovinin, "New challenges for adaptive optics: extremely large telescopes," *Monthly Notices of the Royal Astronomical Society,* vol. 317, no. 3, Sept., pp. 535-544, 2000.

[71] P. Wizinowich *et al*., "Adaptive optics developments at Keck Observatory," in *Proc. of SPIE* , 2006, vol. 6272, no.1, pp.1-9.

[72] R. Contos *et al*., "Laser guide star adaptive optics at the Keck Observatory," in *Proc. of SPIE*, 2003, vol. 4839, no.1, pp. 370-380.

[73] M. Xompero, A. Riccardi, and D. Zanotti, "Adaptive secondary mirror for LBT and its capacitive sensors: how can we calibrate them? " in *Proc. of SPIE*, 2008, vol. 7015, pp. 1-9.

[74] A. Hashmi, A. A. Eftekhar, S. Yegnanarayanan, and A. Adibi, "Analysis of optimal adaptive optics systems for hybrid RF-wireless optical communication for maximum efficiency and reliability," in *Proc. IEEE ICET'08*, 2008, pp. 62-67.

[75] A. Hashmi, A. A. Eftekhar, A. Adibi, and F. Amoozegar, "Adaptive optics based telescope arrays receiver for compensation of optical turbulence effects in a deep-space optical communication link with Mars," in *Proc. IEEE Globecom*, 2009, pp. 1-6.

[76] A. Hashmi, A. A. Eftekhar, A. Adibi, and F. Amoozegar, "Analysis of adaptive optics based telescope array receivers for compensation of atmospheric turbulence effects in a deep-space inter-planetary optical communications between Earth and Mars," *submitted.*

[77] V. A. Vilnrotter and M. Srinivasan, "Adaptive detector arrays for optical communications receivers," *IEEE Transactions on Communications*, vol. 50, no. 7, July, pp. 1091-1097, 2002.

[78] A. Hashmi, A. A. Eftekhar, A. Adibi, and F. Amoozegar, "A novel 2-D adaptive Wiener-filter-based algorithm for mitigation of atmospheric turbulence effects in deep-space optical communications," in *Proc. of SPIE*, 2009, vol. 7442, pp.1-10.

[79] A. Hashmi, A. A. Eftekhar, A. Adibi, and F. Amoozegar, "A novel STAP processor-based algorithm for mitigation of atmospheric turbulence effects in deep-space optical communications," *in preparation.*

[80] H. Hemmati, A. Biswas, and D. M. Boroson, "30-dB data rate improvement for interplanetary laser communication," in *Proc. of SPIE*, vol. 6877, 2008, pp. 1-8.

[81] D. M. Boroson, A. Biswas, and B. L. Edwards, "MLCD: overview of NASA's mars laser communications demonstration system," in *Proc. of SPIE*, vol. 5338, no.1, 2004, pp. 16-28.

[82] C. M. Stickley, M. E. Filipkowski, E. Parra, and E. E. Hach III, "Overview of progress in super high efficiency diodes for pumping high energy lasers," in *Proc. of SPIE*, vol. 6104, 2006, pp. 1-10.

[83] J. B. Glettler *et al*., "InP-based single-photon detector arrays with asynchronous readout integrated circuits," *Optical Engineering*, vol. 47, no. 10, Oct., pp. 100502(3), 2008.

[84] W. H. Farr, J. Gin, and D. Nguyen, **"**Gigahertz bandwidth photon counting," in *Proc. of SPIE*, vol. 7320, 2009, pp. 1-8.

[85] G. M. Smith, "Reliable InP-based Geiger-mode avalanche photodiode arrays," in *Proc. of SPIE*, vol. 7320, 2009, pp. 1-10.

[86] P. Yuan *et al*., "High performance InP Geiger-mode SWIR avalanche photodiodes," in *Proc. of SPIE*, vol. 7320, 2009, pp. 1-9.

[87] H. Hemmati, A. Biswas, and D. M. Boroson, "Prospects for improvement of interplanetary laser communication data Rates by 30 dB," *Proceedings of the IEEE*, vol. 95, no. 10, Oct., pp. 2082-2092, 2007.

[88] A. Biswas and S. Piazzolla, "Deep space optical communications downlink budget from Mars: System parameters," Jet Propulsion Laboratory, Pasadena, CA. Tech. Rep. IPN 42-154, 15 Aug. 2003.

[89] V. N. Mahajan and B. K. C. Lum, "Imaging through atmospheric turbulence with annular pupils," *Applied Optics*, vol. 20, no. 18, Sept., pp 3233-3237, 1981.

[90] R. Gallager, *Information Theory and Reliable Communication*, New York: Wiley, 1968.

[91] B. Moision and J. Hamkins, "Deep-space optical communications downlink budget: Modulation and coding," Jet Propulsion Laboratory, Pasadena, CA. Tech. Rep. IPN 42-154, 15 Aug. 2003.

[92] S. Haykin, *Adaptive Filter Theory,* New Jersey: Prentice Hall, 4th Ed., 2001.

[93] J. D. Barry and G. S. Mecherle, "Beam pointing error as a significant design parameter for satellite-borne free space optical communication systems," *Optical Engineering,* vol. 24, no. 6, Nov., pp. 1049-1054, 1985.

[94] J. D. Barry, K. J. Held, G. S. Merchele, and A. J. Einhorn, "Spacecraft system study: A study to define the impact of laser communication systems on their host spacecraft," Hughes Aircraft communication, Tech. Rep. FR 84-75-717, Apr. 1984: prepared for NASA Goddard Space Flight Center, Greenbelt, MD.

[95] A. Papoulis, *Probability, random variables, and stochastic processes*, New York: McGraw-Hill, c1991.

[96] P. Negrete-Regagnon, "Practical aspects of image recovery by means of the bispectrum," *Journal of the Optical Society of America A*, vol. 13, no. 7, July, pp. 1557-76.

[97] S. O. Rice, "The mathematical analysis of random noise," *Bell Sys. Tech. J.*, vol. 23, pp. 282-332, 1944.

[98] R. J. Noll, "Zernike polynomials and atmospheric turbulence," *Journal of the Optical Society of America*, vol. 66, no. 3, March, pp. 207-211, 1976.

[99] R. J. Sasiela and J. D. Shelton, "Transverse spectral filtering and Mellin transform techniques applied to the effect of outer scale on tilt and tilt anisoplanatism," *Journal of the Optical Society of America A*, vol. 10, no. 4, April, pp. 646-660, 1993.

[100] D. L. Fried, "Least-square fitting a wave-front distortion estimate to an array of phase difference measurements," *Journal of the Optical Society of America*, vol. 67, no. 3, March, pp. 370-375, 1977.

[101] R. H. Hudgin, "Wave-front reconstruction for compensated imaging," *Journal of the Optical Society of America,* vol. 67, no. 3, March, pp. 375-378, 1977.

[102] L. Baker, *C Tools for Scientists and Engineers*, New York: McGraw-Hill, 1989.

[103] M. A. Al-Habash, L. C. Andrews, and R. L. Phillips, "Mathematical model for the irradiance probability density function of a laser beam propagating through turbulent media," *Optical Engineering*, vol. 40, no. 8, Aug., pp. 1554-1562, 2001.

[104] E. L. Bass, B. D. Lackovic, and L. C. Andrews, "Aperture averaging of optical scintillations based on a spectrum with high wave number bump," *Optical Engineering*, vol. 34, no 1, Jan. pp. 26-31, 1995.

[105] R. K. Tyson, *Principles of Adaptive Optics*, Boston: Academic Press, 1998.

[106] Y. Fang and L. R. Taylor, "25 W Raman-fiber-amplifier-based 589 nm laser for laser guide star," *Optics Express*, vol. 17, no. 21, Oct., pp. 19021-19026, 2009.

[107] J. S. Lim, *Two-dimensional Signal and Image Processing*, New Jersey: Prentice Hall, 1990.

[108] Software Products [Online]. Available: http://www.ontar.com.

[109] Software Products [Online]. Available: http://www.oko.com.

VITA

ALI JAVED HASHMI

Hashmi was born in Sialkot, Pakistan. He received a B.E. in Avionics Engineering from National University of Science and Technology (NUST), Rawalpindi, Pakistan in 1996. In 2005, he came to Georgia Institute of Technology to pursue a Ph.D. degree in Electrical and Computer Engineering. He received a Masters in Science degree from Georgia Institute of Technology in 2006. His research interests include optical deep-space communications, adaptive filters theory, and adaptive controls. When he is not working on his research, Mr. Hashmi enjoys spending his time with his family, reading, running, and playing cricket with friends.